Solvothermal routes to new chalcogenide materials

Clare J. Crossland

Abstract

Chapter 1 reviews the literature on the use of solvothermal methods for synthesising metal chalcogenide materials and the structures of copper containing metal chalcogenide materials based on tetrahedral bonding motifs.

Chapter 2 contains details of the structural characterisation, physical property measurements and synthetic methods used throughout this work.

Chapter 3 summarises work on ways of modelling preferred orientation and anisotropic peak broadening in powder X-ray diffraction (PXRD) data using spherical harmonic functions; these are applied to data from compounds discussed elsewhere in this thesis.

Chapter 4 discusses the synthesis of Cu_2MX_4 materials (M = W or Mo; X = S, Se or S/Se) and PPh_4CuWSe_4 using a solvothermal method. The effects of synthesis temperature and pressure on the structures of the materials formed have been investigated. The materials have been characterised by PXRD, the structures of *I* Cu_2WS_4 and PPh_4CuWSe_4 have been solved from powder diffraction data; the structures of other materials have been determined by Rietveld refinement. Variable temperature diffraction experiments and physical property measurements have been performed on selected materials.

Chapter 5 describes structural studies on $(PPh_4)_2M(WS_4)_2$ (M = Co, Ni, Zn) materials. Single crystal diffraction has been used to further investigate the complex superstructure of the known polymorph of the zinc material. A new zinc polymorph has been discovered and its structure studied by PXRD. The structure of the Ni containing material has been determined directly from powder diffraction data.

Chapter 6 outlines preliminary work on materials which are tentatively described as M_xWS_2 intercalates. X-ray diffraction, magnetic measurements and Energy Dispersive X-ray Analysis have all been used to probe their properties.

Chapter 7 is a discussion of the structure solution of $(NH_4)_2WS_3O$ from powder diffraction data and a variable temperature diffraction experiment on the same material.

Solvothermal Routes to New Chalcogenide Materials

Clare J Crossland M.Sci (Dunelm)

Supervisor: Dr John S. O. Evans

A thesis submitted in partial fulfilment of the requirements for the degree of Doctor of Philosophy.

Department of Chemistry

University of Durham

2004

Acknowledgements

The completion of this thesis would not have been possible without the help of several people and I'm very grateful to them all:

My supervisor John Evans for endless patience and knowledge, for explaining things well even when they were very complicated and for giving me the chance to work in such a good group.

Ivana Evans for help with single crystal data collection and analysis, answering all my crystallography questions and most of all for encouragement; without her I wouldn't have started in the first place.

Rich for much advice and encouragement; Simon for showing me how it should be done; Ian for always looking out for me; Neil for showing me how things work, and fixing them when they didn't; Lue for all his help with things involving computers; Loc for always smiling and making tea and Graham for keeping me company after everyone else had gone home.

4th year project students: Malcolm Tait, Nick Warmingham, Rebecca Ward and Richard Harrington, for brightening up the lab with their various contributions. Special thanks to Pete Hickey for all his work on Cu_2WS_4, and for an amazing amount of resilience when things didn't work; and Sarah Lister for being a good friend.

Dr Richard Thompson for collection and analysis of RBS data.

Physicists: Dr. Ken Durose for help collecting SEM images and with EDAX analysis. Dr. Andy Brinkman, Dr. Rainer Schmidt and Ben Cantwell for help with conductivity measurements and Guillaume Zoppi for help with analysis of SEM images and I-V measurements.

Andy and Aileen for being great housemates and for doing all the cooking. Beth, Vics, Emma, Juliet, Ilona, Tara, Chris, Steph, Penny, Grace and Colm for keeping me out of trouble at the weekends. Andy M, Beezly, Bryony, Chris, Harry, Jonny K, Nick and Paul for much needed holiday relief.

Mum, dad, Edward, William and Robert, for support and a home to go to in the holidays.

Matt for putting up with me for all this time and for being my best friend.

Declaration and Statement of Copyright

The work described in this thesis is entirely my own, except where I have acknowledged help from a named person or given a reference to a published source or a thesis.

The research presented was performed in the Department of Chemistry, University of Durham between October 2001 and September 2004, the results of which have not been submitted for a degree in this or any other university.

Table of contents

Table of Figures

Table of Tables

Definitions and abbreviations

CSD	Cambridge Structural Database
DMF	N,N – Dimethylformamide
en	ethylenediamine
EDAX	Energy dispersive X-ray analysis
FOM	Figure of merit
fwhm	full width half maximum
PDF	Powder diffraction file
PV	pseudo-Voigt
PXRD	Powder X-ray diffraction
RBS	Rutherford back scattering
SEM	Scanning electron microscope
SQUID	superconducting quantum interferometry device
THF	tetrahydrofuran
TOPAS	Total Pattern Analysis System

1 Introduction

Metal chalcogenides are materials containing metal ions and ions of group sixteen elements; they may also contain other elements (*e.g.* N, H and C) in charge balancing cations. Research into metal chalcogenides has been driven by the possibility of producing materials with a wide variety of potentially exploitable properties. Potential applications of metal chalcogenides include their use in: non-linear optical devices, optical storage, radiation detection, solar energy conversion, catalysis, semiconducting components and other magnetic or electronic devices.

This thesis discusses the synthesis and characterisation of a number of chalcogenide materials containing either sulfur or selenium which have been synthesised by low temperature solvothermal routes. This introduction is split into two major areas, the first being a discussion of solvothermal synthesis methods and the way they have been applied to chalcogenide materials. The second part of the introduction is a review of the structural chemistry of copper chalcogenide materials which have structures based upon tetrahedral bonding motifs - these are particularly relevant when the structures of the materials synthesised during this work are considered.

1.1 Metal chalcogenides synthesised by solvothermal routes

The conventional method of synthesising metal chalcogenides involves reaction between stoichiometric quantities of solid reagents at high temperature. High temperatures must be used in order to allow the diffusion of atoms or ions required to form the product; consequently these reactions are usually thermodynamically controlled. Recently there has been much interest in milder methods of synthesis, including molten flux and solvothermal synthesis. Both of these methods rely on dissolving inorganic starting materials either in a molten salt (molten flux methods) or a solvent (solvothermal methods); they use much lower temperatures than the high temperature methods, typically 100 – 600 °C for molten flux methods and 100 – 400 °C for solvothermal methods. These reactions are of particular interest because they can proceed under kinetic control so favouring the production of metastable compounds and new low temperature phases.

Solvothermal techniques have been developed over many years. As long ago as 1845 Schafhäutl observed the growth of quartz micro crystals when silicic acid was transformed in a Papin's digestor.[1] Bunsen[2] used glass tubes to heat samples and generate pressure, this method was used to grow $BaCO_3$ and $SrCO_3$ crystals by cooling a solution from 200 °C and 15 bar. Since this time hydrothermal methods of synthesis have been of great importance in geological science, where they are used to investigate the formation of minerals. The pioneer in the use of solvothermal techniques for mineral synthesis was de Sénarmont[3] and the mineral proustite, Ag_3AsS_3, was one of the earliest

to be synthesised using this type of reaction. Since then there has been much development of the equipment used for this kind of synthesis, it is now even possible[4] to use extreme pressure and temperature conditions up to 100 kbar and 1500 °C. The method has been developed and used for several industrial applications, for example in the synthesis of optical quality synthetic emeralds, and in the production of CrO_2 for use in magnetic tapes. Synthetic zeolites, which are some of the most commercially significant synthetic materials, are also produced in closed solvothermal systems.

Solvothermal synthesis involves mixing reagents in a solvent and heating the mixture in a closed vessel under autogenous pressure at temperatures that are typically less than 400 °C. Under these conditions the solvent properties, for example density, viscosity and diffusion coefficient, are significantly different from the properties under ambient conditions. This affects the reactivity and solubility of the reactants, and allows them to thoroughly diffuse together; reactions can therefore occur at relatively low temperatures. The mild reaction conditions allow functional groups, for example rings, chains or polychalcogen units, to stay intact during the reaction, and remain present in the solid product phase. This can allow some control of the structure of the products produced. Solvothermal reactions are generally good for producing low symmetry and low density open crystalline structures made from individual structural units. It may not be possible to synthesise such materials at higher temperatures, as they are frequently less thermodynamically stable than other more dense products.

Solvothermal synthesis is versatile and there are many factors that can be changed in order to influence the identity, morphology and phase homogeneity of the product. As well as acting as a solvent there is also a possibility that solvent molecules can participate in reactions, aiding (or possibly hindering) the formation of products. A mineraliser can be added to facilitate reactions by transporting ions from the starting material to the site of product crystallisation and to enhance the solubility of reagents. There are also many examples of materials which have been synthesised in the presence of a structure directing agent, which can favour specific open framework structures. Counter ion size and charge, pH, time and reaction temperature are also important factors in determining the outcome of a reaction.

Although many solvothermal syntheses have targeted oxide containing phases, they have also been used to make materials containing the other chalcogenides: sulfur, selenium and tellurium. Much research has focused on producing chalcogenide materials with structures analogous to those of zeolites. While framework oxides are generally insulating, it is hoped that the use of other chalcogens in place of oxygen will give multifunctional materials in which properties like semiconduction and

luminescence can be combined with other framework properties such as shape selectivity.

The use of solvothermal synthesis to make chalcogenide materials has resulted in the discovery of a large and varied group of compounds. While it has been main group metal chalcogenides (containing in particular tin, indium, germanium, antimony and arsenic) that have been the most studied, the number of materials containing transition metals has been steadily growing. Many common themes are seen in the synthetic and structural chemistry of these materials. The use of structure directing agents and carefully selected starting reagents and synthetic conditions allows some materials to be specifically targeted. The targeting of particular structures is aided by the fact that many of the materials contain common structural units which can be linked to produce chains, layers or three dimensional frameworks.

The following sections discuss some of the synthetic aspects of producing binary metal chalcogenides (which are illustrative of principles that can be applied to other systems) and some of the structures of other metal chalcogenide materials that have been synthesised using solvothermal methods; these are classified according to the dimensionality of the structure.

1.1.1 Solvothermal synthesis of simple binary chalcogenides

Binary metal chalcogenides have a large number of technological applications in which the morphology and particle size of the material has a significant effect on its properties and potential uses. Synthesis methods where these can be controlled are therefore of particular interest. Solvothermal synthesis is one such method and it has been successfully used to make a large number of binary metal chalcogenides with specific particle morphologies and phase compositions. Many of the syntheses rely on the addition of reagents which participate in the reaction but remain in solution. Solvothermal synthesis makes it easy to add these reagents and to remove them by filtration when the solid product is formed. Some of the reaction conditions used to make different binary metal chalcogenides, along with the identities and morphologies of the products (where reported) are summarised in Table 1.1.

Metal	Reagents	Solvent	Product and morphology
Bi	$BiCl_3$, $Na_2S_2O_3$	H_2O	Bi_2S_3 rod like[5]
	$BiCl_3$, $Na_2S_2O_3$	EtOH	Bi_2S_3 rod like/lamella[5]
	$Bi_2(C_2O_4)_3$, X (X = S/Se/Te)	en	Bi_2X_3 [6]
Pb	$Pb(CH_3COO)_2$, X (X = Se/Te)	$NaOH/N_2H_4{\cdot}H_2O$	PbX spherical[7]
	$Pb(C_2O_4)$, X (X = S/Se/Te)	en	PbX [6]
Sn	$SnCl_4$, Na_2S	toluene	β SnS_2 [8]
	$SnCl_2$, Se	NaOH or $N_2H_4{\cdot}H_2O$	SnSe rod like[9]
	$SnCl_2$, Se	NH_3 or en	SnSe spherical[9]
Ag	$AgNO_3$, Te	N_2H_4 in NH_3(aq)	Ag_2Te Ag_7Te_4 [10]
Cd	Cd, X (X = S/Se/Te)	en	CdX rod like[11]
	Cd, X (X = S/Se/Te)	diethylamine/pyridine	CdX spherical[11]
	$CdCl_2$, CS_2, polyvinylpyrrolidone (PVP)	H_2O	CdS polymer capped nanoparticles[12]
Co	$CoCl_2$, $Na_2S_2O_3$	H_2O	CoS_2 cube shaped nanoparticles[13]
	$Co(CH_3COO)_2$, Na_2S	$N_2H_4{\cdot}H_2O$	CoS lamella[14]
Cu	CuCl, S, $Na_2C_2O_4$	en	$Cu_{1.80}S$, $Cu_{31}S_{16}$ polyhedral particles[15]
	CuCl, Se, $Na_2C_2O_4$	pyridine	$Cu_{2-x}Se$ irregular[15]
	CuCl, Te, $Na_2C_2O_4$	H_2O	$Cu_{1.75}Te$ spherical[15]
	$CuCl_2$	N_2H_4 in NH_3(aq)	$Cu_{2-x}Te$, $Cu_{2.86}Te_2$, Cu_7Te_5, CuTe [10]
Fe	$FeCl_3$, X (X = S, Se, Te)	H_2O, $N_2H_4{\cdot}H_2O$	Fe_7S_8 hexagonal plates[16]
			$FeSe_2$ rod like[16]
			$FeTe_2$ rod like[16]
Ni	$NiCl_2$, $Na_2S_2O_3$ or Na_2SeSO_3	H_2O	NiX_2 [13]
Mo	Na_2MoO_4, $Na_2S_2O_3$ or Na_2SeSO_3	NaOH, $N_2H_4{\cdot}H_2O$	MoX_2 [13]
Zn	$Zn(CH_3COO)_2$, Na_2S	H_2O, $N_2H_4{\cdot}H_2O$	ZnS [17]

Table 1.1 Summary of some synthetic conditions and particle morphologies for binary metal chalcogenides synthesised by solvothermal reactions.

Many binary chalcogenides have been synthesised solvothermally simply because it is a good way of producing crystalline materials. In these reactions the solvent does not directly participate in the reaction, but acts only as a medium in which crystallisation can occur. Factors such as the reaction time and temperature can change the size and crystallinity of the product. CoS and ZnS are both synthesised by reaction of their acetate salts with Na_2S in distilled water. In the case of cobalt, hydrazine must also be added in order for crystallisation to occur, though it is not believed to actually participate in the reaction.[14,17] Copper sulfides, selenides and tellurides can all be synthesised by reaction of CuCl, $Na_2C_2O_4$ and chalcogen powder in either ethylenediamine (sulfur), pyridine (selenium), or distilled water (tellurium) at temperatures between 180 °C and 240 °C. This methodology has been used to make several different copper chalcogenide materials, the nature of which depends upon the stoichiometry of the reagents used.[15] Bi_2S_3 can be made by reaction of $BiCl_3$ with $Na_2S_2O_3$ in either distilled water or ethanol. The morphology changes according to solvent, reaction temperature and reaction time, with water tending to favour rod like morphologies while reaction in ethanol favours the formation of a mixture of lamella and rod like particles.[5] Bi_2X_3 (X = S, Se, Te) can also be prepared by reaction of bismuth oxalate with chalcogen in pyridine or ethylenediamine. Choice of solvent is critical in determining the purity of the product produced by this reaction in the cases of the selenide and the telluride. In ethylenediamine the reaction goes to completion, while if the reaction is done in pyridine, a significant impurity is detected. The same effect is seen for the synthesis of PbX from lead carbonate and selenium/tellurium.[6]

The choice of solvent is also important in determining the outcome of the reaction for other metal chalcogenide syntheses. This is the case for reactions used to synthesise CdX (X = S, Se, Te), which can be produced by reaction of cadmium powder and chalcogen powder in diethylamide or a pyridine/ethylenediamine mixture, though not by reaction in benzene. In ethylenediamine the morphology of the crystallites is rodlike, whereas in diethylamine and pyridine the morphology is spherical.[11] It is also interesting to note that when the reaction takes place in diethylamine a metastable cubic phase of CdSe is formed in preference to the highly stable hexagonal form, an example of solvothermal synthesis being used to make a metastable phase.[18] For the synthesis of β - SnS_2, it is the solvent polarity which is very important, it has been prepared by reaction of $SnCl_4$ with anhydrous Na_2S in toluene. Toluene is a weakly polar solvent in which the reagents dissolve slowly and do not immediately react with each other, slow reaction favours production of a crystalline material. When the reaction was done in THF it occurred immediately on addition of the solvent to the solids, giving an amorphous material which could not be made crystalline by heating under solvothermal conditions.[8]

Several transition metal chalcogenides, MS_2 (M = Ni, Co) and $NiSe_2$, have been synthesised by reaction of $MCl_2.6H_2O$ with $Na_2S_2O_3/Na_2SeSO_3$ in distilled water. In this case the reaction can proceed under solvothermal conditions because the presence of a solvent allows redox active reagents to be used. The $S_2O_3^{2-}/SSeO_3^{2-}$ disproportionates to give SO_4^{2-} and S^{2-}/Se^{2-}; this then reacts with the M^{2+} to form the product.[13] Many other solvothermal syntheses are dependent on the addition of a reducing agent for reaction to occur; the reducing agent which has been used most commonly is hydrazine hydrate. Various non stoichiometric copper and silver tellurides can be made by reaction of $CuCl_2/AgNO_3$ and tellurium powder in water in the presence of hydrazine hydrate.[10] Fe_7S_8, $FeSe_2$ and $FeTe_2$ are synthesised by reaction of $FeCl_3$ and chalcogen powder in hydrazine hydrate solution. In this reaction the hydrazine hydrate reduces both the Fe^{3+} to Fe^{2+} and the elemental chalcogens to X^{2-} allowing reaction by an ion combination pathway. The ion combination can proceed at a temperature significantly lower than would be required for direct combination of the elements, allowing this reaction to occur at the relatively low temperature of 140 °C.[16] A similar mechanism is reported for the reaction of lead acetate with chalcogen in sodium hydroxide to form PbX (X = Se/Te).[7] SnSe can be synthesised from $SnCl_2$ and selenium in three different solvent mixtures: sodium hydroxide, ammonia and ethylenediamine or hydrazine hydrate. The hydrazine hydrate reduces the selenium forming Se^{2-} which then reacts directly with the Sn^{2+} to form the product. If hydrazine hydrate is not present excess Sn^{2+} is required to reduce the selenium. At low temperatures this reaction can only proceed in hydrazine hydrate; tin cannot be used as a reducing agent in these conditions. This has been rationalised in terms of the coordination of nitrogen containing solvents to the Sn^{2+}which prevents it from reducing the selenium. In the presence of nitrogen containing solvent species the reaction only proceeds at higher temperatures, where the nitrogen containing complexes are presumably destroyed.[9] Hydrazine hydrate is also used in the synthesis of MoS_2 from Na_2MoO_4 and $Na_2S_2O_3$; the corresponding $MoSe_2$ can also be prepared by this method. Though the S^{2-}/Se^{2-} can be produced from $S_2O_3^{2-}/SeSO_3^{2-}$ under these conditions, the hydrazine hydrate is required to reduce the molybdenum from Mo^{6+} to Mo^{4+}, $Na_2S_2O_3$ not being sufficiently reducing to achieve this transformation.[13]

One final particularly interesting solvothermal reaction is used when synthesising CdS from $CdCl_2$ and CS_2. The reaction can be done in the presence of PVP (polyvinylpyrrolidone). Addition of this polymer to the reaction mixture results in the formation of nanocrystals of cadmium sulfide capped by polymer. This improves the luminescent properties of the nanoparticles and represents a novel and technologically important adaptation of the solvothermal methodology.[12]

1.1.2 0D chalcogenides prepared by solvothermal routes

Zero dimensional, or molecular materials can be defined as those containing species which are not linked but occur in isolated groups within the solid. Several materials of this type have been synthesised by solvothermal reaction. Many different types of group can be present in these materials, including isolated tetrahedra, units made by connecting a number of smaller building blocks together, and much more complex cluster species. The types of unit seen vary from metal to metal and structures are discussed according to which metal they contain.

For zero dimensional tin compounds, there are direct relationships between the tin species present in different materials. $Sn_2Se_6^{4-}$ units, made up of two edge linked $SnSe_4$ tetrahedra, are found in the $[M(en)_3]Sn_2X_8$ (M = Mn, Zn, X = Se, Te) series of compounds[19] and in $A_4Sn_2Se_6$ (A = Rb,[20] Cs[21]). If two of these units are linked together by sharing a common corner the $Sn_4Se_{11}^{4-}$ unit can be made, this is found[22] in $K_6Sn_4Se_{11}\cdot 8H_2O$ and in $Rb_6Sn_4Se_{11}\cdot xH_2O$.

The species found in antimony sulfides contain a more diverse range of different units. In $[Fe(en)_3][enH]SbSe_4$ there are simple $SbSe_4$ tetrahedra. In $[Fe(en)_3]Sb_2Se_5$ however, the units are $Sb_2Se_5^{4-}$ anions, which contain Sb in trigonal prismatic coordination; one of the three selenium atoms in the trigonal prism is shared with another antimony atom to form the $Sb_2Se_5^{4-}$ units.[23] These antimony and tin structural units are shown in Figure 1.1.

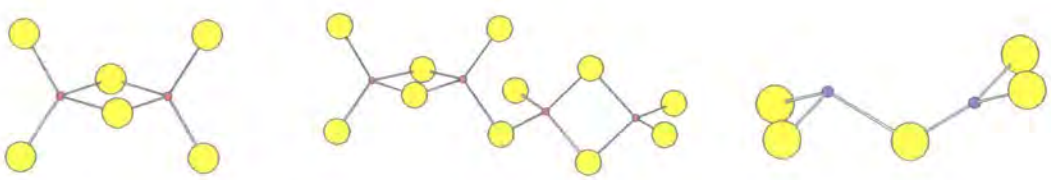

Figure 1.1 The structures of some tin and antimony building blocks. Left: $Sn_2Se_6^{4-}$, middle: $Sn_4Se_{11}^{4-}$ and right: $Sb_2Se_5^{4-}$. Sn is shown in red, Sb in purple and Se in yellow.

The structure of $[C_6H_{16}N]_4In_4S_{10}H_4$ contains isolated $In_4S_{10}H_4$ units. These adamantane-like cages consist of a ring of three corner linked InS_4 tetrahedra, with a fourth InS_4 tetrahedron bonded to all of them. This is shown in Figure 1.2. The terminal sulfur ions have hydrogen atoms bonded to them to give the cages overall charge neutrality.[24]

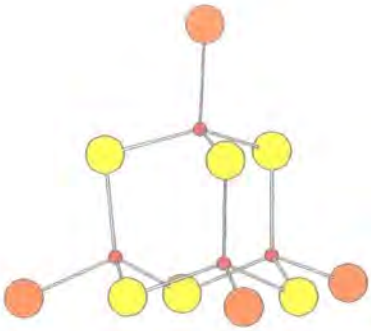

Figure 1.2 The $In_4S_{10}^{4-}$ adamantane like unit, In^{4+} is shown in red, bridging S^{2-} ions in yellow and terminal S^{2-} ions in orange.

The molybdenum selenide clusters found in $(NMe_4)_2Mo_3Se_{13}$ are much more complex in nature than the relatively simple species in the indium, antimony and tin compounds. The units, of formula $Mo_3Se_{13}^{2-}$, consist of a triangular core of molybdenum, a triply bridging Se, two doubly bridging Se_2 units and three terminal Se_2 units.[25] This reflects the ability of selenium to form polyanionic ligands such as S_n^-/Se_n^- which gives rise to a structural flexibility not found in metal oxides.

1.1.3 1D chalcogenides prepared by solvothermal routes

The presence of 1D chains in metal chalcogenide materials is generally favoured by the inclusion of bulky cations, for example $[M(en)_3]^{n+}$ and some of the larger amines, though chains can also form in the presence of simple alkali cations. Many different types of chain are formed; the nature of the chain varying drastically depending on which metals and chalcogenides are present.

$[Ga(en)][GaSe_7(en)]$ and $[Fe(NH_3)]_6AgES_4$ (E = As, Sb) both contain cations made up of metals coordinated to amines; amines were used as the solvent for the synthesis of both materials and ended up being incorporated into the cationic species in the final material. The structures of these materials both consist of chains of edge sharing tetrahedra. GaS_4 units are linked in the gallium material while in the $[Fe(NH_3)]_6AgES_4$ the chains consist of alternating AgS_4 and ES_4 tetrahedra.[26,27] Another material which has chains made by simple linking of tetrahedra is $Cs_2Sn_2Se_5.xH_2O$, in which the chains are an array of pairs of edge linked $SnSe_4$ tetrahedra which link to each other by sharing corners.[22]

The exact nature of the cation can change the bonding within the anionic chains. This is demonstrated by a series of indium tellurides and a series of mercury tellurides, which also incorporate the solvent as a ligand in the cations. $[La(en)_4Cl]In_2Te_4$, $[M(en)_3]In_2Te_6$ (M = Fe, Zn) and $[Mo_3(en)_3Te_3OTe]In_2Te_6$ all contain subtly different counter ions. In $[La(en)_4Cl]In_2Te_4$ the anionic chains are made from edge sharing $InTe_4$ tetrahedra, in

the other two materials however, the $InTe_4$ tetrahedra are linked by either Te or Te_2 units. Similar structural relationships are seen in $[M(en)]_3Hg_2Te_9$ and $[M(en)_3]_2Cl_2Hg_2Te_4$. In the first of these two compounds, five membered Hg_2Te_3 rings are linked by Te_3 units, while in the second, the Hg_2Te_3 rings are linked via sharing of one of the Te atoms in the ring.[19]

Syntheses of many of the one dimensional antimony sulfides have used amines as structure directing agents. $Sb_3S_5 \cdot N(C_3H_7)_4$ contains antimony sulfide rings, in which the antimony is located in an approximately pyramidal coordination environment. These rings are linked to form one dimensional chains.[28] This structure is illustrated in Figure 1.3.

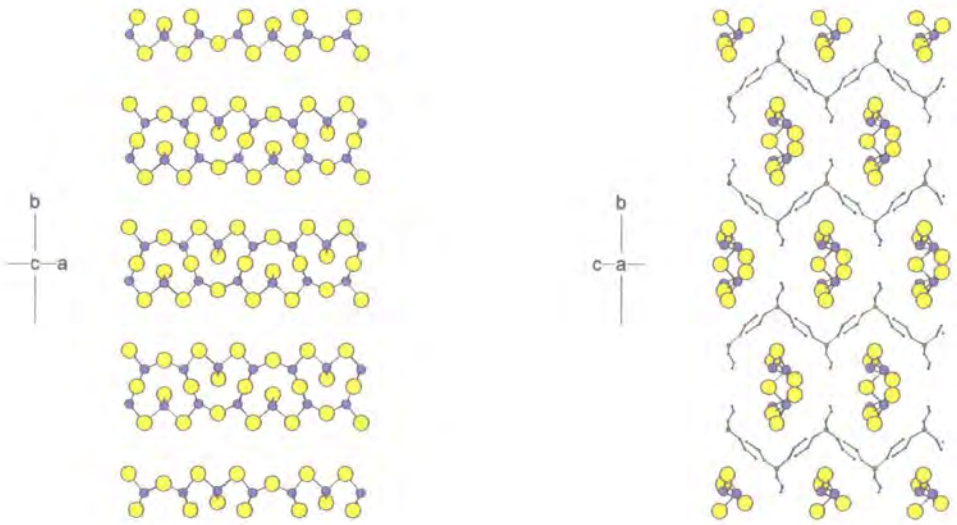

Figure 1.3 The structure of antimony sulfide $Sb_3S_5 \cdot N(C_3H_7)_4$ showing the chain structure without the cations (left) and a view down the chain direction with cations included (right). Sb is shown in purple, S in yellow, N in red and C in blue.

Although they are not present in $Sb_3S_5 \cdot N(C_3H_7)_4$, other arsenic and antimony sulfides often contain the so-called semicube unit; a six membered E_3X_3 ring of alternating E and X, with a fourth X coordinated to one of the E ions. In $(Me_4N)_2As_6S_{10}$, chains are formed by linking the arsenic sulfide semicubes with single sulfur atoms.[29] The structures of $(Me_4N)_2As_4S_7$, $(NH_4)_2Sb_4S_7$ and $H_2(pip)Sb_4S_7$ all contain chains made up of E_3S_4 semicubes linked by corner sharing with a trigonally coordinated ES_3 unit,[28,30,31] this chain type is shown in Figure 1.4. These structures are very similar to that of $Sb_4S_7 \cdot N_2C_4H_8$, discussed in section 1.1.4. If two of these chains are linked together by sharing one of the vertices of the ES_4 unit, then double chains can be formed; these are found[29] in materials like $Et_4As_8S_{13}$.

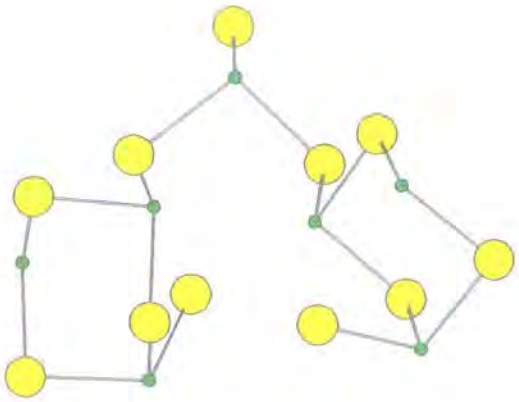

Figure 1.4 An $As_4S_7^{2-}$ chain consisting of As_3S_4 semicubes linked by trigonal AsS_3 units. As is shown in green, S in yellow.

The structure of the chains in $A_2Ag_2GeS_4$ (A = K, Rb) is quite special because they are helical in nature and the structure consists of a mixture of both right handed and left handed chains. Like many materials which contain silver and sulfur, this material was synthesised in the presence of a chelating agent $HSCH_2CH(SH)CH_2OH$, which prevents the formation of silver sulfide, Ag_2S. The chiral helical chains are formed by linking GeS_4 tetrahedra with linear S – Ag – S bridges. Each pair of GeS_4 tetrahedra is linked via two such bridges and it is the relative orientations of these links which gives the chains their chirality.[32]

$K_2Mo_3Se_{18}$ is another molybdenum selenide material which contains complex clusters. The chains are made from $Mo_3Se_7^{4+}$ building blocks, these are connected by Se_3^{2-} and Se_4^{2-} polyselenide units to form zigzag chains.[33] This material contains four different polyselenide units (Se^{2-}, Se_2^{2-}, Se_3^{2-} and Se_4^{2-}) which act as ligands for the molybdenum, again showing the flexibility of heavier chalcogens compared to oxygen.

1.1.4 2D chalcogenides prepared by solvothermal routes

Layered materials are produced when continuous bonding is only present in two dimensions. Often the structures of layered materials are closely related to those of one dimensional materials, but the chains have somehow been linked together, or reside close enough in space to be considered slabs rather than chains.

The indium compounds $[Et_2NH_2]_6In_{10}S_{18}$ and $[C_{13}H_{14}N_2]_4In_9S_{17}$ form in the presence of amines which are incorporated into the structure as templating agents.[24] Both of these materials contain layers of linked indium sulfide clusters. In the first material the cluster is the $In_{10}S_{18}$ supertetrahedron, that is also present in some three dimensional materials discussed in section 1.1.5. These supertetrahedra are corner linked to form layers. The cluster present in $[C_{13}H_{14}N_2]_4In_9S_{17}$ is the In_9S_{20} cluster which is formed by two edge shared adamantane ($In_4S_{10}^{8-}$) units which have two bridging InS_4 tetrahedra attached to

them, these clusters are linked together via corner and edge sharing of the tetrahedra within the clusters. In the indium telluride material $[Ga(en)_3]In_3Te_7$, the layers are made of $InTe_4$ tetrahedra which are linked in two dimensions to form layers. The tetrahedra are linked by a mixture of corner sharing and bonding of two Te atoms to each other.[19]

$(^nPr_4N)Sn_4S_9$ is a material containing Sn_3S_4 semicubes which, like the antimony and arsenic analogues, are clusters consisting of a six membered Sn_3S_3 ring bridged by a fourth sulfur atom. Edge bridged pairs of these semicubes are then linked via SnS_4 units giving layers made up of distorted elliptical rings.[34] The structure is shown in Figure 1.5.

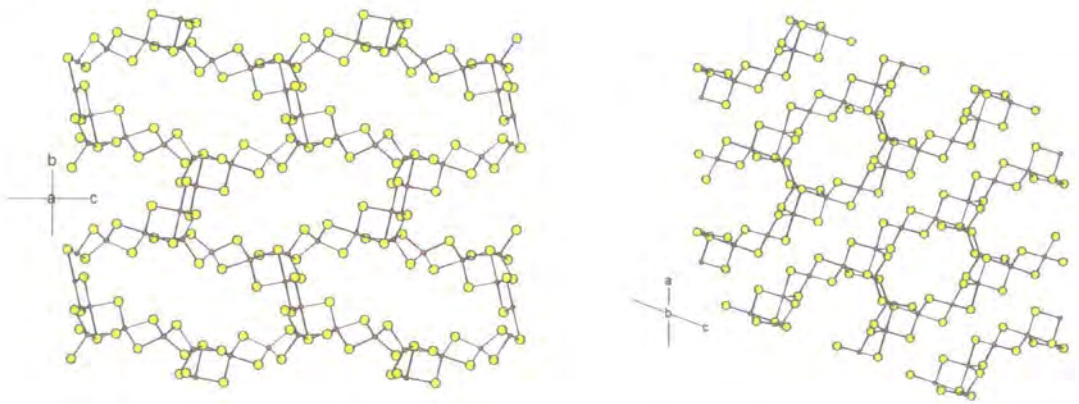

Figure 1.5 The structure of $(^nPr_4N)_2Sn_4S_9$ viewed down the *a* axis (left) showing the distorted elliptical rings and down the *b* axis (right) showing the layered structure. Sn is shown in red and S in yellow, the amine molecules are omitted for clarity.

If the amine is replaced by a metal cation such as Rb or Cs as in $A_2Sn_4Se_9 \cdot H_2O$, similar layers can also be formed.[35] In contrast, the layers in $Cs_4Sn_4Se_{10} \cdot 3.2H_2O$ contain chains of $SnSe_5$ trigonal bipyramids, which link via sharing of two of the vertices. These chains are linked with a $Sn_2Se_6^{4-}$ unit (two edge sharing SbS_4 tetrahedra) to form layers.[36]

The presence of silver as well as tin in $K_4Ag_2Sn_3S_9 \cdot 2KOH$ gives layers of $AgSn_3S_9^{2-}$ containing "adamantane like" clusters that are connected by three coordinate Ag^+ cations. Though the clusters are linked, the positions of the linking silver bridges are such that the material has voids within the layers and it is these voids, not the ones between the layers, that contain the K^+ ions.[37]

Sb_3S_4 semicubes are the building unit in the templated antimony sulfide $Sb_4S_7 \cdot N_2C_4H_8$. The semicubes are linked via SbS_3 pyramids to form rings. Although these are only actually bonded in one dimension to form chains, the chains are very close together in space so the structure is best considered to be two dimensional rather than one dimensional.[28] Chains of Sb_3S_4 semicube units linked by SbS_3 trigonal pyramids are

also present in $Cs_6Sb_{10}S_{18}\cdot 1.2H_2O$; in this case the chains are linked by Cs atoms to form layers.[38] Incorporation of copper into the antimony sulfide framework has given some novel materials containing intercalated ethylenediamine molecules between the layers. The layers consist of antimony atoms in a tetrahedral environment consisting of 3 sulfur atoms and one copper atom. The ethylenediamine molecules can be incorporated either parallel ($Cu_2SbS_3\cdot 0.5en$) or perpendicular ($Cu_2SbS_3\cdot en$) to the layers. In contrast, the caesium containing copper antimony selenide, $Cs_2Cu_2Sb_2Se_5$, contains layers in which antimony selenide trigonal pyramids are linked by sharing selenium atoms in copper tetrahedra.[19]

As in the mercury telluride chain structures, the layered mercury telluride $Rb_2Hg_3Te_4$ contains rings of alternating Hg and Te atoms. There are both six (Hg_3Te_3) and eight (Hg_4Te_4) membered rings which are fused together in order to create layers.

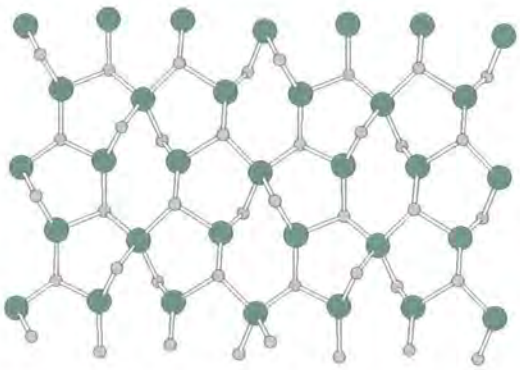

Figure 1.6 A single layer from $Rb_2Hg_3Te_4$ showing its structure of linked rings. Hg is shown in green, Te in grey. Rb is omitted for clarity.

In the presence of antimony however, for example in $AHgSbSe_3$ (A = Rb, Cs) and $RbHgSbTe_3$, it is possible to have HgX_4 tetrahedra. These are linked by sharing X atoms with trigonally coordinated SbX_3.[19]

Both $RbCu_{1.2}Ag_{3.8}Se$ and $CsPdSe_{16}$ contain square planar MSe_4 units which are linked to form layers. In the palladium compound, the $PdSe_4$ units are linked by Se_2^{2-} to form a continuous layer; caesium is accommodated in voids within this layer. This layer alternates with $CsSe_8$ layers, in which caesium ions are located within eight membered rings of selenium. $RbCu_{1.2}Ag_{3.8}Se$ consists of square planar $AgSe_4$ units, which reside in a plane, the other metal atoms are trigonally coordinated to selenium and reside above and below the plane of the $AgSe_4$ units.[19]

1.1.5 3D chalcogenides prepared by solvothermal routes

Much of the work that has been performed on solvothermal synthesis of metal chalcogenides has been driven by the desire to produce open framework materials analogous to zeolites. Zeolites are made from SiO_4 units but unfortunately the SiX_4

(X =S, Se, Te) unit is unstable to hydrolysis, so synthesis of analogous structures from these is not possible under hydrothermal conditions. There has been much work that has looked at making open framework structures from other chalcogenide building blocks. One synthetic strategy that has been successfully used to make a large number of open framework materials is to replace the simple tetrahedron with other larger species, such as the Ge_4X_{10} (X = S, Se) adamantane unit and the $In_{10}S_{20}$ supertetrahedron. By linking these units together, framework structures can be produced.

The presence of individually linked GeX_4 (X = S, Se) tetrahedra is very rare in three dimensional solids synthesised solvothermally, though it is present in $Na_2Ge_2Se_4$, in which the tetrahedra are corner linked together.[39] Much more common is the Ge_4X_{10} adamantane cage, present in materials such as $CuGe_2S_5{\cdot}(C_2H_5)_4N$ and $MnGe_4S_{10}{\cdot}2(CH_3)_4N$.[40,41] Both of these are prepared in the presence of structure directing amines and consist of Ge_4S_{10} cages linked via coordination of the copper or manganese centres to terminal sulfide ions of the adamantane cage. In the copper material, the linkages are linear, while in the manganese material the Mn^{2+} has a distorted tetrahedral geometry; this structure can be seen in Figure 1.7.

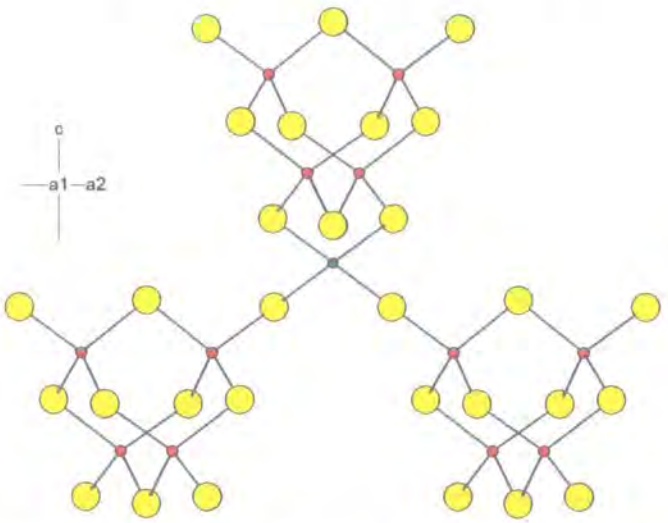

Figure 1.7 The structure the metal sulfide framework in $MnGe_4S_{10}{\cdot}2(CH_3)_4N$ showing an MnS_4 tetrahedron linking Ge_4S_{10} units. Mn is shown in green, Ge in red and S in yellow.

Similar materials have been prepared by linking Ge_4X_{10} cages with Ag,[42] Fe, Cd, Co,[43] Ag_2 and Cu_2 dimers[44] and synthesised using a variety of different amine templates.[45,46] Germanium sulfide networks can also be synthesised in the presence of alkali cations. $A_3AgGe_4Se_{10}{\cdot}2H_2O$ and $A_2[MnGe_4Se_{10}]{\cdot}3H_2O$ (A = Rb, Cs) have metal linked Ge_4S_{10} frameworks analogous to those of materials made using amines as the structure directing agents.[47]

More recently, surfactant molecules have been used as structure directing agents to produce a number of hexagonal mesostructured metal germanium sulfide and selenide materials, some of which have structures analogous to the MCM-n family of mesoporous silicates. These also consist of Ge_4X_{10} adamantane units linked by metal ions which can form materials with a high degree of hexagonal order. An example of a TEM image obtained for a material of this type, containing Ge_4S_{10} units linked using indium ions and templated by cetylpyridinium bromide,[48] is shown in Figure 1.8.

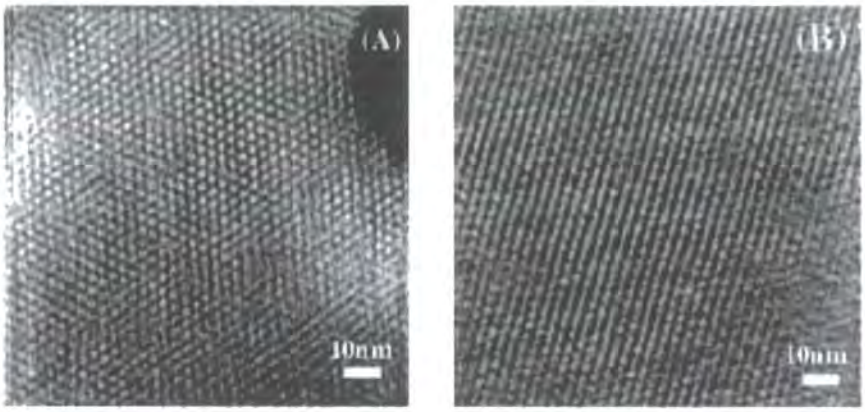

Figure 1.8 TEM images for an indium germanium sulfide framework viewed parallel to the pore tunnels (left) and perpendicular to the tunnels (right). Reproduced from reference 48.

Surfactant templates tend to result in materials which contain much larger pores than those templated by amines. The chain length of the surfactant molecule used to template the structure can be used to tune the size of the pores within it.[49-53]

Similar *nano-* and *meso-* porous materials have been synthesised using tin sulfide and selenide units to make the framework. These tin compounds are different from the germanium compounds because they are built directly from the SnX_4 unit which is a structural analogue of the SiO_4 unit. One such group of materials were synthesised by reaction of metal salt with surfactant and K_4SnSe_4 in formamide.[54] This gave materials of general formula $(Cpy_2)MSnSe_4$ (where M = Mn, Fe, Co, Zn, Gd and Hg; Cpy = cetylpyridinium). Variation of the metal ion and the synthetic conditions used gives different structures varying from disordered wormhole structures, to hexagonal and cubic phases. Although structures with large pores have often been the target of synthesis, more condensed tin phases have also been made[55], for example $Rb_2Sn_2Se_5$. The structure contains chains of edge sharing $SnSe_5$ trigonal bipyramids; the chains are linked into a framework by additional corner sharing of selenium ions.

The structural chemistry of solvothermally synthesised indium sulfides has also been extensively investigated in the search for open framework chalcogenide materials. Many of these contain species such as the $In_{10}S_{20}$ supertetrahedron and the In_4S_{10} adamantane unit though the supertetrahedron is by far the more common. In order to

favour large cavity sizes the indium sulfides are synthesised in the presence of structure directing amines. $In_{10}S_{18}\cdot(HPP)_6(H_2O)_{15}$ and $In_{10}S_{18}\cdot(C_{10}N_2H_{22})_3(H_2O)_7$ use 1,3,4,5,5,8-hexahydro-2H-pyrimido[1,2,α]pyrimidine (HPP) and dipiperidinomethane respectively. Both of these materials are open framework materials containing large cavities, the maximum size of a sphere that could fit in these cavities is ~25.6 Å for $In_{10}S_{18}\cdot(HPP)_6(H_2O)_{15}$ and ~17.2 Å for $In_{10}S_{18}\cdot(C_{10}N_2H_{22})_3(H_2O)_7$, indicating the open nature of the frameworks.[56] $In_{10}S_{18}\cdot(C_6H_{12}NH_2)(C_6H_{12}NH)(H_2O)_5$ has slightly smaller cavities of ~10.9 Å diameter.[57] A representative structure of one of these indium sulfide materials is shown in Figure 1.9.

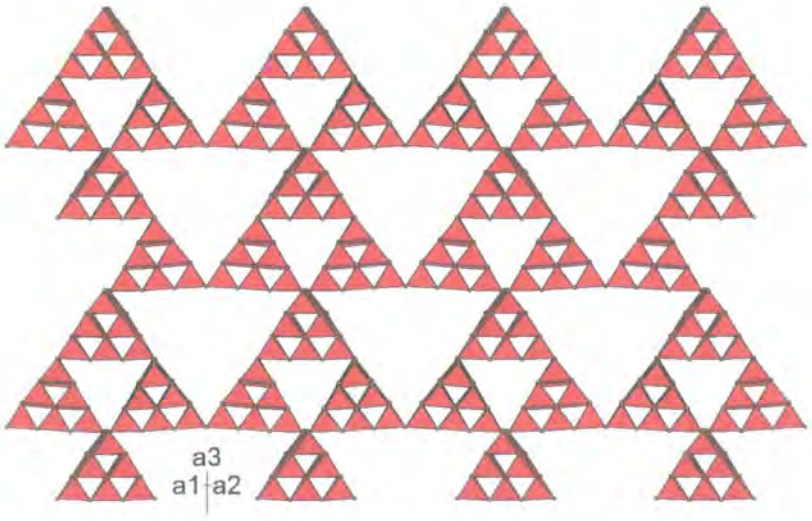

Figure 1.9 Part of the framework of $In_{10}S_{18}\cdot(HPP)_6(H_2O)_{15}$. In tetrahedra are shown in red and S in yellow. Water and HPP are omitted for clarity.

Frameworks based on antimony have not been synthesised with porous structures like the tin, indium and germanium frameworks, but several more condensed frameworks have been made. In $Sb_2S_5\cdot Me_4N$ the antimony is contained in trigonal bipyramidal coordination with 4 sites occupied by sulfur and the fifth site occupied by a lone pair of electrons. The structure is made up of sheets of edge linked Sb_2S_2 rings that are in turn linked to give a structure with channels running in two different directions through it.[58] The structure of $CuSb_6S_{10}\cdot[C_4H_{12}N_2]_{0.5}$ contains $Sb_3S_6^{3-}$ rings made by three trigonally coordinated SbS_3 units sharing corners. In this material the rings adopt a boat-like conformation which contrasts with the Sb_3S_3 rings found in the antimony sulfide semicubes which have a chair-like conformation. These rings are linked to give two dimensional layers which are linked into a three dimensional framework by copper ions.[59]

1.1.6 Summary

Solvothermal synthesis is a very versatile method of synthesising metal chalcogenides. The addition of reagents to reaction mixtures can promote desirable reactions and the

choice of solvent can change the properties and morphology of the materials formed. A lot of syntheses have made use of templating agents in order to favour particular structural types. The solvent can play a very important part: as well as acting as a reaction medium in which reagents can diffuse together, it can sometimes be incorporated into the structure. There are many common structural themes in the materials synthesised. Different metals often form particular structural units and these can be linked together to form chains, layers or frameworks.

As much of the work discussed here demonstrates, there is significant potential for targeted synthesis of metal chalcogenides. The tendency of particular metals to form specific structural building units provides a potential route to materials with specific types of structure. However, there is still much work to be done in order to understand the complex relationships between synthetic conditions and the properties and structure of the materials formed. The work presented in this thesis attempts to expand the work done in this area by using solvothermal synthesis to target some materials made from MoX_4 and WX_4 (X = S, Se) building units.

1.2 Copper chalcogenide structures

This thesis describes the synthesis and characterisation of several copper chalcogenide materials; it is therefore appropriate to consider the structures of other copper chalcogenides which have been previously studied. In view of the structures of the materials discussed later, the focus of this section is materials in which the metal ions are contained in tetrahedral chalcogenide environments. The only exceptions to this are the coordination geometries of Group 1 and 2 metals, which are generally present as charge balancing cations in the structures; no restrictions have been placed on their coordination geometries.

The structures can broadly be categorised into two different groups of similar structures. The first group of structures are those based on close packed sulfide or selenide lattices. The structural differences are the result of occupation of different tetrahedral metal sites within the lattices. The second category is materials which contain charge balancing Group 1 and 2 metal cations as well as metal chalcogen tetrahedra. Among these are materials containing chains, separated layers and continuous frameworks. They will be discussed in groups according to the dimensionality of the structure (1D, 2D or 3D).

1.2.1 Structures based on close packed chalcogenide arrays

Many copper chalcogenide materials have structures that are related to the wurtzite or zinc blende structure types; the zinc blende structure is in turn related to the antifluorite structure. These are all structures in which metal atoms occupy tetrahedral sites within a

close packed anion array, the array being cubic close packed in the case of zinc blende and antifluorite, and hexagonal close packed in the case of wurtzite.

A cubic close packed lattice of anions contains twice as many tetrahedral holes as there are anions; in the antifluorite structure (*e.g.* Na_2O) all of these holes are occupied by metal atoms. The structure contains MX_4 tetrahedra, edge linked in three dimensions to form an infinite array. If all of the metal atoms located just below (or above) a close packed layer (see Figure 1.10) are removed, an infinite array of corner linked tetrahedra remains; this is the zinc blende structure. Equivalent views of the two structures, emphasising the close packed layers, are shown in Figure 1.10.

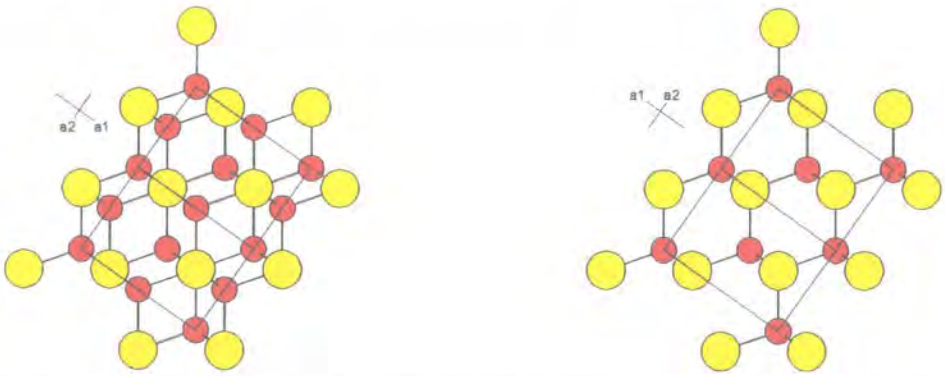

Figure 1.10 The antifluorite (left) and zinc blende (right) structures showing the close packed anion layers in a horizontal direction. Cations are shown in red, anions in yellow.

The wurtzite structure is similar to zinc blende in that it also has half of the tetrahedral holes in the close packed lattice occupied by metal atoms. However, instead of a cubic close packed lattice, the lattice is hexagonal close packed. The structure is shown in Figure 1.11.

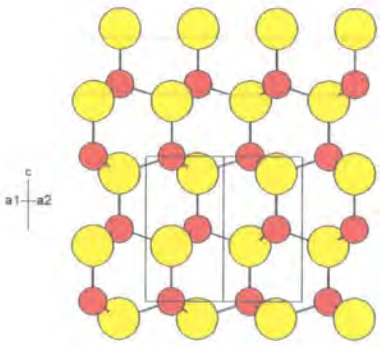

Figure 1.11 The wurtzite structure, close packed anion layers are horizontal. Cations are shown in red, anions in yellow.

The antifluorite and zinc blende structures can also be thought of as a series of layers stacked up along the *c* direction that are alternately occupied by cations and anions (note these anion layers are not the cubic close packed layers emphasised in Figure 1.10).

Viewing the structures in this way allows a simple description of the ordering of metal atoms within the occupied tetrahedral sites which can easily be compared to other materials with related structures. The alternate views of the two structures and schematic representations of the occupancy of metal sites are shown in Figure 1.12.

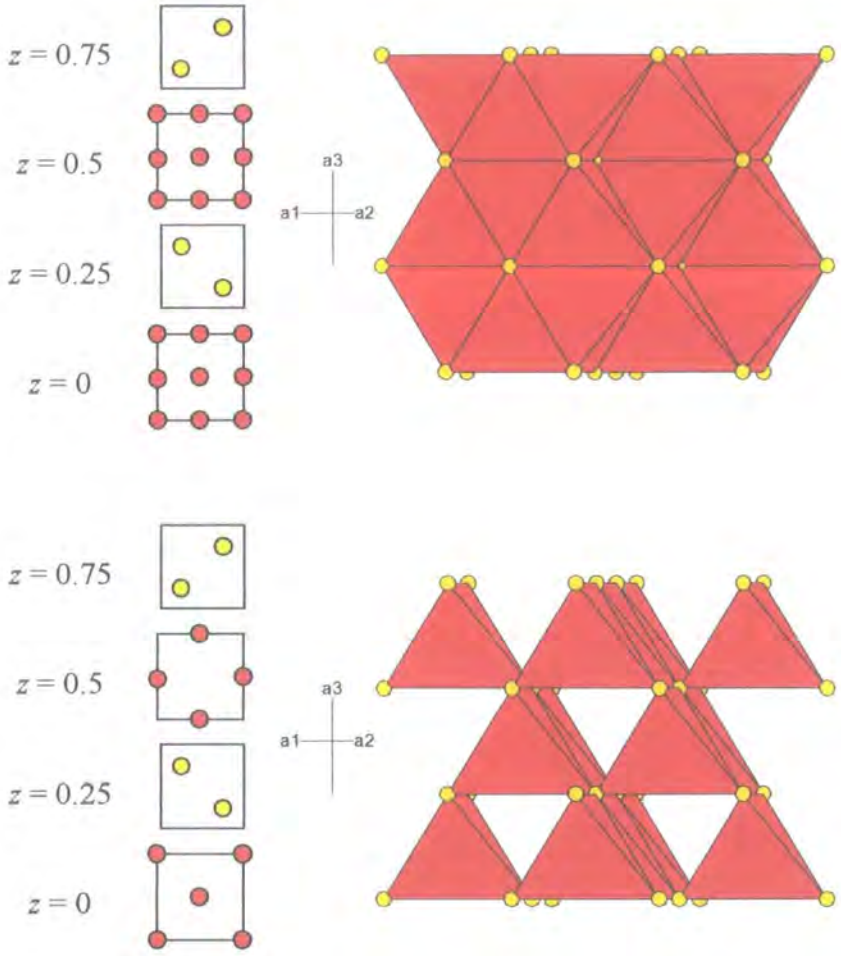

Figure 1.12 Schematic representations of metal ordering in the *ab* plane (left) and polyhedral views (right) of the antifluorite (top) and zinc blende (bottom) structures. Cations and cation centred tetrahedra are shown in red and anions in yellow.

The first group of structures described in this section are all related to the antifluorite and zinc blende types. The materials have unit cells of similar dimensions, with lattice parameters of $a = b \approx c \sim 5 - 6$ Å for primitive cells and $a = b \sim 5 - 6$ Å, $c \sim 10 - 11$ Å for body centred cells. The chalcogenide ions within these cells are located at positions of $x = y \approx z \sim 0.25$ for the primitive cells, $x = y \sim 0.25$, $c \sim 0.25/2$ for the body centred cells. The cubic close packed lattice of chalcogenide ions contains eight crystallographically independent tetrahedral holes and filling of different metal sites gives a variety of networks of tetrahedra, linked by both edge and corner sharing, with two or three dimensional structures. There are seven different structures of this type that have been reported to date; structural differences arise because of variations in the occupancy and metal ordering on the tetrahedral sites, structural details for these are

given in Table 1.2. There are a number of different materials which have each type of structure, some of these have fully ordered metal occupancies on the tetrahedral sites; others show disordered or partial metal occupancy. Representative examples of materials with the different structures are also included in the table.

Structure	Space group	Number of T_d sites occupied	Dimensionality	Types of T_d link	Example compound	Ref.
1	$F\bar{4}3m$	8	3D	E & C	$(Cu_2Fe_2S_3)_{1.33}$	60
2	$P\bar{4}$	4	3D	C	Cu_2FeSnS_4	61
3	$I\bar{4}2m$	4	3D	C	Cu_2MnSnS_4	62
4	$I\bar{4}2d$	4	3D	C	$CuFeS_2$	63
5	$P\bar{4}3m$	4	3D	E	Cu_3VS_4	64
6	$I\bar{4}2m$	5	3D	E & C	Cu_4TiS_4	65
7	$P\bar{4}2m$	3	2D	E	Cu_2WS_4	66

Table 1.2 Summary of structural details and example compounds for structures based on cubic close packed lattices with different metal occupancies; E indicates that layers of metal tetrahedra share edges, C indicates sharing of corners.

The first of the structures is shown in Figure 1.13 and represents the case where all of the available metal sites are occupied.

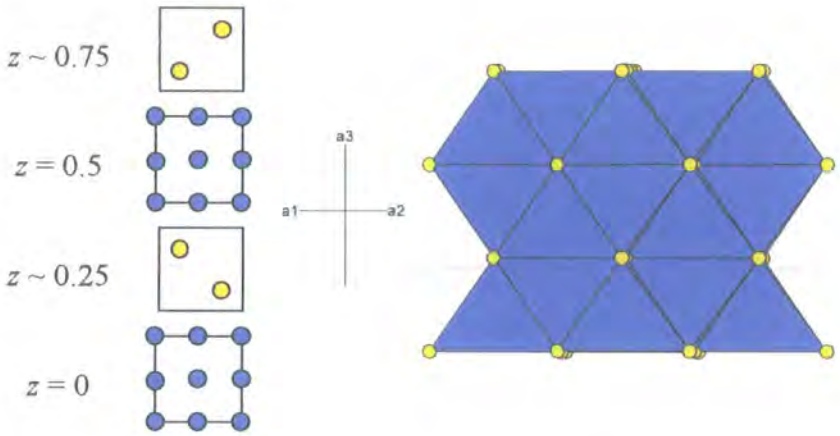

Figure 1.13 Schematic (left) and polyhedral (right) representations of structure 1 (see Table 1.2). S atoms are shown in yellow, metals and metal polyhedra are shown in blue.

This structure is related to the antifluorite structure. The ratio of cation sites to anions suggest that materials with this structure should have the general formula M_8X_4, but some materials which have this structure type do not have this metal to chalcogen ratio. For example, $(Cu_2Fe_2S_3)_{1.33}$ has general formula $M_{5.333}S_4$; the metal sites are only partially occupied, additionally metal atoms are disordered over the tetrahedral sites within the anion lattice.

The other structures within this family include cases with both primitive and body centred cells, and there are distinct relationships between some of them. Many primitive structures have either an equivalent body centred structure or one which is very similar. The first pair of similar structures can be seen in Figure 1.14.

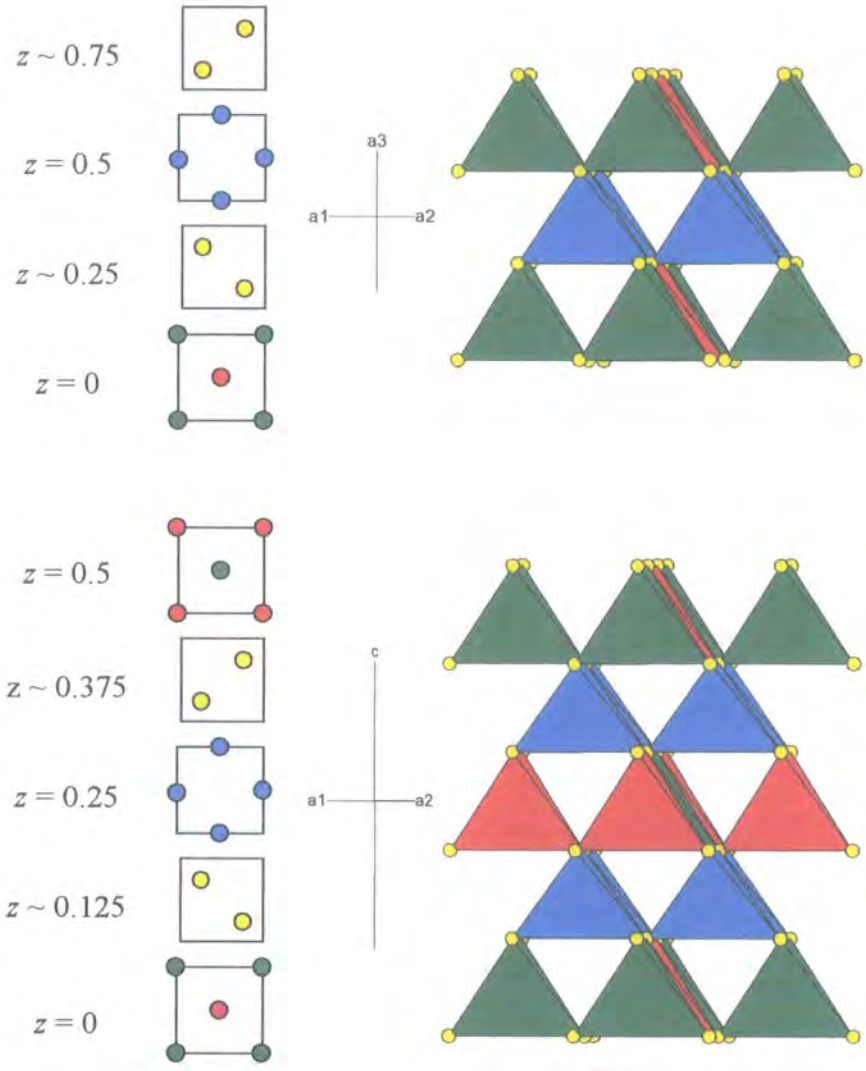

Figure 1.14 Schematic (left) and polyhedral (right) views of structures 2 (top) and 3 (bottom). S atoms are shown in yellow, different metal atoms and polyhedra in blue, green and red.

These two structures are a primitive and body centred pair; they are exactly the same except that in the body centred cell, the metal containing layer at $z = 0.5$ is offset by half a unit cell in the a and b directions relative to the primitive cell. There is a second body centred structure that is closely related to these, it is shown in Figure 1.15.

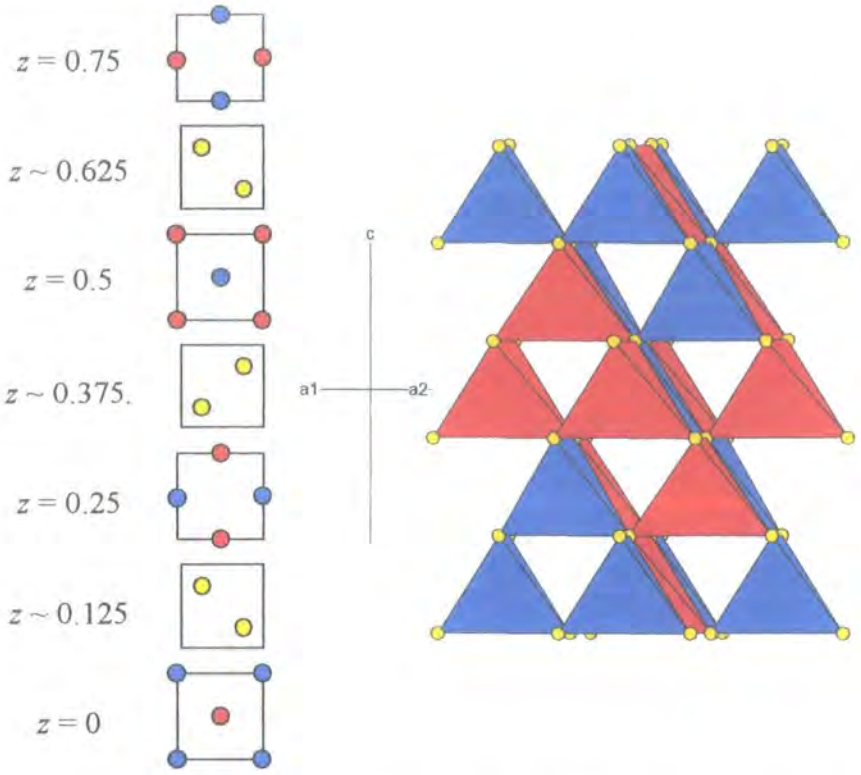

Figure 1.15 Schematic (left) and polyhedral (right) views of structure 4. S is shown in yellow, different metals and metal polyhedra in red and blue.

This structure is the same as those shown in Figure 1.14, except for the fact that there are two different metals occupying the sites in the $z = 0.25$ and $z = 0.75$ layers. This results in the structure having a seven layer rather than a five layer repeat unit. Structures 2, 3 and 4 all contain metal layers in which half of the available tetrahedral sites are occupied, giving an overall occupancy of 4/8 metal sites. The next primitive structure does not have an exactly equivalent body centred structure, though there is one which is very similar, these are shown in Figure 1.16.

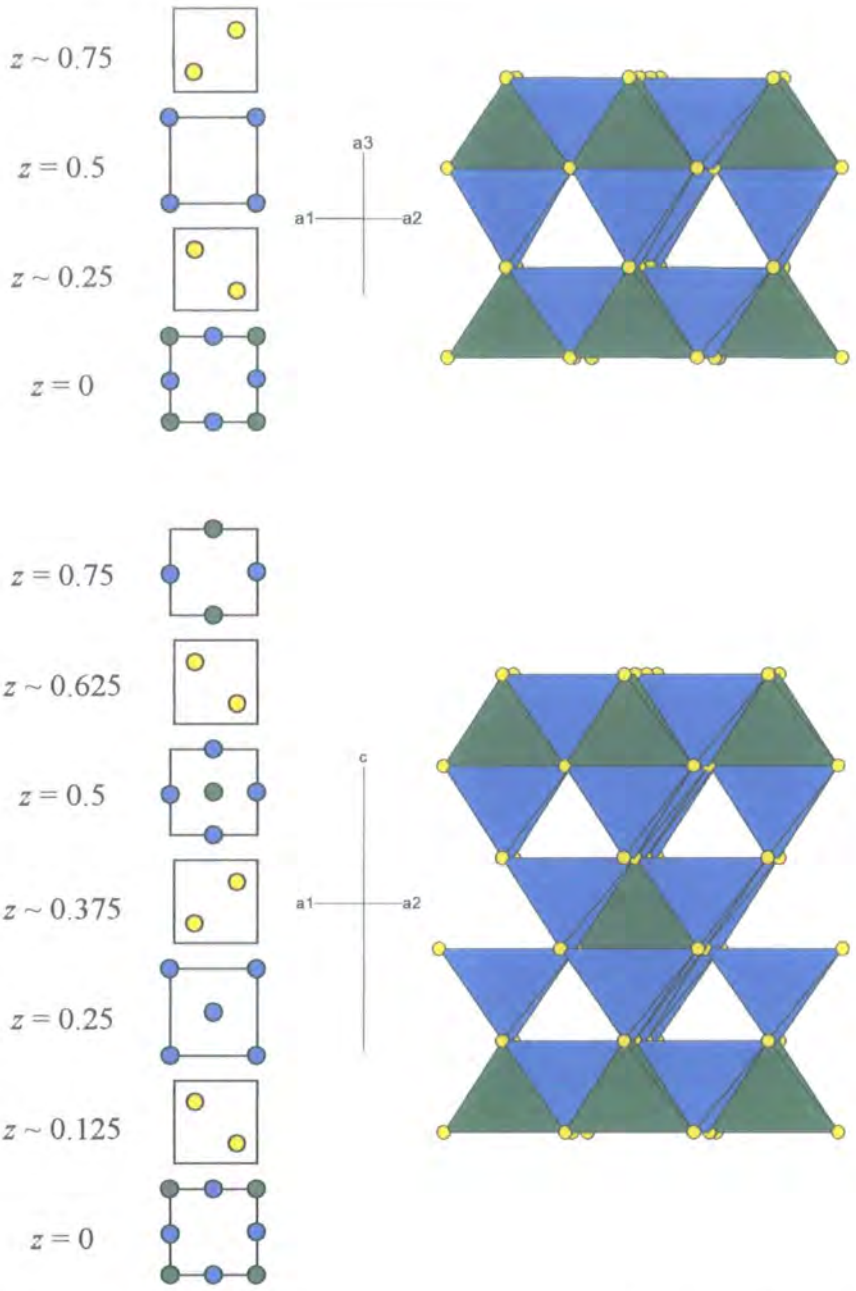

Figure 1.16 Schematic (left) and polyhedral (right) views of structures 5 (top) and 6 (bottom). S is shown in yellow, metal atoms and polyhedra in blue and green.

The difference in these structures arises from the fact that there is an atom in the centre of the $z = 0.25$ layer in the body centred structure (6). This is not present in $z = 0.5$ layer of the primitive structure (5). For structure 5, the number of metal sites occupied alternates between 3/4 and 1/4 in adjacent layers, half of the total number of sites. The addition of an extra metal in structure 6 means that the layers alternate between being 3/4 and 1/2 full, overall five out of a total of eight sites are filled. These structural differences arise because of changes in the oxidation state of the metal atoms involved. For example, the first structure is adopted by Cu_3VS_4, in which vanadium is in the +5

oxidation state. In Cu_4TiS_4, which adopts the second structure type, an additional Cu^+ ion is needed to compensate for the fact that titanium is in the +4 oxidation state.

The final structure in this group is a primitive structure and is shown in Figure 1.17.

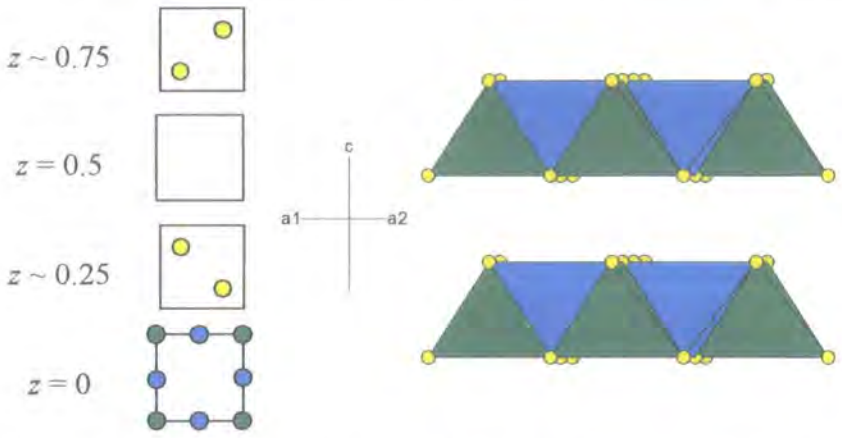

Figure 1.17 Schematic (left) and in polyhedral (right) views of structure 7. S is shown in yellow, metal atoms and polyhedra in green and blue.

This structure is unique in that it is a layered structure, tetrahedra are only linked in the *a* and *b* directions, there are discrete layers, separated by a Van der Waals gap, present along the *c* direction. Additionally, unlike the other structure types, there is only one example of a material which adopts the structure: Cu_2WS_4. This material has 3/4 of the metal sites in the $z = 0$ layer occupied and none of the sites in the $z = 0.5$ layer, giving 3/8 occupancy overall.

Structures 2, 3 and 4 are all metal ordered forms of the zinc blende structure and are networks of corner sharing tetrahedra. Structure 1, the antifluorite structure, contains layers in which the tetrahedra are linked by additional edge sharing. Structures 5, 6 and 7 are related to the antifluorite and zinc blende structures but, in some ways, are intermediate between the two, being structures in which different sites within the lattice are occupied to those in zinc blende. Structure 6 has layers in which the metal tetrahedra alternate between being corner sharing and edge sharing, while in structure 5 alternate layers contain edge sharing tetrahedra and tetrahedra which are not linked to others in the same layer. Structure 7 contains metal layers which contain only edge linked tetrahedra.

There are three other structures which are based on cubic close packed chalcogenide lattices. The first two cannot be described with the same unit cell as the other seven structures - their *a* and *b* unit cell parameters are approximately double those of the structures already discussed because metal ordering occurs over a longer distance. The

structures[67,68] of $Cu_{13}Fe_2Ge_2S_{16}$ and $Cu_6Fe_2SnS_8$ and schematic representations of the occupancy of tetrahedral metal sites for these materials are shown in Figure 1.18.

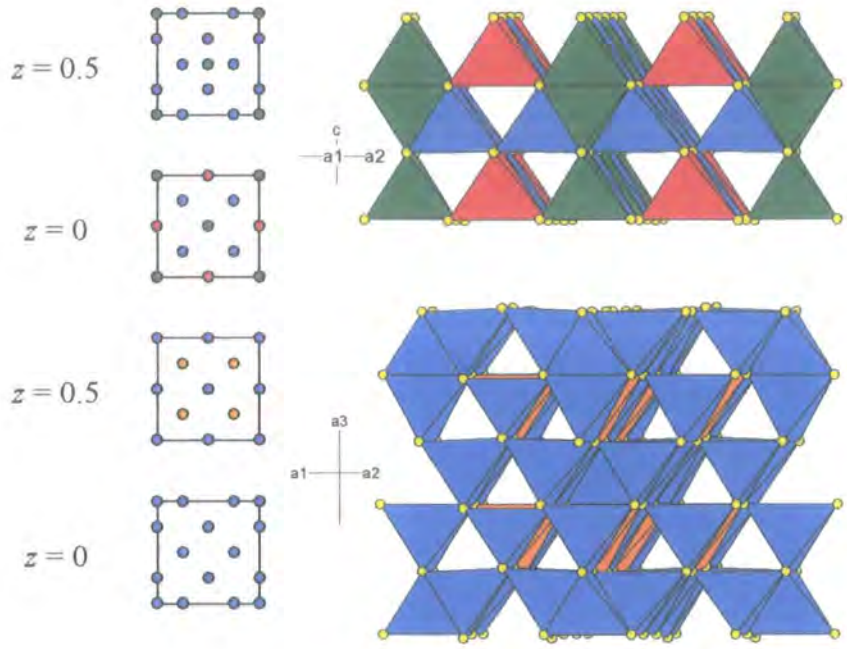

Figure 1.18 Schematic representations (left) and polyhedral views (right) of the structures of $Cu_6Fe_2SnS_8$ (top) and $Cu_{13}Fe_2Ge_2S_{16}$ (bottom). S is shown in yellow, Cu in blue, Sn in red, Fe in green and Ge/Fe in orange.

Instead of the 8 unique tetrahedral metal sites in the other materials, these two have 32 (16 per layer), reflecting the doubling of the *a* and *b* cell parameters. In $Cu_6Fe_2SnS_8$ the layers alternate between having 8/16 and 10/16 sites occupied, giving 18/32 in total. In $Cu_{13}Fe_2Ge_2S_{16}$, layers alternate between having 8/16 and 9/16 of the sites filled, representing 17/32 of the total number of sites being occupied. This is comparable to having 4.5 and 4.25 of the sites in the smaller M_4X_4 cell occupied. The structures are both intermediate between zinc blende and antifluorite, metal layers in both structures alternate between being made exclusively of corner sharing tetrahedra and containing mixtures of corner sharing and edge sharing linkages.

The structure[69] of Cu_2SnS_3 is again based on a cubic close packed lattice of sulfide atoms. It crystallises in the monoclinic space group Cc and has very complex metal ordering within the lattice. The layers consist of corner sharing tetrahedra and this material is another metal ordered form of the zinc blende structure.

All the structures discussed up to this point are related to either the zinc blende or the antifluorite structure types. There are also copper containing metal chalcogenides with structures that are based on hexagonal close packed lattices and thus related to the wurtzite structure type. These are summarised in Table 1.3.

Example compound	Space group	Number of T_d sites occupied	Types of T_d link	Ref.
Cu_3AsS_4	$Pmn2_1$	4	C	70
Cu_2MnGeS_4	$Pmn2_1$	4	C	71
$Cu_5Si_2S_7$	B11b	4	C	72
$CuFe_2S_3$	Pcmn	4	C & E	60
Cu_4SnS_4	Pnma	5	C & E	73

Table 1.3 Summary of structural details and example compounds for structures based on hexagonal close packed lattices with different metal occupancies; E indicates that layers of metal tetrahedra share edges, C indicates sharing of corners.

Some of these materials are related directly to the structure of wurtzite and are materials in which there is more than one metal cation substituted onto the tetrahedral sites in an ordered way. For other materials, the relationship to wurtzite is more complex.

Figure 1.19 Shows wurtzite projected along a direction perpendicular to the hexagonal close packed anion layers.

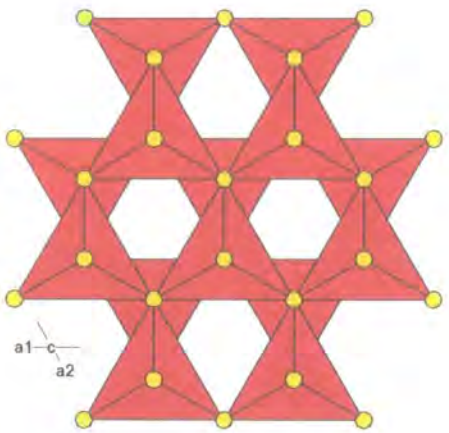

Figure 1.19 The wurtzite structure viewed perpendicular to the close packed anion layers. Anions are shown in yellow and cation tetrahedra in red.

Several materials have a structure in which the same tetrahedral sites are occupied, but with different cation ordering. The enargite form of Cu_3AsS_4, Cu_2MnGeS_4 and $Cu_5Si_2S_7$, which all have general formula M_yX_y are all examples of this. Two of these structures are shown in Figure 1.20.

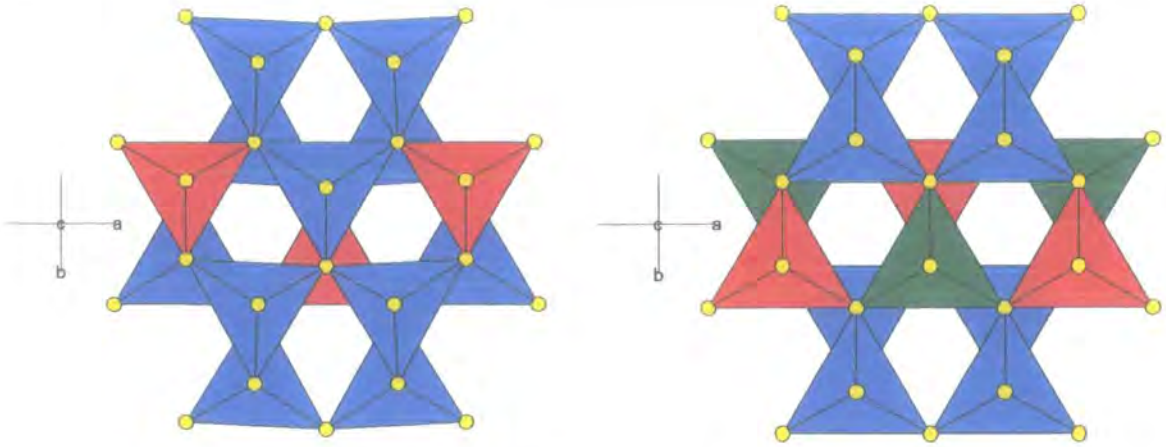

Figure 1.20 The structures of Cu_3AsS_4 (left) and Cu_2MnGeS_4 (right) viewed perpendicular to the close packed sulfide layers. Cu tetrahedra are shown in blue, As/Ge tetrahedra in red, Mn tetrahedra in green and S in yellow.

The relationship of these two materials to wurtzite is similar to the relationship of Cu_2FeSnS_4, Cu_2MnSnS_4 and $CuFeS_2$ to zinc blende. The metal ordering in $CuSi_2S_7$ is much more complex, although the same metal sites are occupied.

The relationship of the structures of Cu_2FeS_3 and Cu_4SnS_4 to wurtzite is not so simple. In wurtzite all the tetrahedra within a single layer are orientated in the same way as a result of the ordered occupation of half of the sites within the hexagonal close packed lattice. The sites which are occupied can all be considered as being just above (or below, depending on viewpoint) a layer of anions. In Cu_2FeS_3 however, the sites which are occupied are not the same as those in wurtzite, although the same proportion of the total number of sites are occupied, they include sites both above and below layers of close packed anions. This means that there are tetrahedra present in two opposing orientations and also introduces edge sharing as well as corner sharing linkages. This structure is shown in Figure 1.21.

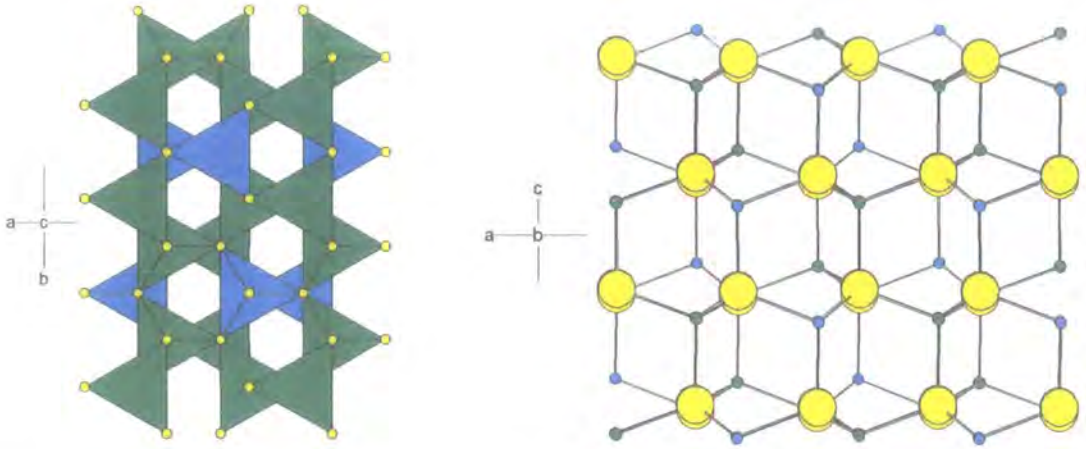

Figure 1.21 The structure of $CuFe_2S_3$ shown looking down on the close packed layers (left) and with the close packed layers horizontal (right). Cu ions and tetrahedra are shown in blue, Fe ions and tetrahedra in green and S in yellow.

The relationship between this structure and the wurtzite structure type is similar to the relationship between the structure of Cu_3VS_4 and zinc blende. The structure of Cu_4SnS_4 is related to the wurtzite structure in a similar way, but there are significant distortions present. The structure is shown in Figure 1.22.

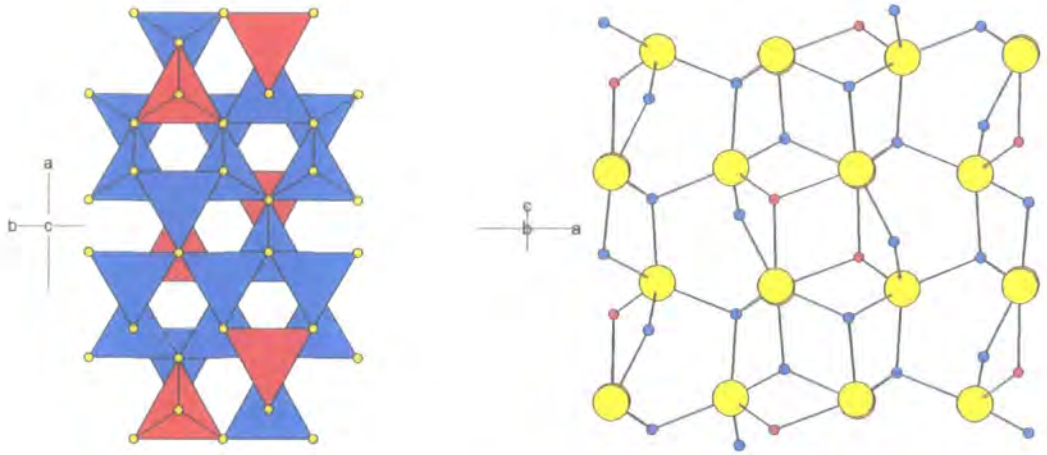

Figure 1.22 The structure of Cu_4SnS_4 looking down in the close packed layers (left) and with the close packed layers horizontal (right). Cu tetrahedra and ions are shown in blue, Sn tetrahedra and ions in red, S in yellow.

In this material 5 out of the 8 unique tetrahedra sites are occupied, giving rise to both edge and corner sharing between tetrahedra. The relationship of this material to wurtzite is similar to that of Cu_4TiS_4 to zinc blende.

1.2.2 1D structures containing A^{n+} cations

Structures containing edge linked tetrahedra which form one dimensional chains are relatively rare. There have been three different types of chain that have been found in materials discovered to date. The first chain type is made of single tetrahedra edge

linked together; the second chain type is made up of two chains of edge linked tetrahedra which are edge linked to each other to give double chains and the third chain type is made up by linking two chains of edge sharing tetrahedra by edge sharing with additional tetrahedral units. These are shown in Figure 1.23.

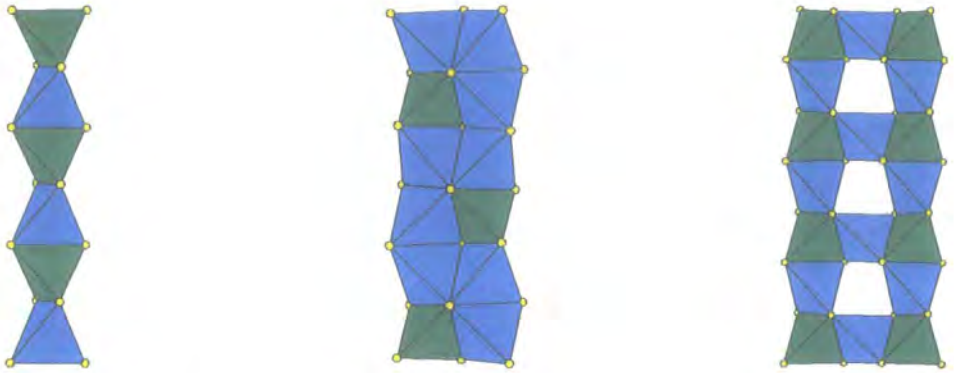

Figure 1.23 The structures of a single chain (left), double chain (middle) and triple chain (right) of edge linked tetrahedra.

The single chains are seen in the A_2CuMX_4 group of structures (sulfides: M = V, Nb A = Rb, K; selenides: M = Nb, Ta, V A = K or M = Nb A = Cs, Rb).[74-76] The chains run along the direction of the *a* axis and are interspaced by A^+ cations. The double chains are present in $Ba_2Cu_3VS_6$, the packing of the chains in space is very similar to that in the A_2CuMX_4 materials.[77] These structures are both shown in Figure 1.24.

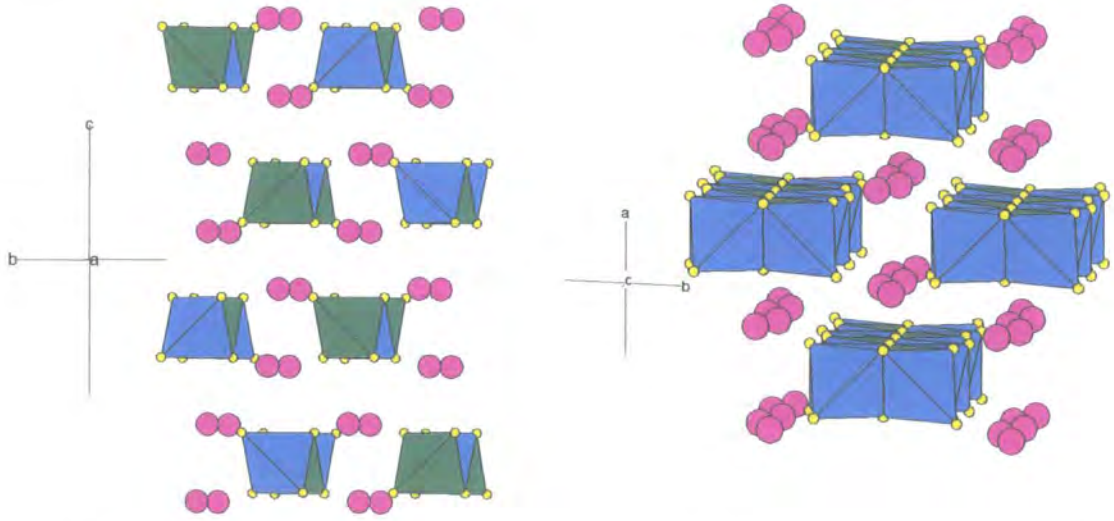

Figure 1.24 The structures of A_2CuMX_4 (left) and $Ba_2Cu_3VS_6$ (right) viewed down the chain direction. Cu tetrahedra are shown in blue, M/V tetrahedra in green, S in yellow and A^{n+} in pink.

The bridged double chains are found in $K_3Cu_3Nb_2S_8$, the structure is shown in Figure 1.25.

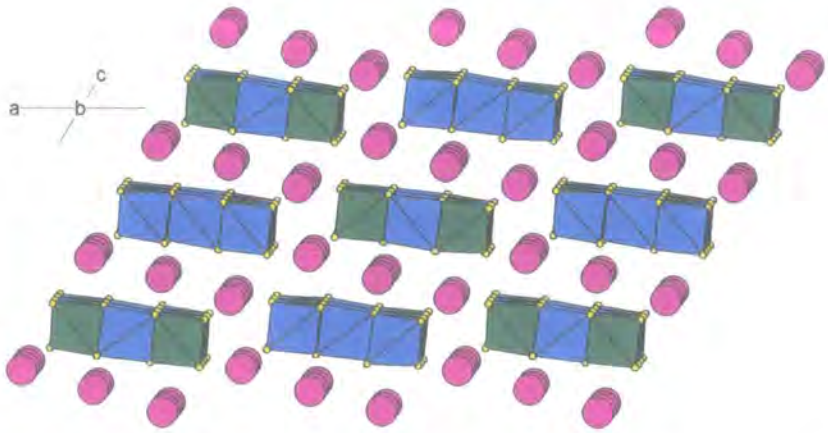

Figure 1.25 The structure of $K_3Cu_3Nb_2S_8$, viewed along the direction of the chains. Cu tetrahedra are shown in blue, Nb tetrahedra in green, S in yellow and K in pink.

These chains are structurally very similar to layers containing only edge sharing tetrahedra found in the materials discussed in section 1.2.1.

1.2.3 2D structures containing A^{n+} cations

Layering in copper containing chalcogenides often results from the inclusion of charge balancing Group 1 or 2 metal ions into the structure. Several different layer types are observed. The first group has single layers of tetrahedra which are planar and similar to those discussed in section 1.2.1, they can be either single layers, or bonded together in groups of two or three. A second group has layers which are disrupted and are no longer planar, instead forming a shape best described as a *zigzag*. Finally there are structures in which the layers are more complex, containing mixtures of edge and corner sharing tetrahedra with a range of orientations. In all the structures the cations are located between the layers.

The materials containing planar layers contain layers with networks of tetrahedra linked by corner sharing, edge sharing or a mixture of the two. $A_2TiCu_2X_4$ (A = Cs X = Se or A = Rb X = S) and $Rb_2Cu_2SnS_4$ both have primitive unit cells.[78,79] The $A_2TiCu_2X_4$ materials have a tetragonal cell while $Rb_2Cu_2SnS_4$ has an orthorhombic cell with cell parameters of $a = 5.528$ Å, $b = 11.418$ Å, $c = 13.700$ Å (b ~ 2a). Planar layers of edge sharing metal sulfide tetrahedra are centred at $z = 0.25$ and $z = 0.75$ and the Group 1 metal cations are located in the layers at $z = 0$ and $z = 0.5$. The orthorhombic cell in $Rb_2Cu_3SnS_4$ is a reflection of the slightly more complex nature of the metal ordering in the structure. Schematic views of the metal layers and polyhedral views of the structures are shown in Figure 1.26.

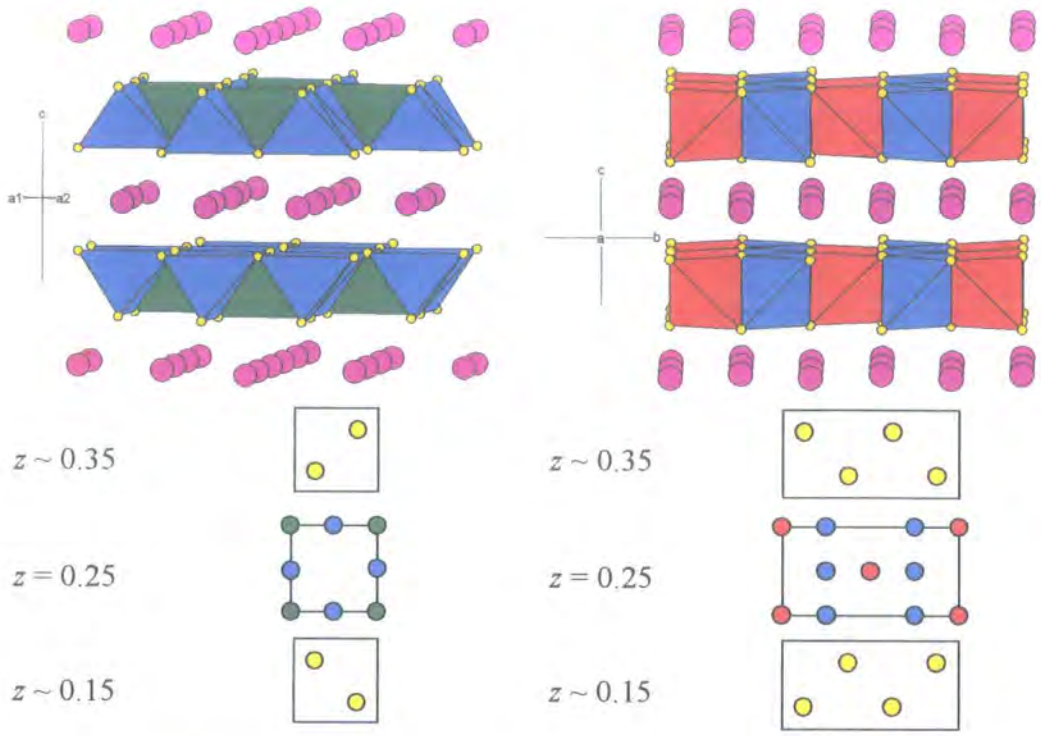

Figure 1.26 The structures of $A_2TiCu_2X_4$ (left) and $Rb_2Cu_2SnS_4$ (right) and schematic views of metal ordering in the layers (bottom). Ti is shown in green, Sn in red, Cu in blue and S in yellow.

For $A_2TiCu_2X_4$, 3 out of the 4 available tetrahedral metal sites within the layer are occupied, for $Rb_2Cu_3SnS_4$, 6 out of the 8 available sites are occupied.

The structures of KCu_4X_3 and $KCuFeX_2$ (X =S, Se) contain similar rigid layers.[80,81] The layers in these materials are extended networks of edge sharing tetrahedra, with no vacant sites, the same as those found in $(Cu_2Fe_2S_3)_{1.33}$. In $KCuFeX_2$, this is a single layer of tetrahedra and the copper and iron are randomly distributed throughout the tetrahedral sites. In KCu_4X_4 there are double layers of tetrahedra, which are bonded together via edge linkages. In both structures there are layers of potassium ions between the metal sulfide layers.

$K_2CuGa_3Se_6$ and $Rb_2Cu_2Sn_2S_6$ have essentially the same structure, though in the gallium selenide material some of the sites which were occupied by copper in the tin sulfide material are occupied by gallium.[79,82] The structure contains a layer of copper tetrahedra which are corner linked together. SnS_4 units are located above and below this plane of copper tetrahedra. The tin tetrahedra are linked together by corner sharing to make one dimensional chains, these chains are then linked to the copper layer via corner sharing links, the tin tetrahedra effectively bridge between two copper tetrahedra. The structure is shown in Figure 1.27.

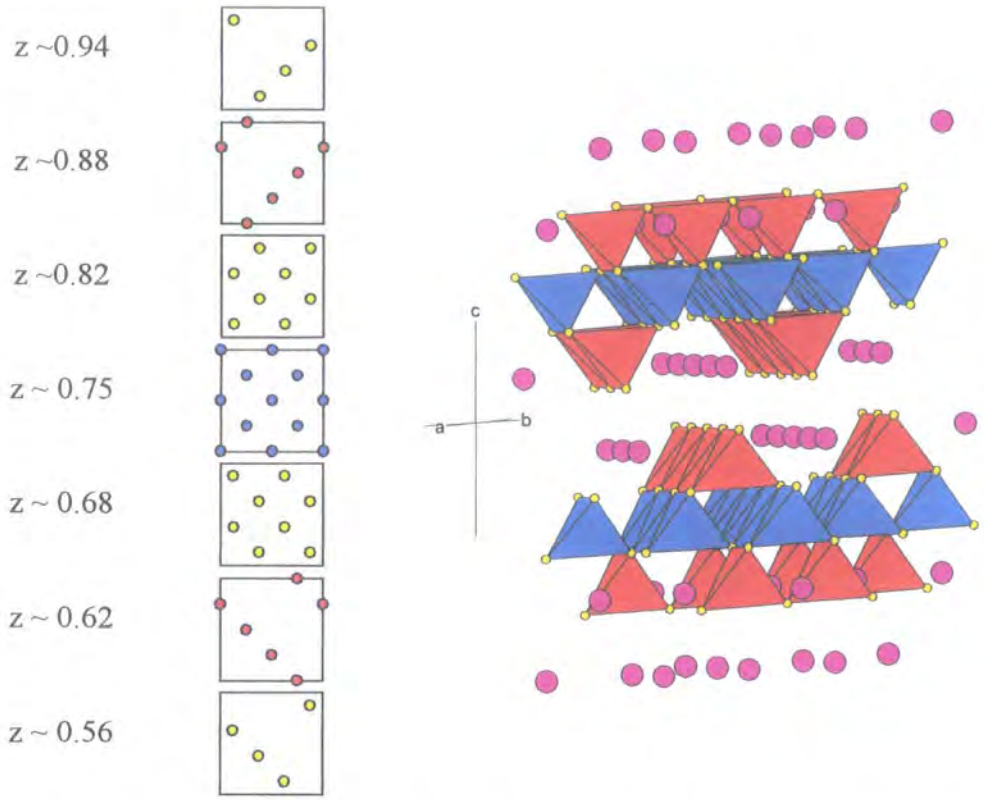

Figure 1.27 Schematic representation of metal ordering in layers and polyhedral view of $Rb_2Cu_2Sn_2S_6$. Cu ions and tetrahedra are shown in blue, Sn ions and tetrahedra in red, S in yellow and Rb in pink.

In the copper containing layers, half of the tetrahedral sites are occupied, for the tin containing layers only a quarter of the sites are occupied.

The zigzag layer structure is adopted[74,83-86] by KCu_2VX_4, $NaCu_2NbS_4$, KCu_2NbSe_4 and $RbCu_2VS_4$ and is shown in Figure 1.28.

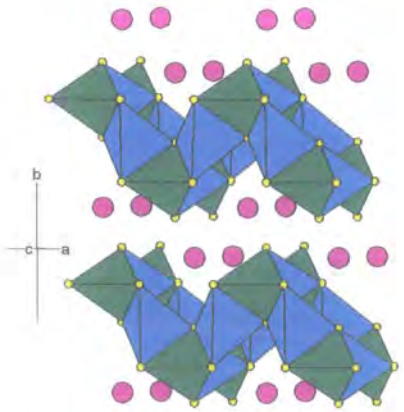

Figure 1.28 The zigzag layers in the structure of KCu_2VS_4, Cu tetrahedra are shown in blue, V tetrahedra in green, S in yellow and K in pink.

The structure is made up of structural units very similar to those seen in the extended structures in section 1.2.1 and in the chains in $K_3Cu_3Nb_2S_8$, discussed in section 1.2.2.

Rings of 8 tetrahedra are linked together by two tetrahedra which are attached to the corners of the ring. These linking tetrahedra are attached in the direction perpendicular to the ring direction giving the zigzag layers.

In $Na_3CuSnSe_4$ the layers consist of pairs of edge sharing CuS_4 and SnS_4 tetrahedra. These are linked to other pairs of tetrahedra via corner sharing links to make an extended layer, sodium ions are located between the layers.[87] The structure is shown in Figure 1.29.

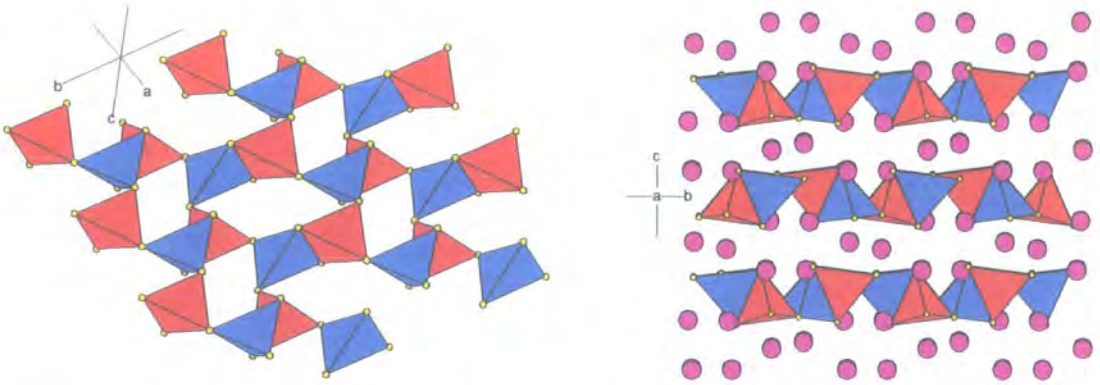

Figure 1.29 A single layer of $Na_3CuSnSe_4$ with cations omitted (left) and a view of the layers (right). Cu tetrahedra are shown in blue, Sn tetrahedra in red, Na in pink and S yellow.

The structure of $SrCu_2GeS_4$ contains layers that consist of groups of three tetrahedra which are all linked by sharing a common edge, these units are linked by corner sharing of the other two vertices of the tetrahedron.[88] This is shown in Figure 1.30.

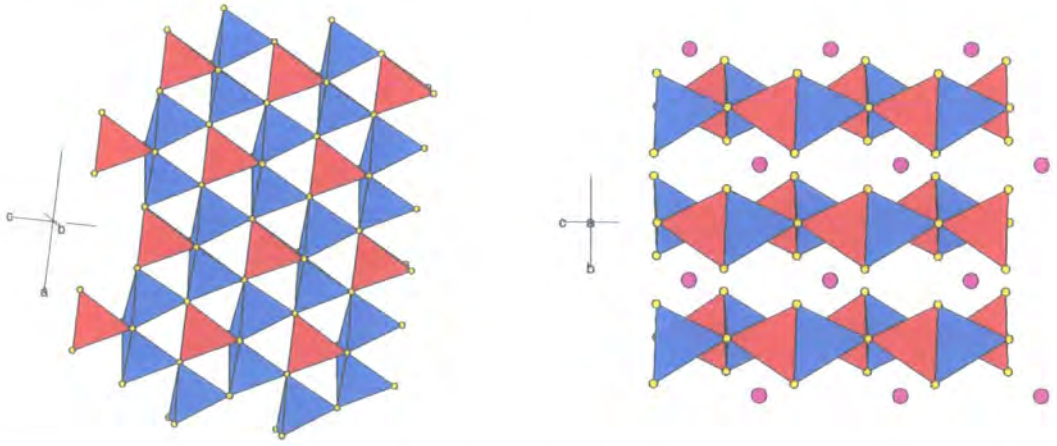

Figure 1.30 The structure of a single layer (left) and layer packing (right) in $SrCu_2GeS_4$. Cu tetrahedra are shown in blue, Ge tetrahedra in red and S in yellow.

1.2.4 3D structures based on edge sharing structural motifs

Condensed three dimensional framework materials containing A^{n+} cations are rare but do exist, $BaCu_4S_3$ being an example of a material with this kind of structure. The structure of $BaCu_4S_3$ contains CuS_4 tetrahedra which are linked via a mixture of edge

and corner linkages to form a three dimensional framework in which the Ba cations reside.[89] Viewed down the *b* axis the structure consists of edge linked groups of tetrahedra which form a "chair like" shape. These units are linked to each other in both the *a* and *c* directions. This view of the structure is shown in Figure 1.31.

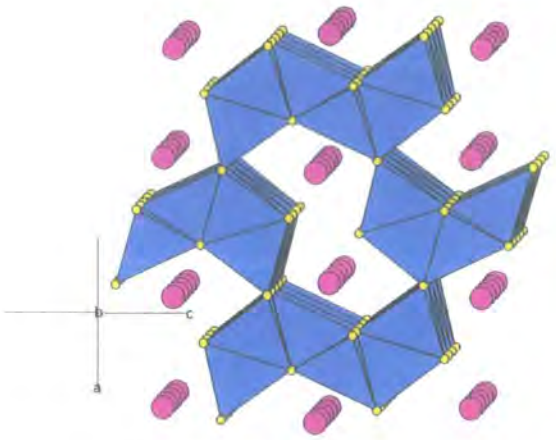

Figure 1.31 Polyhedral representation of $BaCu_4S_3$ viewed down the *b* axis. Ba is shown in pink, Cu tetrahedra in blue and S in yellow.

1.2.5 Summary

The structures of the copper containing metal chalcogenides discussed here have several common themes. Many are based on cubic close packed or hexagonal close packed chalcogenide arrays with structural variations being a result of differences in occupation of metal sites and different metal ordering within the lattice. A large number of these structures are closely related to the wurtzite and zinc blende structure types. The introduction of Group 1 and 2 metal cations results in different structural motifs, though many of these show structural similarities to the materials with close packed anion lattices. Some of the materials have structures that are very closely related to those described later in this thesis; this will be discussed further in chapter 4.

1.3 References

1. K. F. E. Schafhäutl, *Gelehrte Anzeigen Bayer. Akad.*, 1845, 557, 561, 569, 593.
2. R. Bunsen, *Ann.*, 1848, **65**, 70.
3. H. d. Sénarmont, *Ann. Chim. Phys.*, 1851, **32**, 129.
4. J. J. Capponi, *Thése Université Scientifique et Médicale, Grenoble*, 1973.
5. Y. Chen, H. Kou, J. Jiang, et al., *Mater. Chem. Phys.*, 2003, **82**, 1-4.
6. S. Yu, J. Yang, Y. Wu, et al., *J. Chem. Mater.*, 1998, **8**, 1949-1951.
7. C. Wang, G. Zhang, S. Fan, et al., *J. Phys. Chem. Solids*, 2001, **62**, 1957-1960.
8. X. F. Qian, X. M. Zhang, C. Wang, et al., *J. Phys. Chem. Solids*, 1999, **60**, 415-417.
9. C. Wang, Y. D. Li, G. H. Zhang, et al., *Inorg. Chem.*, 2000, **39**, 4237-4239.
10. J. Yang, S. H. Yu, Z. H. Han, et al., *J. Solid State Chem.*, 1999, **146**, 387-389.
11. Y. Li, H. Liao, Y. Ding, et al., *Inorg. Chem.*, 1999, **38**, 1382-1387.
12. S. H. Liu, X. F. Qian, J. Yin, et al., *J. Phys. Chem. Solids*, 2003, **64**, 455-458.
13. X. Chen and R. Fan, *Chem. Mater.*, 2001, **13**, 802-805.
14. J. H. Zhan, Y. Xie, X. G. Yang, et al., *J. Solid State Chem.*, 1999, **146**, 36-38.
15. Z. H. Han, Y. P. Li, H. Q. Znao, et al., *Mater. Lett.*, 2000, **44**, 366-369.
16. Y. Xie, L. Zhu, X. Jiang, et al., *Chem. Mater.*, 2001, **13**, 3927-3932.
17. Y. Qian, S. Yi, X. Yi, et al., *Mater. Res. Bull.*, 1995, **30**, 601-605.
18. Y. Li, H. Liao, Y. Fan, et al., *Materials Chemistry and Physics*, 1999, **58**, 87-89.
19. J. Li, Z. Chen, R.-J. Wang, et al., *Coord. Chem. Rev.*, 1999, **190-192**, 707-735.
20. W. S. Sheldrick and B. Schaaf, *Z. Anorg. Allg. Chem.*, 1994, **620**, 1041-1045.
21. W. S. Sheldrick and H. G. Braunbeck, *Z. Naturforsch., B: Chem. Sci.*, 1989, **44**, 851-852.
22. A. Loose and W. S. Sheldrick, *Z. Anorg. Allg. Chem.*, 1999, **625**, 233-240.
23. Z. Chen, R. Wang, X. Huang, et al., *Acta Cryst.*, 2000, **C56**, 1100-1103.
24. C. L. Cahill and J. B. Parise, *J. Chem. Soc., Dalton Trans.*, 2000, 1475-1482.
25. J. Liao, J. Li and M. G. Kanatzidis, *Inorg. Chem.*, 1995, **34**, 2658-2670.
26. A. Fehlker, R. Blachnik and H. Reuter, *Z. Anorg. Allg. Chem.*, 1999, **625**, 1225-1228.
27. G. L. Schimek, J. W. Kolis and G. J. Long, *Chem. Mater.*, 1997, **9**, 2776-2785.
28. J. B. Parise and Y. Ko, *Chem. Mater.*, 1992, **4**, 1446-1450.
29. V. Vater and W. S. Sheldrick, *Z. Naturforsch., B: Chem. Sci.*, 1998, **53**, 1259-1264.
30. V. Vater and W. S. Sheldrick, *Z. Naturforsch., B: Chem. Sci.*, 1997, **52**, 1119-1124.
31. G. Dittmar and H. Schafer, *Z. Anorg. Allg. Chem.*, 1977, **437**, 183-187.
32. Y. An, M. Baiyin, X. Liu, et al., *Inorg. Chem. Commun.*, 2004, **7**, 114-116.
33. J. Liao and M. G. Kanatzidis, *Inorg. Chem.*, 1992, **31**, 431-439.
34. T. Jiang, A. J. Lough, G. A. Ozin, et al., *Chem. Mater.*, 1995, **7**, 248-248.

35. A. Loose and W. S. Sheldrick, *Z. Naturforsch., B: Chem. Sci.*, 1998, **53**, 349-354.

36. A. Loose and W. S. Sheldrick, *J. Solid State Chem.*, 1999, **147**, 146-153.

37. Y. An, M. Ji, M. Baiyin, et al., *Inorg. Chem.*, 2003, **42**, 4248-4249.

38. J. B. Parise, *Chem. Commun.*, 1990, 1553-1554.

39. B. Eisenmann, J. Hansa and H. Schäfer, *Rev. Chim. Miner.*, 1984, **21**, 817-823.

40. K. Tan, A. Darovsky and J. B. Parise, *J. Am. Chem. Soc.*, 1995, **117**, 7039-7040.

41. O. M. Yaghi, Z. Sun, D. A. Richardson, et al., *J. Am. Chem. Soc.*, 1994, **116**, 807-808.

42. J. B. Parise and K. Tan, *Chem. Commun.*, 1996, 1687-1688.

43. O. Achak, J. Y. Pivan, M. Maunaye, et al., *J. Solid State Chem.*, 1996, **121**, 473-478.

44. C. L. Bowes, W. U. Huynh, S. J. Kirkby, et al., *Chem. Mater.*, 1996, **8**, 2147-2152.

45. C. L. Cahill and J. B. Parise, *Chem. Mater.*, 1997, **9**, 807-811.

46. C. L. Cahill, Y. Ko, J. C. Hanson, et al., *Chem. Mater.*, 1998, **10**, 1453-1458.

47. A. Loose and W. S. Sheldrick, *Z. Naturforsch., B: Chem. Sci.*, 1997, **52**, 687-692.

48. K. K. Rangan, P. N. Trikalitis and M. G. Kanatzidis, *J. Am. Chem. Soc.*, 2000, **122**, 10230-10231.

49. P. N. Trikalitis, K. K. Rangan and M. G. Kanatzidis, *J. Am. Chem. Soc.*, 2002, **124**, 2604-2612.

50. M. Wachhold and M. G. Kanatzidis, *Chem. Mater.*, 2000, **12**, 2914-2923.

51. M. Wachhold, K. K. Rangan, M. Lei, et al., *J. Solid State Chem.*, 2000, **152**, 21-36.

52. M. J. MacLachlan, N. Coombs, R. L. Bedard, et al., *J. Am. Chem. Soc.*, 1999, **121**, 12005-12017.

53. M. J. MacLachlan, N. Coombs and G. A. Ozin, *Nature*, 1999, **397**, 681-684.

54. P. N. Trikalitis, K. K. Rangan, T. Bakas, et al., *Nature*, 2001, **410**, 671-675.

55. W. S. Sheldrick and H. G. Braunbeck *Z. Naturforsch., B: Chem. Sci.*, 1992, **47**, 151-153.

56. H. Li, A. Laine, M. O'Keeffe, et al., *Science*, 1999, **283**, 1145-1147.

57. H. Li, M. Eddaoudi, A. Laine, et al., *J. Am. Chem. Soc.*, 1999, **121**, 6096-6097.

58. J. B. Parise, *Science*, 1991, **251**, 293-294.

59. A. V. Powell, R. Paniagua, P. Vaqueiro, et al., *Chem. Mater.*, 2002, **14**, 1220-1224.

60. J. T. Szymanski, *Z. Kristallogr.*, 1674, **140**, 240-248.

61. J. Llanos, M. T. Mujica, J. Oro-Sole, et al., *Boletin de la Sociedad Chilena de Quimica*, 2000, **45**, 605-609.

62. T. Fries, Y. Shapira, F Palacio, et al., *Phys. Rev. B: Condens. Matter.*, 1997, **56**, 5424-5431.

63. L. Pauling and L. O. Brockway, *Z. Kristallogr.*, 1932, **82**, 188-194.

64. C. Mujica, G. Carvajal, J. Llanos, et al., *Z. Kristallogr.*, 1998, **213**, 12.

65. K. O. Klepp and D. Gurtner, *J. Alloys Compd.*, 1996, **234**, 19-22.

66. E. A. Pruss, B. S. Snyder and A. M. Stacy, *Angew. Chem. Int. Ed. Engl.*, 1993, **32**, 256-257.

67. R. T. Tettenhorst and C. E. Corbato, *Am. Mineral.*, 1984, **69**, 943-947.

68. J. T. Szymanski, *Mineralogiceskij Zhurnal*, 1981, **3**, 79-86.

69. M. Onoda, X. A. Chen, S. Sato, et al., *Mater. Res. Bull.*, 2000, **35**, 1563-1570.

70. L. J. Karanovic, L. J. Cvetkovic, D. Poleti, et al., *Neues Jahrbuch fuer Mineralogie. Monatshefte*, 2002, 241-253.

71. J. Allemand and M. Wintenberger, *Bulletin de la Societe Francaise de Mineralogie et de Cristallographie*, 1970, **93**, 14-17.

72. M. Dogguy, S. Jaulmes, P. Laruelle, et al., *Acta Cryst.*, 1982, **B38**, 2014-2016.

73. S. Jaulmes, J. Rivet and P. Laruelle, *Acta Cryst.*, 1977, **B33**, 540-542.

74. C. Rumpf, R. Tillinski, C. Naether, et al., *Eur. J. Solid State Inorg. Chem.*, 1997, **34**, 1187-1198.

75. W. Bensch, P. Duerichen and C. Weidlich, *Z. Kristallogr.*, 1996, **211**, 931-931.

76. Y. J. Lu and J. A. Ibers, *Inorg. Chem.*, 1991, **30**, 3317-3320.

77. C. Mujica, C. Ulloa, J. Llanos, et al., *J. Alloys Compd.*, 1997, **255**, 227-230.

78. F. Q. Huang and J. A. Ibers, *Inorg. Chem.*, 2001, **40**, 2602-2607.

79. J. H. Liao and M. G. Kanatzidis, *Chem. Mater.*, 1993, **5**, 1561-1569.

80. D. B. Brown, J. Zubieta, P. A. Vella, et al., *Inorg. Chem.*, 1980, **19**, 1945-1950.

81. C. Mujica, J. Paez and J. Llanos, *Zapiski Vserossijskogo Mineralogicheskogo Obshchestva*, 1981, **110**, 468-473.

82. H. W. Ma, G. C. Guo, M. S. Wang, et al., *Inorg. Chem.*, 2003, **42**, 1366-1370.

83. W. Bensch, P. Duerichen and C. Weidlich, *Z. Kristallogr.*, 1996, **221**, 933-933.

84. R. Tillinski, C. Naether and W. Bensch, *Acta Cryst.*, 1999, **C55**, 1959-1961.

85. Y. J. Lu and J. A. Ibers, *J. Solid State Chem.*, 1991, **94**, 381-385.

86. C. Rumpf, C. Naether, I. Jeb, et al., *Eur. J. Solid State Inorg. Chem.*, 1997, **34**, 1165-1177.

87. K. O. Klepp and F. Fabian, *Eur. J. Solid State Inorg. Chem.*, 1997, **34**, 1155-1163.

88. M. Tampier and D. Johrendt, *Z. Anorg. Allge. Chemie*, 2001, **627**, 312-320.

89. J. E. Iglesias, K. E. Pachali and H. Steinfink, *Phase Transitions*, 1992, **38**, 127-220.

2 Experimental methods

The work presented in this thesis has involved the use of several characterisation and synthetic techniques. This chapter describes these techniques, which include X-ray powder diffraction, X-ray single crystal diffraction,[1] measurement of magnetic properties using a SQUID magnetometer and conductivity measurements. It also includes details of the methods used for analysis of powder diffraction data and information about synthetic conditions used for different reactions.

2.1 Rietveld Refinement

The Rietveld method[2,3] is a non linear least squares method of refinement which allows an experimental powder pattern to be fitted using a structural model. The model can contain information about the crystal structure, the physical properties of the sample and the instrument used to collect the data. Parameters commonly included in this model include sample specific details *e.g.* atomic coordinates, thermal factors and a peak shape model, and global parameters *e.g.* a background model, terms to describe the instrument peak shape function (including asymmetry) and a sample height correction. These parameters are all refined to give the best possible fit between the observed data and the calculated pattern. The quality of this fit can be judged by considering the values of a number of parameters, called R-factors.[4]

The most commonly quoted R-factor is the weighted R-factor, $_wR_p$, which is based on the main experimental observable fitted during refinement and is described by equation 2.1. w_i is the weighting factor for the ith data point, $y_i(obs)$ is the intensity for the ith data point in the observed pattern and $y_i(calc)$ is the intensity for the ith point in the calculated pattern.

$$ {}_wR_p = \left\{ \frac{\sum_i w_i [y_i(obs) - y_i(calc)]^2}{\sum_i w_i [y_i(obs)]^2} \right\}^{\frac{1}{2}} \qquad [2.1] $$

For a refinement of high quality, the weighted R value, $_wR_p$, should approach the value of R_{exp}; this is judged by the ratio of these two values, and called the goodness of fit, or χ^2. R_{exp} and χ^2 are defined by equations 2.2 and 2.3; n is the number of observations and p is the number of parameters.

$$ R_{exp} = \left\{ \frac{(n-p)}{\sum_{i=1}^{n} w_i y_i^{\,2}} \right\}^{\frac{1}{2}} \qquad [2.2] $$

$$\chi^2 = \frac{{}_w R_p}{R_{exp}} \qquad [2.3]$$

The value of χ^2 should ideally be between 1 and 1.5, with values of less than 1 indicating that more parameters are being refined than are justified by the quality of the data. The value of this parameter should be interpreted with care as it is strongly influenced by factors such as the data collection time used. Long data collection times will make R_{exp} low, artificially increasing the value of χ^2; short data collection times will give a high value of R_{exp} and hence a low value of χ^2.

The R_{Bragg} factor is arguably the most reliable indication of the quality of fit between a structural model and an observed powder pattern and is comparable to the R-factors reported for single crystal data; it is given by equation 2.4, where $I_{hkl} = mF_{hkl}^2$ (m = multiplicity).

$$R_{Bragg} = \frac{\sum_{hkl} \left| I_{hkl}('obs') - I_{hkl}(calc) \right|}{\sum_{hkl} I_{hkl}('obs')} \qquad [2.4]$$

Although this is the most reliable R-factor for judging the quality of structural model, the values of $I_{hkl}('obs')$ are based not on real observations but on values calculated using values derived from the structural model, so they are somewhat biased in favour of the model being used.

2.2 The Total Pattern Analysis System, TOPAS

Final Rietveld refinements reported throughout this work have used local version 46 of 'The Total Pattern Analysis System' or TOPAS.[5] TOPAS can be operated in two modes, graphical (GUI) mode, or input file mode. Simple refinements, phase purity checks etc. were all carried out using the graphical mode; this mode allows parameters to be input via a system of menus. Input mode TOPAS was used for all refinements which were slightly more complex in nature. In input file mode, the instrument and structural parameters are specified using a simple programming language specific to the TOPAS software, input files for all Rietveld refinements are included in the e-appendix.

2.3 Indexing powder patterns using ITO and TOPAS

Indexing a powder pattern is the process of determining possible unit cell parameters which are consistent with the observed peak positions. This has been done using two different computer programs: the *multiviss* routine, a modified FORTRAN routine for controlling ITO,[6,7] and the singular value decomposition (SVD) indexing routine within TOPAS.[8] Before a pattern can be indexed it is first necessary to determine accurate positions for the peaks observed in the powder pattern, these should typically have

errors of less than 0.01 °. This was done using the peak fitting facility in TOPAS, each peak is fitted using a pseudo-Voigt peak shape, allowing accurate determination of the peak positions, even for overlapping reflections.

For indexing using the *multiviss* routine a list of peak positions is prepared and each of the peaks is given a flag of "0" or "1" according to how confident one feels as to the precision to which its 2θ value can be determined and whether it is due to the main phase (*e.g.* one might chose to flag weak peaks, severely overlapping peaks or peaks with a significantly larger fwhm than others as "0"). The indexing program then selects a total of 20 peak positions at a time, which includes all those flagged "1" and random combinations of the remaining positions. For each of these combinations an attempt is made to derive unit cell parameters. The best solution is then selected by considering the figure of merit and the proportion of peaks fitted by all the indexing solutions suggested. The figure of merit (FOM) is defined by equation 2.5.

$$FOM = \frac{Q_{20}}{2\varepsilon N_{20}} \qquad [2.5]$$

where N_{20} is the number of different calculated Q values up to Q_{20}, Q_{20} is the Q value ($Q = 1/d^2$) for the 20th observed and indexed line and ϵ is the average discrepancy in Q for these 20 lines.[9]

For indexing using TOPAS, the only requirement is a list of the peak positions which are passed to the program via an input file; attempts are then made to assign unit cell parameters to the observed positions. The FOM in this case is the same as that used in ITO except that it is scaled according to the number of unindexed peaks, $N_{impurity}$; it is defined using equation 2.6.

$$FOM_{TOPAS} = \frac{Q_{20}}{2\varepsilon N_{20}(N_{impurity} + 1)} \qquad [2.6]$$

Using ITO one would expect a *FOM* of >20 for a solution to be plausible. FOM_{TOPAS} may be considerably lower for a correct solution if a number of impurity peaks are present.

2.4 Structure solution by simulated annealing

Simulated annealing is a method of structure solution which uses direct space methods to determine a structure. For powder diffraction data, structure solution by direct methods is only possible in a very small number of cases, and is unlikely to be successful for structures containing both light and heavy elements; simulated annealing is therefore a good alternative. Although it can, in principle, be used to determine a structure starting from only the unit cell dimensions and the cell contents, it is

particularly useful in cases where something is already known about the structure; for example if the structure contains rigid tetrahedra, benzene rings, or other well defined structural motifs.

Simulated annealing is the process of placing atoms in the unit cell and moving them around in a stochastic manner in order to get the best agreement between calculated and observed powder patterns. Traditionally, simulated annealing uses a temperature regime to govern the magnitude of the random jumps; however, a slightly modified method of annealing has been used for work presented in this thesis. The annealing process used here places the contents randomly in the unit cell then the structure is refined by Rietveld refinement. Once the refinement has converged, random changes, which are directed by the user, are made to the structure. The powder pattern is recalculated and the structure refined again. This process of randomisation is repeated thousands of times, and the final solution retained is the one with the lowest $_{w}R_{p}$ value. (See section 2.37). In our experience the use of Rietveld refinement during the structure solution process greatly increases the likelihood of successful solution in that close but wrong structural models can be "pulled towards" the correct answer.

The exact way in which the structure is changed during this annealing process must be carefully controlled, with factors such as the symmetry of the cell and the symmetry of the cell contents being taken into account. Structural units must be moved sufficiently in each cycle of annealing to ensure that all of parameter space is being explored. It may also be necessary to apply restraints or penalty functions to the refinement. These can be used, for example, to keep bond distances within chemically sensible ranges, or to prevent atoms from bumping into each other.

Though individual atoms could be placed in the cell and their positions annealed and refined, even for very simple structures this would give the problem a large number of degrees of freedom (3 per atom). For successful structure solution every single atom in the unit cell would have to be close to its correct position after a single cycle of annealing/refinement, this is highly unlikely to happen within a reasonable length of computational time. Also, for powder data, the quality of fit is judged by considering the value of $_{w}R_{p}$; different structures can give very similar $_{w}R_{p}$ values, so it would be very difficult to judge which the best structural solution was without applying some sensible chemical criteria. Simulated annealing is therefore much more useful in the case of structures where there is prior structural knowledge. This can be used, for example, to describe the structure in terms of rigid structural units, defined by calculating the positions of all of the atoms relative to a common point. The atomic positions relative to this point are fixed, and it is only the position of the point within the cell and rotations of the rigid body around each of the unique axis, that is refined. In

this way a complex unit with many atoms can be described using only 6 parameters, which cuts down the degrees of freedom and therefore the computational time significantly. In some cases, it is appropriate to define additional refineable parameters in order to fully describe a structural unit. For example in a tetraphenylphosphonium unit, the phenyl rings can twist relative to the C — P bond axis, a torsion angle can be refined to account for this. An example input file for simulated annealing, used for the structure solution of $(PPh_4)_2Ni(WS_4)_2$, is included in Appendix 2.1. Following the identification of a plausible solution by simulated annealing, it is common to perform a more detailed Rietveld refinement to obtain an optimal structural model.

2.5 X-ray powder diffraction methods

2.5.1 Siemens D5000 diffractometer

All samples described in this thesis were tested to determine phase purity and crystallinity using a Siemens D5000 diffractometer. Quick checks were done using a scan time of 1 hour, longer scan times of 12-16 hours were used to collect good quality data for Rietveld refinements. The diffractometer operates in flat plate mode and uses a CuKα radiation X-ray source (average λ = 1.54195 Å). Before irradiating the sample, the radiation passes through both soller slits and divergence slits. The divergence slits can be set to be either variable, giving an area of irradiated sample of width either 6 mm (v6) or 20 mm (v20) across the whole powder pattern; or fixed to give a constant 1 ° irradiated angle. After diffraction by the sample, the diffracted beam passes through another soller slit, a graphite (*001*) monochromator and a 0.2 mm receiving slit before it is detected by a scintillation counter. The machine is controlled using the Bruker *Diffrac+ v4.0* suite of programs.

Samples were prepared using one of two methods, depending on the amount of sample available and the nature of the sample. All samples were ground before preparation using an agate pestle and mortar. Large samples were packed into bulk holders, of diameter 20 mm or 6 mm, the samples were placed into the holder and pressed down using a glass slide to give a flat surface. For small samples and those in which preferred orientation was a problem, samples were sprinkled onto an amorphous glass slide which was coated with a thin layer of Vaseline.

2.5.2 Bruker d8 Advance diffractometer

A Bruker d8 Advance diffractometer was used for collection of high quality data and variable temperature diffraction experiments (see section 2.6). The diffractometer has a Ge (*111*) monochromated Kα_1 source (λ= 1.540598 Å). It can operate in two modes: reflection and transmission. In flat plate reflection mode the monochromatic X-rays pass through a 6 mm aperture slit and an anti-scatter tube to a fixed soller slit and divergence

slit usually set to 1 °. After diffraction from the sample the diffracted beam passes through a radial soller and is then detected by a Braun PSD-50M linear position sensitive detector (PSD). For transmission mode the diffractometer has only an extended "nose cone" before the sample and a radial soller preceding the PSD counter. The machine is controlled using the Bruker *Diffrac+ v4.0* software. Measurements can be made on samples contained in air, under vacuum or under an inert nitrogen atmosphere.

For room temperature data collections in flat plate reflection mode, samples were passed through a fine mesh sieve and sprinkled onto a Vaseline coated, zero background silicon wafer. For transmission data only capillary mode was used, although the diffractometer can also operate in flat plate transmission mode. Samples were prepared be sieving (as for flat plate samples) then loading the sieved powder into a glass capillary. Capillary diameters between 0.3 and 0.5 mm were used according to the absorption and scattering properties of the sample. The capillary was tapped to ensure that the powder was tightly packed and the end was flame sealed. The capillary was mounted in the goniometer using bees' wax and centred in the X-ray beam before data were collected. The capillaries were spun during data collection.

2.6 Variable temperature diffraction experiments

The Bruker d8 Advance diffractometer can be used to collect X-ray diffraction data over a wide range of temperatures using several different attachments. The PheniX ccr cryostat operates between 15 and 300 K, the Anton Paar TTK450 cryostat between 77 and 723 K and the Anton Paar HTK1200 oven-camera between 300 and 1473 K. Temperature control of the TTK450 and the HTK1200 is via the Bruker *Diffrac+ v4.0* suite of programs, while the PheniX ccr uses the CryoPad software. For experiments using the HTK1200 and the TTK450, the sample was contained in an inert atmosphere (HTK1200) or vacuum (TTK450) chamber and samples were heated before data were collected (heating rates used between data collections for experiments in this thesis were 12 K/min for the HTK and 30 K/min for the TTK). For experiments using the PheniX the sample was contained in a vacuum chamber and heating or cooling was continuous. Average temperatures for each data collection were extracted after completion of the experiment by comparison of the PheniX log file, in which temperatures are logged at 30 second intervals throughout the experiment, to the start and end times of each data collection. This is done using the local FORTRAN routine *phenixlogfile*.[10]

Samples were prepared by sprinkling onto a Vaseline coated aluminium disk (PheniX and TTK450) or onto a Vaseline coated silica disk (HTK1200). A summary of all the variable temperature diffraction experiments which have been undertaken is given in Table 2.1.

Compound	Sample ID	Data collection number	d8 attachment	Heating rate /Khr^{-1}	Temp. range /K	Time per scan /mins
Cu_2WS_4	cjc026	d8_02602	PheniX	−17	300 – 17	30
Cu_2WS_4	cjc026	d8_02501	HTK1200	+46	303-623	30
Cu_2WSe_4	cjc089	d8_02604	PheniX	−17	300 – 17	30
PPh_4CuWSe_4	cjc176	d8_02628	PheniX	−9	300 – 17	30
$(PPh_4)_2Zn(WS_4)_2$	cjc171	d8_02626	PheniX	−17	300 – 17	30
$(PPh_4)_2Ni(WS_4)_2$	cjc156	d8_02606	PheniX	−17	300 – 17	30
$(NH_4)_2WS_3O$	cjc008	d8_01502	TTK450	+15	100 – 470	40

Table 2.1 Summary of variable temperature diffraction experiments.

For variable temperature diffraction data, it is often necessary to analyse large numbers of sets of data collected at regularly spaced temperature increments. In order to do this quickly and simply a DOS based batch program is used to control Rietveld refinements in the command line version of TOPAS; this is generated using the FORTRAN routine *multitopas*. The first set of data are fitted using the input mode in TOPAS in order to create a 'seed' file; the other sets of data are then automatically fitted by refinement of this seed file .The results of one refinement are used as a starting point for refinement against data collected at the next temperature in the sequence in order to minimise computational time. Parameters of interest, along with the temperature at which data were collected are automatically written to a results file. Seed files and a summary of results as excel spreadsheets for each variable temperature experiment are included in the e-appendix.

2.7 Single crystal diffraction experiments

The single crystal diffraction experiment in this thesis was performed using a Bruker SMART 6000 diffractometer. The diffractometer has a goniometer head with a fixed chi angle of 54.7 ° and data were collected by scanning through omega in 0.3 ° frames for four sets of orthogonal phi angles. The diffractometer has a Mo source (λ= 0.71073 Å) with a graphite monochromator, the diffracted beam is detected by a CCD (charge coupled device) area detector. The crystal was mounted on the goniometer using perfluoropolyether oil to prevent reaction with the air and cooled to 120 K using an Oxford Cryosystems nitrogen cryostream in which the crystal is cooled by a flow of chilled nitrogen gas. The diffractometer was controlled by a PC using the SMART software.

2.8 Measurement of magnetic properties

Magnetic property measurements were made using a Quantum Design Magnetic Property Measurement System containing a superconducting quantum interference

device (SQUID). Samples were prepared by loading a known mass of the powder into half of a gelatin capsule and using the second half of the capsule to hold the powder in place. The two halves of the capsule were fixed together and then fixed to the inside of a plastic straw using a mixture of varnish and solvent (10:1 ethanol: toluene). The capsule is fixed in the centre of the straw to allow it to be easily centred in the machine. The measurements made were field sweeps, in which the magnetisation was measured as a function of magnetic field, and temperature sweeps, in which magnetisation is measured in a fixed field as a function of temperature.

2.9 Conductivity measurements

Variable temperature conductivity measurements were made using a 2-probe measurement technique. Samples were prepared by pressing a 5 mm pellet and depositing metal contacts onto the pellet surface by evaporation. Copper wires were then fixed to the contacts using quick drying silver paint. The contacts must have ohmic properties in order to obtain meaningful results; this was tested using simple I–V measurements in which the variation of the current passing through the sample as the potential difference was changed was recorded.

Variable temperature resistance measurements were made using a Keithly Instruments electrometer attached to a pellet of the sample contained in a helium filled Oxford Instruments cooling chamber. The sample chamber temperature is controlled by an Oxford Instruments temperature controller via a PC using a Visual Basic 6.0 program which also recorded the resistance measurements.[11] In order to obtain accurate measurements which give a true picture of the variation of resistance with temperature it is important to ensure that the sample has reached the desired temperature and is in thermal equilibrium with its surroundings before the resistance is measured. This is achieved by measuring the temperature in the sample chamber and the temperature immediately beneath the sample - only when these two readings were the same was the sample judged to be in thermal equilibrium. Two resistance readings were then taken at a nine second interval, these had to be within 1 % of each other before the final measurement was made; the value recorded was an average of 20 readings taken at time intervals of ~2 s.

2.10 Synthetic details

This section summarises synthetic details for all compounds described elsewhere in this thesis. Compounds are organised according to the chapter in which they are discussed; starting reagent preparations are discussed before the synthesis in which they are used. The procedures used for handling $H_2S(g)$ are also included.

Diffraction patterns were recorded to confirm the identity of all starting materials using either a Siemens D5000 or a Bruker d8 Advance diffractometer (see sections 2.5.1 and 2.5.2); an index of these measurements is included in the e-appendix. Unless otherwise stated, compounds were judged to be air stable by comparison of diffraction patterns measured within a time interval of a few weeks. Combustion analyses were performed by Mrs Jarika Dostal using an Exeter Analytical E-400 elemental analyser.

All manipulations of air sensitive compounds were carried out under an inert atmosphere using standard Schlenk techniques or a Vacuum Atmospheres nitrogen filled glovebox. With the exception of THF and DMF, which were dried before use when required, all reagents were used as supplied. THF was dried by distillation under a nitrogen atmosphere over sodium wire. DMF was degassed and stored over 4 Å 8 – 12 mesh molecular sieves prior to use. Reagent sources and purities are given in Appendix 2.2.

2.10.1 Procedure for handling H_2S

H_2S is a highly toxic gas and must therefore be handled with care. The equipment used for reactions involving $H_2S(g)$ was designed to minimise the risk of emission of the gas to the atmosphere. It consisted of a series of glass vessels linked by PVC tubing; Teflon tape was used to ensure that all joints were properly sealed and this was tested by passing $N_2(g)$ through the equipment before $H_2S(g)$ was introduced. The $H_2S(g)$ was delivered to the reaction mixture via a glass tube, diameter ~8 mm; a flow rate of ~2 bubbles per second was used. Gas emitted from the reaction vessel was passed through an empty container, followed by two 1 L containers half filled with bleach. The gas then passed through a bubbler containing a small amount of acidified $KMnO_4$ solution, an additional empty vessel and a final 1 L vessel half filled with bleach, it was then released into the fume hood. This is shown schematically in Figure 2.1.

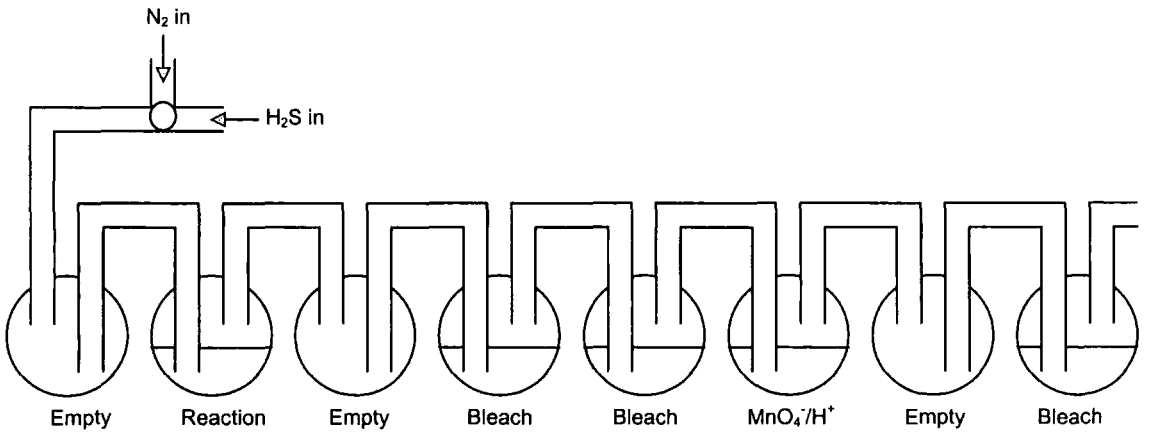

Figure 2.1 Schematic view of equipment used for reactions involving $H_2S(g)$.

The role of the bleach in the first two containers was to oxidise any unreacted $H_2S(g)$ forming solid sulfur and other soluble sulfur containing species. If any gas did pass through the first two bleach containers without reacting, it was instead oxidised by the potassium permanganate which decolourised, indicating that the bleach solutions in the first two vessels needed to be replaced by fresh bleach. The final bleach scrubber ensures that as the $KMnO_4$ vessel becomes inactive there is still bleach left to oxidise the $H_2S(g)$. The empty vessels were included as a precaution against "suck back" which happens if the flow of $H_2S(g)$ is not sufficient to maintain reaction in the reaction vessel. The resulting drop of pressure in the reaction vessel can lead to bleach from the scrubber being sucked towards the reaction vessel or the contents of the reaction vessel being sucked into the $H_2S(g)$ delivery tube. The empty vessels prevented bleach from coming into contact with the reaction mixture and the reaction mixture from contaminating the gas delivery line. Once a reaction was completed the equipment was purged with $N_2(g)$ forcing any unreacted $H_2S(g)$ into the bleach containing containers where it was oxidised. The solid product was then recovered by filtration and the supernatant liquid neutralised by reaction with bleach. All the equipment which had come into contact with the $H_2S(g)$ was immersed in diluted bleach for at least 24 hours to remove the last traces of $H_2S(g)$ before being removed from the fume hood.

2.10.2 $Cu(CH_3CN)_4BF_4$ – cjc001[12]

Cu_2O (4.0 g, 28 mmol) was added to 80 ml of CH_3CN to form a red suspension. HBF_4 (15 cm^3, 48 % by weight in H_2O) was added dropwise to this suspension; the solution was heated to 70 °C then filtered to remove a black solid. The colourless solution was cooled and kept at −20 °C for 17 hours; white crystals were formed. The crystals were washed with Et_2O and recrystallised at −20 °C from a 1:1 mixture of CH_3CN and Et_2O. The air sensitive solid product was dried under vacuum and stored in an inert atmosphere. C:H:N analysis: measured: C 28.23 %, H 3.50 %, N 16.50 %; calculated: C 30.55 %, H 3.85 %, N 17.81 %. The XRD pattern was recorded with the sample held under a vacuum in a Bruker d8 diffractometer and Rietveld fitted using the structure determined[13] from single crystal data to confirm its identity.

2.10.3 $(NH_4)_2WS_4$ – cjc010[14]

NH_4OH (40 ml) was added to H_2WO_4 (5.0350 g, 20 mmol) to form a suspension of white powder in a colourless solution. The suspension was saturated by slow addition of $H_2S(g)$ for about 20 minutes at room temperature, then filtered to remove a green solid. The bright yellow filtrate was heated to 60 °C with stirring and a continuous flow of $H_2S(g)$ bubbling through the solution (rate ~1-2 bubbles per second) for 4.5 hours, resulting in the formation of a yellow solid. The solution was purged with N_2 and cooled; the solid was isolated by filtration and dried under vacuum. Yield 1.9653 g, 28 %. C: H: N analysis: measured: C: 0 %, H: 2.15 %, N 7.25 %; calculated: C 0 %,

H 2.32 %, N 8.05 %. Identity was confirmed by comparison of the PXRD pattern to the PDF[15] (48-1663).

2.10.4 $(NH_4)_2WS_4$ – cjc012

The experimental method used was the same as that for cjc010 with the following modifications: 5.0619 g of H_2WO_4 was used; the solution was heated with H_2S gas flow for 7.25 hours; the solution was left at room temperature overnight before purging with N_2. Yield 4.1411 g, 59 %. C: H: N analysis: measured: C 0 %, H 2.35 %, N 7.90 %; calculated: C 0 %, H 2.32 %, N 8.05 %. Identity was confirmed by comparison of the PXRD pattern to the PDF (48-1663).

2.10.5 $(NH_4)_2MoS_4$ – cjc045[14]

Na_2MoO_4 (5.0 g, 24.3 mmol) was dissolved in H_2O (10 ml) and concentrated NH_4OH (30 ml) giving a clear, colourless solution. The solution was saturated with H_2S by bubbling gas through it; gas flow was maintained while the solution was heated to 60 °C. The solution changed colour sequentially from yellow to orange and finally red. Gas flow was maintained (rate ~1-2 bubbles per second) for 2.5 hours then the mixture was purged with N_2 and cooled in an ice bath resulting in the formation of dark red solid. The solid was isolated by filtration and washed with ^{i}PrOH and Et_2O before drying under vacuum. Yield 4.7509 g, 75 %. C:H:N analysis: measured: C 0 %, H 3.12 %, N 10.47 %; calculated C 0 %, H 3.10 %, N 10.76 %. Identity was confirmed by comparison of the PXRD pattern to the PDF (48-1662).

2.10.6 K_2Se_3 – cjc067

K (0.7531 g, 19.3 mmol) and Se (2.2813 g, 28.9 mmol) were placed in a flask fitted with a cold finger condenser under an Ar atmosphere. A stopper was fitted to one neck of the flask and joints were not tied with rubber bands in case of an accidental build up of gas pressure. In a fume hood, the flask was purged by passing NH_3(g) through it, NH_3 was then condensed by cooling the flask in an acetone/CO_2 bath and adding CO_2(s) and acetone to the cold finger condenser. Care was taken to ensure that no pipes became frozen and that gas flow was not restricted during cooling. After ~250 ml of NH_3 had been condensed to form a red-brown solution, the NH_3(g) flow was stopped and the temperature was maintained at −78 °C for 2 hours under a small positive pressure of Ar while the solution was stirred. The solution was then allowed to warm up to room temperature resulting in evaporation of the NH_3 over a 6 hour period, and leaving a grey solid. The air sensitive solid was dried under vacuum and stored in an inert atmosphere. Yield 2.805 g, 92 %. Identity was confirmed by comparison of the PXRD pattern, recorded with the sample under an inert atmosphere, to the PDF (71-0235).

2.10.7 $(PPh_4)_2WSe_4$ – cjc080[16]

Dry, degassed N,N dimethylformamide (50 ml) was added to $W(CO)_6$ (1.0032 g, 2.85 mmol) and K_2Se_3 (1.1971 g, 3.80 mmol, cjc067) under an argon atmosphere to produce a green solution. The solution was heated to 90 °C for 1 hour resulting in a change in colour from green to red. $(C_6H_5)_4PBr$ (2.3906 g, 5.70 mmol) was added and the solution was transferred via canula through a frit into a Schlenk. Dry, degassed THF (50 ml) was added and the Schlenk was stored at 4 °C overnight. The red solid that formed was isolated by filtration and washed with demineralised H_2O to remove a KBr impurity before drying in air at 50 °C. Yield 2.3746 g, 71 %. The solid showed some long term instability in air so was stored in the glove box. C:H:N analysis: measured: C 46.57 %, H 3.31 %, N 0 %; calculated: C 48.92 %, H 3.42, N 0 %. Identity was confirmed by Rietveld fitting the PXRD pattern using the structural model determined from single crystal data.[16]

2.10.8 $(PPh_4)_2MoSe_4$ – cjc099[16]

The material was synthesised using the same methodology as was used to make the tungsten analogue. $Mo(CO)_6$ (0.7515 g, 2.85 mmol) and K_2Se_3 (1.1976 g, 3.80 mmol, cjc067) were dissolved in DMF to give a green-brown solution, which became blue on heating. Addition of $(C_6H_5)_4PBr$ (2.3879 g, 5.70 mmol) and THF followed by storage at 4 °C overnight resulted in the formation of a blue solid. Yield 1.7914 g, 58 %. The solid showed some long term instability in air so was stored in the glove box. C:H:N analysis: measured: C 47.22 %, H 3.39 %, N 0 %; calculated: C 52.86 %, H 3.70 %, N 0 %. Identity was confirmed by Rietveld fitting of the PXRD pattern using the structural model determined from single crystal data.[16]

2.10.9 P Cu_2WS_4 – pjh013

This sample was prepared by Peter Hickey using the methodology of Pruss.[17,18]

$Cu(CH_3CN)_4BF_4$ (0.14 g, 0.45 mmol) was dissolved in degassed butyronitrile (15 ml) under an inert atmosphere and the resulting colourless solution was added via canula to a flask containing a yellow solution of $(NH_4)_2WS_4$ (0.1019 g, 0.29 mmol) in degassed N,N dimethylformamide (15 ml) also under an inert atmosphere. This resulted in the formation of an orange solution. The solution was heated with stirring at reflux (135 °C) under an inert atmosphere for 24 hours. After cooling the orange supernatant liquid was removed using a canula and the product was dried under vacuum. Yield 0.0469 g, 48 %. Identity was confirmed by comparison of the PXRD pattern to the PDF (81-1159).

2.10.10 Cu_2MX_4 – general procedure for solvothermal synthesis

Cu_2MX_4 (M = W or Mo, X = S or Se or S/Se) materials were synthesised by reaction of $Cu(CH_3CN)_4BF_4$ and one or more of the following materials: $(NH_4)_2WS_4$, $(NH_4)_2MoS_4$, $(PPh_4)_2WSe_4$ or $(PPh_4)_2MoSe_4$. Details of the reagents, temperatures, reagent stoichiometries, synthesis times and products obtained are summarised in Tables 2.2 to 2.6 and additional information is included in the e-appendix.

The required amounts of $(A)_2MX_4$ and $Cu(CH_3CN)_4BF_4$ were placed in a Teflon lined Parr autoclave (23 ml capacity) and a 1:1 mixture of DMF and butyronitrile (8 ml) was added. The vessel was sealed and heated to the reaction temperature required at a rate of 5 °C/min. After heating for the required amount of time (48 hours unless stated otherwise) the reaction vessel was cooled to room temperature in the oven. The solid produced was separated from the supernatant liquid by centrifugation then washed with 3 portions (~4 ml) of Et_2O before drying in air. Identities were confirmed by PXRD.

Sample Code	Temp. /°C	Mass $Cu(CH_3CN)_4BF_4$ /g	Mass $(NH_4)_2WS_4$ /g	Product phase
cjc079	110	0.1410	0.1005	*P*
cjc018	135	0.0706	0.0509	*P*
cjc029	143	0.0708	0.0499	*I*
cjc030	152	0.0707	0.0509	*I*
cjc023	160	0.0701	0.0511	*I*
cjc024	180	0.0702	0.0526	*I*
cjc026	200	0.0707	0.0497	*I*
cjc094	220	0.0694	0.0500	*I*
cjc027	250	0.0711	0.0507	Amorphous

Table 2.2 Synthetic details for Cu_2WS_4 phases synthesised at different temperatures.

Sample Code	Temp. /°C	Time /hrs	Mass $Cu(CH_3CN)_4BF_4$ /g	Mass $(PPh_4)_2WSe_4$ /g	Product phase
cjc072	135	48	0.1074	0.1854	*P*
cjc073	160	48	0.0771	0.1232	*P*
cjc082	180	48	0.0686	0.1314	*P* + *I*
cjc142	185	48	0.0704	0.1308	*P* + *I* + PPh_4CuWSe_4
cjc125	190	48	0.0692	0.1298	*P* + *I* + PPh_4CuWSe_4
cjc178	190	12	0.0704	0.1318	*P* + *I* + PPh_4CuWSe_4
cjc179	190	24	0.0679	0.1308	*P* + *I* + PPh_4CuWSe_4
cjc180	190	48	0.0690	0.1313	*P* + *I* + PPh_4CuWSe_4
cjc181	190	90	0.0675	0.1315	*P* + *I* + PPh_4CuWSe_4
cjc139	195	48	0.0707	0.1302	*P* + *I* + PPh_4CuWSe_4
cjc087	200	48	0.0681	0.1296	*I*
cjc126	210	48	0.0675	0.1305	*I*
cjc089	220	48	0.0699	0.1287	*I*

Table 2.3 Synthetic details for Cu_2WSe_4 phases synthesised at different temperatures.

Sample Code	Temp. /°C	Mass $Cu(CH_3CN)_4BF_4$ /g	Mass $(NH_4)_2WS_4$ /g	Mass $(PPh_4)_2WSe_4$ /g	Product phase
cjc096	220	0.0684	0.0100	0.0981	*I*
cjc090	200	0.0702	0.0191	0.0680	*I*
cjc091	200	0.0715	0.0291	0.0355	*I*

Table 2.4 Synthetic details for $Cu_2WS_xSe_{4-x}$ phases synthesised at different temperatures.

Sample Code	Temp. /°C	Mass $Cu(CH_3CN)_4BF_4$ /g	Mass $(NH_4)_2MoS_4$ /g	Product phase
cjc057	110	0.1045	0.0560	*P*
cjc053	135	0.1047	0.0565	*P* + *I*
cjc177	150	0.1086	0.0562	*P* + *I*
cjc060	165	0.1069	0.0562	Amorphous
cjc056	175	0.1076	0.0562	Amorphous
cjc055	200	0.1065	0.0555	Amorphous

Table 2.5 Synthetic details for Cu_2MoS_4 phases synthesised at different temperatures.

Sample Code	Temp. /°C	Mass $Cu(CH_3CN)_4BF_4$ /g	Mass $(PPh_4)_2MoSe_4$ /g	Product phase
cjc101	135	0.0706	0.1213	*P* + CuSe + $CuSe_2$
cjc102	150	0.0753	0.1202	*P* + CuSe + $CuSe_2$
cjc103	175	0.0770	0.1196	*P* + Cu_2Se
cjc104	200	0.0683	0.1206	Cu_2Se
cjc114	220	0.0730	0.1221	Cu_2Se

Table 2.6 Synthetic details for Cu_2MoSe_4 phases synthesised at different temperatures.

2.10.11 *P* Cu_2WS_4 heated in solvothermal bomb – cjc084

P Cu_2WS_4 (0.0118 g, cjc079) was placed in a hydrothermal bomb in a 1:1 (v:v) mixture of DMF and butyronitrile (4 ml). The bomb was heated at a rate of 5 °C/min to 200 °C; this temperature was maintained for 12 hours before the bomb was cooled in the oven. The orange solid produced was isolated by centrifuge and washed with 3 portions of Et_2O before drying in air. Yield 0.0058 g, 49 %.

2.10.12 *P* Cu_2WS_4 treated under pressure – cjc083

P Cu_2WS_4 (0.0773 g, cjc079) was placed in a 5 mm pellet die and compressed at a pressure of ~1.9×10^5 kPa for 21 hours.

2.10.13 *P* Cu_2WS_4 heated under vacuum – cjc086

P Cu_2WS_4 (0.0324 g, cjc079) was pressed into a pellet using a 5 mm die and a pressure of ~1.9×10^5 kPa. The pellet was sealed into a quartz tube under vacuum and heated at 5 °C/min to 200 °C for 16.5 hours before being cooled in the oven to room temperature.

2.10.14 *P* Cu_2WS_4 heated under pressure – cjc088

A 5 mm pellet of Cu_2WS_4 (cjc086), was placed in a glass lined autoclave (volume 120 ml) fitted with a gas pressure gauge. The autoclave was purged with N_2, then sealed and pressurised with N_2 to give a pressure of ~500 kPa. The vessel was heated to 200 °C, causing the pressure to increase to ~700 kPa. This temperature was maintained for 14 hours before cooling.

2.10.15 PPh_4CuWSe_4 – cjc176

$(PPh_4)_2WSe_4$ (0.1872 g, 0.16 mmol) and $Cu(CH_3CN)_4BF_4$ (0.0453 g, 0.14 mmol) were placed in a Teflon lined Parr autoclave (23 ml capacity) and a 1:1 mixture of DMF and butyronitrile (8 ml) was added. The vessel was sealed and heated at 5 °C/min to 190 °C; this temperature was maintained for 24 hours before the oven was allowed to cool to room temperature. The red solid produced was separated from the orange supernatant liquid by centrifuge then washed with 3 portions (~4 ml) of Et_2O before drying in air.

Yield 0.1270 g, 98%. C:H:N analysis: measured: C 32.13 %, H 2.27 %, N 0 %; calculated: C 31.94 %, H 2.23 %, N 0 %. Identity was confirmed by PXRD.

2.10.16 $(PPh_4)_4[Co(WS_4)_2]$ – cjc157[19]

A solution of $Co(NO_3)_2 \cdot 6H_2O$ (0.0728 g, 0.25 mmol) in a 1:1 (v:v) mixture of H_2O/CH_3CN (5 ml), acidified with a few drops of glacial acetic acid, was added to a solution of $(NH_4)_2WS_4$ (0.1747 g, 0.50 mmol) in a 1:3 (v:v) mixture of H_2O/CH_3CN (5 ml) to give a dark brown solution. A solution of $(C_6H_5)_4PCl$ (0.7511 g, 2.0 mmol) in a 1:1 (v:v) mixture of H_2O/CH_3CN (7 ml) was added to this mixture resulting in the formation of a dark green solid. The solid was isolated by filtration, washed with EtOH and Et_2O then dried in a vacuum. The solid showed long term instability in air, it was therefore stored in the glove box. C:H:N analysis: measured: C 40.94 %, H 2.81 %, N 0 %; calculated: C 42.33 %, H 2.96 %, N 0%. Identity was confirmed by Rietveld fitting of the PXRD pattern using the structural model determined[20] from single crystal data.

2.10.17 $(PPh_4)_4[Ni(WS_4)_2]$ – cjc156[19]

The compound was made using the same methodology as the cobalt analogue. The solution of $NiCl_2$ (0.0324 g, 0.25 mmol) and $(NH_4)_2WS_4$ (0.1758 g, 0.53 mmol) was red, addition of a solution of $(C_6H_5)_4PCl$ (0.7059 g, 1.88 mmol) resulted in the formation of a pale brown solid which showed some long term instability in air, it was therefore stored in the glove box. C:H:N analysis: measured: C 40.16 %, H 2.84 %, N 0 %; calculated: C 42.34 %, H 2.96 %, N 0 %. Identity was confirmed by PXRD.

2.10.18 $(PPh_4)_4[Zn(WS_4)_2]$ – cjc171[19]

The compound was made using the same methodology as the cobalt analogue. The solution of $ZnCl_2$ (0.0343 g, 0.25 mmol) and $(NH_4)_2WS_4$ (0.1749 g, 0.50 mmol) was bright orange, addition of a solution of $(C_6H_5)_4PCl$ (0.7517 g, 2.01 mmol) resulted in the formation of a bright orange solid which showed some long term instability in air, it was therefore stored in the glove box. C:H:N analysis: measured: C 39.27 %, H 2.80 % N 0 %; calculated: C 42.13 %, H 2.95 %, N 0 %. Identity was confirmed by PXRD.

2.10.19 Cu_2WS_4 synthesised in the presence of $FeCl_2$ – cjc108

$(NH_4)_2WS_4$ (0.0702 g, 0.20 mmol), $Cu(CH_3CN)_4BF_4$ (0.0616 g, 0.20 mmol) and $FeCl_2$ (0.0273 g, 0.22 mmol) were placed in a Teflon lined hydrothermal autoclave (volume 23 ml) and a 1:1 mixture of DMF and butyronitrile (8 ml) was added resulting in the formation of an orange solid in an orange-brown liquid. The mixture was heated at a rate of 5 °C/min to 200 °C and the temperature was maintained for 48 hours before the vessel was cooled in the oven. Yield 0.0492 g.

2.10.20 "Fe_xWS_2" – cjc121

$(NH_4)_2WS_4$ (0.1051 g, 0.30 mmol) and $FeCl_2$ (0.0333 g, 0.26 mmol) were placed in a Teflon lined hydrothermal autoclave (volume 23 ml) and a 1:1 mixture of DMF and butyronitrile (8 ml) was added. The orange-red mixture was heated at a rate of 5 °C/min to 200°C and the temperature maintained for 48 hours before cooling in the oven. The black solid formed was isolated from solution by centrifugation and washed with 3 portions of Et_2O before drying in the air. Yield 0.0621 g, 68 % based on W and an assumed formula of $FeWS_2$.

2.10.21 "Co_xWS_2" – cjc123

The compound was prepared using the same methodology as the iron analogue using $(NH_4)_2WS_4$ (0.0897 g, 0.26 mmol) and $CoCl_2$ (0.0261 g, 0.20 mmol) which reacted to give a blue solution. A black solid was produced; yield 0.0802 g, 101 % based on W and an assumed formula of $CoWS_2$. (For an explanation of why this is only an assumed formula see Chapter 6).

2.10.22 "Mn_xWS_2" – cjc124

The compound was prepared using the same methodology as the iron analogue using $(NH_4)_2WS_4$ (0.0702 g, 0.20 mmol) and $MnCl_2$ (0.0258 g, 0.21 mmol) which reacted to give a bright orange solution. A black solid was produced; yield 0.0437 g, 72 % based on W and an assumed formula of $MnWS_2$.

2.10.23 "Ni_xWS2" – cjc131

The compound was prepared using the same methodology as the iron analogue using $(NH_4)_2WS_4$ (0.0700 g, 0.20 mmol) and $NiCl_2$ (0.0262 g, 0.20 mmol) which reacted to give a yellow solution. A black solid was produced; yield 0.0488 g, 79 % based on W and an assumed formula of $NiWS_2$.

2.10.24 $(NH_4)_2WS_3O$ – cjc008[14]

NH_4OH (4.0 ml) was added dropwise to H_2WO_4 (5.0 g, 20 mmol) to form a suspension of white powder in a colourless solution. The suspension was saturated with H_2S(g) at room temperature and filtered to remove a pale green solid. The yellow filtrate was added to 200 ml of ^{i}PrOH which was cooled in an ice bath, and formed a bright yellow precipitate. The solid was isolated by filtration and dried under vacuum. C: H: N analysis: measured: C 0.07 %, H 2.43 %, N 8.60 %; calculated: C 0 %, H 2.43 %, N 8.43 %. Identity was confirmed by PXRD.

2.11 References

1. M. M. Woolfson, An Introduction to X-ray Crystallography, Cambridge University Press, 1997.
2. H. M. Rietveld, *J. Appl. Cryst.*, 1969, **2**, 65-71.
3. R. A. Young, The Rietveld Method, Oxford Science Publications, 1993.
4. L. B. McClusker, R. B. Von-Dreele, D. E. Cox, et al., *J. Appl. Cryst.*, 1999, **32**, 36-50.
5. A. A. Coelho, *TOPAS v3.0 General Profile and Structure Analysis Software for Powder diffraction data, Bruker AXS, Karlsruhe*, 2001.
6. J. S. O. Evans, *multivisser - A Fortran Routine for controlling Visser*, 2001.
7. J. W. Visser, *J. Appl. Cryst.*, 1969, **2**, 89-95.
8. A. A. Coelho, *J. Appl. Cryst.*, 2003, **36**, 86-95.
9. P. M. de-Wolff, *J. Appl. Cryst.*, 1968, **1**, 108 - 113.
10. J. S. O. Evans, *phenixlogfile - a Fortran routine for extracting average temperatures from PheniX logfiles*, 2000.
11. R. Schmit, *Production and performance of thin and thick film NTCR thermistors based on* $NiMn_2O_4^+$, PhD Thesis, University of Durham, 2003.
12. G. J. Kubas, *Inorg. Synth.*, 1979, **19**, 90-92.
13. A. L. Spek, *Cryst. Struct. Commun.*, 1982, **A11**, 413-416.
14. J. W. McDonald, G. D. Friesen, L. D. Rosenhein, et al., *Inorg. Chim. Acta*, 1983, **72**, 205-210.
15. *Powder Diffraction File, International Centre for Diffraction Data, Pennsylvania*, 1998.
16. S. C. O'Neal and J. W. Kolis, *J. Am. Chem. Soc.*, 1988, **110**, 1971-1973.
17. E. A. Pruss, B. S. Snyder and A. M. Stacy, *Angew. Chem. Int. Ed. Engl.*, 1993, **32**, 256-257.
18. P. J. Hickey, *M. Chem. Thesis*, University of Durham, 2004.
19. A. Müller, E. Diemann and H. H. Heinsen, *Chem. Ber.*, 1971, **104**, 975-980.
20. A. Müller, N. Mohan and H. Bogge, *Z. Naturforsch., B: Anorg. Chem. Org. Chem.*, 1978, **33**, 978-982.

3 The use of spherical harmonic functions for powder data fitting

3.1 Introduction[1]

The physical properties of a polycrystalline sample, in particular crystallite size, internal strain and crystallite orientation can have a significant effect on the powder X-ray diffraction pattern obtained from that material. These effects may cause changes in the observed intensity (orientation) or in the peak widths in a pattern (size and strain). For some samples these effects are isotropic, however they can also be anisotropic. This chapter looks at ways of modelling the anisotropic effects and extracting information about the physical properties of a powder sample from the diffraction pattern.

Peak shape broadening is the result of a combination of factors including the nature of the sample itself and features of the instrument and radiation source used for data collection. All peaks have an inherent width, known as the Darwin width, a result of the diffraction process itself. The radiation source used causes additional broadening due to the effects of spectral distribution. For a diffractometer in which radiation of more than one wavelength is used, the different components (e.g. $K\alpha_1$ and $K\alpha_2$) will tend to spread out as 2θ increases; at moderate 2θ, this can make the peak profiles very broad before individual components become resolved. This effect can be eliminated by using a monochromator, though this does itself introduce another source of peak broadening. Other instrument based sources of broadening include: the X-ray source image, axial divergence of the beam and the soller slits used, the use of receiving slits, and collection of data in flat plate mode. If the sample being studied is transparent to X-rays, diffraction takes place at more than one sample height, an additional cause of broadening.

Peak shape broadening from the sample is primarily the result of size and strain effects. If a crystallite is below ~1μm in size then size broadening is a significant effect. The simplest description of this effect was devised by Scherrer,[2] and the size dependence of the full width half maximum (fwhm) of a peak profile is approximated by equation 3.1, where *rad* is the goniometer radius in mm, λ is the X-ray wavelength in nm and τ is the crystallite size in nm.

$$fwhm = \frac{0.1 \times rad \times \lambda}{\tau \cos\theta} \qquad [3.1]$$

Strain effects cause broadening which can be described by equation 3.2; ϵ is a term describing the strain and k is a constant, the value of which depends on the definition of strain used.

$$fwhm = k\varepsilon \tan\theta \qquad [3.2]$$

When fitting powder data it is important to use a peak shape model which is appropriate for the sample and data collection method used. Different methods of collecting data tend to result in characteristic peak shapes and a slightly different model is appropriate. For X-ray diffraction data, a typical peak profile will be slightly asymmetric in nature primarily due to axial divergence effects. The models developed to describe X-ray diffraction peaks are combinations of the symmetric Gaussian and Lorentzian functions; which can be combined with an axial divergence model[3] to account for peak asymmetry. Functions which are commonly used include the Voigt function,[4,5] a convolution of Gaussian and Lorentzian functions, and the pseudo-Voigt function[6] in which the overall profile is determined by the value of a refined mixing parameter, which determines the proportion of Gaussian and Lorentzian functions respectively. The commonly used peak shape functions model strain and size broadening as isotropic phenomena; the resultant peak broadening is modelled as varying smoothly with the value of 2θ. However it is possible to get samples in which there is anisotropic peak broadening, giving a powder pattern in which certain *hkl* reflections are broader than others, in this case the isotropic peak shape model might not adequately model the peak shape.

Like broadening effects, sample orientation effects can also show strong *hkl* dependence, though this is seen not in the peak shape, but in the peak intensities. These preferred orientation effects are often the result of crystallites having a well defined shape with a tendency to align in a particular orientation in a flat plate experiment, for example a plate like crystallite would tend to lie down on its largest face rather than one of the thin edge faces. This can be especially problematic when bulk samples are prepared because the action of pressing them into a holder can result in strong directional preference. The effect of this on the diffraction pattern is that certain reflections will have artificially high intensity compared to the ideal case where all the crystallites are randomly orientated. Although preferred orientation effects can sometimes be reduced by careful sample preparation, for example sprinkling powders onto a surface rather then pressing them into a bulk holder, or collecting data from a sample contained in a rotating capillary, it is not always possible to totally remove the effect.

Both preferred orientation and anisotropic strain broadening have directional dependence and within any given powder pattern only certain *hkl* reflections will be affected by them. The standard methods of modelling powder data do not take into account any directional dependence of peak width or intensity. For samples where either peak intensity or peak width show strong directional dependence these standard

methods may be inadequate and lead to poor agreement between calculated and observed powder patterns. If anisotropic effects are to be successfully modelled then mathematical functions with directional dependence must be used.

Although there are other ways of modelling directional dependence in powder patterns, the approach used here involves the use of spherical harmonic functions. Spherical harmonics are a special class of simple mathematical functions. They are functions described in the spherical polar coordinate system and their magnitude at a given point is dependent on theta, θ, and phi, φ, *i.e.* they are orientation dependent. This means that a sum of spherical harmonic functions can be used to describe any function on the surface of a sphere just as any 1D function can be described by a summation of a number of Fourier series. When used in powder data fitting each of these expressions contains a normalisation constant, which has a value such that the maximum possible value for any individual function is 1. The expressions have the general formula: $Y_{l,m}(\theta,\varphi)$; for example:

$$Y_{22p} = cos(2\varphi)\times sin2(\theta) \quad [3.3]$$

$$Y_{40} = (3-30\times cos^2(\theta)+35\times cos^4(\theta))/8 \quad [3.4]$$

$$Y_{62p} = 0.6454\times cos(2\varphi)(1-18\times cos^2(\theta)+33\times cos^4(\theta)\times sin^2(\theta)) \quad [3.5]$$

The functions have very distinct shapes, some examples are shown in Figure 3.1.

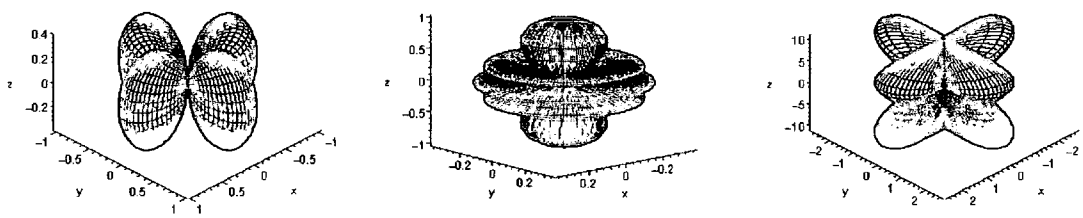

Figure 3.1 The shapes of the Y_{22p} (left), Y_{40} (middle) and Y_{62p} (right) functions. The functions are displayed with arbitrary axes.

In order to use spherical harmonic functions to model direction dependent effects in powder data, they are incorporated as scaling factors in the model. In the case of preferred orientation it is the overall peak intensity that is scaled, for orientation dependent peak shapes it is the fwhm of the peak. The spherical harmonic used to fit a particular data set must have the same directional dependence as the data itself and this is achieved by using a sum of the individual $Y_{l,m}$ functions. Each of these functions has a shape that follows the same point symmetry operations as are found in crystals *i.e.* rotations, reflections and inversions. For the factors studied here - intensity effects and size or strain peak broadening, it is generally sufficient to consider only the Laue class of the crystal when selecting spherical harmonic functions with the correct symmetry to

match the data.[7] The overall spherical harmonic function is then determined by refining a coefficient for each of the individual functions. The shape of the spherical harmonic function which is needed to fit the data can give some physical information about the crystal, it can show in which direction crystallites are orientated (preferred orientation) or give directional information about internal strain or crystallite size (peak shape fitting).

For the work presented in this thesis it is particularly important to be able to model anisotropic orientation and peak broadening effects. Many of the materials discussed are layered, and consequently prone to preferred orientation. Additionally, many are synthesised at relatively low temperatures, which often results in significant internal strain in the crystallites. The development and validation of the use of spherical harmonics for our work within the TOPAS[8] program is described in this chapter. The examples used are materials whose chemistry and structures are discussed elsewhere in this thesis.

3.2 Visualisation of spherical harmonic functions

If spherical harmonic functions are to be used to model effects of physical properties of crystallites, it is important to have some way of visualising them. Visual representations of the functions used in this work have been produced by plotting 3D scatter plots which show the magnitude of the spherical harmonic function applied as a function of *hkl*. Each *hkl* is represented in terms of a direction relative to the origin of the graph, the magnitude of the function in that direction being the distance of the point from the origin.

In order to produce these scatter plots a list containing the *hkl* indices of all the reflections in the powder pattern and the magnitude of the spherical harmonic function that is applied to that reflection is output from TOPAS. For each *hkl* a direction is defined relative to three orthogonal axes (used to represent h, k and l) using spherical polar coordinates, the Cartesian *hkl* values are replaced by r, θ and ϕ. The values of the spherical harmonic functions themselves are defined only by the values of θ and ϕ (see equations 3.3 to 3.5) consequently for each family of reflections for which θ and ϕ are the same (*e.g. 001*, *002*, *003* ...) only one point is plotted on the graph. The position of the points in the 3D scatter plot is calculated in Cartesian coordinates using equations 3.6 to 3.8, the values of θ and ϕ are defined by the values of *hkl*, m is the magnitude of the spherical harmonic for that particular reflection.

$$x = m \times \cos(\phi)\sin(\theta) \quad [3.6]$$

$$y = m \times \sin(\phi)\sin(\theta) \quad [3.7]$$

$$z = m \times \cos(\theta) \quad [3.8]$$

In order to create the full 3D plot, the symmetry equivalents of each reflection are also included. As a further guide to the eye, each point is coloured to indicate the relative magnitude of the correction for a given reflection. For each point in the graph the magnitude of the correction is converted to be on a linear scale and the maximum is given a value of 100 and the minimum a value of 0. Colours are assigned to each point according to its value on this scale. The colours used for all plots in this thesis are summarised in Table 3.1.

Relative magnitude of correction	Colour	Relative magnitude of correction	Colour
0 – 9		60 – 69	
10 – 19		70 – 79	
20 – 29		80 – 89	
30 – 39		90 – 99	
40 – 49		100	
50 – 59			

Table 3.1 Colours used to indicate magnitude of correction in spherical harmonic scatter plots.

An example plot is shown in Figure 3.2.

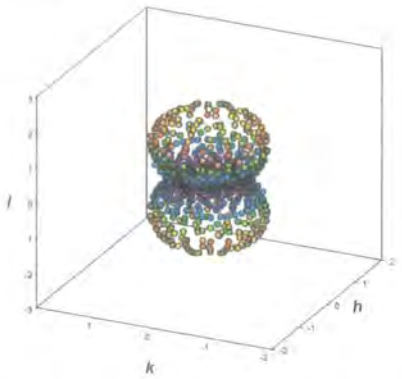

Figure 3.2 An example of a spherical harmonic function represented as a 3D scatter plot; axes indicate the magnitude of the correction.

This example plot shows a case where the magnitude of the spherical harmonic function is smallest for reflections with lots of h or k character *i.e.* those for which the values of h and/or k are larger than that of l. As the l character of the reflection increases, the magnitude of the function increases and reaches its maximum for *00l* type reflections. This is indicated by both the shape of the graph and the colour of the points which are "cold" around the $l = 0$ plane and become "warm" as the value of l becomes greater than that of h and k. It is important to note that the numbers on the axes indicate the magnitude of the correction in any particular direction and not the values of h, k and l.

3.3 Spherical harmonic functions used to correct preferred orientation effects

Spherical harmonic functions can be used to correct for preferred orientation effects by using the function as a simple scale factor which multiplies the intensity of each peak by the value of the spherical harmonic function determined for its particular values of *h*, *k* and *l*. The spherical harmonic function used is a sum of individual functions with the same point symmetry as the crystal; coefficients for each function in the sum are determined by a least squares fitting procedure in TOPAS.

3.3.1 Cu_2WSe_4

Cu_2WSe_4 is a material which was synthesised at 220 °C using a solvothermal method. Its structure has been determined by refinement of the structural model obtained from a related material; it is layered and contains layers of edge linked $CuSe_4$ and WSe_4 tetrahedra separated by a Van der Waals gap. The synthesis and structural characterisation are discussed in detail in section 4.3. Two powder patterns were collected for this material using a sample mounted by sprinkling onto a flat sample holder and a sample contained in a capillary. Flat plate data were collected using a Siemens D5000 diffractometer on a sample sprinkled onto an amorphous glass slide coated in a layer of Vaseline. Data were collected over a 2θ range of 5 to 120 °, using a step size of 0.02 °, a time per step of 10 s and 1 ° divergence slits. Capillary data were collected on a Bruker d8 Advance diffractometer, operating in transmission mode with the sample loaded into a 0.3 mm capillary. Data were collected over a 2θ range of 10 to 120 °, using a step size of 0.0144 ° and a time per step of 5 s. Five individual sets of data were collected and data from all scans were summed, giving a total measurement time of ~52 hours. The two powder patterns are shown in Figure 3.3.

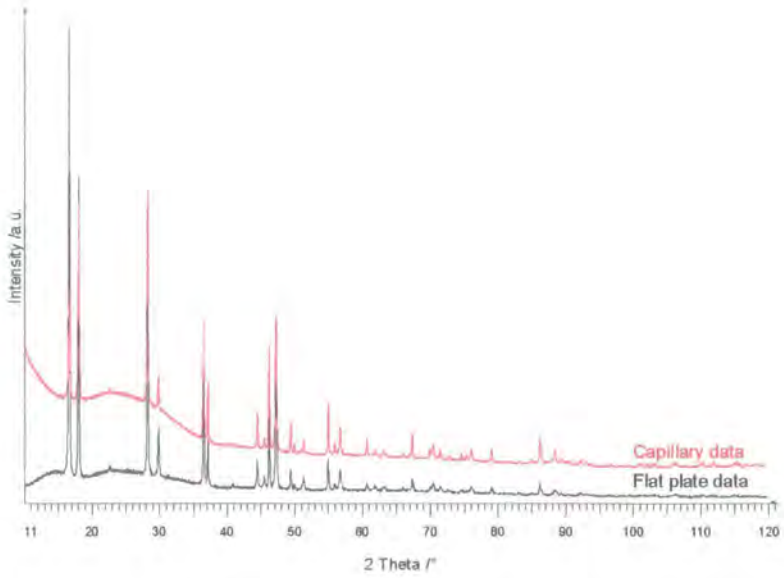

Figure 3.3 Powder patterns of Cu_2WSe_4 collected on a sample sprinkled onto a flat plate and on a sample contained in a capillary. Patterns are offset in the *y* direction for clarity.

As Figure 3.3 shows, there are significant discrepancies in the pattern of intensities in the powder patterns collected using the two different methods. It is highly likely that these discrepancies are due to preferred orientation in the flat plate data. Collection of data in capillary mode is likely to reduce preferred orientation because the sample is spun therefore the orientation of crystallites is constantly changing. These data provide an excellent opportunity to test the effectiveness of the use of a spherical harmonic function to correct for the effects of preferred orientation. The structure determined from the flat plate data with and without such a correction can be compared to the structure determined from data collected in capillary mode (which is assumed to be unaffected by preferred orientation) in order to see if the correction leads to an improved structural model. The reliability of the correction can be further tested by using a preferred orientation correction on the capillary data, to see what effect, if any, this has on the structure determined.

To fit the data a total 35 parameters were refined for the flat plate data and 29 for the capillary data. These comprised of: 15 (capillary) or 21 (flat plate) coefficients of a Chebychev polynomial to describe the smoothly varying background, a simple axial model term to describe the peak asymmetry; a zero point error, a scale factor, 6 pseudo-Voigt peak shape parameters, 2 cell parameters, 2 atomic coordinates and 1 temperature factor. For refinements which used a preferred orientation correction, 5 extra parameters (the coefficients of a 6^{th} order spherical harmonic) were refined.

A summary of refinement and structural data for all refinements is given in Table 3.2. TOPAS input files for all refinements are included in the e-appendix.

	Flat plate	Flat plate + correction	Capillary	Capillary + correction
${}_wR_p$ /%	10.654	7.402	2.922	2.719
R_{Bragg} /%	11.653	2.196	2.505	1.247
χ^2	2.46	1.71	2.56	2.38
No of refined parameters	35	40	29	34
a /Å	5.5571 (2)	5.5573 (1)	5.5576 (1)	5.5576 (1)
c/ Å	10.6877 (6)	10.6873 (3)	10.6878 (2)	10.6875 (2)
Se *x* coordinate	0.2494 (5)	0.2403 (5)	0.2430 (2)	0.2406 (3)
Se *z* coordinate	0.1120 (3)	0.1286 (3)	0.1189 (6)	0.1329 (2)
U_{iso} /Å^2	0.095 (2)	0.055 (1)	0.0148 (3)	0.0140 (4)
W – Se /Å	2.296 (4)	2.336 (4)	2.364 (2)	2.365 (2)
Cu – Se /Å	2.301 (2)	2.399 (2)	2.409 (1)	2.426 (1)
Se – W – Se /°	105.77 (8)	107.9 (2)	107.79 (8)	106.16 (9)
	117.2 (2)	110.25 (8)	110.32 (4)	111.15 (4)
Se – Cu – Se /°	105.5 (2)	106.0 (2)	107.29 (9)	107.07 (9)
	105.9 (2)	110.1 (1)	109.35 (6)	108.30 (6)
	117.3 (2)	112.4 (2)	111.80 (9)	113.11 (9)

Table 3.2 Summary of selected structural and refinement details for Cu_2WSe_4 obtained from flat plate and capillary data, with and without a preferred orientation correction.

The data in Table 3.2 shows many important relations. Firstly the cell parameters show very little variation on application of the preferred orientation correction. Preferred orientation is a phenomenon which affects only peak intensities, so any variation in the cell parameters on application of the correction would suggest that it was causing an unrealistic change in the structural model.

Comparing the flat plate data with and without correction suggests that the correction gives a significantly improved fit to the data. It is immediately apparent that there is a large drop in the weighted profile R-factor, ${}_wR_p$, on introduction of the spherical harmonic function, indicating a considerable improvement in the quality of fit. Perhaps more importantly from a structural viewpoint there is a concurrent reduction in R_{Bragg} from 11.6 to 2.2 %. The Rietveld fits with and without the correction are shown in Figure 3.4.

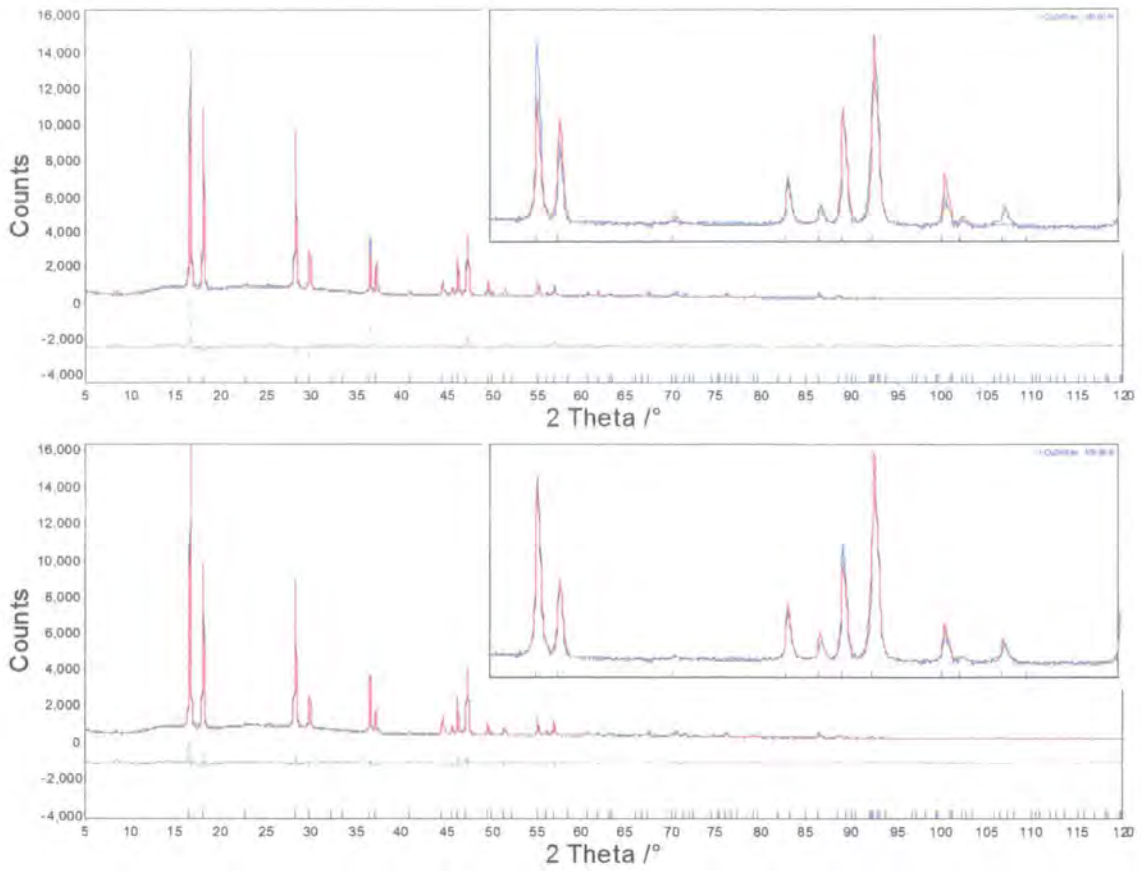

Figure 3.4 The powder pattern of Cu_2WSe_4 collected in flat plate mode and fitted with (bottom) and without (top) a preferred orientation correction. Insets show the region between 35 and 55 ° 2θ. Observed data are shown in blue, calculated in red and difference in grey.

There are significant structural changes on application of the correction which are the result of a change in the position of the Se atoms. W – Se and Cu – Se bond lengths increase and the tetrahedral coordination geometry around the metal centres become notably less distorted.

The structure determined from the flat plate data using a preferred orientation correction is very similar to that determined from the capillary data without any correction. Bond lengths differ by 0.03 Å for the W – Se bond and 0.01 Å for the Cu – Se bond (c.f. 0.04 Å and 0.10 Å differences respectively between the flat plate uncorrected and corrected models). Similarly small differences are observed in the bond angles (mean difference 0.7 ° compared to a mean difference of 3.7 ° between angles in structures from corrected and uncorrected flat plate data).

The structure determined from the capillary data with a spherical harmonic correction is also very closely related to the structure determined from capillary data without a correction and that determined from flat plate data without a correction. Differences in bond lengths of 0.001 Å for W – Se and 0.02 Å for Cu – Se are observed between the

capillary data models with and without correction. The mean deviation in bond angles between these two models is 1.0 °.

The shapes of the spherical harmonic corrections applied to the flat plate and capillary data are shown in Figure 3.5.

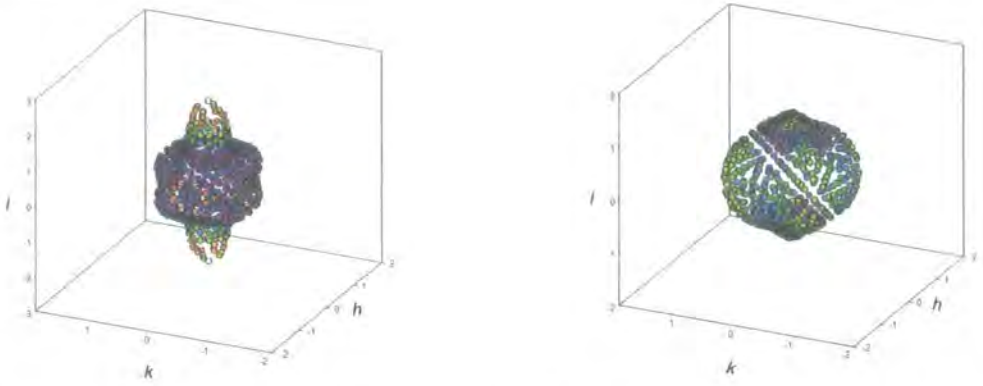

Figure 3.5 The shapes of the spherical harmonic functions used to correct flat plate data (left) and capillary data (right) for Cu_2WSe_4.

The shape of the function used for the flat plate data shows that there is a significant correction for the peak intensities for peaks with a high degree of *l* character. The correction to the peak intensity varies from a maximum increase of +127 % for *00l* peaks to a maximum decrease of −35 % for the *0k0* peaks. The magnitude of the correction is much smaller for the capillary data, varying from a maximum increase of +18 % for the *00l* reflections to a maximum decrease of −11 % for the *0kl* reflections. The shape of the flat plate data correction suggests that this material is prone to orientation in which the crystallites are orientated with the *ab* plane parallel to the plane on which the sample is mounted; this artificially increases the intensity of *00l* reflections and other reflections with a high degree of *l* character. The material is a layered material in which the layers are in the *ab* plane; this type of orientation effect is very common for this type of material. For the capillary data there may also be a small amount of orientation in the sample, though crystallites would be orientated in a different way to those in the flat plate sample. An alternative explanation for these observations is the presence of minor stacking faults which cause the intensities of peaks in a particular direction to be artificially low. If there were more of these types of fault in the planes of the layers in the material than there were in the direction perpendicular to the planes then they would have a greater effect on non *00l* type reflections than on *00l* type reflections, which would explain the observed intensity variations.

The shapes and magnitudes of these functions confirm that there is a significant amount of preferred orientation in the flat plate data. Comparison of the structures determined

from these data with and without a correction show that the orientation causes significant structural distortions. However, if a preferred orientation correction is used, similar structural parameters to those determined from capillary data are obtained. This is good evidence for the validity of such corrections. If there was no preferred orientation in the capillary data then no structural changes would be expected if a preferred orientation correction were applied. If a correction is applied to the capillary data it causes only very small structural changes. Although these are unexpected it is impossible to say for sure that collecting data using a sample in a capillary totally removes all orientation effects, the preferred orientation model may be correcting for a small amount of residual orientation, rather than causing an artificial change of the structure.

3.3.2 $(PPh_4)_2Ni(WS_4)_2$

The structure of $(PPh_4)_2Ni(WS_4)_2$ was determined from powder diffraction data collected on a sample prepared by sprinkling the material through a 100 mesh sieve onto a Vaseline coated silicon wafer. Full data collection details and a discussion of the structure can be found in section 5.3. Rietveld analysis of the powder pattern suggested that preferred orientation was artificially increasing the intensity of the *h11* reflections; similar orientation effects had previously been observed in powder patterns on samples prepared for data collection in various ways. If these effects are modelled using spherical harmonic functions, it is possible that application of such a correction will mask structural subtleties; equally, it is possible that if no correction is applied, the structure will be distorted as it changes to fit more intensity to the artificially intense peaks. In order to determine if the application of such a correction was reasonable in this case, the structures determined with and without the correction were carefully compared.

This material is a triclinic molecular solid, space group $P\bar{1}$, and the structure consists of isolated PPh_4^+ cations and $Ni(WS_4)_2^{2-}$ anions which are made by linking two WS_4^{2-} tetrahedra to a Ni^{2+} ion, which ends up with square planar coordination geometry. There is one WS_4^{2-} tetrahedron, half of a Ni^{2+} ion and one PPh_4^+ cation in the asymmetric unit. This gives 4 independent W – S distances, 2 independent Ni – S distances, 6 S – W – S bond angles and 2 S – Ni – S bond angles (the third is constrained by symmetry to be 180 °). The PPh_4^+ cations are modelled as rigid bodies, their positions are described by three rotational and three translational parameters and the rotation of the phenyl rings about the P – C bonds is also refined. Full details of the refinement can be found in Chapter 5. The values of several of the structural parameters for data fitted with and without a 4^{th} order spherical harmonic preferred orientation correction are shown in Table 3.3.

Parameter	Value without SH correction	Value with SH correction
$_wR_p$ /%	4.44	3.92
R_{Bragg} /%	2.54	1.62
χ^2	2.52	2.23
No. of refined parameters	60	74
a /Å	9.3735 (2)	9.3730 (2)
b /Å	12.4951 (3)	12.4951 (3)
c /Å	12.5192 (3)	12.5189 (3)
α /°	65.814 (2)	65.814 (1)
β /°	83.751 (2)	83.751 (1)
γ /°	69.570 (2)	69.571 (1)
W – S /Å	2.06 (2)	2.03 (2)
	2.12 (2)	2.11 (2)
	2.17 (1)	2.16 (1)
	2.27 (1)	2.17 (1)
W – S mean /Å	2.16	2.12
W – S standard deviation /Å	0.08	0.06
Ni – S /Å	2.10 (1)	2.20 (1)
	2.12 (2)	2.25 (2)
Ni – S mean /Å	2.11	2.19
Ni – S standard deviation /Å	0.01	0.03
W – Ni /Å	2.823 (3)	2.820 (3)
S – W – S mean /°	109.3 (1)	109.3 (1)
S – W – S max – min /°	25.6 (1)	13.1 (1)
S – Ni – S mean*/°	90.0	90.0
S – Ni – S max – min /°	15.8 (1)	13.2 (1)
x_{rot} PPh_4 /°	−344.5 (1)	−344.0 (2)
y_{rot} PPh_4 /°	27.1 (1)	26.4 (2)
z_{rot} PPh_4 /°	202.1 (1)	203.0 (2)
P – C bond rotation /°	16.6 (6)	17.1 (8)
	−67.6 (6)	−67.7 (7)
	16.2 (6)	18.9 (6)
	90.1 (6)	83.2 (7)

Table 3.3 Selected structural and refinement data for $(PPh_4)_2Ni(WS_4)_2$ with and without a spherical harmonic preferred orientation correction. Note that the angles marked * are constrained by symmetry to sum to 90° and that the third unique S – Ni – S angle is 180 ° and is not included in this analysis.

The shape of the spherical harmonic function used to model the preferred orientation is shown in Figure 3.6. The shape of this function shows that the biggest increases in peak intensity (+30 %) occur for reflections for which *h*, *k* and *l* all have similar values, while the biggest decrease in intensity (−30 %) is for peaks for which the value of *l* is small and *h* and *k* have significantly different values. This is a fairly complex orientation effect, which is what might be expected for a triclinic, molecular solid. In terms of the structure this suggests either that the crystallites are tending to orientate so that the NiS_4 square planes are aligned parallel to the surface on which the sample is mounted or that there are fewer stacking faults in the direction perpendicular to the NiS_4 square planes than in other directions.

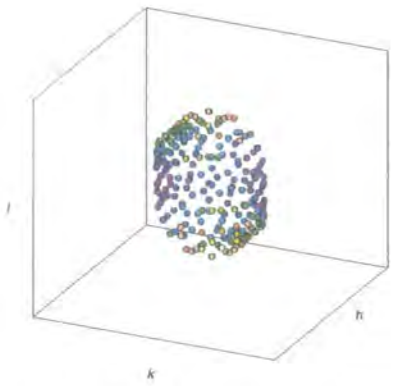

Figure 3.6 The shape of the spherical harmonic function used to model preferred orientation in the powder pattern of $(PPh_4)_2Ni(WS_4)_2$.

The data in Table 3.3 show that there are relatively subtle differences between the structures determined with and without the preferred orientation correction. Cell parameters are almost identical, which confirms that the preferred orientation correction is not affecting peak positions. R_{Bragg} drops by 0.92 % on the inclusion of the preferred orientation correction; this is a moderately large drop and reflects an improvement in agreement between the structure and the observed powder pattern. Rietveld refinements with and without the correction are shown in Figure 3.7.

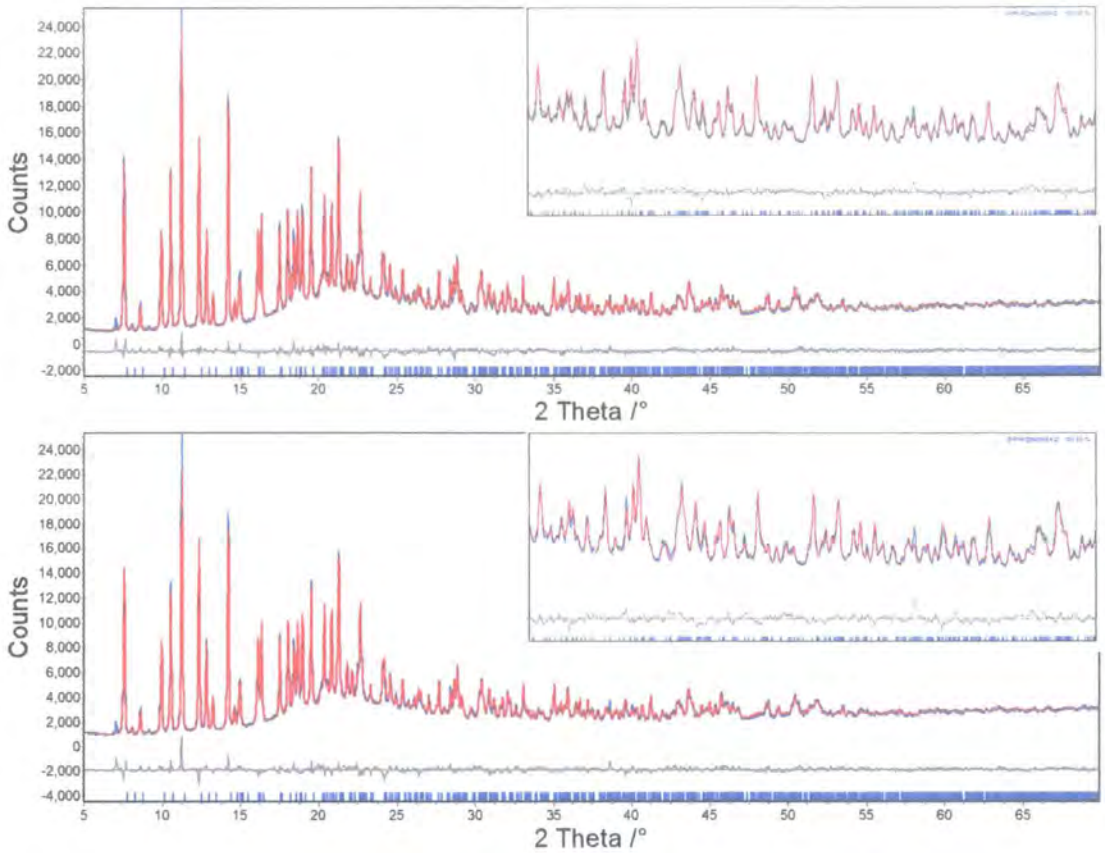

Figure 3.7 Rietveld refinements of $(PPh_4)_2Ni(WS_4)_2$ with (top) and without (bottom) a preferred orientation correction. The inset shows zooms of the region between 25 and 45 ° 2θ. Observed data are shown in blue, calculated in red and difference in grey.

The atomic positions in the two structures are very close; this is shown schematically in Figure 3.8.

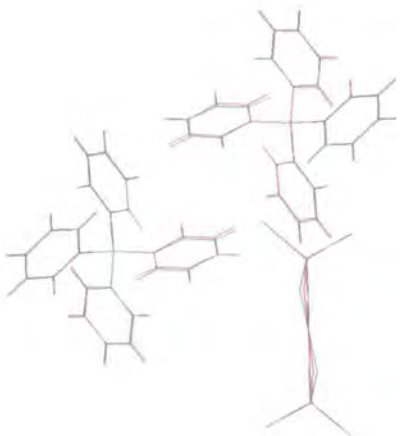

Figure 3.8 Skeletal representation of the atomic positions in $(PPh_4)_2Ni(WS_4)_2$ for structures determined with (green) and without (red) a preferred orientation correction.

The slight differences in atomic positions are shown in the bond lengths and angles, which show small variations between the two structures. These differences are only

found in the anionic units, as the bond lengths and angles in the PPh_4^+ cations have the same, fixed, values. The only refined parameters for the rigid PPh_4 units are rotations around the three crystallographic axes and the rotations of the phenyl rings about the P – C bonds, the values of these parameters are very close in the two structures. For the anion units, there is variation in both the W – S and Ni – S bond lengths. The mean W – S bond length is longer in the structure determined without using a preferred orientation correction, however, this is strongly influenced by one particularly long W – S bond length (2.27 (1) Å), if this is not included, a mean of 2.12 Å is obtained. Both average bond lengths are short in comparison to the value determined for W – S bond lengths in an isolated WS_4^{2-} tetrahedron[9] (2.177 Å) and the range of other bond lengths observed in similar coordination environments in structures contained in the CSD[10] (96% are in the range 2.16 – 2.30 Å). In contrast, the average Ni – S bond length is longer in the structure determined using a preferred orientation correction and values have a larger standard deviation. The average bond length for the structure that uses a preferred orientation correction, (2.19 Å) is well within the ranges seen for Ni in a similar coordination environment in structures in the CSD (97 % are in the range 2.12 – 2.25 Å), though for the structure determined without this correction the bond length (2.11 Å) is at the lowest end of the commonly observed range. The metal – metal distances within the anions are the same, within the bounds of experimental error.

The average bond angles for both metal centres in both structures are identical. However, for the structure determined without a preferred orientation correction, there is a much larger range of values observed, a range of 25.6 ° for the S – W – S bond angles reflects the fact that maximum and minimum bond angles of 95.7 (5) and 121.3 (5) ° are observed. These bond angles represent significant distortion of metal tetrahedra, much larger than distortions seen in other related compounds.

Overall the structures determined with and without a preferred orientation correction are very similar. However, the geometry of the anions in the structure determined without preferred orientation correction is more distorted than is the case if a correction is used, the W – S bond lengths are short in both cases and more realistic Ni – S bond lengths (judged by comparison to bond lengths in similar coordination environments) are found in the structure where a correction has been used.

This is not a clear cut case where it is obvious whether or not a preferred orientation correction should be applied to the data. It could be said that because the structure is very similar in both cases a correction is not necessary. However, although the differences are slight, there is evidence for improvement in the structural model when a correction is applied. Firstly, there is a drop in R_{Bragg}, the most reliable criterion on which the quality of fit between a structural model and observed data can be judged.

Assessing the quality of a structure by comparison of bond lengths and angles to those in structures already calculated is not an infallible method. However, in this case the structural parameters determined when a correction was used probably do give a more accurate representation of the structure, particularly given the fact that there has been no evidence of such large distortion in the tungsten tetrahedra in a series of related $(PPh_4)_2M(WS_4)_2$ (M = Zn, Mn, Co) compounds. For these reasons it can be concluded that the application of a spherical harmonic preferred orientation correction for these data is advantageous and that the final structure presented should be the one determined using this correction.

3.4 Spherical harmonic functions for modelling anisotropic peak broadening

Spherical harmonics can be used to model anisotropic peak broadening by using the functions to scale the fwhm values for different peaks according to their *hkl* values. One approach that has been previously[11] tried is to use an instrument peak shape and then add/convolute an anisotropic peak shape with this in order to describe sample effects. In order to determine an instrument peak shape, data from a standard material with similar scattering properties to the material in question and which shows minimal sample broadening, must be collected using the same diffractometer set up as that used to collect the diffraction pattern of the material being studied. The peak shape which fits this pattern is the instrument peak shape. As this kind of data was not always available for our materials, an alternative approach was used, this modelled the isotropic part of the peak shape (which includes all instrument based broadening) using either a pseudo-Voigt function or a combination of Gaussian and Lorentzian strain terms, an anisotropic contribution was then combined with this to give the overall *hkl* dependent peak shape.

3.4.1 Cu_2WS_4

Cu_2WS_4 is an extended inorganic solid that was prepared by refluxing reagents at low temperature by Hickey[12] using the method previously described by Pruss;[13] this material is further discussed in section 4.2. The structure and physical properties of the powder were investigated using powder diffraction.

Powder XRD data were collected using a Bruker d8 Advance operating in transmission mode on a sample loaded into a 0.5 mm capillary. The data were collected over a 2θ range of 5 to 120 ° using a step size of 0.0144 ° and a time per step of 2.5 s. The measurement was repeated 15 times and data for all scans summed, giving a total time per step of 37.5 s. Close examination of the diffraction pattern revealed that there were significant variations in the widths of the observed peaks. Some representative peaks are shown in Figure 3.9.

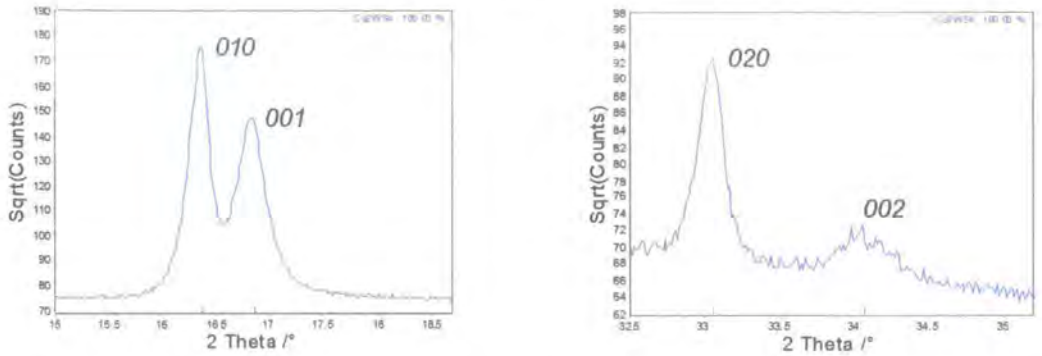

Figure 3.9 Part of powder pattern of Cu_2WS_4 showing the regions between 15 and 18.75 ° 2θ (left) and between 32.5 and 35.5 ° 2θ (right).

The peaks shown in Figure 3.9 clearly illustrate the differences in peak widths observed for this pattern; the *00l* reflections are much broader than the *0k0* reflections. Anisotropic broadening such as this can be indicative of anisotropic strain or variation of crystallite size. In order to further investigate the pattern of peak widths in this powder pattern, the fwhm of each peak was determined independently. This was done using the peak fitting facility in TOPAS. Unit cell parameters were used to predict the positions of all the peaks in the powder pattern, and a peak was placed at each of these predicted 2θ values. For each peak an intensity and a fwhm parameter were refined, a parameter determining the Lorentzian component of each peak shape was refined but constrained to be the same for all peaks. The TOPAS input file for this procedure is included in the e-appendix. The fwhm for each peak determined using this method are plotted against 2θ and shown in Figure 3.10.

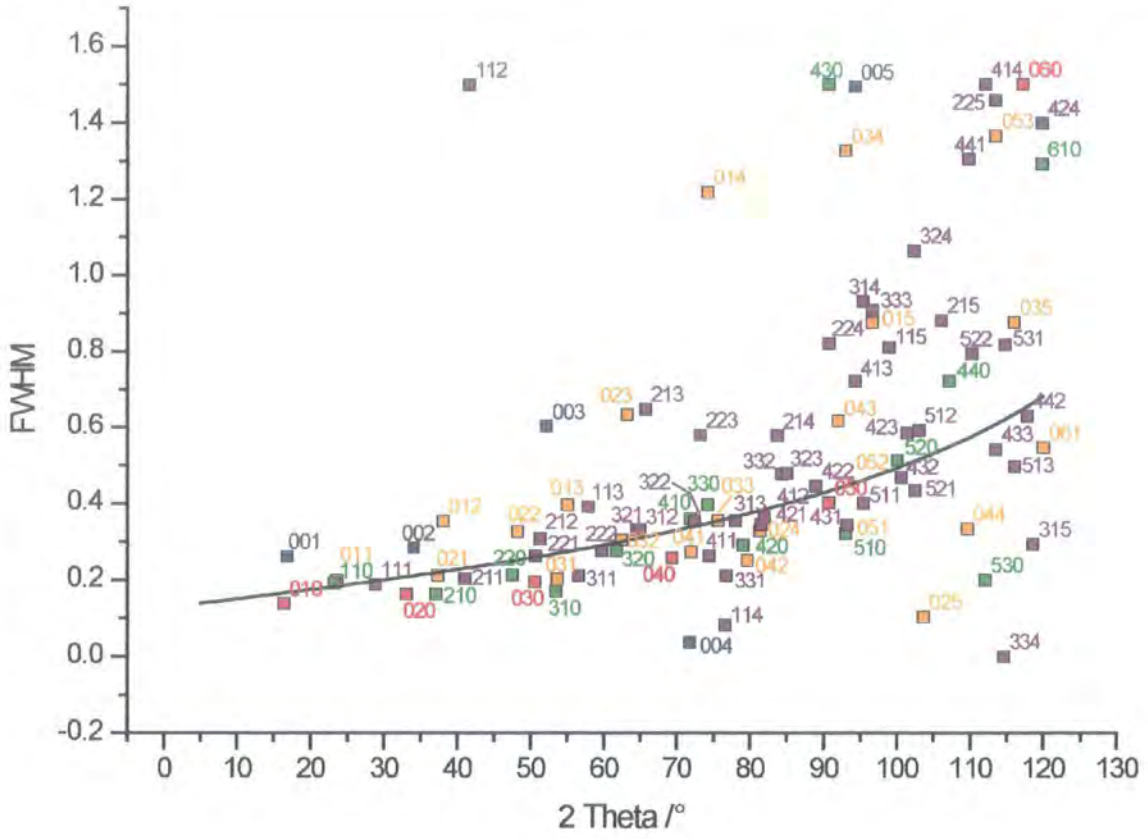

Figure 3.10 FWHM values for peaks in the powder pattern of Cu_2WS_4. *00l* reflections are shown in blue, *0k0* in red, *0kl* in orange, *hk0* in green and *hkl* in purple. The black line indicates the FWHM calculated for a PV peak shape used to fit the whole pattern.

The way that fwhm is determined will inevitably lead to some errors in the fwhm values. Peaks for which the intensity is very low or those with significant peak overlap (*e.g.* at high angles) may have large errors in the fwhm value that is determined. Despite this, the values determined show several general trends.

The data in Figure 3.10 confirm that the *00l* reflections (shown in blue) are significantly broader than the *0k0* reflections (shown in red), the only exception to this trend being the *060* and *004* reflections, both of which have very low intensities and consequently large associated errors. The *hk0* reflections (shown in green) are also generally fairly sharp, though there are a few exceptions to this at higher 2θ. *0kl* (orange) and *hkl* (purple) reflections show a much broader range of fwhm values, particularly at high angle. The large scatter in values at high angle may be partially explained by the fact that this is the region of the pattern for which there is most peak overlap and for which peaks generally have low intensities. These data do show anisotropic broadening, with a tendency for peaks with a high degree of *l* character to be the broadest. Attempts to model these effects used spherical harmonic functions, which were incorporated into the peak shape model in a number of different ways.

3.4.2 Methods of applying spherical harmonic corrections

Peak shape anisotropy can be modelled in a number of different ways. In order to investigate which is the best model for these data, different peak shape models were tested using a Pawley fitting method.[14] A Pawley fit was employed so that the structural model was not a biasing factor in the comparison. For each fit several parameters were refined in addition to the peak shape parameters, these were: an intensity for each of the peaks in the pattern (95 in total), 13 coefficients of a Chebychev polynomial to describe the background, a zero point correction, an axial correction to model peak asymmetry and 2 cell parameters. Several different peak shape models were used, these are summarised in the following paragraphs and in Table 3.4 and Table 3.5.

With one exception, the peak shape models tested used an isotropic peak shape function to give the underlying peak shape; the anisotropic spherical harmonic functions were then combined with this to give the overall model. The exception was a model which used only the anisotropic model and did not include an isotropic contribution. Two isotropic peak shape models were used, these were: the pseudo-Voigt peak shape (a combination of a Gaussian and Lorentzian function, requiring 6 parameters to be refined) and a model that used a combination of Gaussian and Lorentzian strain dependent terms (requiring only 2 parameters to be refined). The anisotropic contribution of the spherical harmonic functions was either added/subtracted from the isotropic peak shape, or used as a scaling factor for either a Gaussian or Lorentzian function which was convoluted with the isotropic model. Both Gaussian and Lorentzian functions scaled by a spherical harmonic were included and parameters were refined to define the relative contributions of each one. The spherical harmonic functions were also scaled by a factor of either $\tan\theta$ or $1/\cos\theta$ to model effects on peak width caused by strain and crystallite size respectively (see equations 3.2 and 3.1). Several combinations of these approaches were tried and both 4^{th} and 6^{th} order spherical harmonic functions were tested. A summary of data obtained from these refinements is given in Table 3.4 and Table 3.5. Input files for Pawley fits using all peak shape models are included in the e-appendix and a summary of the way the different peak shapes were applied using TOPAS is given in Appendix 3.1.

Peak shape model	a /Å	c/Å	$_wR_p$	No. of parameters	SH shape
PV only	5.4141	5.2537	3.074	118	–
G/L strain	5.4151	5.2543	3.913	114	–
PV convoluted G/L strain	5.4142	5.2537	3.074	120	–
PV add size SH4	5.4146	5.2542	2.245	122	
PV add strain SH4	5.4146	5.2545	2.084	122	
PV convoluted size SH4	5.4146	5.2544	2.178	123	
PV convoluted strain SH4	5.4147	5.2546	2.048	123	
G/L strain convoluted size SH4	5.4145	5.2542	2.286	119	
G/L strain convoluted strain SH4	5.4148	5.2546	2.550	119	
PV convoluted size/strain SH4	5.4147	5.2546	2.047	125	
G/L strain convoluted size/strain SH4	5.4147	5.2544	2.165	121	
4th order size/strain SH only	5.4147	5.2544	2.164	119	

Table 3.4 Cell parameters and R-factors for Pawley fits using isotropic peak shape models and anisotropic models which included 4th order spherical harmonic functions.

Peak shape model	a /Å	c/Å	$_wR_p$	No. of parameters	SH shape
PV only	5.4141	5.2537	3.074	118	–
G/L strain	5.4151	5.2543	3.913	114	–
PV convoluted G/L strain	5.4142	5.2537	3.074	120	–
PV add size SH6	5.4145	5.2543	2.201	124	
PV add strain SH6	5.4146	5.2545	2.082	124	
PV convoluted size SH6	5.4146	5.2544	2.161	125	
PV convoluted strain SH6	5.4147	5.2546	2.039	125	
G/L strain convoluted size SH6	5.4145	5.2543	2.235	121	
G/L strain convoluted strain SH6	5.4149	5.2548	2.521	121	
PV convoluted size/strain SH6	5.4147	5.2546	2.039	127	
G/L strain convoluted size/strain SH6	5.4146	5.2544	2.150	123	
6th order size/strain SH only	5.4146	5.2544	2.150	121	

Table 3.5 Cell parameters and R-factors for Pawley fits using isotropic peak shape models and anisotropic models which included 6th order spherical harmonic functions.

The R-factors for the different peak shape models presented in the table suggest that an isotropic peak shape alone is not sufficient to fit the powder data satisfactorily. Inclusion of an anisotropic component to the peak shape model greatly improved the agreement between observed and calculated data. For the isotropic models a pseudo-Voigt function gave significantly better agreement between calculated and observed data than a model which used a simple convolution of Gaussian and Lorentzian strain terms, although the decreases in R-factor are partially due to the refinement of extra parameters. This observation extends to other peak shape models, and it is generally true that using a pseudo-Voigt function as the isotropic part of the peak shape model gives a better result than using a combination of isotropic Gaussian and Lorentzian strain terms. The fitted powder patterns for the two isotropic peak shape models ($_wR_p$ = 3.07 % for Pseudo-Voigt and 3.91 % for Gaussian and Lorentzian strain) are shown in Figure 3.11.

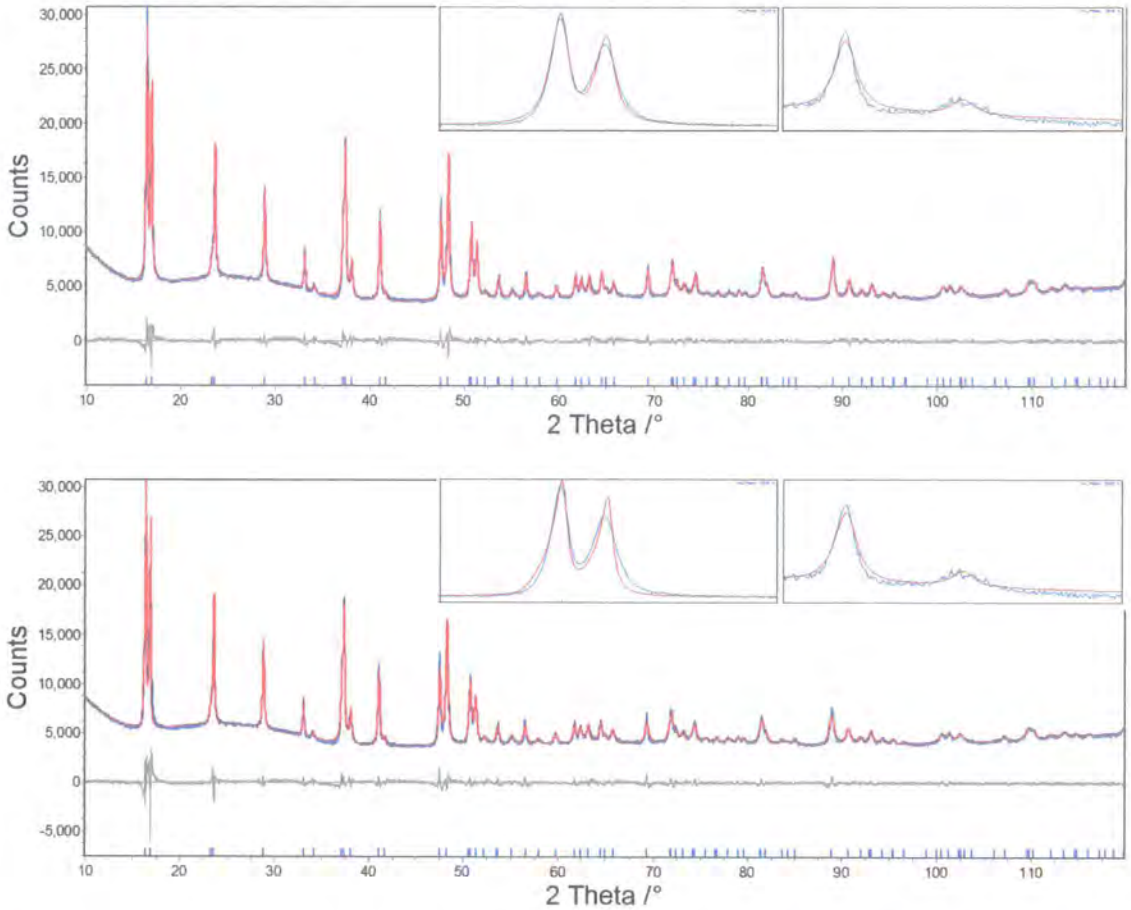

Figure 3.11 Powder pattern of Cu_2WS_4 Pawley fitted using a pseudo-Voigt function (top) and a convolution of Gaussian and Lorentzian strain terms (bottom) to model peak shape. The insets show zooms of the *010* and *001* peaks (left) and *020* and *002* peaks (right), the *y* axis for these is shown on a square root scale. Observed data are shown in blue, calculated in red and difference in grey.

For comparison the data were also fitted using only an anisotropic spherical harmonic peak shape model. This gives a significantly better agreement ($_wR_p$ = 2.16 %) between observed and calculated data than the isotropic models, though it is not quite as good as the models obtained by combining both isotropic and anisotropic contributions. The fit using just this anisotropic model is shown in Figure 3.12.

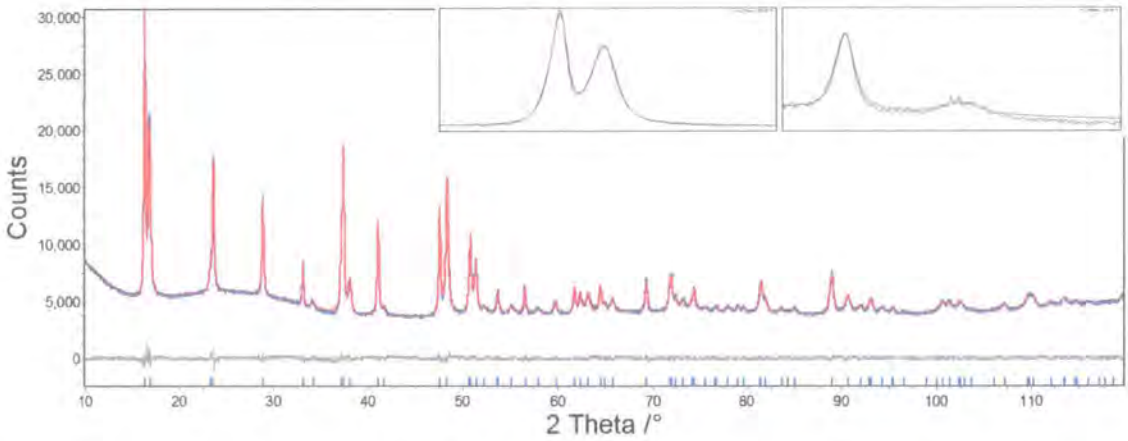

Figure 3.12 Powder pattern of Cu_2WS_4 Pawley fitted using a 4th order spherical harmonic peak shape model. The inset shows zooms of the *010* and *001* peaks (left) and *020* and *002* peaks (right), the *y* axis for these is shown on a square root scale. Observed data are shown in blue, calculated in red and difference in grey.

The shapes of all of the anisotropic functions suggest that the highest fwhm values are being used to fit peaks with a high degree of *l* character; this is consistent with the real trends in the fwhm values shown in Figure 3.10. The use of 6th order spherical harmonics (which require two extra parameters to be refined compared to the 4th order case) does give a small improvement to the fit compared with the 4th order case, but this improvement is so slight, that is it reasonable to conclude that a 4th order spherical harmonic is sufficient to model the peak shape anisotropy.

The R-factors for fits which use peak shapes where the spherical harmonic is scaled by a factor of tanθ, (*i.e.* shows the same 2θ dependence as strain) are generally slightly better than those for peak shapes which are scaled using 1/cosθ (size type dependence). Additionally if both size and strain type spherical harmonic convolutions are used and their relative contributions refined, then the size type contribution is much smaller than the strain type contribution. These observations suggest that the anisotropic peak broadening can be better approximated by a strain type function rather than a size type function. For the 4th order spherical harmonic functions, the lower R-factors are obtained by convoluting the spherical harmonic term with the pseudo-Voigt function, rather than by adding contributions for the two functions together. The peak shape model which gives the best balance between R-factors and number of refined parameters is the pseudo-Voigt function convoluted with a 4th order strain type spherical

harmonic ($_wR_p$ = 2.18 %). For this refinement, both Gaussian and Lorentzian strain contributions were refined, however, since the Gaussian type contribution refines to zero, only a component with a Lorentzian shape is required to model the pattern. The fit to the observed data is shown in Figure 3.13.

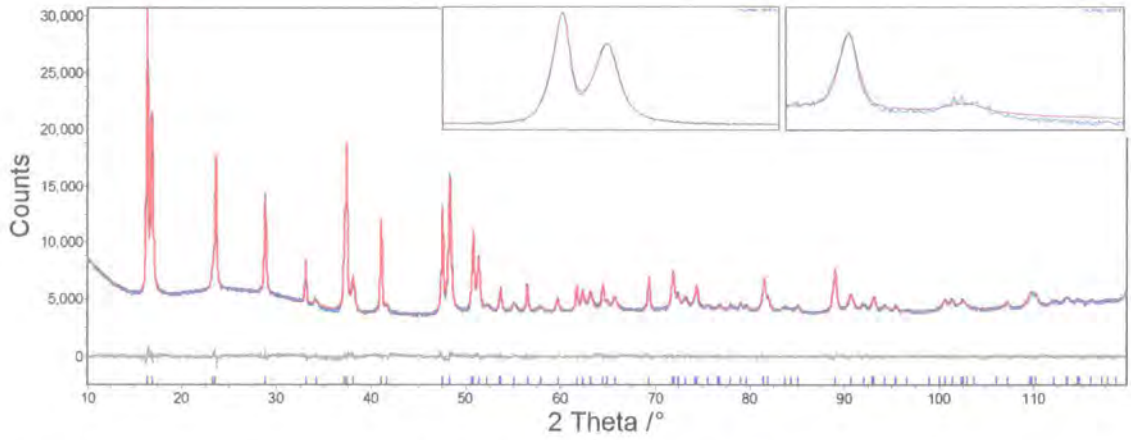

Figure 3.13 The powder pattern of Cu_2WS_4 Pawley fitted using a pseudo-Voigt function convoluted with a 4th order strain type spherical harmonic peak shape. The inset shows zooms of the *010* and *001* peaks (left) and *020* and *002* peaks (right), the *y* axis for these is shown on a square root scale. Observed data are shown in blue, calculated in red and difference in grey.

Although this peak shape model requires the refinement of additional peak shape parameters and gives only a small decrease in R-factor compared to the case where only a 4th order spherical harmonic function was used to model peak shape, it was chosen because the results obtained from it can be interpreted in a slightly more physically meaningful way. If a 4th order spherical harmonic were the only peak shape model then its shape would show the broadening caused by both sample and instrument effects. Instrument effects cause isotropic broadening, so if the peak shape is modelled using a combination of isotropic and anisotropic functions the shape of the spherical harmonic will not be influenced by instrument broadening. The approach is also directly applicable in cases where the instrument function is known. Of course, some sample broadening is isotropic, and this is incorporated into the pseudo-Voigt peak shape. Therefore the shape of the spherical harmonic represents only the excess strain broadening which is of an anisotropic nature.

In order to determine how well the spherical harmonic was really modelling the variation in peak shape, the calculated pattern was written out in xy format and individual pseudo-Voigt peaks (each with its own fwhm allowed to refine freely) fitted to these calculated data *i.e.* the same protocol was used as for the experimental data in Figure 3.10. The two values can then be compared; they are shown in Figure 3.14.

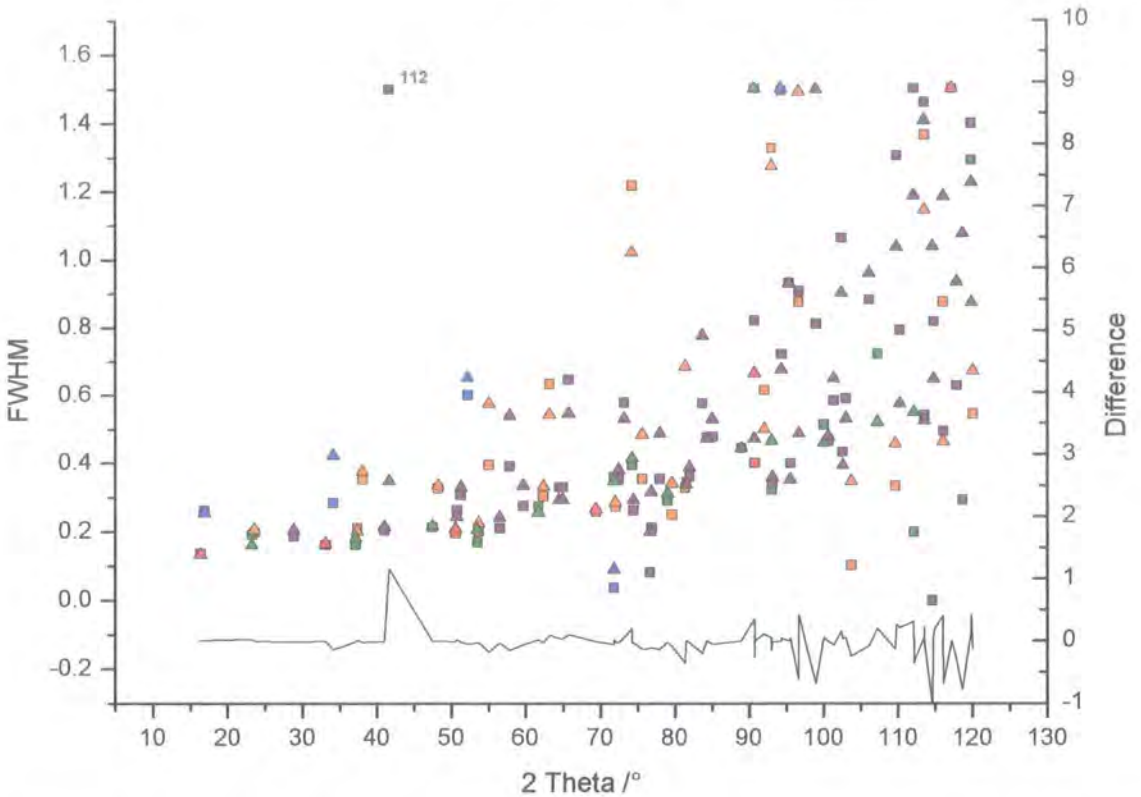

Figure 3.14 FWHM values for peaks in the experimental powder pattern of Cu_2WS_4 (squares) and for the calculated pattern for the model which used a spherical harmonic peak shape (triangles). *00l* reflections are shown in blue, *0k0* in red, *0kl* in orange, *hk0* in green and *hkl* in purple. The black line shows the difference between values for the raw data and the calculated pattern.

The fwhm values of peaks from the observed and calculated data show fairly close agreement up to a 2θ value of ~ 70°. The major exception to this is the peak at ~42 °, for which the fwhm is very large for the raw data. The difference between values increases dramatically at high 2θ. However, these major differences are due to difficulty in accurately determining the fwhm of a very low intensity peak (such as the one at ~42 ° 2θ) or of peaks that have significant overlap, such as those at high angle. The good agreement between the observed and calculated fwhm values confirms that the spherical harmonic function being used to fit the data is a realistic model of the peak width anisotropy. The shape of the spherical harmonic function is shown in Figure 3.15.

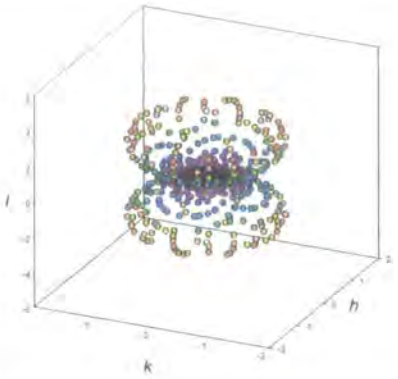

Figure 3.15 The shape of the 4th order strain type spherical harmonic used to model peak shape anisotropy in Cu_2WS_4.

This spherical harmonic function changes the pseudo-Voigt fwhm by amounts between −5 % and +274% with biggest reduction in peak width for the *0k0* reflections and the biggest increase in peak width for the *00l* reflections. In general the peak widths are largest for peaks with a high degree of *l* character.

The spherical harmonic in the optimal peak shape model has a 2θ dependence the same as that of strain so its shape may be an indication of the excess strain within the crystallites. The largest strain is in the direction of the *c* axis, which is perhaps unsurprising for a layered material in which layers of edge linked copper and tungsten sulfide tetrahedra are stacked along this direction. It is, however, also possible that the broadening observed is due to stacking faults of two forms of the material (intergrowths of the *P* and *I* forms discussed in Chapter 4), which would again seem plausible for a material of this type.

3.4.3 Effect of broadening on the structure

It is often the structure of a material which is of most interest when analysing powder data, so the values of structural parameters are perhaps more important than those of the peak shape function used. The values obtained for these may be affected by the use of functions to model anisotropic peak broadening. In order to asses the effect on the structural parameters of Cu_2WS_4, two structural fits were done using two different peak shape models, one of which was isotropic and the other anisotropic.

The structure of Cu_2WS_4 was reported by Pruss and this model was used to fit the data. There are only 3 atoms in the asymmetric unit, two of which (copper and tungsten) are on special positions. The only parameters that were refined for the structures were the cell parameters, a scale factor, a temperature factor (constrained to be the same for all atoms), and the atomic coordinates for the sulfur atoms; this gives a total of 6 refined structural parameters. Peak shape parameters and those describing the background, axial divergence and zero error, were fixed at the values obtained from the corresponding

Pawley fits. Two fits were done, the first used the pseudo-Voigt peak shape function; the second used the best anisotropic model from the Pawley fits - the pseudo-Voigt function convoluted with a 4th order strain type spherical harmonic. A summary of the structural parameters obtained for these fits is given in Table 3.6.

	PV peak shape	SH peak shape
$_wR_p$ /%	5.52	4.10
R_{Bragg} /%	5.40	3.96
χ^2	3.94	2.92
a /Å	5.4143 (1)	5.4150 (1)
c /Å	5.2546 (2)	5.2549 (2)
x coordinate S	0.2316 (5)	0.2380 (4)
z coordinate S	0.2692 (7)	0.2542 (5)
U_{iso} /Å^2	−0.0138 (2)	−0.0184 (2)
W – S /Å	2.268 (4)	2.260 (3)
Cu – S /Å	2.384 (2)	2.336 (2)
S – W – S /°	102.8 (2)	107.5 (1)
	112.9 (1)	110.4 (1)
S – Cu – S /°	104.9 (2)	105.2 (1)
	107.2 (1)	110.3 (1)
	116.6 (2)	113.0 (1)

Table 3.6 Refinement details and selected structural parameters for two structural fits for Cu_2WS_4 which used an isotropic and an anisotropic peak shape model.

The structural data presented in this table shows that changing the way in which the peak shape is modelled can have an effect on the structural data obtained from a refinement. Although the cell parameters determined are almost exactly the same in both cases, a small movement of the sulfur site results in some changes in the observed bond lengths and angles for the tungsten and copper tetrahedra. Both the W – S and Cu – S bond lengths are shorter when a spherical harmonic peak shape model is used compared to the case when a pseudo-Voigt peak shape is used. Differences in bond angles of up to 4.7 ° are also seen on changing the peak shape model. It is worth noting that the spherical harmonic peak shape leads to more regular MS_4 tetrahedra.

It is clear from these data that changing the peak shape model to account for the peak shape anisotropy does slightly change the structural model obtained. However, since allowing for the peak shape anisotropy leads to a significant improvement between observed and calculated patterns and significantly reduced R_{Bragg}, it is likely to lead to improved structural models if used with care.

3.5 Summary

Spherical harmonics have been successfully used to model the effects both of preferred orientation and peak width anisotropy on materials of relevance to this thesis. As well as improving the quality of fit between observed and calculated data, the use of such functions can improve the structural parameters obtained from Rietveld fits.

Preferred orientation corrections have been used on data from an extended 2D inorganic solid, Cu_2WSe_4, collected in flat mode and results compared to those determined from data collected in a capillary. This showed that preferred orientation can be successfully modelled and that structural parameters obtained from a Rietveld fit which uses the correction are comparable with those obtained from capillary data. A preferred orientation correction has also been used on data from a molecular solid, $(PPh_4)_2Ni(WS_4)_2$. Although the structures obtained with and without the correction were very similar, it is believed that the correction did give a slight improvement in the structural model.

Anisotropic peak shape modelling has been used to model data from another layered inorganic solid, Cu_2WS_4. As well as demonstrating that spherical harmonic functions be used to give physically sensible peak widths, this was shown to have a significant effect on structural parameters determined by Rietveld refinement.

The modelling of anisotropic peak shapes and preferred orientation using spherical harmonics should be performed with some caution because it is possible that they may mask structural subtleties. For peak shape modelling particular care is required to avoid mistaking split peaks (for example due to the true metric symmetry being lower than that used in the refinement) for peaks that displayed anisotropic broadening. For preferred orientation, it is important to be sure that the structural model is reasonable before any orientation correction is applied, therefore it might not be appropriate to use a preferred orientation correction in the early stages of structure solution.

3.6 References

1. R. A. Young, The Rietveld Method, Oxford Science Publications, 1993.
2. P. Scherrer, *Gött. Nachr.*, 1918, **2**, 98-100.
3. R. W. Cheary and A. A. Coelho, *J. Appl. Cryst.*, 1998, **31**, 862-868.
4. J. I. Langford, *J. Appl. Cryst.*, 1978, **11**, 10-14.
5. D. E. Cox, B. H. Toby and M. M. Eddy, *Aust. J. Phys.*, 1988, **41**, 117-131.
6. R. A. Young and D. B. Wiles, *J. Appl. Cryst.*, 1982, **15**, 430-438.
7. M. Järvinen, *J. Appl. Cryst.*, 1993, **26**, 225-531.
8. A. A. Coelho, *TOPAS v3.0 General Profile and Structure Analysis Software for Powder diffraction data, Bruker AXS, Karlsruhe*, 2001.
9. A. Müller, E. Diemann, R. Jostes, et al., *Angew. Chem. Int. Ed. Engl.*, 1981, **20**, 934-955.
10. F. H. Allen and O. Kennard, *Chem. Des. Autom. News*, 1993, **8**, 31.
11. V. Honkimäki, *J. Appl. Cryst.*, 1996, **29**, 625 - 631.
12. P. J. Hickey, *M. Chem. Thesis*, University of Durham, 2004.
13. E. A. Pruss, B. S. Snyder and A. M. Stacy, *Angew. Chem. Int. Ed. Engl.*, 1993, **32**, 256-257.
14. G. S. Pawley, *J. Appl. Cryst.*, 1981, **14**, 357-361.

4 Cu_2MX_4 and related materials

The metal chalcogenide Cu_2WS_4 was first prepared by Pruss who used a low temperature synthesis method to form this extended 2D inorganic solid.[1] The method used by Pruss has been adapted and used to make other chalcogenide materials, including four other members of the Cu_2MX_4 family (M = W or Mo and X = S or Se or S/Se), a new polymorph of Cu_2WS_4 and a related tungsten selenide phase, PPh_4CuWSe_4. This chapter describes the syntheses, structural chemistry and some of the physical properties of these materials.

4.1 Synthetic Methodology

The synthetic methodology used was developed from the method used by Pruss, which followed the general scheme:

$$2Cu^+ + MX_4^{2-} \rightarrow Cu_2MX_4 \qquad [4.1]$$

Pruss reacted a mixture of $(NH_4)_2WS_4$ and $Cu(CH_3CN)_4BF_4$ in a 1:1 mixture of N, N - dimethylformamide (DMF) and butyronitrile at reflux (135 °C) for 24 hours. In this work we have investigated similar reactions in which reagents were dissolved in a mixture of DMF and butyronitrile and heated in a Teflon lined hydrothermal autoclave for times between 6 and 96 hours. This resulted in the production of solid materials.

The Cu^I salt used was the same as that employed by Pruss: copper (I) tetrakis tetraacetonitrile tetrafluoroborate, $Cu(CH_3CN)_4BF_4$. This salt was chosen because the CH_3CN ligands are relatively labile and easily displaced by MX_4^{2-}. The tungsten and molybdenum sources chosen were materials in which MX_4 tetrahedra already existed, these structural units were preserved during the reaction and are linked together by the Cu^+ ions to form extended structures. For the sulphide materials ammonium tetrathiotungstate/molybdate was the source of MX_4; for the selenide materials the corresponding tetraphenylphosphonium salts were used instead.

$Cu(CH_3CN)_4BF_4$ was synthesised by adding HBF_4 to a suspension of Cu_2O in acetonitrile, the mixture was then heated to 70 °C and the product crystallised from this solution by cooling to -20 °C. $(NH_4)_2MS_4$ materials were synthesised by passing $H_2S(g)$ though a solution of H_2WO_4 or Na_2MoO_4 in NH_4OH at 60 °C. For the tungsten material gas flow was maintained for 8 hours, for the molybdenum material only 2.5 hours of gas flow were required. The products precipitated from solution on cooling. Synthesis of the selenium containing ammonium salts by an analogous method would require the use of H_2Se, a highly toxic gas, so tetraphenylphosphonium salts were employed instead. $(PPh_4)_2MSe_4$ were synthesised by reaction of $M(CO)_6$ with K_2Se_3 in DMF. After heating at 90 °C for 1 hour, $(C_6H_5)_4PBr$ and THF were added in order to precipitate the

products. The selenium source, K_2Se_3, was made by a combination of stoichiometric amounts of the elements in $NH_3(l)$, as such, no toxic H_2Se was required. Full synthetic details are given in section 2.10.

The syntheses of Cu_2MX_4 materials involved the use of a sealed autoclave, in which there is significant autogenous pressure at elevated temperatures. Initial experiments were therefore carried out in order to estimate the pressure in the reaction vessel at different synthesis temperatures. This was done by heating a mixture of the solvents: butyronitrile, DMF and a very small amount of acetonitrile (volume ratio 1:1:0.01) in a stainless steel autoclave lined with a glass vessel of approximate capacity 120 ml and fitted with a pressure gauge. This was filled to a level of 40 %, in order to mimic as closely as possible the conditions in the hydrothermal autoclave used for synthesis (which contains 8 ml of solvent in a 20 ml container). The autoclave was then heated from room temperature to 220 °C and the pressure measured as a function of temperature. The variation in pressure is shown in Figure 4.1.

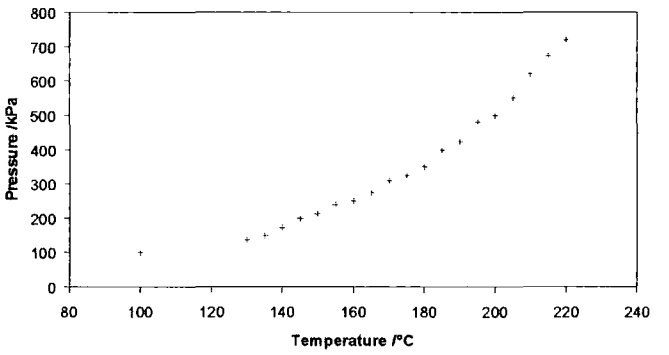

Figure 4.1 The variation of pressure with temperature in a solvothermal bomb containing a mixture of DMF, butyronitrile and acetonitrile.

This gave an approximate estimate of the pressure in the autoclave during synthesis of ~150 kPa at 135 °C, ~500 kPa at 200 °C and ~720 kPa at 220 °C.

In total five different members of the Cu_2MX_4 family and one related tungsten selenide material were synthesised. A summary of the materials made and the temperature and pressure ranges over which synthesis was attempted is given in Table 4.1.

Material	M source (s)	Temperature range /°C	Pressure range /kPa
Cu_2WS_4	$(NH_4)_2WS_4$	110 – 220	100 – 720
Cu_2WSe_4	$(PPh_4)_2WSe_4$	135 – 220	150 –720
$Cu_2WS_xSe_{4-x}$	$(NH_4)_2WS_4$ & $(PPh_4)_2WSe_4$	200 – 220	500 – 720
PPh_4CuWSe_4	$(PPh_4)_2WSe_4$	190	~425
Cu_2MoS_4	$(NH_4)_2MoS_4$	110 – 200	100 – 500
Cu_2MoSe_4	$(PPh_4)_2MoSe_4$	110 – 220	100 -720

Table 4.1 Summary of materials made using solvothermal methods and the temperatures at which synthesis was attempted.

Each of these materials was synthesised at several different temperatures and the temperature was found to be strongly influential in determining the outcome of the reaction. For the tungsten selenide system, reaction time was also found to be an important factor. The factors which influence the outcome of the reaction for the different systems are further discussed for individual compounds.

4.2 Cu_2WS_4

4.2.1 Synthetic Studies

Cu_2WS_4 was initially synthesised using the solvothermal method described in section 4.1, at a temperature of 135 °C. This produced an orange solid. In order to investigate the effect of temperature on this synthesis, it was attempted at several more temperatures in the range 135 to 250 °C. At all temperatures from 135 to 220 °C orange powders were produced, diffraction data for these are shown in Figure 4.2. The sample produced at 250 °C was a brown powder, shown to be amorphous by X-ray powder diffraction; its diffraction pattern is therefore not included.

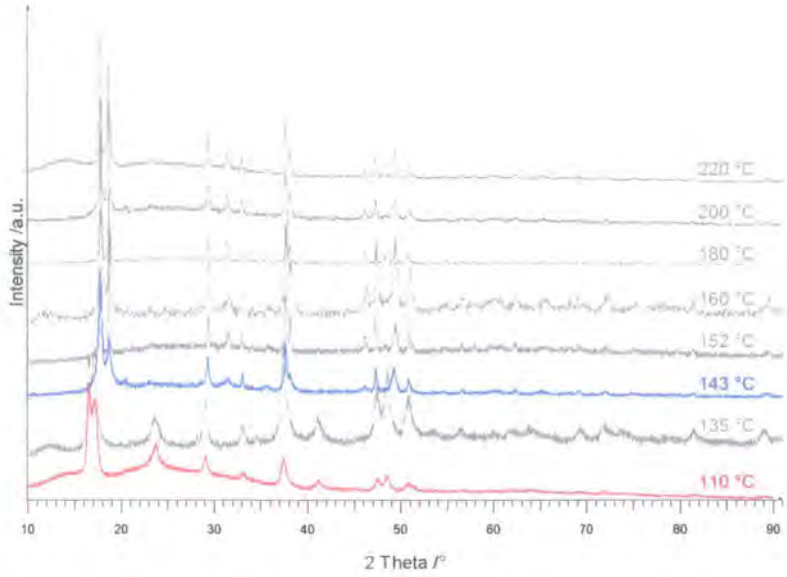

Figure 4.2 XRD patterns of Cu_2WS_4 produced at synthesis temperatures between 110 °C and 220 °C. The patterns are offset in the *y* direction for clarity.

It can be seen from Figure 4.2 that the diffraction pattern changes with increasing temperature such that by 143 °C, none of the reflections of the phase produced at 135 °C are present. These powder patterns were compared to that of the material previously characterised by Pruss. The positions of the peaks in the pattern of the material produced at low temperature suggested that it was the same material as that which Pruss reported, although it was less crystalline. The pattern could be fitted by Rietveld refinement of Pruss's structure. The diffraction patterns of materials produced above 135 °C although the same as each other, did not have peak positions that corresponded to Pruss's material, or to any other material contained in the PDF.[2] In order to try and determine the identity of this material, structure solution from the powder diffraction data was attempted using data from the sample synthesised at 200 °C.

4.2.2 Structure solution of the new material

The powder pattern of the material was collected on a Siemens D5000 diffractometer in the range 5 – 120 ° with a step size of 0.02 °, a time per step of 9.25 s and v20 variable divergence slits, the sample was prepared by sprinkling onto an amorphous glass slide coated with Vaseline as an adhesive. Peak positions were determined using the peak fitting facility in TOPAS[3] and the pattern was indexed using the *multiviss* routine, a modified FORTRAN routine for controlling ITO,[4,5] as described in section 2.3.

The best solution determined using this procedure gave a unit cell with the following unit cell parameters:

$a = b = 5.4456$ Å $c = 10.0643$ Å $\alpha = \beta = \gamma = 90$ ° FOM = 147

This cell was used to fit the data using a Pawley fit[6] in the lowest symmetry tetragonal space group, P4. This gave an excellent fit to the data ($_wR_p$ = 7.4 %) and accounted for all the peaks in the pattern. Comparison of the cell volume (298 Å^3) to that of the Pruss material (V = 154 Å^3) shows the cell volume is approximately doubled and suggests cell contents of $Cu_4W_2S_8$. In order to determine the space group of the new material, the powder pattern was examined to determine its systematic absences. This was done by fitting the data using a Pawley fit in space group P4 and examining the pattern and calculated intensities to see which peaks were predicted but were actually absent. The reflections present were: (*00l*) l = 2n; (*0k0*) k = 2n; (*0kl*) $k + l$ = 2n; (*hh*0) h = n; (*hk0*) $h + k$ = 2n; (*hhl*) l = 2n; (*hkl*) $h + k + l$ = 2n. These observations are consistent with body centring and allow a number of possible choices of space group: I4/mmm and several related lower symmetry space groups. In order to determine the correct choice of space group, structure solution was attempted in two space groups using the EXPO program,[7,8] a direct methods solution program, modified for powder data. All attempts to solve the structure in space group I4/mmm failed; however, when solution was attempted in space group $I\bar{4}2m$ a physically sensible solution was obtained and positions for all 3 unique atoms in the asymmetric unit in the unit cell were located. Structural refinement was therefore attempted in this space group.

Refinement of the structure of the new material was attempted using high quality data collected on a Bruker d8 Advance diffractometer, with the sample sprinkled onto an amorphous SiO_2 disk. 3 identical sets of data were collected and data from all the scans were summed. The trial structure was refined using the Rietveld method[9] within the TOPAS program. Close examination of the pattern indicated a minor $(NH_4)_2SO_4$ impurity and which was introduced as a second phase.[10] In final cycles of refinement a total of 45 parameters were refined including: 2 scale factors, 18 coefficients of a Chebychev polynomial to describe the smoothly varying background, sample displacement, 6 pseudo-Voigt peak profile parameters, cell parameters, atomic coordinates and isotropic temperature factors. The Rietveld fit is shown in Figure 4.3 and refinement and data collection data are summarised in Table 4.2. An input file for this refinement is included in the e-appendix.

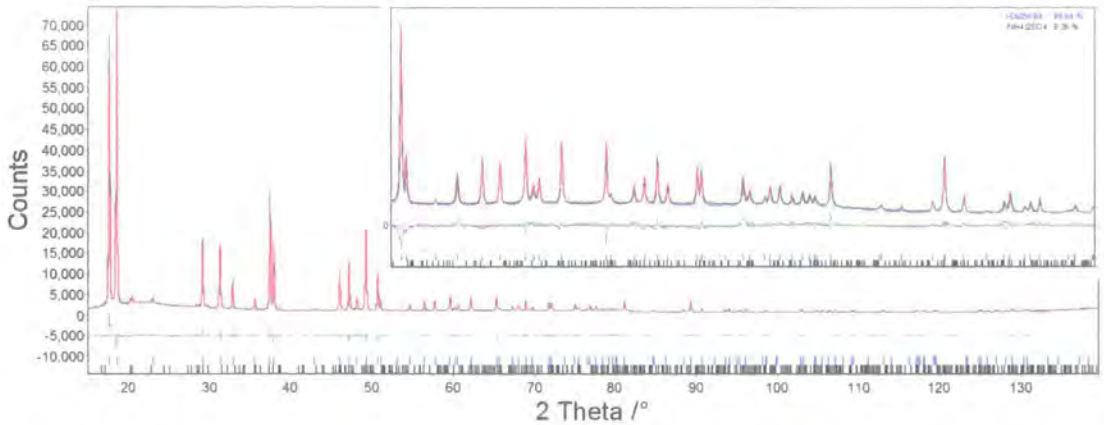

Figure 4.3 Rietveld fit of the new phase of Cu_2WS_4, observed data are shown in blue, calculated in red and the difference in grey. *hkl* tick marks are shown in black for $(NH_4)_2SO_4$ and blue for Cu_2WS_4. The inset shows the region between 50 and 100 ° 2θ.

Space Group	$I\bar{4}2m$	2θ range	15 – 140 °
$a = b$	5.4443 (1) Å	2θ step	0.0144 °
c	10.0687 (2) Å	Time per step	22.5 s
$\alpha = \beta = \gamma$	90 °	$_wR_p$	6.87 %
No. of refined parameters	45	R_{Bragg}	5.02 %
		χ^2	2.82

Table 4.2 Selected crystallographic, data collection and refinement details for Cu_2WS_4.

This material is a new polymorph of Cu_2WS_4. It has a unit cell that is body centred rather than being primitive, and consequently hereafter it will denoted the "*I*" form of the material, while the form discovered by Pruss will be denoted the "*P*" form.

The new *I* form of the material contains layers of alternating, edge-sharing WS_4 and CuS_4 tetrahedra separated by a van der Waals gap. Adjacent layers are offset from each other by half a unit cell in the *a* and *b* directions, giving the material its body centring. The atomic arrangement in a single layer of the material is shown in Figure 4.4 and a view of the layer packing is given in Figure 4.5.

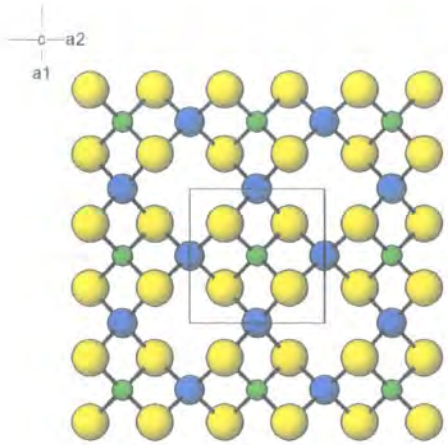

Figure 4.4 The atomic arrangement within a single layer of *I* Cu_2WS_4. W atoms are shown in green, Cu atoms in blue and S in yellow.

This structure of this material is closely related to those of some of the materials discussed in section 1.2. It is based on a cubic close packed array of sulfur atoms, with metal atoms occupying tetrahedral sites within this lattice. Only sites in alternate layers are occupied; within these layers 3/4 of the available sites are filled, giving 3/8 occupancy overall. The structure and a schematic representation of the metal ordering are shown in Figure 4.5. Fractional atomic coordinates are given in Table 4.3.

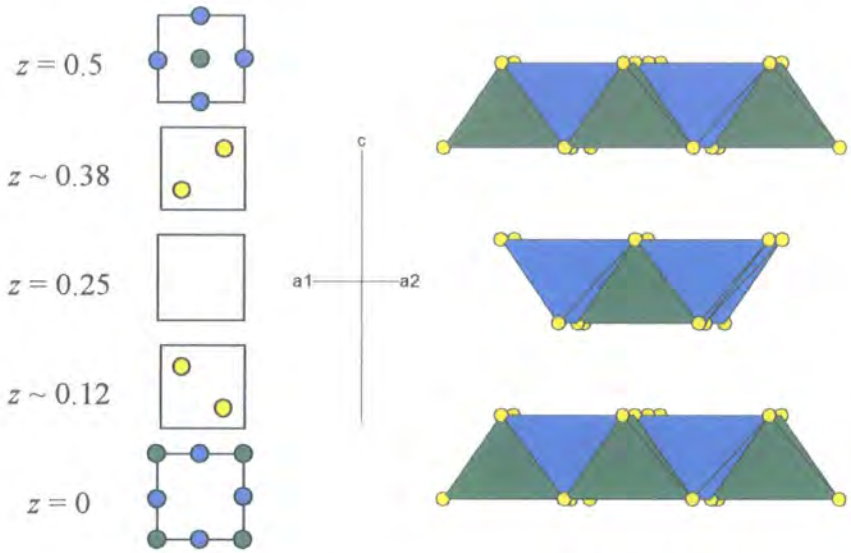

Figure 4.5 Schematic representation of the metal ordering (left) and polyhedral view (right) of *I* Cu_2WS_4. W atoms and tetrahedra are shown in green, Cu atoms and polyhedra in blue and S in yellow.

Atom	*x/a*	*y/b*	*z/c*	U_{iso} /Å^2
W	0.0000	0.0000	0.0000	0.0397 (3)
Cu	0.5000	0.0000	0.0000	0.0477 (6)
S	0.2381 (3)	0.2381 (3)	0.1189 (6)	0.0418 (6)

Table 4.3 Fractional atomic coordinates and isotropic temperature factors for the new polymorph of Cu_2WS_4.

The structure of this new polymorph is closely related to that of the *P* phase material. The intralayer structure in both *P* and *I* forms is similar, however in the new polymorph alternate planes of metal atoms are offset by half a unit cell in the *a* and *b* directions. This means that tungsten atoms in one layer lie above metal vacancies in adjacent layers, minimising electrostatic interactions between them. This gives a unit cell with body centring and a *c* axis double the length of the primitive form. The same proportion of tetrahedral metal sites within the cubic close packed lattice are occupied; within the occupied layers the metal ordering is the same in both forms. This structural relationship is the same as that seen in some other pairs of materials described in section 1.2.

Bond Lengths /Å		Bond Angles /°	
W–S	2.189 (2)	S–W–S	107.4 (1)
Cu–S	2.268 (1)	S–W–S	113.8 (1)
		S–Cu–S	116.3 (1)
		S–Cu–S	102.1 (1)
		S–Cu–S	110.2 (1)

Table 4.4 Bond lengths and bond angles in the new phase of Cu_2WS_4.

Bond lengths and angles for *I* Cu_2WS_4 are given in Table 4.4. There are small but significant differences between the values determined here and those reported for *P* Cu_2WS_4. Pruss reported W – S bond lengths of 2.354 Å, whilst bond lengths in the new polymorph (2.189 Å), are significantly shorter and nearer to the 2.177 Å bond length observed in isolated WS_4^{2-} tetrahedron.[11] The Cu – S bond length (2.268 Å) is also slightly shorter than that observed by Pruss (2.356 Å). A more recent determination of the structure of *P* Cu_2WS_4 by Hickey[12] has, however, suggested W – S and Cu – S bond lengths of 2.260 Å and 2.336 Å respectively. These are slightly nearer those in the *I* polymorph than those previously reported by Pruss. The WS_4 tetrahedra show slight deviation from tetrahedral geometry, the range of S – W – S bond angles is 107.4 ° to 113.8 °. There is more distortion in the CuS_4 tetrahedra, with S – Cu – S angles ranging from 102.1 ° to 116.3 °. Both the W – S and the Cu – S bond lengths are within the

range found for S atoms bridging a tungsten and two copper atoms in polynuclear clusters found in the Cambridge Structural Database.[13]

Precise cell parameters for the new material were determined in the presence of an internal silicon standard. A sample of the material was mixed with silicon in a ratio such that the intensities of the most intense peaks in the diffraction patterns of each phase were approximately equal. Data were collected on a sample sprinkled onto an amorphous SiO_2 disk using a Bruker d8 Advance diffractometer. The data were collected over a 2θ range of 10 to 140 ° using a step size of 0.0144 ° and a time per step of 6 s. The data were fitted using a two phase refinement in which the cell parameters of the Silicon were fixed at the NIST standard[14] value of 5.4312 Å. A 2θ calibration curve was applied to correct for minor systematic errors due to diffractometer misalignment, sample height/absorption and PSD calibration. This procedure gave cell parameters of a = 5.4443 (1) Å and c = 10.0687 (2) Å. The fitted pattern is shown in Figure 4.6.

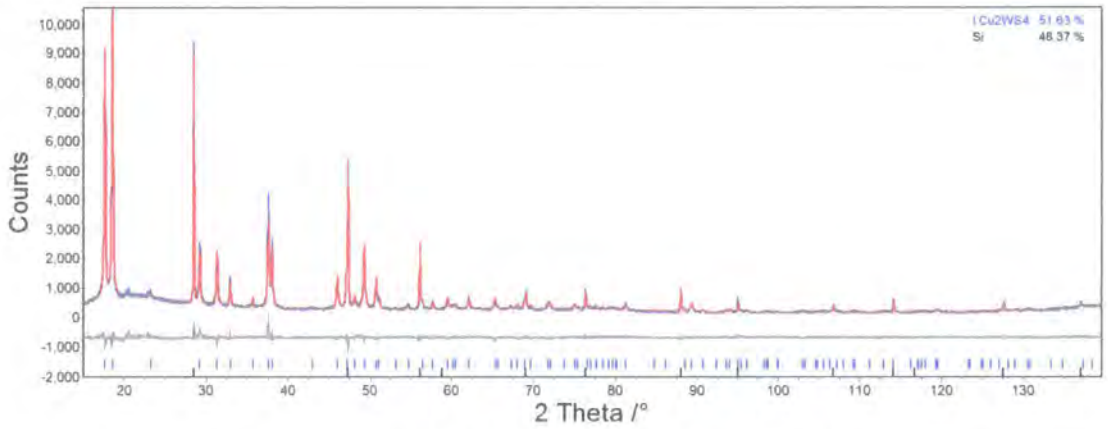

Figure 4.6 Rietveld fitted pattern of Cu_2WS_4 with an internal Si standard. Observed data are shown in blue, the calculated pattern in red and the difference in grey. Tick marks for Cu_2WS_4 are blue, and for Si they are black.

4.2.3 Investigation of the relationship between the two forms of Cu_2WS_4

It is clear from the work described above that the structure of copper thiotungstate varies with synthesis temperature; in order to try and gain insight into the reasons for this, several further experiments were performed. The most obvious difference between a reflux and synthesis at 200 °C in a solvothermal bomb is the autogenous pressure generated inside the solvothermal bomb. In light of this, conversion from one form to the other was attempted using different temperature and pressure conditions. The first was heating the P form at 200 °C in a 1:1 mixture of DMF and butyronitrile for 24 hours. This resulted in full conversion from the P to the I form. A sample of the P phase material was pressed in a pellet press (pressure ~1.9×10^5 kPa) overnight to try and achieve the transformation by pressure alone. A second sample, pressed into a pellet

(pressure ~1.9×10^5 kPa), was heated in a vacuum at 200 °C overnight in order to try and achieve the transformation by temperature alone. Neither of these experiments resulted in any structural change in the material. A fourth experiment involved heating a pellet of the material under a pressure of ~700 kPa of N_2 at 200 °C for 12 hours to see if conversion could occur in the solid state. This treatment did produce a small amount of *I* phase material, but a large proportion of *P* Cu_2WS_4 still remained. This leads to the conclusion that while conversion can be achieved by applying pressure and heating in the solid state, it is much more facile in a solvent.

The reason for the formation of the *I* form at higher temperature and pressure may be explained by considering the volume per formula unit in the two materials. The volume is smaller for the *I* form (149 Å^3) than for the *P* form (154 Å^3). Presumably the reduction in the interlayer distance (Δa *P* → *I* = +0.4%, Δc *P* → *I* = −3.8%) is sufficient that the body centred cation arrangement, with larger W–W separations (W has a formal oxidation state of +6), becomes more stable. Interlayer W–W, W–Cu and Cu–Cu distances in the *I* and *P* polymorph are 6.337/5.234, 5.723/5.895 and 5.034/5.234 Å respectively.

4.2.4 Variable temperature diffraction studies

In order to further probe the structure of Cu_2WS_4, variable temperature diffraction experiments were undertaken. The primary aim of this investigation was to look for Cu^+ ion mobility at elevated temperature and to see if there were any phase transitions in the material as the temperature was varied.

Low temperature data were collected using a Bruker d8 Advance diffractometer fitted with an Oxford cryosystems PheniX ccr. Data were collected on a sample of *I* phase material, synthesised at 200 °C and sprinkled onto an aluminium sample holder coated with a thin layer of Vaseline. The sample was cooled at a rate of 17 K/hour, and data collected while the sample was being cooled over a 2θ range of 10 to 120 ° with a step size of 0.0144 ° and a time per step of 0.2 s, giving a time per scan of approximately 30 minutes. A total of 39 scans were therefore recorded during cooling, with each scan separated in average temperature by ~8 K. The average temperature for each scan can be obtained by examining the PheniX log file using the *phenixlogfile* routine[15] and cell parameters were obtained using *multitopas* methodology as described in section 2.6. The refinement used a structural fit for the Cu_2WS_4 and a Pawley fit for peaks due to the Al sample holder. Two sample heights were refined to describe the slightly different heights of the aluminium sample holder and the sample.

Data at elevated temperatures were obtained using a Bruker d8 Advance diffractometer fitted with an Anton Parr HTK1200 furnace. The sample was sprinkled onto an

amorphous SiO_2 disk coated with a thin layer of Vaseline. The sample was heated in 20 K steps from 303 K to 623 K and at each temperature a diffraction pattern was measured (data collection at 483 K was accidentally omitted). Data were collected over a 2θ range of 5 to 120 ° with a step size of 0.0144 ° and a time per step of 1.05 s, giving scan times of ~1 hour.

The cell parameters obtained over the whole temperature range are shown in Figure 4.7.

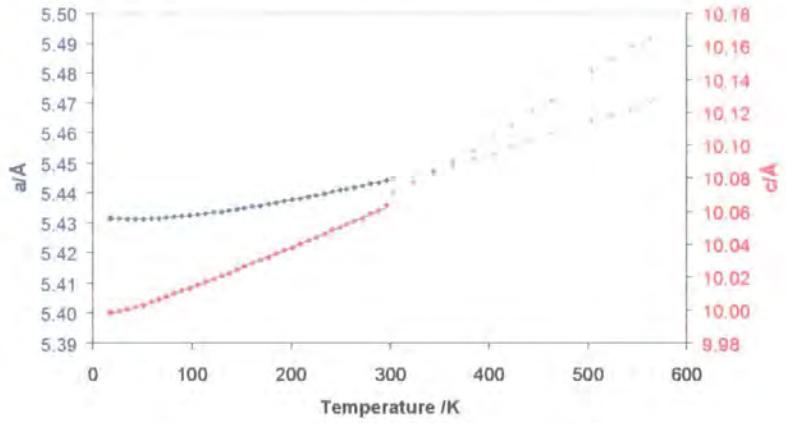

Figure 4.7 The variation of cell parameters in Cu_2WS_4 with varying temperature measured using the PheniX (closed symbols) and HTK1200 (open symbols). The *a* cell parameter is shown in blue and the *c* cell parameter in red, the grey line shows values of the a cell parameter calculated from the Reeber equation (equation 4.2).

Over the temperature range studied, increasing temperature causes an expansion of the unit cell up until 583 K when the sample decays and becomes amorphous in nature. As Figure 4.7 shows, the *a* cell parameter varies smoothly with temperature over the whole temperature range from 16 to 563 K. For the *c* cell parameter, at ~300 K there is a significant step in the data; this is due to a systematic experimental error and is not believed to indicate any real deviation from smooth expansion. The Si standardised *c* parameter (10.069 Å) falls in between the two values obtained for *c* at 303 K (10.071 Å) and 296 K (10.064 Å). Only the use of an internal standard during the variable temperature diffraction experiment would allow unambiguous determination of cell parameters and calibration of temperatures across the whole range. The *a* cell parameters obtained for the material at 303 K and 296 K are very close to the value determined in the presence of an internal Si standard (5.4448 Å and 5.4444 Å respectively, compared with a standardised value of 5.4443 Å).

The smooth expansion in the cell parameters suggests that there are no phase transitions in this material over the temperature range studied. This kind of expansion can be modelled using equation, 4.2, the Reeber equation.[16] a_0 is the ideal cell parameter at

0 K, c_i terms are constants, the values of which is dependant on the particular system being studied, θ_i is the i^{th} Einstein temperature and T is the temperature in Kelvin.

$$\ln a_{calc} = \ln a_0 + \sum_0^i \frac{c_i \theta_i}{\exp(\theta_i / T) - 1} \qquad [4.2]$$

This equation includes a simple model of the physical processes leading to thermal expansion and is found to model experimental data from a variety of systems reasonably well. Comparison of experimental data to a fitted curve can give a good idea of whether there are phase transitions in the sample or unexpected thermal expansion behaviour. For some samples expansion can be modelled using only one term in the expansion of the equation, this is the case for all materials for which the thermal expansion is described in this thesis. However, it is sometimes necessary to include additional terms to fully describe thermal expansion; this is the case for the aluminium sample holder used in the PheniX experiments for which two terms must be used.

The thermal expansion behaviour of aluminium has already been comprehensively studied by Wang and Reeber.[17] Values of θ_1, θ_2, c_1 and c_2 can be determined from their data for an ideal aluminium crystal (231 (31) K, 1459 (200) K, 21×10^{-6} (2) K^{-1} and 13×10^{-6} (1) K^{-1} respectively). These values were used to fit the aluminium expansion and only the value of a_0 was changed in order to give a good fit to the data. Good agreements between observed and calculated cell parameters for the Al sample holder are observed, giving us confidence that the measured and true sample holder temperatures are in good agreement. The aluminium cell parameter is included as a check to ensure that the observed changes in cell parameter for the sample are not artefacts of the refinement procedure; the fitted data are shown in Figure 4.8. A value of 4.03157 (5) Å was obtained for a_0 for these data.

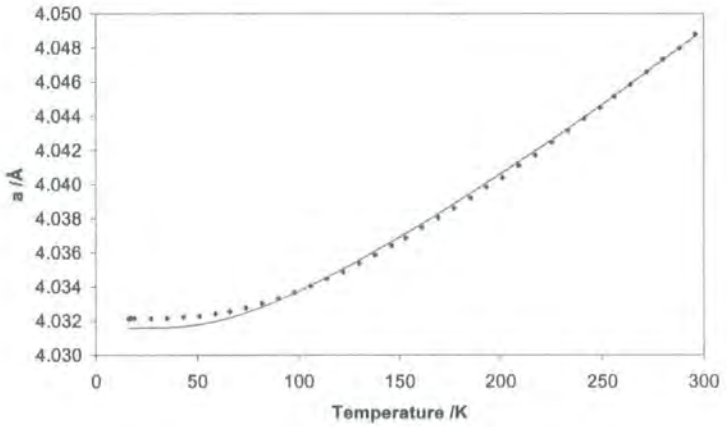

Figure 4.8 The variation in the cell parameter of the aluminium cell parameter during the PheniX experiment. Observed data are shown in black values calculated from the Reeber equation in grey.

The values of a_0, c_1 and θ_1 for Cu_2WS_4 were obtained by using a least squares refinement procedure within the TOPAS program to fit this equation to the experientially determined cell parameters over the temperature region 15 to 300 K, *i.e.* data obtained using the PheniX. The value of α, a measure of the amount of expansion in the cell parameter over the whole temperature range, is calculated from equation 4.3.

$$\alpha_1 = \frac{(a_{T2} - a_{T1})/a_{T1}}{T_2 - T_2} \qquad [4.3]$$

The values of these parameters are summarised in Table 4.5.

	a	*c*
a_0 /Å	5.43147 (3)	9.9987 (2)
θ_1 /K	318 (5)	96 (4)
c_1 /K^{-1}	14.3 (2) × 10^{-6}	25.3 (2) × 10^{-6}
$\alpha_{15K\text{-}300K}$ /K^{-1}	8.5 (1) × 10^{-6}	22.6 (2) × 10^{-6}

Table 4.5 Thermal expansion parameters for Cu_2WS_4.

The values of α show that the expansion in the direction of the *c* axis is relatively larger than that in the direction of the *a* axis. The bonding in the plane of the layers is rigid, whereas layers are separated by a Van der Waals gap, the bonding between the layers is weak and expansion can occur more easily in this direction.

4.2.5 Physical Properties

The magnetic and electrical properties of Cu_2WS_4 were investigated. Magnetic properties were measured using a powdered sample of the material contained in a gelatin capsule, using a SQUID magnetometer (as described in section 2.8). The variation of the magnetisation of the sample with the applied field confirmed the material was diamagnetic, as expected for a material containing Cu^I (d^{10}) and W^{VI} (d^0).

Attempts were made to measure the temperature dependence of the conductivity of Cu_2WS_4 using a two probe measurement technique. Aluminium, indium and gold were all tried as possible contact materials, but simple room temperature I-V experiments showed that the contacts were not ohmic in nature. An essential requirement for meaningful conductivity data is that the contacts are ohmic and therefore reliable measurements could not be made. However, an approximate indication of the magnitude of the resistance can be obtained from the I-V measurements; this suggested a value of ~10^6 Ω at room temperature.

4.3 Cu_2WSe_4

4.3.1 Synthetic Studies

Cu_2WSe_4 was synthesised from $Cu(CH_3CN)_4BF_4$ and $(PPh_4)_2WSe_4$ at a total of nine temperatures between 135 °C and 220 °C; a purple-brown coloured powder was formed at each temperature. The XRD patterns of the materials synthesised at different temperatures are shown in Figure 4.9.

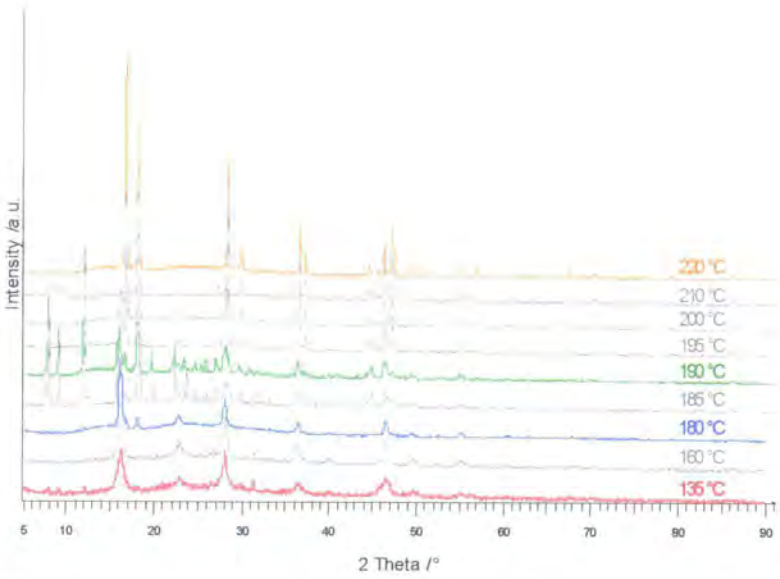

Figure 4.9 The XRD patterns of Cu_2WSe_4 synthesised at temperatures between 135 °C and 220 °C. Patterns are offset in the *y* direction for clarity.

The powder patterns of the materials formed change with synthesis temperature. At low temperature a material with broad diffraction peaks is formed. As the temperature is increased to 180 °C additional peaks are seen in the diffraction pattern, these peaks are much sharper. Increasing temperature causes the proportion of the material with sharper peaks to gradually increase and the proportion of the material with the broad peaks to gradually decrease until at 220 °C there is none present at all. At 185 and 190 °C another set of peaks are observed in the powder pattern.

These observations can be explained by comparison of the powder patterns to those of the two polymorphs of Cu_2WS_4 already discussed. The material with broad diffraction peaks formed at low temperature has a powder pattern very similar to that of *P* Cu_2WS_4, with slightly different cell parameters. This is confirmed by the fact that the powder pattern can be fitted by Rietveld refinement using the structural model of the sulfur containing material. The material which forms at the highest synthesis temperatures has a powder pattern which is similar to that of *I* Cu_2WS_4; this pattern can also be fitted by Rietveld refinement of the structure of the corresponding sulfur containing material. For

Cu_2WSe_4 intermediate synthesis temperatures give mixtures of two different phases, this behaviour contrasts with that of the sulfide material, for which only phase pure materials are observed. The surprising observation that an additional material is formed exclusively at 185 and 190 °C was repeated in several different experiments. The material cannot be identified by comparison of its PXRD pattern to those of materials in the PDF and it turned out to be a previously unknown phase, PPh_4CuWSe_4; its characterisation is discussed in section 4.7.

4.3.2 Structure

The structures of the low and high temperature forms of Cu_2WSe_4 are essentially isostructural with the two forms of Cu_2WS_4. However there are small structural differences and the structures of both materials were studied in detail to allow comparison to the sulfide materials already described.

Data for the low temperature *P* phase of the material were collected using a Siemens D5000 diffractometer on a sample of Cu_2WSe_4 synthesised at 160 °C, sprinkled onto a Vaseline coated amorphous glass slide. The structure was refined using the structure of *P* Cu_2WS_4 as a starting point. In final cycles of refinement a total of 22 parameters were refined, including 9 coefficients of Chebychev polynomial to describe the background, sample displacement, 6 peak shape parameters, 1 scale factor, cell parameters, atomic coordinates and an overall temperature factor, constrained to be the same for all atoms.

Refinement data are summarised in Table 4.6, the Rietveld fit is shown in Figure 4.10 and bond distances and angles are given in Table 4.7. Structural parameters have not been determined to a high degree of accuracy because of the relatively poor crystallinity of the sample.

Space Group	$P\bar{4}2m$	2θ range	5 – 90 °
$a = b$	5.531 (2) Å	2θ step	0.02 °
c	5.552 (5) Å	Time per step	10 s
$\alpha = \beta = \gamma$	90 °	$_wR_p$	9.145 %
No. of refined parameters	22	R_{Bragg}	2.972 %
Se x coordinate	0.246 (8)	χ^2	1.238
Se z coordinate	0.242 (8)	U_{iso} /Å^2	0.044 (3)

Table 4.6 Selected crystallographic, data collection and refinement details for *P* Cu_2WSe_4.

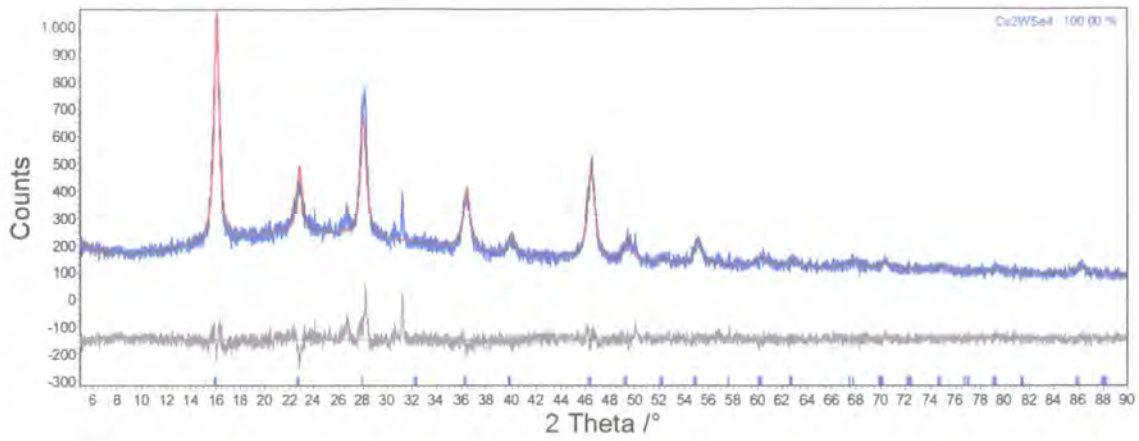

Figure 4.10 Rietveld fit for *P* Cu_2WSe_4, observed data are shown in blue, calculated in red and difference in grey.

Bond Lengths /Å		Bond Angles /°	
W – Se	2.35 (6)	Se – W – Se	109 (1)
Cu – Se	2.37 (3)	Se – W – Se	110 (2)
		Se – Cu – Se	108 (3)
		Se – Cu – Se	109 (3)
		Se – Cu – Se	110 (2)

Table 4.7 Bond lengths and angles in *P* Cu_2WSe_4.

Structural information for the high temperature phase was determined from the sample made at 220 °C using data collected on a Bruker d8 Advance diffractometer, operating in transmission mode with the sample loaded into a 0.3 mm capillary. Five individual sets of data were collected and data from all scans were summed, giving a total measurement time of ~52 hours. Cell parameters and atomic coordinates from the structure of *I* Cu_2WS_4 were used as initial values for the structure refinement.

Data were refined using 15 coefficients of a Chebychev polynomial to describe the smoothly varying background; the high order of this polynomial reflects the large increase in background at low angle due to scattering of X-rays by air and the capillary. A simple axial model term was used to describe the peak asymmetry; a zero point error was also refined. Refinement of a scale factor, 6 peak shape parameters, cell parameters, atomic coordinates and temperature factors gave a total of 31 parameters. The Rietveld fit is shown in Figure 4.11, refinement details and structural information are shown in Table 4.8; bond lengths and angles are in Table 4.9. Input files used for refinement of models for both phases of Cu_2WSe_4 are included in the e-appendix.

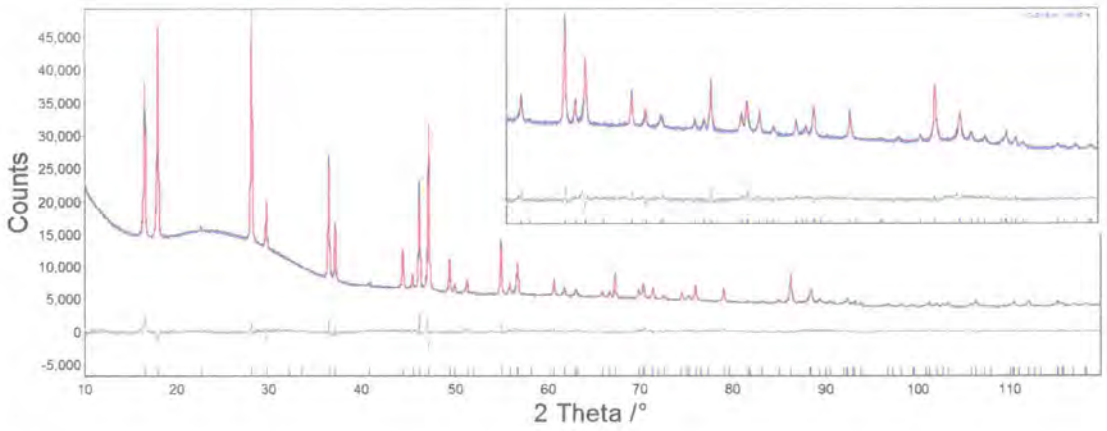

Figure 4.11 Rietveld fit for *I* Cu_2WSe_4. Observed data are shown in blue, calculated in red and difference in grey. The inset shows the region between 50 and 100 ° 2θ.

Space Group	$I\bar{4}2m$	2θ range	10 – 120 °
$a = b$	5.5577 (1) Å	2θ step	0.0114 °
c	10.6940 (4) Å	Time per step	25 s
$\alpha = \beta = \gamma$	90 °	$_wR_p$	2.922 %
Se x coordinate	0.2430 (2)	R_{Bragg}	2.505 %
Se z coordinate	0.1189 (6)	χ^2	2.554
U_{iso} W /Å^2	0.0143 (7)	No. of refined parameters	31
U_{iso} Cu /Å^2	0.010 (1)		
U_{iso} Se /Å^2	0.0166 (6)		

Table 4.8 Selected crystallographic, data collection and refinement details for *I* Cu_2WSe_4.

Bond Lengths /Å		Bond Angles /°	
W – Se	2.364 (2)	Se – W – Se	107.79 (8)
Cu – Se	2.409 (1)	Se – W – Se	110.32 (4)
		Se – Cu – Se	107.29 (9)
		Se – Cu – Se	109.35 (6)
		Se – Cu – Se	111.80 (9)

Table 4.9 Bond lengths and angles in *I* Cu_2WSe_4.

Accurate cell parameters for this phase were again determined in the presence of a silicon standard. Silicon was mixed with a sample of the material in a ratio that gave roughly equal intensities for the most intense peak in the diffraction pattern of each phase. This mixture was sprinkled onto an amorphous glass slide and data were collected with a Siemens D5000 diffractometer using 1 ° divergence slits, over a 2θ range of 10 to 120 ° with a step size of 0.02 ° and a time per step of 10 s. The data were fitted using a two phase refinement and internal calibration function with the cell

parameter of silicon fixed at 5.4312 Å. This gave cell parameters of a = 5.5577 (1) Å and c = 10.6940 (4) Å. The fitted pattern is shown in Figure 4.12.

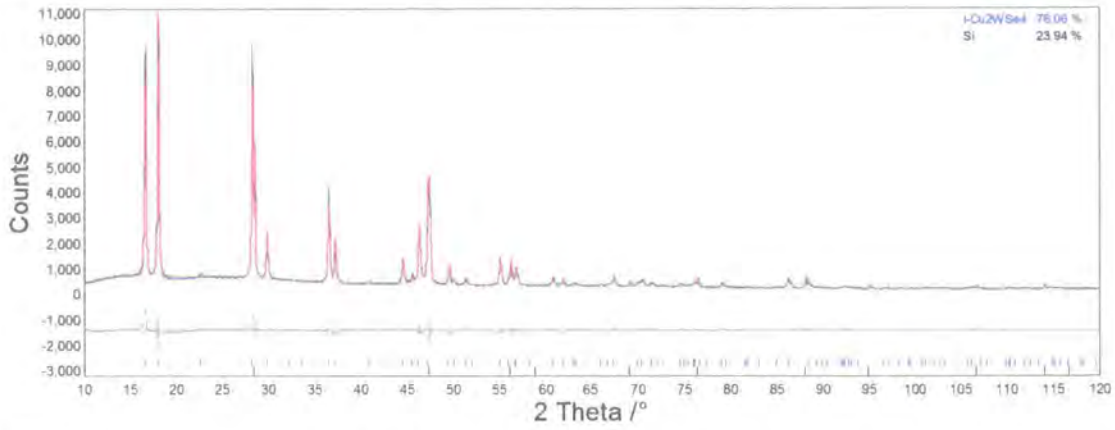

Figure 4.12 Rietveld fit of *I* Cu_2WSe_4 with an internal silicon standard. Observed data are shown in blue, the calculated pattern in red and the difference in grey. *hkl* tick marks are shown in blue for Cu_2WSe_4 and black for Si.

Comparison of the structures of *P* and *I* Cu_2WSe_4 with those of the two phases of Cu_2WS_4 shows that the selenide phases are both very similar to their sulfide analogues. Selected relevant structural data for the materials is summarised in Table 4.10 and Table 4.11.

	P Cu_2WS_4 [1]	*I* Cu_2WS_4	*P* Cu_2WSe_4	*I* Cu_2WSe_4
a /Å	5.4244	5.4443	5.531	5.5577
c /Å	5.2336	10.0687	5.552	10.6950
W – X /Å	2.345 (2.260)	2.189	2.35	2.364
Cu – X /Å	2.356 (2.336)	2.268	2.37	2.409
X – W – X /°	108.6 (107.5)	107.4	108	107.8
X – W – X /°	109.9 (110.4)	113.8	110	110.3
X – Cu – X_{min} /°	108.9 (105.2)	102.1	108	107.29
X – Cu – X_{max} /°	110.3 (113.0)	116.3	110	111.80

Table 4.10 Summary of some structural parameters for Cu_2WX_4 materials, values for bond lengths and angles determined by Hickey[12] for the *P* form of Cu_2WS_4 are given in brackets.

	Cu_2WS_4	Cu_2WSe_4
Δa ($P \rightarrow$ I) /%	+0.4	+0.5
Δc ($P \rightarrow$ I) /%	−3.8	−3.7
ΔV ($P \rightarrow$ I) /%	−3.1	−2.8

Table 4.11 Comparative values for cell parameters in Cu_2MX_4 materials. The c parameter and cell volume for the *P* form are compared to half of the c parameter and cell volume for the *I* form to compensate for the effect of the body centring in the *I* form.

Comparison of the cell parameters and unit cell volumes for the different polymorphs of the materials shows that the contraction of the unit cell on changing from the *P* to the *I* form is similar for both the sulfides and selenides. If the cell parameters of the sulfides to the selenides are compared to each other (both the *P* and the *I* forms) they reveal that the selenides have slightly larger unit cells than the sulfides, as would be expected given the larger ionic radius[18] of Se^{2-} compared with S^{2-}. However, the expansion in cell parameters is not uniform in all directions. Comparison of the *a* cell parameters in both the *I* and *P* forms of the material reveals an increase of ~2 % on changing from sulfur to selenium ($\Delta a(P)$ S→ Se = 2.0 %, $\Delta a(I)$ S→ Se = 2.1 %). A similar comparison of the *c* cell parameter shows a larger increase of ~ 6 % ($\Delta c(P)$ S→ Se = 6.1 %, $\Delta c(I)$ S→ Se = 6.2 %). In the *c* direction, comparison of the inter and intra layer sulfur - sulfur and selenium - selenium distances shows that the change in the *c* cell parameter is the effect of a combination of an increase in the size of the layer in the direction of the *c* axis (intralayer X – X distances), and a change in interlayer spacing (interlayer X – X distances). The relevant distances are summarised in Table 4.12.

		S	Se	Δ S → Se /%
P	Intra layer X–X distance	2.739 (2.671)	2.687	−1.9 (+0.6)
	Inter layer X–X distance	2.494 (2.583)	2.865	+14.9 (+10.9)
I	Intra layer X–X distance	2.394	2.543	+9.8
	Inter layer X–X distance	2.640	2.804	−1.5
Δ *P*→ *I* /%	Intra layer X–X distance	−12.6 (−10.3)	−5.4	
	Inter layer X–X distance	+5.9 (+2.2)	−2.1	

Table 4.12 Intra and inter layer sulfur – sulfur and selenium – selenium distances in Cu_2WX_4 materials. Values given in brackets are from the Hickey model.[12]

The data in this table suggest that for the *P* phase materials the origin of the expansion along the *c* direction is an increase in the interlayer separation. However, in the case of the *I* phase materials the expansion is primarily due to an increase in the size of the layers with a slight decrease in the interlayer separation.

It is interesting to note that in the sulfide material, on changing from the *P* to the *I* form a large decrease in the intralayer X – X distance is observed while there is a slight increase in the inter layer separation. This contrasts with the behaviour of the selenide material for which the change from the *P* to the *I* phase material results in a decrease in both the intra and inter layer X – X separations.

Although the bond lengths change as a result of changing from sulfur to selenium, there is little change in the range of bond angles seen around the metal tetrahedra. In the *P* forms of both materials bond angles do not deviate significantly from 109.5 °, the

tetrahedral angle. In the *I* forms however, the tetrahedra are somewhat more distorted, and bond angles deviate more significantly from 109.5 °, with the deviation being greatest in the case of the sulfide.

4.3.3 Variation of phase composition with temperature and reaction time

When Cu_2WSe_4 is synthesised at different temperatures, the relative amounts of *P* Cu_2WSe_4, *I* Cu_2WSe_4 and the impurity phase, PPh_4CuWSe_4 (see section 4.7) varies, as previously noted in section 4.3.1. It is possible to determine the phase fraction of each of the *I* and *P* phases for different samples in order to gain insight into the effect of synthesis temperature on the identity of the material produced. Phase fractions were determined by Rietveld refinement. If major crystalline impurity phases were present they were included in the refinements; this improves the quality of the refinement and the values obtained from it. Amorphous impurity phases were not taken into account; therefore the numbers given represent relative amounts of the two phases, given on a percentage scale, rather than absolute values. The relative amounts of *I* and *P* phase material formed at different temperatures are shown in Figure 4.13.

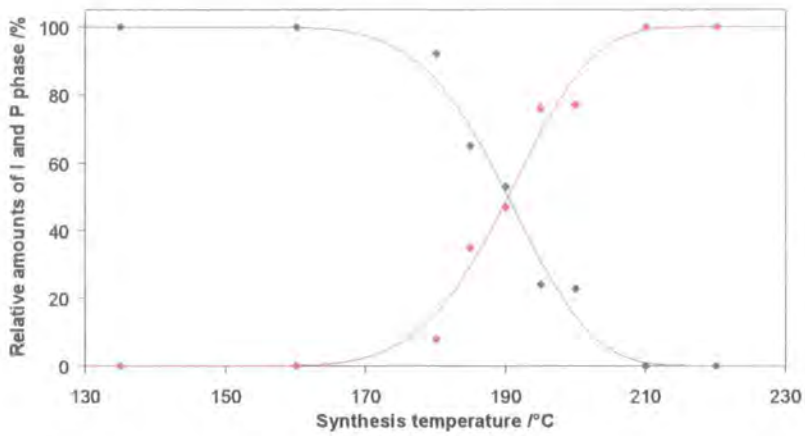

Figure 4.13 Variation in the relative amounts of *P* Cu_2WSe_4 (blue) and *I* Cu_2WSe_4 (red) for samples synthesised at different temperatures. Lines are included as guides to the eye.

At low temperature, the reaction produces purely *P* phase material, on increasing the temperature the amount of *I* phase material gradually increases; by 210 °C only *I* phase material is formed. The increase in the amount of *I* phase material occurs fairly smoothly with temperature. The impurity phase PPh_4CuWSe_4 is present in samples synthesised at between 185 and 195 °C, which curiously is the temperature at which there are similar amounts of the two phases of Cu_2WSe_4, rather than one of the two forms being dominant. In order to try and gain more insight into this observation, the effect of reaction time on the outcome of the reaction was also tested.

Several samples of Cu_2WSe_4 were synthesised at 190 °C, using reaction times of 12, 24, 48 and 96 hours. This temperature was chosen because it was the temperature at which the most significant quantity of PPh_4CuWSe_4 was formed. The proportion of each phase present in each of the samples was then analysed by Rietveld refinement, they are shown in Figure 4.14 and given on a relative percentage scale.

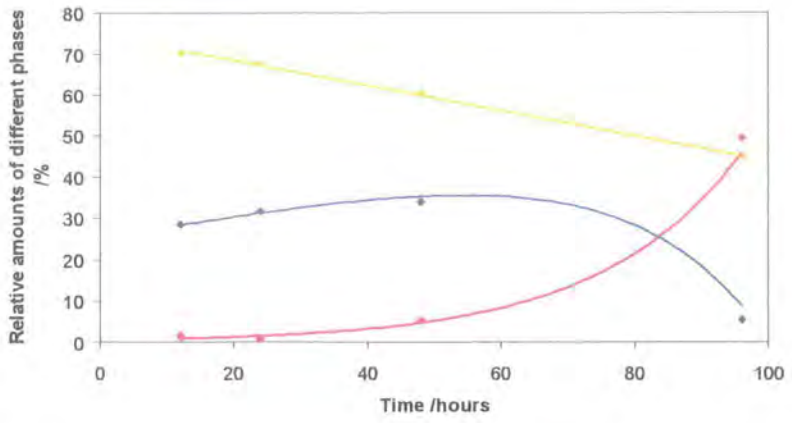

Figure 4.14 Variation of the relative amounts of *P* Cu_2WSe_4 (blue), *I* Cu_2WSe_4 (red) and PPh_4CuWSe_4 (yellow) in samples synthesied using different reaction times. Lines are added as guides to the eye.

The data in this graph suggest that initially a mixture of *P* Cu_2WSe_4 and PPh_4CuWSe_4 forms, as time passes, the *P* Cu_2WSe_4 disappears and *I* Cu_2WSe_4 is produced. The amount of PPh_4CuWSe_4 steadily decreases over a longer period.

The data presented suggests that the balance of stabilities between the three materials - PPh_4CuWSe_4, *P* Cu_2WSe_4 and *I* Cu_2WSe_4 - is very subtle. Longer reaction times and higher temperatures favour *I* Cu_2WSe_4 over *P* Cu_2WSe_4 while the formation of PPh_4CuWSe_4 appears to be very sensitive to temperature, for reactions of a 48 hour duration it forms only in a 10 °C window. Presumably if temperature dependent reaction studies were carried out using different reaction times the relative stabilities of the three phases would be different and the impurity may be observed at different temperatures. The outcome of this reaction is clearly dependent on both the reaction time and temperature, but the nature of the relationship of these two factors to the outcome of the reaction is complex.

4.3.4 Variable temperature diffraction studies

Variable temperature diffraction data were collected using a Bruker d8 Advance diffractometer fitted with the PheniX ccr. The sample used was pure *I* phase material that had been synthesised at 220 °C and sprinkled onto a Vaseline coated aluminium sample holder. The sample was cooled at a rate of 17 K/hour and diffraction data were collected continuously during cooling. Data were collected over the 2θ range 10 to

120 ° using a step size of 0.0144 ° and a time per step of 0.2 s, each scan took about 30 mins, giving a total of 37 scans during cooling (steps of ~8 K). Cell parameters were determined using the *multitopas* methodology (see section 2.6), with a Rietveld fit for Cu_2WSe_4 and a Pawley fit for the aluminium. The average temperature for each scan was extracted from the PheniX logfile using the *phenixlogfile* routine. The cell parameters for both the Cu_2WSe_4 and the Al sample holder (included as a check on the refinement) are shown in Figure 4.15.

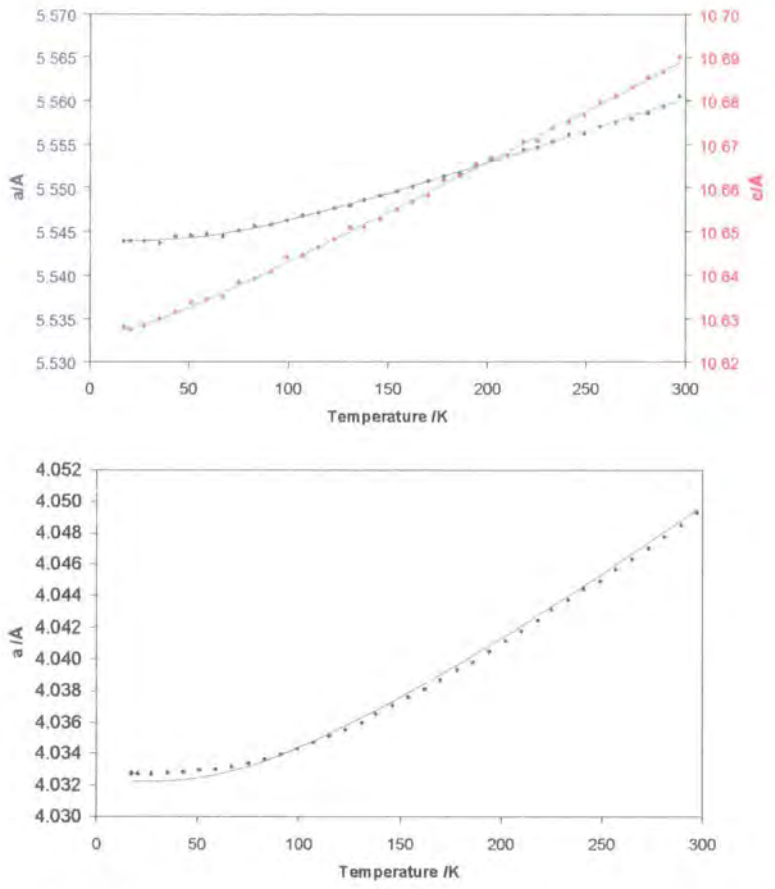

Figure 4.15 The variation of cell parameters with temperature in *I* Cu_2WSe_4 (top) and Al (bottom). The *a* cell parameter is shown in blue, *c* in red and the Al cell parameter in black. Values calculated from the Reeber equation are shown in grey.

The cell parameters, like those in the sulfur analogue (section 4.2.4) show a smooth expansion with temperature, giving no evidence for phase transitions in the temperature range investigated. The values of a_0, c_1, θ_1 and α were obtained by fitting the experimentally determined cell parameters using the Reeber equation (4.2), the values obtained are summarised in Table 4.13.

	a	*c*	*a* Al
a_0 /Å	5.54399 (8)	10.6276 (4)	4.03226 (5)
θ_1 /K	207 (8)	78 (7)	
c_1 /K^{-1}	14.1 (2) × 10^{-6}	22.1 (2) × 10^{-6}	
$\alpha_{15K\text{-}300K}$ /K^{-1}	10.3 (2) × 10^{-6}	20.3 (4) × 10^{-6}	

Table 4.13 Thermal expansion parameters for Cu_2WSe_4.

This material shows similar expansion behaviour to its sulphide analogue, Cu_2WS_4 (see section 4.2.4); with a larger relative expansion in the direction of the *c* axis than in the direction of the *a* axis.

4.3.5 Physical Properties

The magnetic and conductivity properties of Cu_2WSe_4 were measured using a sample of pure *I* phase material, synthesised at 220 °C. Magnetic measurements were made on a powdered sample contained in a gelatin capsule using a SQUID magnetometer as described in section 2.8. They showed that the material, like its sulfur analogue, is diamagnetic.

Conductivity data were measured using a Keithly instruments electrometer on a pellet of sample contained in an Oxford Instruments cooling device, as described in section 2.9. The powdered sample was pressed into a pellet using a 5 mm pellet die and a pressure of ~2 tons. Contacts were evaporated onto the pellet using a metal evaporator. Indium and gold were both tested as potential contact materials, but only gold gave ohmic contacts. Copper wires were attached to the contacts using silver paint as the adhesive. The contacts were circular with a radius of 4 mm and the pellet depth (distance between contacts) was 0.44 mm. The temperature was varied from 300 K to 80 K and measurements were taken every 5 K. Data were collected once on cooling and again as the sample was heated, the measurements were repeated a second time with the current passing through the sample in the opposite direction to check that the direction of flow of current had no effect on the readings obtained.

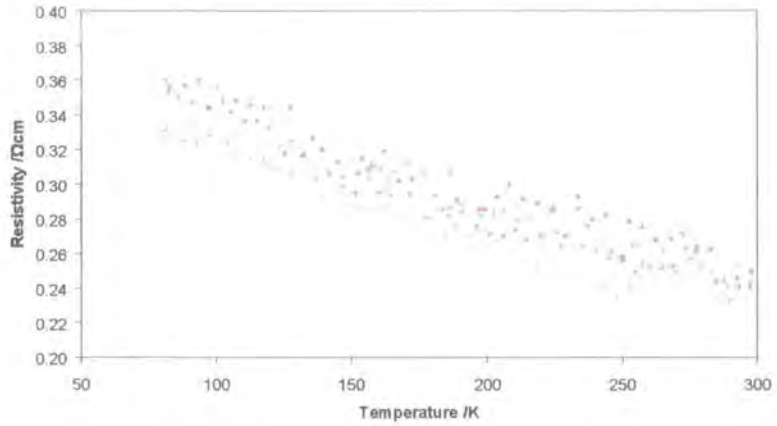

Figure 4.16 The variation in resistivity of Cu_2WS_4 with temperature. Red and orange points are data measured on heating, light blue and dark blue data collected on cooling.

These data show a general trend of the resistivity decreasing as the temperature increases, which suggests that the material is a semiconductor. There is a large amount of scatter on the points, believed to be due to problems with the electrometer and also the method used to collect the data. The resistance of the sample is low, so measurement using a two probe technique such as the one used here is not ideal, factors such as the residual contact resistance and the impedance of the wires can affect the values obtained.[19]

4.4 $Cu_2WS_xSe_{4-x}$

Pure, crystalline Cu_2WS_4 and Cu_2WSe_4 can both be synthesised using solvothermal reactions. It was decided to try and extend this idea and use a mixture of both tungsten sulfide and tungsten selenide to try and produce a mixed anion material.

$Cu_2WS_xSe_{4-x}$ solid solutions were made by reacting stoichiometric amounts of $Cu(CH_3CN)_4BF_4$ with mixtures of $(NH_4)_2WS_4$ and $(PPh_4)_2WSe_4$. Synthesis was done using three different reagent ratios, which correspond to $x = 1$, 2 and 3 in the formula $Cu_2WS_xSe_{4-x}$ and were carried out at either 200 °C ($x = 2$, 3) or 220 °C ($x = 1$), as these were the temperatures at which the best quality Cu_2WS_4 and Cu_2WSe_4 samples were formed. The reactions gave materials which varied in colour from orange-brown ($x = 3$) to purple-brown ($x = 1$). The powder patterns were obtained using samples sprinkled onto amorphous glass slides, data were collected using a Siemens D5000 diffractometer over a 2θ range of 10 to 120 °, with a step size of 0.02 °, a time per step of 10 s and used a 1 ° divergence slit; they are shown in Figure 4.17.

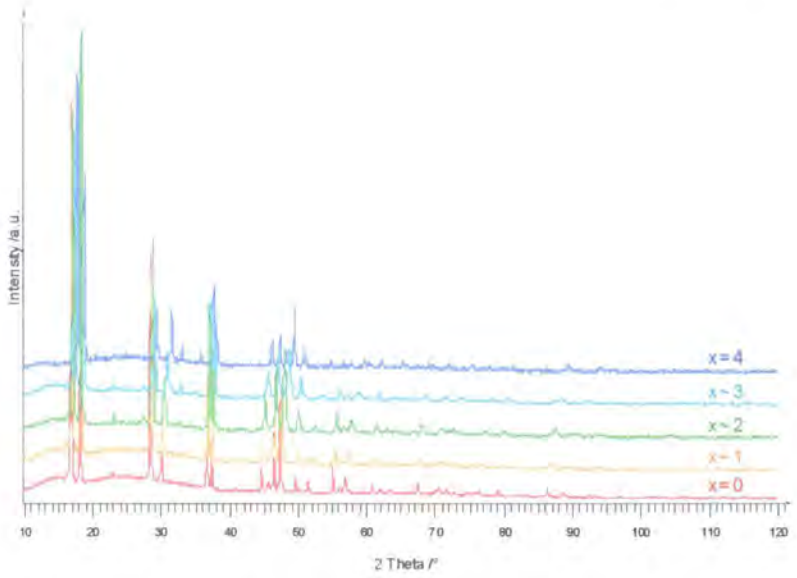

Figure 4.17 XRD patterns of $Cu_2WS_xSe_{4-x}$ phases, patterns are offset in the *y* direction for clarity.

The materials are all highly crystalline, have diffraction patterns similar to those of *I* phase Cu_2WS_4 and Cu_2WSe_4, and show smooth variation of cell parameters as the sulfur: selenium ratio changes. The powder patterns can be fitted using a structural model identical to those used for *I* phase Cu_2WX_4 (X = S, Se), with a mixture of sulfur and selenium on the site previously occupied by S or Se. The powder patterns do not show any evidence of ordering of S^{2-} and Se^{2-} within the anion lattice. Anion ordering would result in additional peaks in the diffraction pattern due to a lowering in the symmetry of the material. There is only one extra peak observed in the patterns, this is at ~27.5 °. However this is believed to be a minor impurity phase rather than a peak from the main $Cu_2WS_xSe_{4-x}$ phases because its position does not change as the composition varies; other peak positions change significantly as a result of the change in cell parameters. We presume that the MX_4 units remain intact during the reaction, implying that the anion disorder is not completely random. The structure presumably consists of three structural units: WS_4^{2-}, WSe_4^{2-} and Cu^+, the disorder comes from random mixing of the tungsten sulfide and tungsten selenide units throughout the lattice

The cell parameters for the different phases were determined by Rietveld refinement using a model based on the structure of *I* phase Cu_2WX_4, with a mixture of sulfur and selenium on the X site. The occupancy of the site was refined, with the sum of the occupancies of sulfur and selenium constrained to equal one. One temperature factor was refined and constrained to be the same for all sites. In addition to these a further 26 parameters were refined for each phase: 2 cell parameters, 2 atomic coordinates for the X site, a scale factor, sample displacement, a simple axial model to describe peak asymmetry, 13 coefficients of a Chebychev polynomial to describe the background and 6 peak shape parameters. A summary of the structural details for each phase is

presented in Table 4.14. Parameters for Cu_2WS_4 and Cu_2WSe_4 are included in the table for comparison. To allow a direct comparison, values for the site occupancy and a single temperature factor were refined for these materials using the models previously described (sections 4.2.2 and 4.3.2), no other parameters were refined.

In order to determine additional information about the strain and crystallite size within the samples the pseudo-Voigt model of peak shape was replaced with a model that used a combination of a Gaussian size dependent term and a Gaussian strain dependent term. All other parameters were fixed and values for these two parameters were refined, they are also included in the table for each material.

	$x = 0$	$x \sim 1$	$x \sim 2$	$x \sim 3$	$x = 4$
Synthesis x	0	1.04	1.92	2.96	4
a /Å	5.5576 (1)	5.5344 (2)	5.5095 (2)	5.4748 (3)	5.4443 (1)
c /Å	10.6940 (4)	10.6009 (6)	10.4920 (6)	10.2723 (7)	10.0687 (2)
X x coordinate	0.2430 (2)	0.2464 (5)	0.2422 (5)	0.2410 (7)	0.2381 (3)
X z coordinate	0.1189(6)	0.1145 (3)	0.1227 (3)	0.1187 (4)	0.1189 (6)
S occupancy	0.000 (5)	0.205 (9)	0.390 (7)	0.700 (6)	0.996 (1)
Rietveld x	0.00 (2)	0.82 (4)	1.56 (3)	2.80 (2)	4.06 (1)
U_{iso}	1.17 (2)	5.50 (8)	3.81 (9)	0.046 (1)	3.27 (2)
Size /nm	69.0 (6)	77 (1)	63 (1)	59 (1)	55.1 (2)
Strain	0.283 (4)	0.56 (1)	0.737 (9)	0.86 (1)	0.0 (3)

Table 4.14 Selected structural details for $Cu_2WS_xSe_{4-x}$ phases.

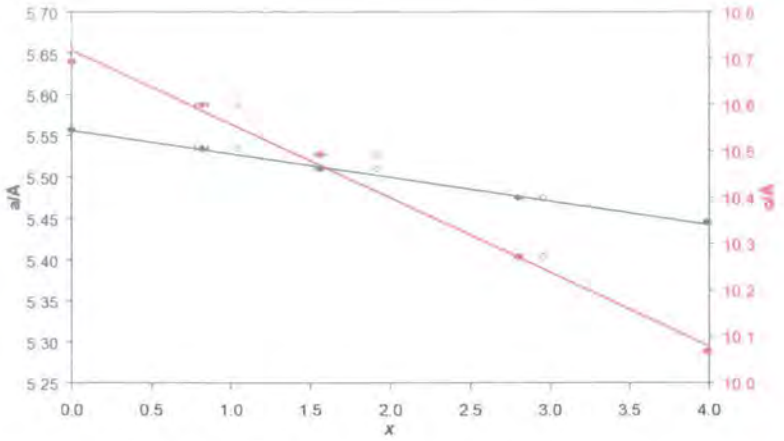

Figure 4.18 Change in cell parameters in $Cu_2WS_xSe_{4-x}$ phases with varying x. The a cell parameter is shown in blue, the c cell parameter in red. Open symbols are values plotted against synthesis x, closed symbols are plotted against Rietveld refined x.

The variation in cell parameter for this series of materials is shown in Figure 4.18. This smooth variation in cell parameters is consistent with a solid in which the anions are disordered and in which the structure remains essentially the same as the composition changes. The variation in the size and strain parameters for the different materials is shown in Figure 4.19.

These data show that the size of the crystallites shows no strong correlation with the composition of the material. The strain however, is larger for those materials in which there is a mixture of selenide and sulfide present. This is further evidence for the random occupation of sites in the anion lattice by sulfide and selenide ions, which would be expected to introduce local strain effects.

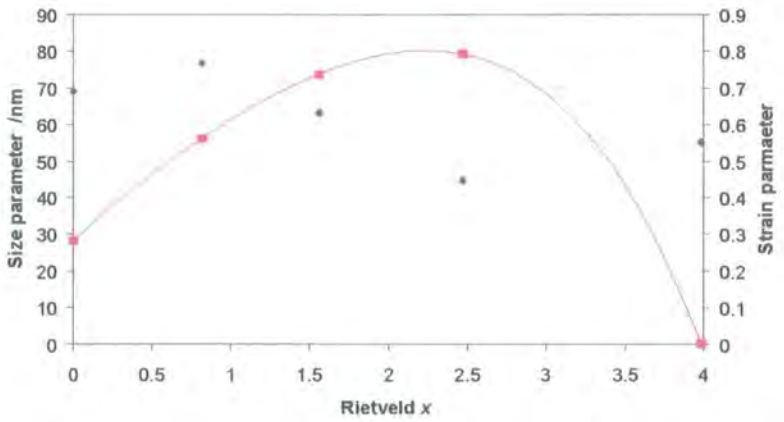

Figure 4.19 The variation in size (blue) and strain (red) parameters for $Cu_2WS_xSe_{4-x}$ as the value of x changes. For the strain a line is added as a guide to the eye.

4.5 Cu_2MoS_4

4.5.1 Synthetic studies

Attempts to synthesise copper thiomolybdate using the solvothermal method described in section 4.1 were made at a range of temperatures from 110 to 200 °C. At temperatures of 150 °C and below, poorly crystalline purple-brown coloured powders were produced. At temperatures above 150 °C only an amorphous brown solid was recovered. The powder patterns of the materials produced at low temperature are shown in Figure 4.20.

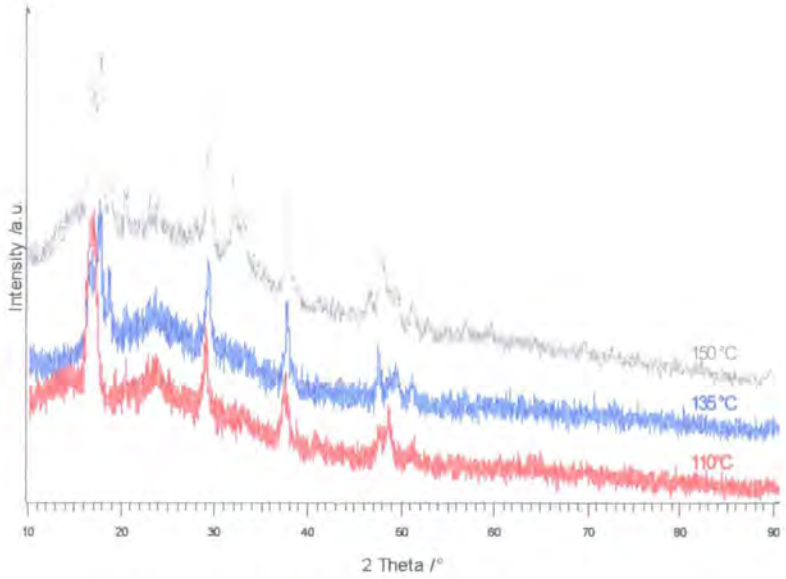

Figure 4.20 XRD patterns of Cu_2MoS_4 produced between 110 °C and 150 °C. Patterns are offset in the *y* direction for clarity.

Despite the poor crystallinity, the powder patterns of these materials can be fitted using structural models analogous to the *I* and *P* phases of Cu_2WS_4. Due to the poor crystallinity of the samples produced, no attempt has been made to refine fractional atomic coordinates. The material made at 110 °C has a structure analogous to the *P* phase material, the Rietveld fit is shown in Figure 4.21.

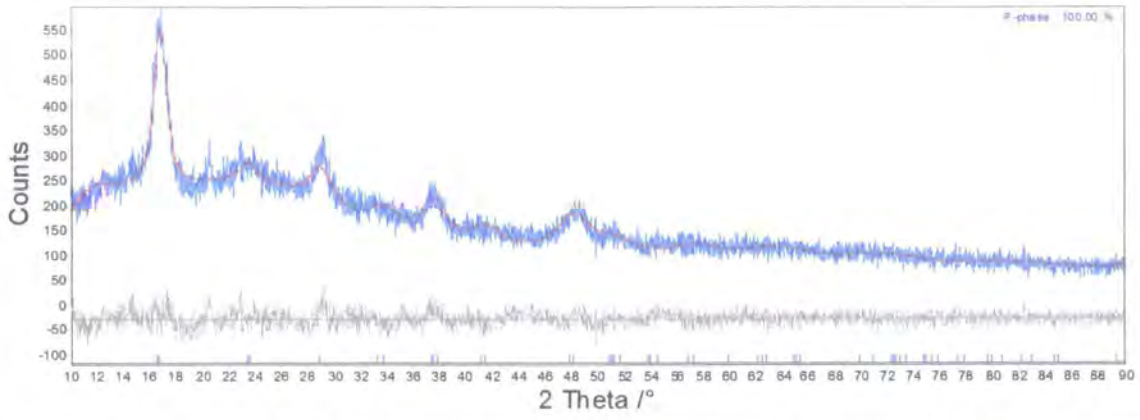

Figure 4.21 Rietveld fit of *P* Cu_2MoS_4, observed data are shown in blue, calculated in red and difference in grey.

The materials made at 135 °C and 150 °C have powder patterns that show a mixture of phases is present, additional peaks at ~19.5 ° can be fitted by introduction of a second phase with a structure analogous to *I* Cu_2WS_4. The Rietveld fit for the sample synthesised at 135 °C is shown in Figure 4.22.

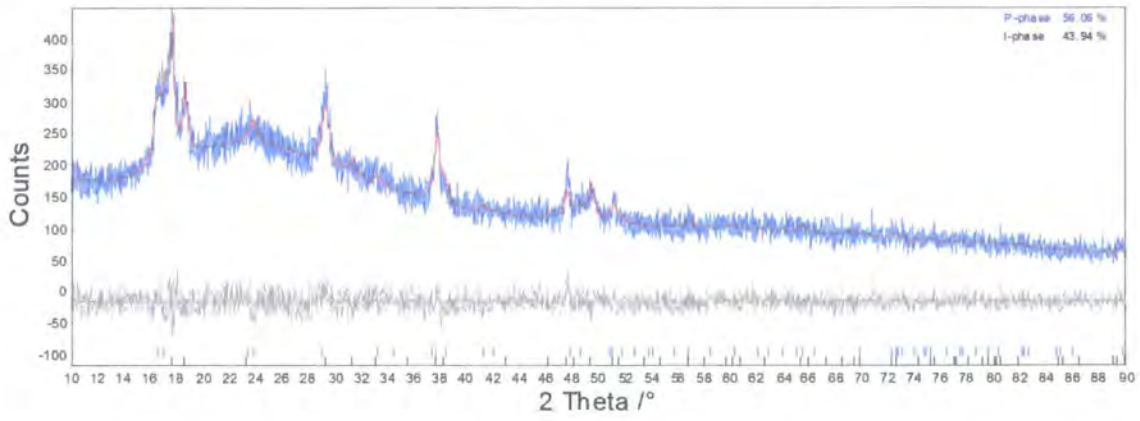

Figure 4.22 Rietveld fit of a mixture of *P* and *I* phase Cu_2MoS_4. Observed data are shown in blue, calculated in red and difference in grey. *hkl* tick marks for the *P* phase are shown in blue and for the *I* phase they are shown in black.

The cell parameters obtained for the two phases of Cu_2MoS_4 are summarised in Table 4.15

	P Cu_2MoS_4	*I* Cu_2MoS_4	$\Delta P \rightarrow I$
a	5.381 (5)	5.410 (2)	+0.5 %
c	5.28 (1)	10.35 (6)	−2.0 %

Table 4.15 Cell parameters for the *I* and *P* phases of Cu_2MoS_4.

The cell parameters suggest that the relationship between the two polymorphs is slightly different to that between the two polymorphs of Cu_2WS_4. The change in *a* cell parameter on changing from the *P* to the *I* phase (+0.5 %) is comparable with that of the

tungsten material (+0.4%). The change in the *c* parameter (−2.0%) is slightly smaller than that seen for the tungsten material (−3.8 %). The precision in the cell parameters is, however, poor.

The formation of amorphous solids at temperatures above 150 °C is believed to be related to the relative stabilities of the WS_4^{2-} and MoS_4^{2-} ions under these reaction conditions. The MoS_4^{2-} unit is presumably decaying, while the WS_4^{2-} unit can remain intact even at high temperatures and is present in the product phase. Müller has reported[11] that on heating, the decomposition of $(NH_4)_2MoS_4$ produces MoS_3, which is amorphous; it is possible that a similar decomposition is taking place under the solvothermal reaction conditions and preventing the formation of Cu_2MoS_4.

4.6 Cu_2MoSe_4

4.6.1 Synthetic Studies

Like the other materials discussed in this chapter, Cu_2MoSe_4 was synthesised by solvothermal reaction at a number of different temperatures between 135 and 220 °C, which resulted in products of different composition. The powder patterns of the solids produced by reaction at different temperatures are shown in Figure 4.23.

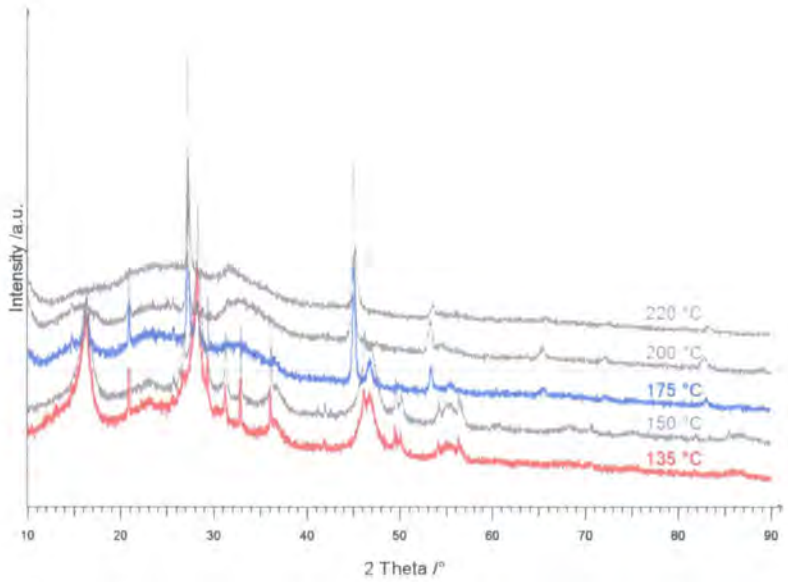

Figure 4.23 XRD patterns of Cu_2MoSe_4 synthesised between 135 °C and 220 °C. Patterns are offset in the *y* direction for clarity.

At 175 °C or below the materials formed were complex mixtures of various different copper selenide impurity phases and a material analogous to *P* Cu_2WS_4. Tick marks indicating which peaks correspond to which phase can be found in Figure 4.24. At temperatures of 175 °C and higher the Berzelianite form[20] of Cu_2Se becomes the major impurity phase, and by 220 °C this is the only crystalline material present. All of the

powder patterns also show broad humps in the background, suggesting that as well as the crystalline impurities, there are also amorphous impurity phases.

The powder pattern of the materials produced at 135 and 150 °C can be fitted using a structural model analogous to that of *P* Cu_2WS_4 (only cell parameters were refined due to the poor crystallinity of this material) and introducing structural fits for the $CuSe_2$ and CuSe impurity phases. The fitted pattern of the sample synthesised at 135 °C is shown in Figure 4.24.

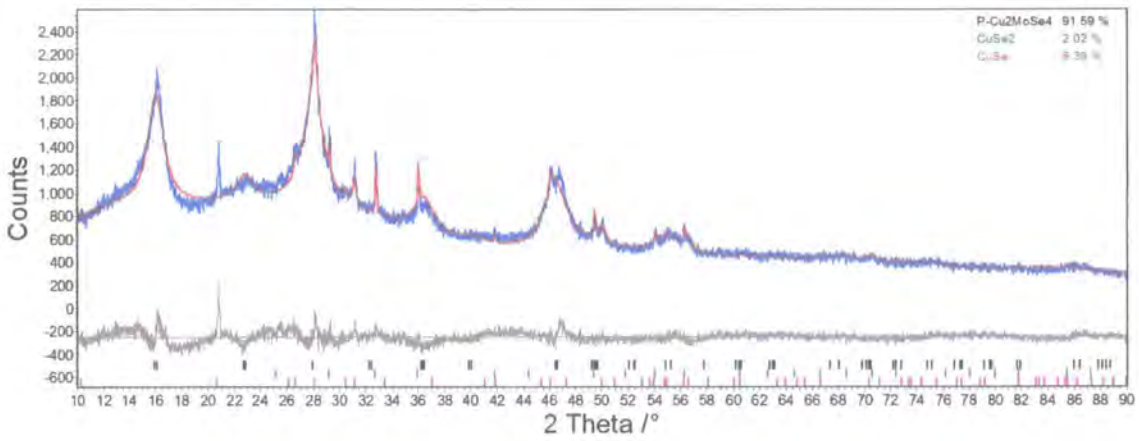

Figure 4.24 Rietveld fit of powder pattern of Cu_2MoSe_4 synthesised at 135 °C. Observed data are shown in blue, calculated in red and difference in grey. *hkl* tick marks for *P* Cu_2WSe_4 are shown in black, for $CuSe_2$ they are green and for CuSe they are pink.

Cell parameters of $a = b = 5.507$ (3) and $c = 5.553$ (7) Å were obtained for *P* Cu_2MoSe_4. The increase in the cell parameters of *P* Cu_2MoX_4 on changing from sulfur to selenium is +2.3 % in the *a* axis and +4.6 % in the *c* axis. These values show a slightly larger increase in the *a* axis and a slightly smaller increase in the *c* axis compared to the *P* Cu_2WX_4 materials for which expansions of +2.0 % and +6.1 % are observed for the *a* and *c* axes respectively.

These observations suggest that at higher temperatures, under the synthesis conditions used, Cu_2MoSe_4 is unstable with respect to copper selenide. There may also be an amorphous molybdenum selenide phase produced, accounting for the broad background humps in the diffraction pattern. It is only at the lowest reaction temperatures that Cu_2MoSe_4 can be produced and even then copper selenide is present, suggesting that the $MoSe_4^{2-}$ units are decaying even at this temperature. This suggests that Cu_2MoSe_4 is less stable than its tungsten analogue, mirroring the relative stabilities of the corresponding sulfides.

4.7 Structure solution of PPh_4CuWSe_4

As previously discussed in section 4.3.1, a significant impurity phase was produced when Cu_2WSe_4 was synthesised in a narrow temperature range (185 to 190 °C), it had a powder pattern which could not be matched with that of any known compound by comparison with the PDF. The fact that this material is formed only in a very narrow temperature range is unexpected, but the behaviour was reproducible over several syntheses. In order to try and gain insight and understanding of this observation, attempts were made to discover the identity and structure of this material by structure solution from powder data. The XRD patterns obtained from samples of Cu_2WSe_4 synthesised at 190 °C were complex and contained copper selenide impurities as well as a mixture of *P* and *I* phase Cu_2WSe_4. In order to try and overcome this problem attempts were made to deliberately target a pure sample of the unknown phase.

It was discovered that whilst stoichiometric ratios of copper and tungsten reagents only led to formation of the impurity phase at 190 °C, small amounts of this phase could also be produced at lower temperature by increasing the W:Cu ratio. This observation suggested that the impurity phase could be copper deficient relative to Cu_2WSe_4. Phases containing a 1:1 ratio of metals such as $(NH_4)CuMoS_4$ and $(NH_4)CuWS_4$ have been reported[21,22] and it was thought that the impurity phase may be similar to these. Attempts to synthesise a pure sample of this material were therefore made using a $(PPh_4)_2WSe_4$: $Cu(CH_3CN)_4BF_4$ ratio of 1:1 and heating to 190 °C for 48 hours. This resulted in the formation of a red powder, the XRD pattern of this material corresponded with that of the impurity phase previously observed. Elemental analysis of the material was consistent with a structural formula of PPh_4CuWSe_4 (Observed C:H 32.13: 2.27 %; Calculated C:H 31.94: 2.23 %). Rutherford back scattering (RBS) data were consistent with a Cu:W ratio of 1:1.

A high quality powder pattern of the material was collected using a Bruker d8 Advance diffractometer on a sample prepared by sprinkling the powder onto a zero-background silicon wafer coated with a thin layer of Vaseline. Data were collected over a range of 5 to 90 ° with a step size of 0.0144 ° and a time per step of 3 s. The measurement was repeated 11 times giving a total data collection time of ~54 hours; data from individual scans were summed.

The powder pattern was indexed using the TOPAS singular value decomposition indexing routine[23] as described in section 2.3. Two possible unit cells, both monoclinic, were suggested by this procedure:

Cell 1: $a = 11.352$ Å $b = 11.297$ Å $c = 19.709$ Å $\beta = 92.90$ $FOM_{TOPAS} = 7.35$

Cell 2: $a = 11.103$ Å $b = 11.332$ Å $c = 20.098$ Å $\beta = 91.58$ $FOM_{TOPAS} = 8.12$

Although these cells are similar, they are not related. Pawley fits of both of the cells to the data using space group P2 gave excellent agreement, with $_wR_p$ of 4.215 % for cell 1 and 4.065 % for cell 2. Despite the marginally better R-factor for the second cell, attempts to solve the structure using this unit cell were totally unsuccessful; consequently cell 1 was used for further analysis.

The pattern was examined to find the systematic absences and assign a space group. The pattern had *00l* ($l \neq 2n$), absences, which are consistent with the space group P2/c. However the complex nature of the pattern made assignment of this space group ambiguous, so structure solution was attempted in two space groups, P2/c and P2, in order to confirm that the choice of P2/c was indeed correct. The unit cell volume was 2525 Å^3, comparison to the cell volumes of other metal sulfide complexes containing PPh_4^+ cations (for example[24] $[(PPh_4)_2][Co(WS_4)_2]$, cell volume 5075 Å^3, $z = 4$) and consideration of the charges of the species present suggested that cell contents of four PPh_4^+ units, four Cu^+ ions and four WSe_4^{2-} units would be reasonable. The structure was solved by simulated annealing in TOPAS (see section 2.4). For the initial solution, cell parameters, height correction, axial divergence and peak shape parameters were all fixed at the values determined from the Pawley fit. For solution in space group P2/c one PPh_4^+ cation, one WSe_4^{2-} and one Cu^+ are needed in the asymmetric unit to give the correct cell contents. The WSe_4^{2-} unit and the PPh_4^+ cation were modelled as rigid bodies, with the positions of the selenium, carbon and hydrogen atoms specified relative to the tungsten or phosphorus atoms respectively. Space group P2/c has three different types of site: general positions (multiplicity 4), sites on 2-fold axes (multiplicity 2), and sites on a centre of inversion (multiplicity 2). WSe_4 tetrahedra could only lie on either a general position, in which case only WSe_4 unit would be required in the asymmetric unit, or on the two fold axis, which would require two WSe_4 units. Two half occupied WSe_4 tetrahedra were used rather than one single fully occupied WSe_4 unit; this means that they can either occupy two sites on the 2-fold axis, or refine onto the same general position, giving more flexibility than there would be if only one fully occupied unit was used. Similar principles can be applied to the Cu; two half occupied copper atoms were therefore also used for annealing. One single fully occupied PPh_4 unit was the final rigid body used; this was defined so that each of the four phenyl rings was able to freely rotate around the P – C bond. For the solution in space group P2 these cell contents were doubled.

During annealing six parameters were varied for each of the rigid bodies: three translations, describing the position of the central atom within the unit cell, and three rotations, describing rotation of the body around the *x*, *y* and *z* axes. For the PPh_4 unit, four additional parameters describing the rotations of the phenyl rings around the P – C bonds were also varied. For the copper atoms, only three translational parameters were

varied. Finally, a single temperature factor was refined for all the atoms. For each cycle of annealing, each of these parameters was set to a random value, positions were moved by distances up to ±5 Å, rigid body rotations were given a random value between ±180 °, torsion angles were given a value between ±30 °, and the temperature factor was returned to 0.01 $Å^2$. Hundreds of thousands of cycles of randomisation followed by full Rietveld refinement were done in order to determine the best solution.

The initial structure solutions obtained gave very similar results in both of the two space groups. Metals atoms were located in chains along the direction of the *a* axis at $y \sim 0.5$, $z \sim 0.25$ and the PPh_4 units were located in the gaps between the chains. These chains had approximate two-fold symmetry and it seems very surprising that they were not located along the two-fold axes which lie parallel to the *b* axis. Several attempts were made to change the position of the chains within the cell and force them to lie along the 2-fold axes, however, none of these gave a fit the experimental data as good as the one obtained with the chains lying along the *a* axis, so this was taken as being the correct solution.

If the chains were located along the *a* axis, the presence of the two fold axis perpendicular to the chain means that they must contain a disordered array of Cu/W sites. A chain is shown in Figure 4.25.

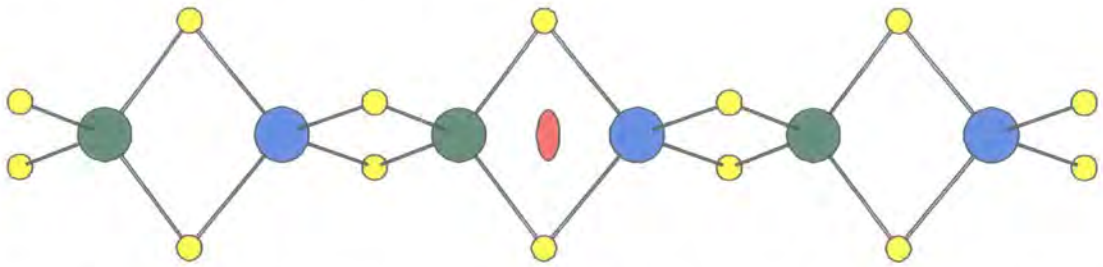

Figure 4.25 A chain of edge linked tetrahedra, Cu and W are shown in blue and green, S is shown in yellow. The red shape indicates a position that a 2-fold axis could pass through the chain.

The only way a two fold axis can pass perpendicular to the chain is at a position between two metal atoms; an example is indicated in red in Figure 4.25. This means that the two metal atoms must be equivalent, *i.e.* within the chain the copper and tungsten atoms must be disordered over the metal sites. In order to model this, the four half occupied metal atoms located in the chain were replaced by two MSe_4 tetrahedra, M being the atom with a number of electrons equal to the average number in Cu and W *i.e.* Sb. The metals are all given full occupancy but the Se atoms are given only half occupancy, to allow them to occupy the same position and link up to form chains. Further cycles of simulated annealing were then performed. The result of this annealing was a structure in which there are continuous chains of edge sharing metal tetrahedra. Examination of the positions of the Se atoms revealed that some of them are located on

special positions; the structure was modified slightly to reflect this. This trial structure was then further refined to give the final structure solution. The final R-factors determined for the two different solutions are summarised in Table 4.16.

	P2/c	P2
$_wR_p$	7.847	7.516
R_{Bragg}	2.880	2.928
No. of refined parameters	60	86

Table 4.16 R-factors for refinements of the structure of PPh_4CuWSe_4 in space groups P2/c and P2.

These R-factors are not dramatically different; the smaller value for the P2 solution would be expected given the extra parameters that are refined. Visual comparison of the fitted powder patterns shows that there are only small differences in the quality of the two fits, mainly in the fitting of small peaks between 16 and 19 ° 2θ. Part of the fitted powder pattern for the two space groups is shown in Figure 4.26.

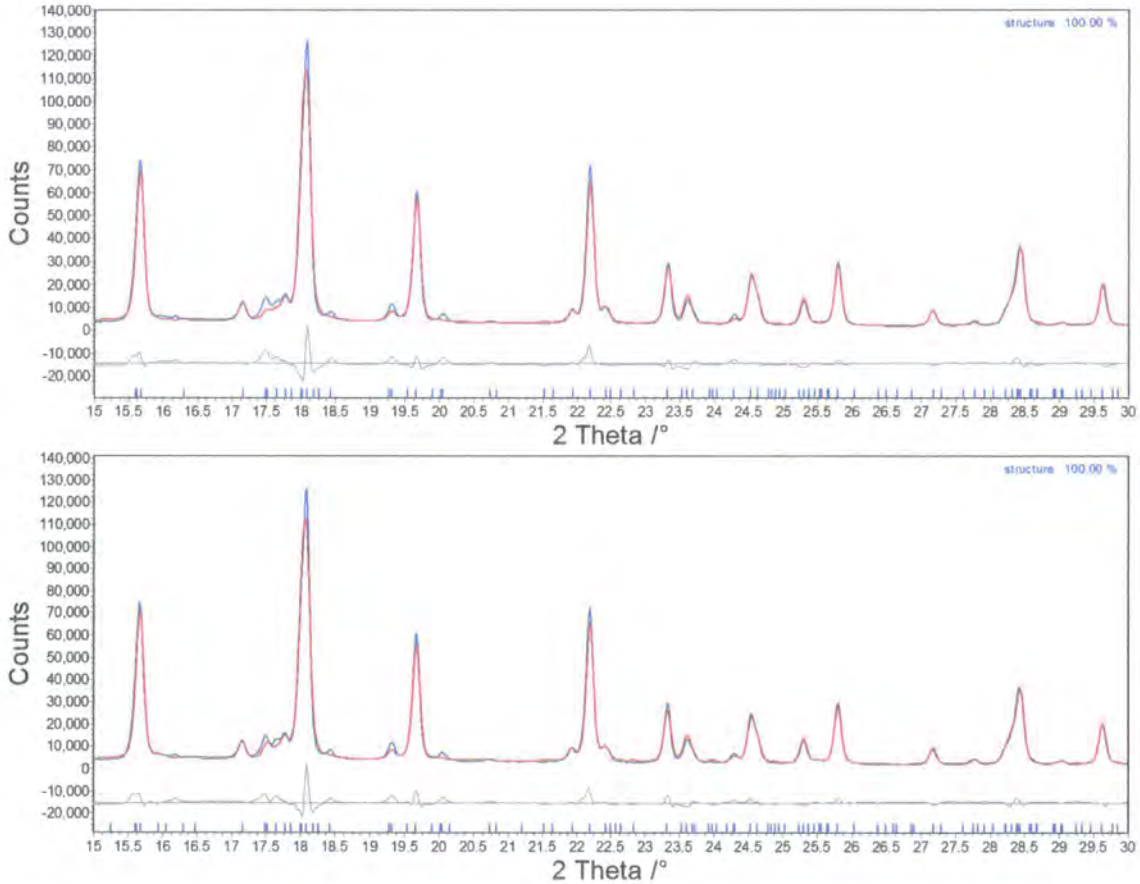

Figure 4.26 The fitted powder patterns for structures in space group P2/c (top) and P2 (bottom) zoomed over the 2θ region of 15 to 30 °. Observed data are shown in blue, calculated in red and the difference in grey. A fit of the full range is shown in Figure 4.28.

The atomic coordinates in the two space groups can also be compared. The final structures determined in the two space groups are shown schematically in Figure 4.27.

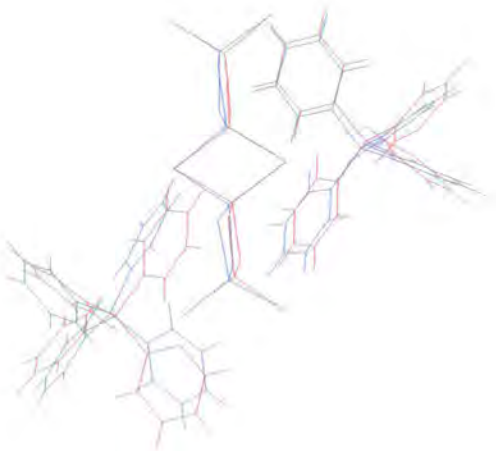

Figure 4.27 Skeletal representation of the structures of PPh_4CuWSe_4 determined in space group P2 (blue) and P2/c (red).

Figure 4.27 shows that the two structures are very similar. The metal atoms are located in almost exactly equivalent positions, and the Se atoms are also very close to each other, the only structural differences are in the position of the PPh_4^+ units. The phosphorus atoms in the two solutions are in slightly different places, < 0.4 Å apart, and the orientation of the phenyl rings is also slightly different.

Neither of the two structures determined give a perfect fit between calculated and observed data. One possible reason for this is that the model of metal disorder (with metals randomly distributed over the tetrahedral sites in the chain) is not adequate to fully describe the structure. To investigate this further the structure determined in P2/c was transformed into space group $P\bar{1}$, there is no 2-fold symmetry required in this space group so metal ordering within the chains becomes a possibility. However, attempts to model metal ordering and refine the structure in $P\bar{1}$ did not give an improvement in fit of the model to the data.

Given the fact that none of these fits are perfect, the solution in P2/c is an adequate structural description. The discrepancies between observed and fitted data are probably due to structural subtleties, such as only short range order existing between adjacent chains, which cannot be fully characterised from this powder data. There are striking structural similarities between this structure and that of $(PPh_4)_2Zn(WS_4)_2$, discussed in section 5.2.1. The structure of $(PPh_4)_2Zn(WS_4)_2$ is very complex and even with high quality single crystal data it was very difficult to fully characterise, it is therefore unsurprising that the PPh_4CuWSe_4 structural model obtained here from powder data is not perfect.

In final cycles of refinement a total of 61 parameters were refined, including 18 coefficients of a Chebychev polynomial to describe the background, sample displacement, a simple axial model to describe peak asymmetry, a scale factor, 6 peak shape parameters, 16 atomic coordinates for atoms in the anionic chains, 10 parameters to describe rotation, translation and torsion angles in the PPh_4^+ cation and four temperature factors (two for the metal sites, one for selenium sites and one for atoms in PPh_4^+ cation). The positions of the phenyl rings were specified in relation to the phosphorus atom, using a P – C bond length of 1.792 Å (the mean bond length for P – C bonds in PPh_4 groups found in structures in the Cambridge Structural Database[13]) and idealised tetrahedral geometry around the phosphorus atom. The phenyl rings were modelled with C – C bond lengths of 1.39 Å. Data collection and refinement details are given in Table 4.17, the Rietveld fit is shown in Figure 4.28, fractional atomic coordinates for the atoms in the anion units are given in Table 4.18 and structural data for the PPh_4^+ cations in Table 4.19. A full list of fractional atomic coordinates for all atoms can be found in Appendix 4.1 and the TOPAS input file for the final refinement is included in the e-appendix.

Space Group	P2/c	2θ range	5 – 90 °
a	11.3521 (2) Å	2θ step	0.0144 °
b	11.3007 (2) Å	Time per step	33 s
c	19.7072 (4) Å	$_wR_p$	7.847 %
β	92.899 (1) °	R_{Bragg}	2.880 %
$\alpha = \gamma$	90 °	χ^2	6.47
No. of refined parameters	60		

Table 4.17 Selected crystallographic, data collection and refinement details for PPh_4CuWSe_4.

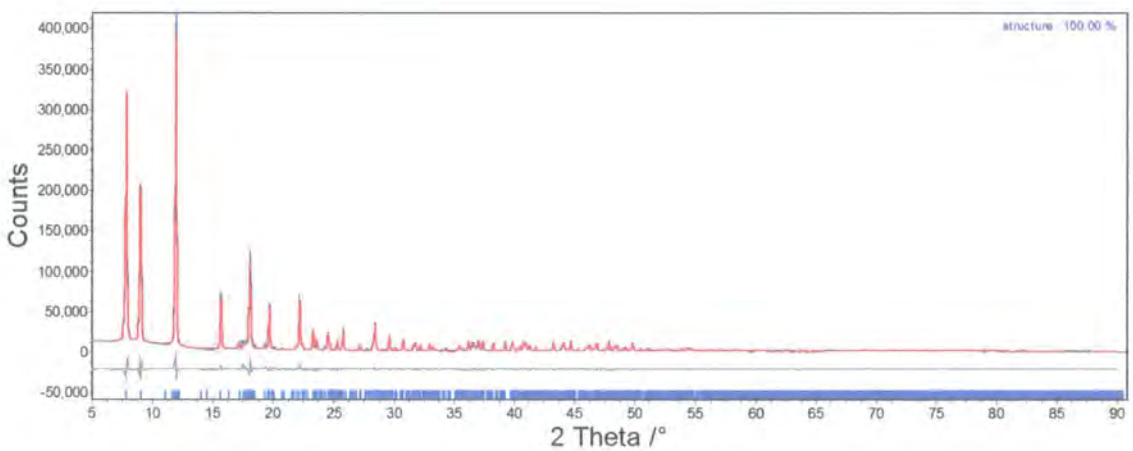

Figure 4.28 Rietveld fit for the PPh_4CuWSe_4 structure in space group P2/c. Observed data are shown in blue, calculated in red and difference in grey. A zoomed region is shown in Figure 4.26.

Atom	*x/a*	*y/b*	*z/c*	U_{iso} /Å^2
M1	0.124 (1)	0.4956 (9)	0.2485 (5)	0.118 (5)
M1	0.3734 (9)	0.4998 (8)	0.2480 (4)	0.092 (5)
Se1	0.0	0.329 (2)	0.25	0.098 (1)
Se2	0.0	0.652 (2)	0.25	0.098 (1)
Se3	0.235 (1)	0.500 (1)	0.153 (1)	0.098 (1)
Se4	0.255 (2)	0.512 (1)	0.344 (1)	0.098 (1)
Se5	0.5	0.672 (2)	0.25	0.098 (1)
Se6	0.5	0.329 (2)	0.25	0.098 (1)
P1	0.235 (1)	0.1028 (4)	0.5071 (6)	0.051 (3)

Table 4.18 Fractional atomic coordinates and temperature factors for atoms in PPh_4CuWSe_4.

x_{rot} /°	116.8 (2)
y_{rot} /°	27.8 (3)
z_{rot} /°	51.2 (3)
torsion 1 /°	7 (1)
torsion 2 /°	76 (1)
torsion 3 /°	62 (1)
torsion 4 /°	−21 (1)

Table 4.19 Torsion angles and rotations about the axes for the rigid Ph_4 unit in PPh_4CuWSe_4.

As previously discussed, the structure consists of chains of metal atoms that run in a direction parallel to the *a* axis with PPh_4^+ cations residing between these chains. Although the chains have been modelled as disordered, we presume that the WSe_4^{2-} units remain intact during the reaction, implying that individual chains must have alternating copper and tungsten sites. The disorder is a result of there being no long range order in the packing of adjacent chains relative to each other. The structure is shown in Figure 4.29.

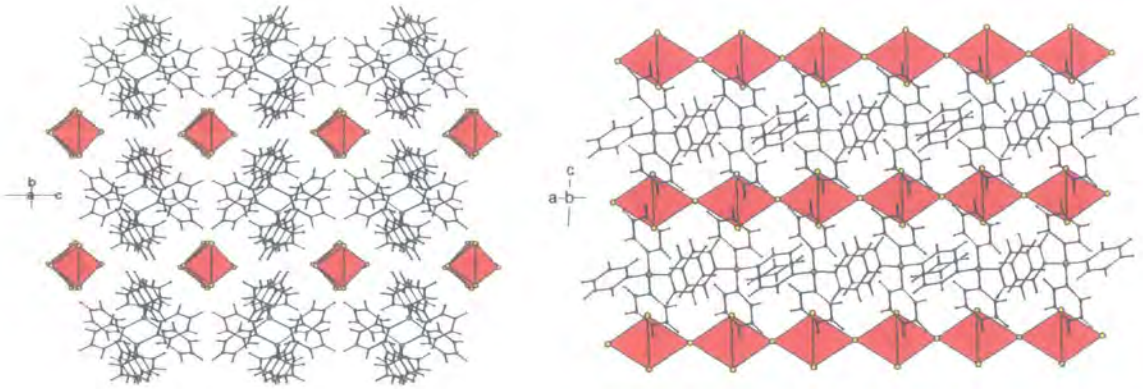

Figure 4.29 The structure of PPh_4CuWSe_4 viewed down the chain direction (left) and perpendicular to the chain direction (right). MSe_4 tetrahedra are shown in red, Se in yellow, P in green, C in blue and H in grey.

The structure was analysed using Platon[25] to check if there was void space in which solvent molecules could be contained - this would be another possible explanation for the slight differences in observed and calculated powder patterns. This analysis showed that there was no space for solvent molecules within the structure, and is consistent with the analytical data.

The M – Se bond lengths within the chains are in the range 2.25 to 2.42 Å, this is within the range of Cu – Se and W – Se bond lengths for tetrahedral metal coordination in polynuclear clusters for structures found in the CSD. In general the M – Se bond lengths are slightly longer for the M2 site than for the M1 site. The distortion from ideal tetrahedral geometry is about the same for the two different sites. Bond lengths and angles are given in Table 4.20.

Bond Lengths/Å		Bond Angles/°	
M1 – Se	2.26 (2)	Se – M1 – Se	104.6 (6)
	2.33 (2)	Se – M1 – Se	107.2 (5)
	2.35 (2)	Se – M1 – Se	107.5 (6)
	2.35 (2)	Se – M1 – Se	111.1 (5)
		Se – M1 – Se	112.1 (5)
		Se – M1 – Se	114.7 (5)
M2 – Se	2.34 (2)	Se – M2 – Se	104.6 (4)
	2.38 (2)	Se – M2 – Se	106.8 (4)
	2.40 (2)	Se – M2 – Se	107.4 (3)
	2.42 (2)	Se – M2 – Se	112.3 (3)
		Se – M2 – Se	112.4 (4)
		Se – M2 – Se	113.4 (3)

Table 4.20 Bond lengths and angles in the anionic chains in PPh_4CuWSe_4.

This material is very similar to some other copper sulfide and selenide materials. One material that is particularly closely related is $(NH_4)CuMoS_4$, which has a structure that contains chains of alternating MoS_4 and CuS_4 tetrahedra with NH_4 cations located between the chains. The material crystallises in a tetragonal unit cell, space group $I\bar{4}$.

Although PPh_4CuWSe_4 is formed under the same synthesis conditions as Cu_2WSe_4, there is no evidence that an analogous sulfur containing material formed during the synthesis of Cu_2WS_4. This could be explained by the fact that the sulfur containing Cu_2MX_4 materials are made from ammonium salts rather than tetraphenylphosphonium salts. It is possible that in the solvothermal synthesis conditions used, the ammonium cations do not stabilise the precipitation of this 1D structure as the bulkier PPh_4^+ cations do.

4.7.1 Variable Temperature Diffraction Studies

In order to further investigate the structural chemistry of PPh_4CuWSe_4, a variable temperature diffraction experiment was undertaken. This involved cooling the sample from room temperature to 16 K using the PheniX ccr. A sample was prepared by sprinkling the powder onto a Vaseline coated aluminium sample holder and cooling it at a rate of 9 K/hour whilst diffraction data were collected over a 2θ range of 5 to 90 °, with a step size of 0.0144 ° and a time per step of 0.25 s; this gave a scan time of ~30 minutes and temperature steps of ~4.5 K. A total of 69 data sets were collected on cooling. Cell parameters were determined using *multitopas* methodology (section 2.6) and fitting the data using the structural model determined in space group P2/c; atomic positions were not refined. The cell parameters are shown in Figure 4.30.

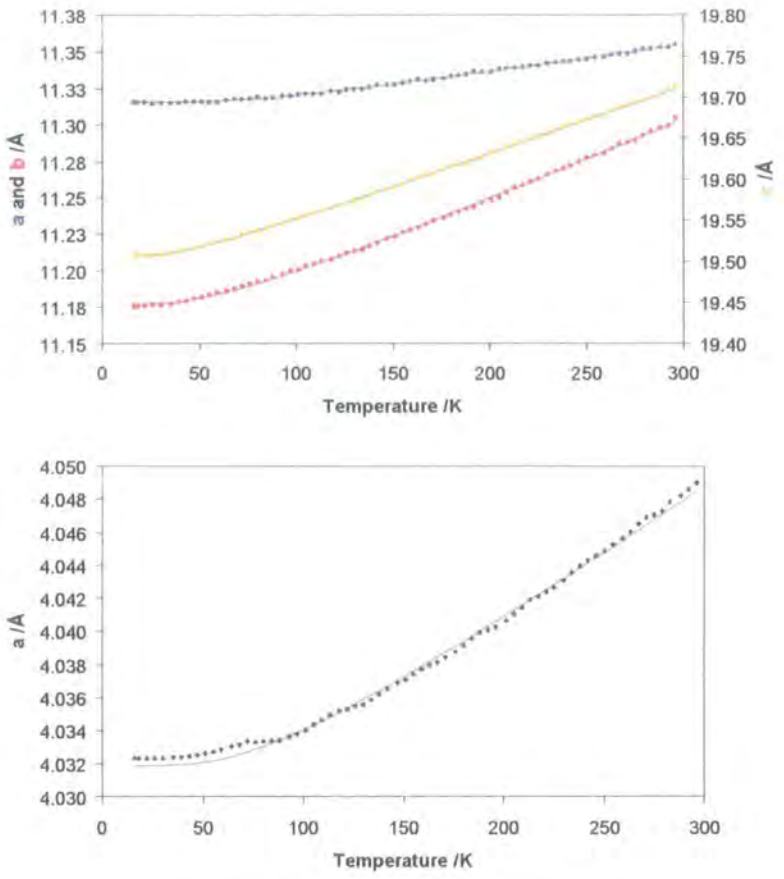

Figure 4.30 The variation of cell parameters for PPh_4CuWSe_4 (top) and Al (bottom) with varying temperature. The *a* cell parameter is shown in blue, *b* in red and *c* in yellow, the Al cell parameter is shown in black. Grey lines show values calculated from the Reeber equation.

All of the cell parameters show smooth expansion of the material from 16 K up to 300 K, indicating that there are no phase transitions in the sample over this temperature range. The scatter in the aluminium cell parameters is due to the fact that only 3 peaks in the aluminium powder pattern were collected, severely limiting the accuracy of the cell parameters that are determined. The expansion of each cell parameter has been fitted to the Reeber equation (4.2) using a least squares fitting procedure. The value of a_0 for the aluminium cell parameter was 4.03190 (4) Å, the expansion parameters for PPh_4CuWSe_4 are given in Table 4.21.

	a	*b*	*c*
a_0 /Å	11.3154 (2)	11.1774 (4)	19.5069 (4)
θ_1 /K	255 (6)	160 (4)	112 (2)
c_1 /K^{-1}	17.4 (2) × 10^{-6}	49.3 (4) × 10^{-6}	42.6 (2) × 10^{-6}
$\alpha_{15K\text{-}300K}$ /K^{-1}	12.3 (2) × 10^{-6}	39.6 (4) × 10^{-6}	37.2 (2) × 10^{-6}

Table 4.21 Thermal expansion parameters for PPh_4CuWSe_4.

The values of these parameters show that the expansion in the direction of the *a* axis is less than the expansion in the *b* and *c* directions. Expansion along the direction of the chains would be expected to be more difficult than expansion in other directions as there is continuous bonding in the chain direction; interactions are weaker in other directions.

4.8 Summary

Several new materials have been synthesised using a solvothermal synthesis route. These materials fall into two groups, the majority have the general formula Cu_2MX_4 and are all layered materials consisting of layers of edge linked copper and MX_4 tetrahedra. PPh_4CuWSe_4 is a material consisting of chains of edge sharing copper selenide and tungsten selenide tetrahedra, the chains are separated by PPh_4^+ cations. The structures of all the materials have been solved and refined using powder diffraction data.

The chemistry of Cu_2MX_4 materials varies according to the nature of M. The molybdenum containing materials can only be synthesised using mild reaction conditions (low temperature and pressure); otherwise the MoX_4^{2-} units decay before reacting to form crystalline products. The tungsten containing materials can be synthesised over a larger temperature range. There are two structural forms of the materials, one with primitive lattice centring and one with a body centred lattice. The tungsten containing materials and the molybdenum sulfide material can adopt either structural form, the molybdenum selenide has only been observed in the primitive form. The relative amount of the different phases is dependent on both reaction temperature and reaction time, formation of the body centred material being favoured by long reaction times and high temperatures. Variable temperature diffraction experiments have been performed on both of the Cu_2WX_4 materials, their expansion behaviour is similar and neither show evidence of phase transitions in the temperature regions studied. Both of the tungsten materials are diamagnetic, and the tungsten selenide is a semiconductor.

The synthesis conditions used to make Cu_2WSe_4 give a delicate balance of stabilities between three materials: *P* and *I* Cu_2WSe_4 and PPh_4CuWSe_4. For the standard reaction time of 48 hours, a large amount of PPh_4CuWSe_4 is produced only in a small temperature range between 185 and 190 °C. This balance of stabilities has been shown to be time as well as temperature dependent; at 190 °C longer reaction times favour production of *I* Cu_2WSe_4.

4.9 References

1. E. A. Pruss, B. S. Snyder and A. M. Stacy, *Angew. Chem. Int. Ed. Engl.*, 1993, **32**, 256-257.
2. *Powder Diffraction File, International Centre for Diffraction Data, Pennsylvania*, 1998.
3. A. A. Coelho, *TOPAS v3.0 General Profile and Structure Analysis Software for Powder diffraction data, Bruker AXS, Karlsruhe*, 2004.
4. J. W. Visser, *J. Appl. Cryst.*, 1969, **2**, 89-95.
5. J. S. O. Evans, *multivisser - A Fortran Routine for controlling Visser*, 2001.
6. G. S. Pawley, *J. Appl. Cryst.*, 1981, **14**, 357-361.
7. A. Altomare, M. C. Burla, G. Cascarano, et al., *J. Appl. Cryst.*, 1995, **28**, 842-846.
8. A. Altomare, G. Cascarano, C. Giacovazzo, et al., *J. Appl. Cryst.*, 1994, **27**, 435-436.
9. H. M. Rietveld, *J. Appl. Cryst.*, 1969, **2**, 65-71.
10. E. O. Schlemper and W. C. Hamilton, *J. Chem. Phys.*, 1966, **44**, 4498-4509.
11. A. Müller, E. Diemann, R. Jostes, et al., *Angew. Chem. Int. Ed. Engl.*, 1981, **20**, 934-955.
12. P. J. Hickey, *M. Chem. Thesis*, University of Durham, 2004.
13. F. H. Allen and O. Kennard, *Chem. Des. Autom. News*, 1993, **8**, 31.
14. NIST Specification Certificate for Silicon (SRM640c), https://srmors.nist.gov/view_cert.cfm?srm=640C.
15. J. S. O. Evans, *phenixlogfile - a Fortran routine for extracting average temperatures from PheniX logfiles*, 2000.
16. K. Wang and R. R. Reeber, *Appl. Phys. Lett.*, 2000, **76**, 2203-2204.
17. K. Wang and R. R. Reeber, *Philos. Mag. A*, 2000, **80**, 1629-1643.
18. R. D. Shannon, *Acta Cryst.*, 1976, **A32**, 751-767.
19. A. K. Cheetham and P. Day, Solid State Chemistry Techniques, Oxford Science Publications, 1987.
20. K. Yamamoto and S. Kashida, *J. Solid State Chem.*, 1991, **93**, 202-211.
21. W. P. Binnie, M. J. Redman and W. J. Mallio, *Inorg. Chem.*, 1970, **9**, 1449-1452.
22. A. Müller and R. Menge, *Z. Anorg. Allg. Chem.*, 1972, **393**, 259-265.
23. A. A. Coelho, *J. Appl. Cryst.*, 2003, **36**, 86-95.
24. A. Müller, N. Mohan and H. Bogge, *Z. Naturforsch., B: Anorg. Chem. Org. Chem.*, 1978, **33**, 978-982.
25. A. L. Spek, *J. Appl. Cryst.*, 2003, **36**, 7-13.

5 $(PPh_4)_2M(WS_4)_2$ materials

Tetraphenylphosphonium-bis-tetrathiotungstatometalates were first synthesised by Müller in the early 1970's. They contain $M(WS_4)_2^{2-}$ units which consist of a transition metal centre bound to two tungsten sulfide tetrahedra. This makes them possible precursors for synthesis of transition metal containing Cu_2MX_4 type materials. Although materials of this type were not successfully made, the structural chemistry of the $(PPh_4)_2M(WS_4)_2$ materials is interesting and has been studied in some detail using both powder and single crystal diffraction methods, this is described in this chapter.

5.1 Synthesis

$(PPh_4)_2M(WS_4)_2$ (M = Ni, Fe, Co, Zn) materials were first synthesised[1] by a combination of aqueous solutions of ammonium tetrathiotungstate, $(NH_4)_2WS_4$, tetraphenylphosphonium chloride, PPh_4Cl, and simple metal (II) salts ($NiCl_2$, $FeSO_4$, $Co(NO_3)_2$ or $ZnSO_4$). However, attempts to replicate this synthesis and make the cobalt, nickel and zinc containing materials were unsuccessful, producing only brown, amorphous powders. An improved method of making ammonium salts of $[Ni(WS_4)_2]^{2-}$ was reported by Callahan,[2] this used mixtures of acetonitrile and water as solvents, and it was this solvent mixture that was used to make the complexes studied here.

Complexes were prepared by mixing solutions of M(II) salts (M = Ni, Co, Zn) and $(NH_4)_2WS_4$, all manipulations were carried out under an inert atmosphere. The solid starting reagents were dissolved in 1:1 solvent mixtures of water and acetonitrile, slightly acidified by the addition of a few drops of acetic acid. The acid is particularly important in the case of the nickel, because it prevents formation of NiS. This was followed by the addition of a solution of PPh_4Cl, also in a 1:1 mixture of H_2O and CH_3CN, which resulted in the rapid precipitation of the powdered products. The nickel salt was pale brown, the cobalt salt green and the zinc salt bright orange. Full synthetic details are given in section 2.10.

The materials were initially characterised by X-ray powder diffraction. The crystal structures of both the cobalt and zinc salts have been previously reported[3,4] and the powder patterns of the materials formed were compared to those of the reported structures. The structure of the cobalt salt was the same as that previously determined, the zinc compound had a different structure to that reported and the structure of the nickel salt has never been determined. The structures of the as-prepared zinc and nickel salts were therefore investigated further using powder diffraction. As well as this, single crystals of the zinc compound were obtained and single crystal diffraction methods were also used to investigate the structure. The structural characterisation of both the zinc and the nickel materials is discussed in the remainder of this chapter.

5.2 $(PPh_4)_2Zn(WS_4)_2$

The structure of $(PPh_4)_2Zn(WS_4)_2$ has previously been determined using single crystal diffraction,[4] the cell was reported as being tetragonal with a = 13.292 Å, c = 6.890 Å. In order to compare this to the material that we had synthesised, attempts were made to fit this unit cell to the powder diffraction data. However, these attempts were unsuccessful, suggesting that the material was a new polymorph of $(PPh_4)_2Zn(WS_4)_2$. In order to further investigate this observation, powder data were examined more closely and single crystals were grown in order to investigate the structure using single crystal diffraction methods. This work revealed that there are actually two different polymorphs of $(PPh_4)_2Zn(WS_4)_2$.

5.2.1 Determination of the structure of $(PPh_4)_2Zn(WS_4)_2$ from single crystal data

Single crystals of $(PPh_4)_2Zn(WS_4)_2$ were grown from a solution of the powdered compound in DMF, ethanol was layered onto this solution and the two liquids were allowed to diffuse together at 4 °C over a few days. This resulted in the production of orange needle shaped crystals. Although many of the crystals produced by this method were of poor quality, a few gave diffraction data of a sufficient quality for structural analysis.

Data were collected using a Bruker AXS SMART 6000 diffractometer with a CCD detector, on a crystal of dimensions 0.08 × 0.08 × 0.3 mm. Two full spheres of data were collected with a frame width of 0.3 ° and a counting time of 10 s per frame. Frames were integrated using the program SAINT.[5] The most intense reflections could be indexed using a tetragonal unit cell of dimensions $a = b$ =13.2295 Å, c = 6.7770 Å. However, there were a significant number of additional diffraction spots which were not indexed by this unit cell, if these were included the data required a tetragonal supercell of dimensions $a = b$ = 18.722 Å, c = 13.564 Å *i.e.* $a_{sup} \sim \sqrt{2}a_{sub}$, $c_{sup} \sim 2c_{sub}$. A multiscan absorption correction[6] was applied to the raw data and the resulting R_{int} was 1.9 % for the subcell and 3.0 % for the supercell reflections.

The diffraction data showed an interesting feature. All frames showed some diffraction spots which were clear and well defined while other spots showed significant streaking, a sign of disorder within the crystal structure. Closer inspection shows that all of the well defined spots can be indexed as subcell reflections, while the reflections which show streaking are indexed only to the supercell. A representative frame, with *hkl* overlays showing subcell and supercell reflections, is shown in Figure 5.1.

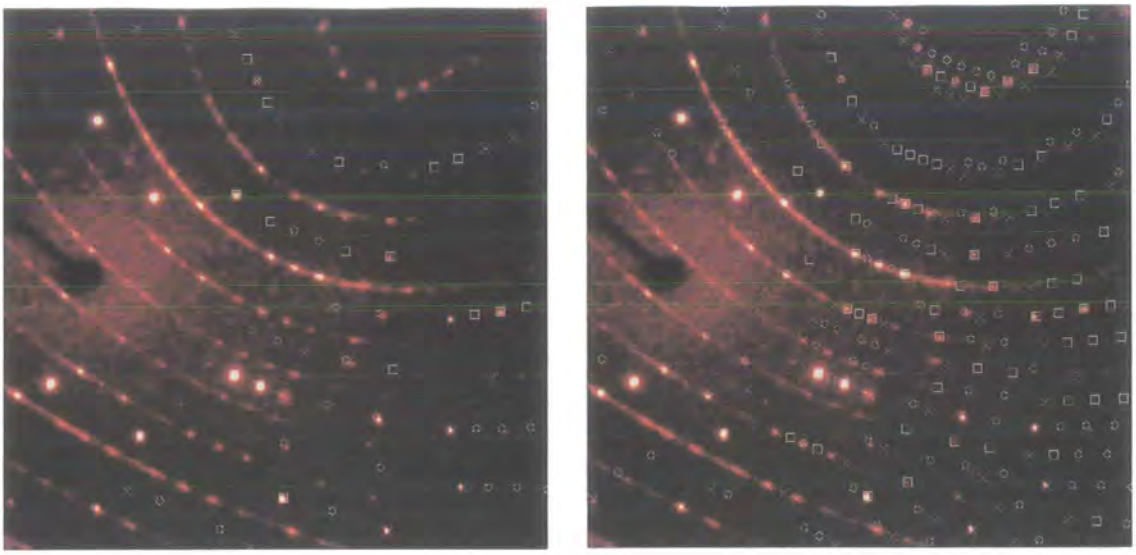

Figure 5.1 Diffraction data for crystals of $(PPh_4)_2Zn(WS_4)_2$ with predicted reflections for the subcell (left) and supercell (right) overlaid. Predicted reflections are shown by crosses for reflections centred on this particular frame, squares for reflections centred a few frames before this one and circles for reflections centred a few frames after this one.

These observations concur with those made by the authors of the paper in which the structure of $(PPh_4)_2Zn(WS_4)_2$ was first reported.[4] Although the structure of this tetragonal polymorph has already been determined, only a general description of the superstructure was given; no atomic coordinates or other structural data (except the cell parameters) were published. Full structure solution was attempted in order to see if any improvement could be obtained on the reported model, particularly for the superstructure, and any further insight could be gained into the structural chemistry of this material.

The substructure was solved using direct methods (SIR92[7]) and refined using the crystals software.[8] Hydrogen atoms were placed geometrically and treated using the riding model. An optimum weighting scheme was applied in the form of a 3rd order Chebychev polynomial.[9] The cif file is included in the e-appendix, selected refinement details are summarised in Table 5.1.

Chemical Formula	$[P(C_6H_5)_4]_2Zn(WS_4)_2$	T	120 K
Molecular Weight	1368.38 a.m.u.	Calculated Density	1.916 gcm^{-3}
Crystal system	Tetragonal	μ	5.793 mm^{-1}
Space group	$I\bar{4}$	Total no. of reflections	20241
a	13.2295(3) Å	No. of unique reflections	1292
b	13.2295(3) Å	No. of observed reflections	1175
c	6.7770(2) Å	No. of refined parameters	83
α	90 °	R_{int}	1.9 %
β	90 °	R	1.76 %
γ	90 °	R_w	3.96 %
V	1186.11(5) $Å^3$		

Table 5.1 Selected structural and refinement details for the substructure of the tetragonal form of $(PPh_4)_2Zn(WS_4)_2$.

The substructure model does not account for all of the structural subtleties in the material, but it does give a good overall picture of the packing arrangement. An ordered view of the structure is shown in Figure 5.2, though it should be noted that the real structure is disordered. Full lists of atomic coordinates, temperature factors and interatomic distances and angles are given in Appendix 5.1.

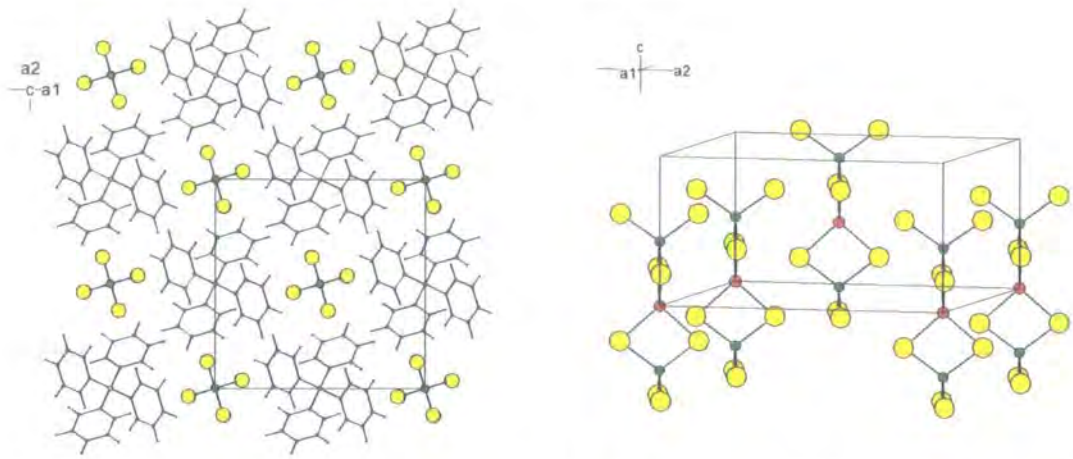

Figure 5.2 An ordered view of the substructure of the tetragonal polymorph of $(PPh_4)_2Zn(WS_4)_2$, viewed down the *c* axis (left) and perpendicular to the *c* axis (right) with the cations omitted. Note that only half of the anion sites are shown. W is shown in green, Zn in red, S in yellow, P in orange, C in blue and H in grey.

The structure contains isolated $Zn(WS_4)_2^{2-}$ units, which are made up of three edge linked tetrahedra with the zinc atom in the central position. These units lie along the $\bar{4}$ axes which run parallel to *c*, with the W – Zn – W vector directly along this direction. Anions are offset in the *c* direction relative to their nearest neighbours, presumably to minimise electrostatic interactions between anionic groups. The anion units are

interspaced by PPh_4^+ cations. Although only half of the anions are shown in the ordered view of the structure in Figure 5.2, the anion units are in fact disordered with a site occupancy of 50 % (as required by symmetry). This gives pseudo-infinite chains of tungsten and zinc sulfide tetrahedra along the *c* axis. The two different cation positions in the pseudo-chains are shown in Figure 5.3

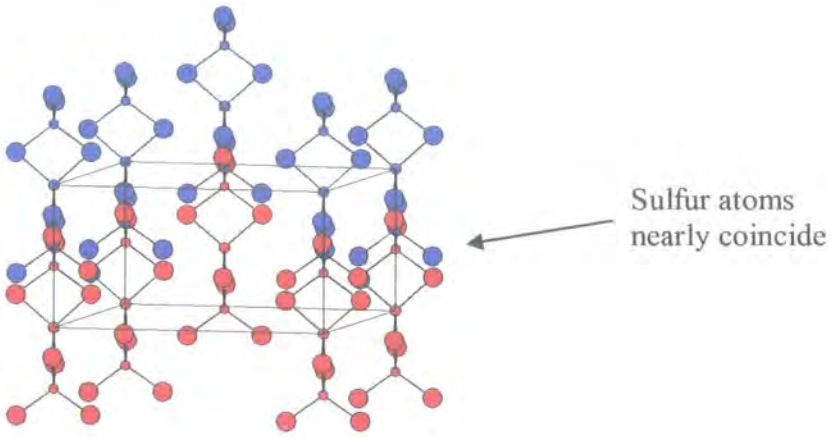

Figure 5.3 Schematic representation of the anion sites in $(PPh_4)_2Zn(WS_4)_2$, the two different sites are shown in red and blue. The cell is orientated as in Figure 5.2.

The origin of the disorder of the anion units may be explained by the fact that the tungsten sites for two adjacent anion positions are only ~1 Å apart in the direction of the *c* axis, the sulfide ion positions for adjacent units are correspondingly close. Either of the two possible anion sites can therefore be occupied, with minimal effect on the arrangement of the sulfur sites and therefore minimal effect on the interdispersed cations. Presumably anions are fully ordered within individual chains but there is little long range correlation in the ordering between adjacent chains.

Bond lengths /Å		Bond angles /°	
Zn1 – S1	2.387 (1)	S1 – Zn1 – S1	116.07 (3)
W1 – S1	2.234 (1)	S1 – Zn1 – S1	96.95 (6)
W1 – S2	2.161 (1)	S1 – W1 – S1	106.20 (7)
P1 – C1	1.791 (3)	S1 – W1 – S2	110.38 (5)
C1 – C2	1.403 (4)	S1 – W1 – S2	110.50 (5)
C1 – C4	1.395 (4)	S2 – W1 – S2	108.88 (8)
C2 – C3	1.385 (4)	C1 – P1 – C1	110.21 (9)
C3 – C5	1.375 (5)	C1 – P1 – C1	107.99 (18)
C4 – C6	1.382 (4)		
C5 – C6	1.402 (5)		

Table 5.2 Selected bond lengths and angles for the substructure of the tetragonal polymorph of $(PPh_4)_2Zn(WS_4)_2$.

Selected bond lengths and angles for the substructure model are given in Table 5.2. Comparison of the Zn – S and W – S bond lengths shows them to be within the range of bond lengths observed for four coordinate metal ions in a sulfide environment. The coordination geometry around the metal centres is a fairly regular tetrahedron for the tungsten centre, but for the zinc centre, there is significant distortion from tetrahedral geometry. This distortion is presumably caused by metal - metal repulsions within the edge shared anion unit. The coordination geometry of the PPh_4 unit does not deviate from that which is expected, C – C and C – P bond lengths are also within acceptable ranges. The substructure model is essentially identical to that previously reported.

The structure subtleties and in particular the streaks of diffuse scatter observed for the tetragonal polymorph of $(PPh_4)_2Zn(WS_4)_2$ were further probed by determining the superstructure. The superstructure was solved using direct methods (SIR92) and refined with the crystals software.[8] An optimum weighting scheme was applied in the form of a 3rd order Chebychev polynomial. During structure solution it became apparent that a number of sites had "shadows" which seemed to indicate the presence of additional symmetry operations (mirror planes) in the unit cell; this is a sign that the crystal was twinned. Twinning of the sort observed here, in which a tetragonal crystal with Laue group 4/m mimics the symmetry of a crystal with Laue group 4/mmm is common. The following twin law was applied:

$$\begin{pmatrix} 0 & 1 & 0 \\ 1 & 0 & 0 \\ 0 & 0 & \bar{1} \end{pmatrix}$$

A parameter was refined to describe the relative proportions of the two twin elements, which were constrained to sum to 1.The phenyl rings in the PPh_4 unit were restrained using soft restraints, to have regular hexagonal geometry and be planar; hydrogen atoms were added geometrically and refined using the riding model. Isotropic temperature factors were refined for all atoms. The cif file for the superstructure is included in the e-appendix along with a full list of interatomic distances and angles, selected refinement data are summarised in Table 5.3. Full details of atomic coordinates and temperature factors are given in Appendix 5.2.

Chemical Formula	$[P(C_6H_5)_4]_2Zn(WS_4)_2$	T	120 K
Molecular Weight	1368.38 a.m.u.	Calculated Density	1.912 gcm^{-3}
Crystal system	Tetragonal	μ	5.781 mm^{-1}
Space group	$I\bar{4}$	Total no. of reflections	82669
a	18.723 (4) Å	No. of unique reflections	4564
b	18.723 (4) Å	No. of observed reflections	2471
c	13.563 (4) Å	No. of refined parameters	142
α	90 °	R_{int}	3.0 %
β	90 °	R	4.97 %
γ	90 °	R_w	5.94 %
V	4754 (2) $Å^3$	Twin element parameter	24.5 (5) %

Table 5.3 Selected structural and refinement details for the superstructure of the tetragonal form of $(PPh_4)_2Zn(WS_4)_2$.

The superstructure model is broadly similar to the substructure and is also disordered. However, the nature of this disorder is not quite as simple as that found for the substructure model. Within the superstructure there are two crystallographically independent chains running along the direction of the *c* axis. Both of these chains display disorder similar to that found in the substructure, this is shown for an individual chain in Figure 5.4.

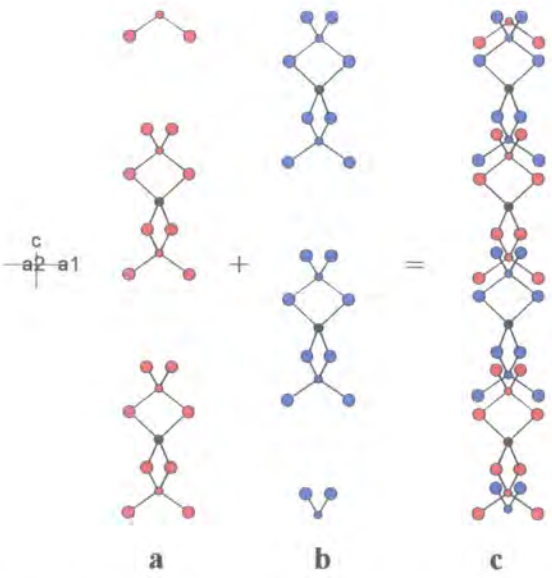

Figure 5.4 Disordered chain in the superstructure of the tetragonal form of $(PPh_4)_2Zn(WS_4)_2$ viewed down the *b* axis. Major anion sites are shown in red, minor anion sites in blue. Views a and b are offset in the direction of the *a* axis for clarity.

For each chain there are two possible sites which can be occupied by the anion units. In the substructure model these sites have equal occupancies; in the superstructure sites in

the same chain are occupied in a ratio of ~ 7:3. The anion sites with ~70 % occupancy, referred to as major sites, are shown in red in Figure 5.4. The sites with ~30% occupancy are referred to as minor sites and are shown in blue in Figure 5.4.

Disorder of the $Zn(WS_4)_2^{2-}$ units was modelled by refining occupancy parameters to describe the relative occupancies of major and minor sites in the two crystallographically independent chains. Constraints were used to keep the overall contents of the unit cell correct. Site occupancies for all the sites in each of the major units were constrained to be the same, as were the occupancies of all sites in each of the minor units. The occupancy of sites in the major and minor units in the same chain was also constrained to sum to 1. The refined occupancies for different sites in the two crystallographically independent chains are summarised in Table 5.4.

	Chain 1 $x = 0, y = 0$	Chain 2 $x = 0.5, y = 0$
Occupancy major sites /%	64.212 (3)	77.202 (3)
Occupancy minor sites /%	35.788 (3)	22.798 (3)

Table 5.4 Occupancies for major and minor sites within the anionic chains in the superstructure of the tetragonal form of $(PPh_4)_2Zn(WS_4)_2$.

The refined major/minor site occupancies are similar but not identical in the two crystallographically independent chains. It is this disorder that presumably gives rise to the lines of diffuse intensity observed in Figure 5.1. Within a given chain there will be complete anion order, whereas in a crystallographically related adjacent chain there is a ~30 % chance that a stacking fault occurs and the chain adopts the 'alternate' position. The refined occupancies suggest that the coherent length of order between adjacent chains is extremely small, leading to the observed diffuse scatter.

The origin of the superstructure in this material is the non random occupation of the anion sites. Comparison of the atomic positions in the substructure and superstructure shows that there is very little displacement of atoms between the two models. The characterisation of the exact nature of the disorder in this material is a significant improvement on the superstructure model previously reported.

5.2.2 Determination of the structure of $(PPh_4)_2Zn(WS_4)_2$ from powder data

Powder diffraction data collected on a polycrystalline sample of $(PPh_4)_2Zn(WS_4)_2$ could not be fitted using the tetragonal unit cell used for the single crystal data, showing that a polycrystalline sample's structure was different from that of the single crystals. Comparison with the powder pattern of $(PPh_4)_2Co(WS_4)_2$ showed that the two materials

had very similar powder patterns and suggested not only that it may be possible to fit the data using a monoclinic cell (cell parameters for Co containing species $a = 18.542$ Å, $b = 15.443$ Å, $c = 18.713$ Å, $\beta = 108.73$ °) but also that the two compounds may be isostructural. Attempts to fit the powder pattern using a Pawley fit and the cell parameters reported for the monoclinic cobalt species were successful; full structural modelling of this new monoclinic polymorph of $(PPh_4)_2Zn(WS_4)_2$ was therefore attempted by Rietveld refinement using the structure of $(PPh_4)_2Co(WS_4)_2$ as the starting point.

Data were collected using a Bruker d8 Advance diffractometer operating in flat plate mode and using 0.5 ° divergence slits. The sample was prepared by sieving the powder onto a silicon wafer coated with Vaseline as an adhesive. Data were collected over a 2θ range of 4.5 to 70 °, with a step size of 0.0144 ° and a time per step of 4.5 s. The measurement was repeated a total of 20 times and data from all scans summed.

In final cycles of refinement a total of 97 parameters were refined, these included 12 coefficients of a Chebychev polynomial to describe the background, sample displacement, an axial model parameter to describe peak asymmetry, a scale factor, 6 peak shape parameters, 15 coefficients of a spherical harmonic function to describe preferred orientation, 4 cell parameters, 33 coordinates of atoms in the anion, and 4 temperature factors. The PPh_4 units were modelled as rigid bodies with P – C distances of 1.79 Å, C – C distances of 1.39 Å and C – H distances of 0.998 Å. 6 parameters were refined to describe the rotations and translations of these units relative to the x, y and z axes, 4 torsion angles were also refined for each unit to describe the rotation of the phenyl rings around the P – C bonds. The TOPAS input file for this refinement is included in the e-appendix.

Refinement and data collection details are summarised in Table 5.5, the final Rietveld refinement is shown in Figure 5.5.

Space Group	$P2_1/c$	2θ range	4.5 – 70 °
a	18.6397 (4) Å	2θ step	0.0144 °
b	15.3693 (5) Å	Time per step	90 s
c	18.9822 (5) Å	$_wR_p$	6.38 %
β	109.239 (2) °	R_{Bragg}	1.72 %
No. of refined parameters	97	χ^2	10.55

Table 5.5 Selected crystallographic, data collection and refinement details for the monoclinic polymorph of $(PPh_4)_2Zn(WS_4)_2$.

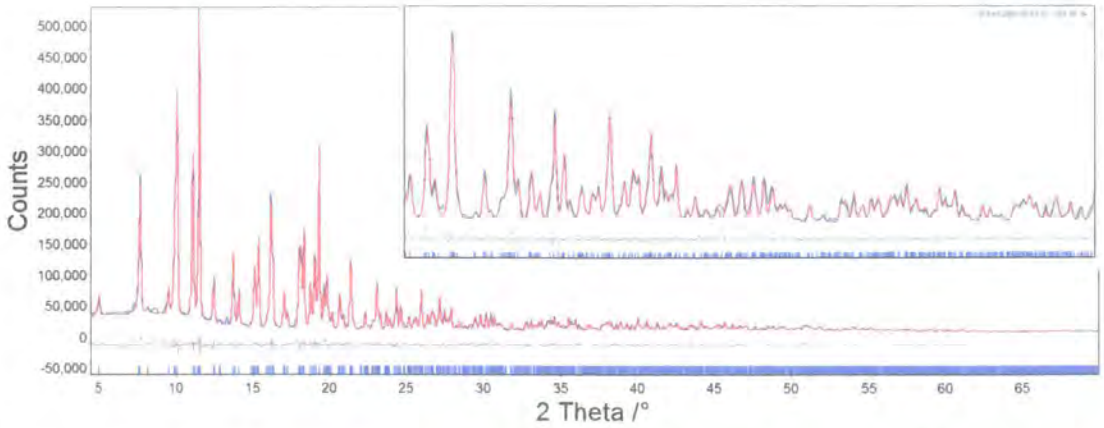

Figure 5.5 Rietveld refinement of monoclinic form of $(PPh_4)_2Zn(WS_4)_2$. Observed data are shown in blue, calculated in red and difference in grey. The inset shows a close up of the region between 20 and 40 ° 2*θ*.

Selected atomic coordinates are given in Table 5.6 and parameters describing the rotation of the rigid PPh_4 units about the axes and the torsion angles which define the position of the rings are given in Table 5.7. A full list of atomic coordinates including all the carbon and hydrogen atoms can be found in Appendix 5.3.

Atom	*x/a*	*y/b*	*z/c*	U_{iso} /Å^2
W1	0.1830 (3)	0.0195 (4)	−0.0784 (4)	0.125 (3)
W2	0.2612 (3)	0.3761 (5)	0.0079 (4)	0.125 (3)
Zn1	0.2214 (7)	0.194 (1)	−0.0312 (8)	0.084 (6)
S1	0.286 (1)	0.078 (2)	−0.047 (1)	0.168 (5)
S2	0.168 (1)	−0.030 (2)	−0.190 (2)	0.168 (5)
S3	0.179 (1)	−0.087 (2)	−0.013 (2)	0.168 (5)
S4	0.106 (1)	0.127 (2)	−0.065 (1)	0.168 (5)
S5	0.253 (2)	0.277 (2)	0.083 (2)	0.168 (5)
S6	0.239 (2)	0.320 (2)	−0.100 (2)	0.168 (5)
S7	0.191 (1)	0.459 (2)	0.018 (2)	0.168 (5)
S8	0.382 (1)	0.430 (2)	0.054 (2)	0.168 (5)
P1	0.8851 (5)	0.327 (1)	0.2266 (6)	0.112 (5)
P2	0.5391 (5)	0.092 (1)	0.2111 (6)	0.112 (5)

Table 5.6 Selected fractional atomic coordinates and isotropic temperature factors for the monoclinic polymorph of $(PPh_4)_2Zn(WS_4)_2$.

	Cation 1	Cation 2
x_{rot} /°	−94.4 (3)	−234.9 (4)
y_{rot} /°	145.9 (2)	−76.5 (2)
z_{rot} /°	−180.1 (2)	27.4 (4)
torsion 1 /°	73 (1)	−67 (1)
torsion 2 /°	−19 (1)	21 (1)
torsion 3 /°	−21 (1)	79 (1)
torsion 4 /°	83 (1)	13 (1)

Table 5.7 Angles of rotation about the axis and torsion angles in the two crystallographically independent PPh_4 units in monoclinic $(PPh_4)_2Zn(WS_4)_2$.

The structure consists of isolated $Zn(WS_4)_2^{2-}$ units, the central zinc atoms are stacked up along the *b* axis, the W – Zn – W vectors are aligned at an angle to this axis. There are two different ways in which units are tilted relative to the *b* axis, with the direction of tilt alternating in adjacent chains. The anionic units are interspaced by the PPh_4^+ cations. The structure is shown in Figure 5.6. Bond distances and angles for the anion units are given in Table 5.8.

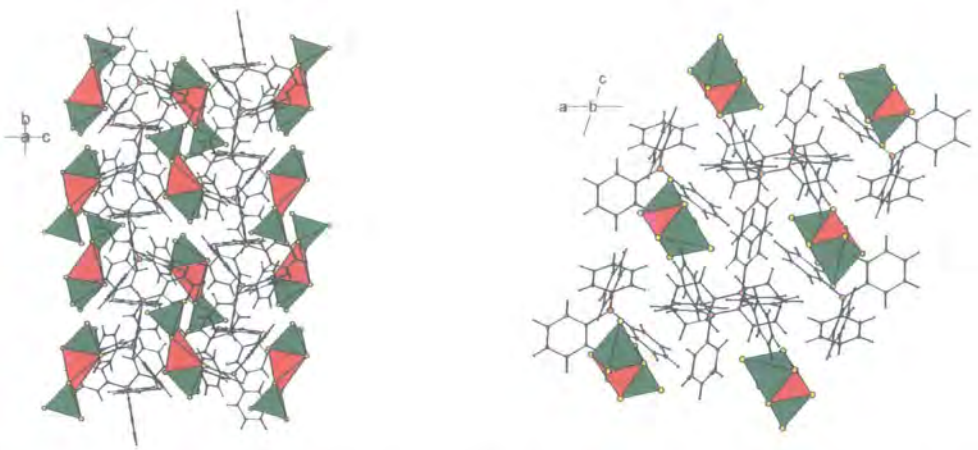

Figure 5.6 The structure of monoclinic $(PPh_4)_2Zn(WS_4)_2$ viewed down the *a* axis (left) and down the *b* axis (right). W tetrahedra are shown in green, Zn tetrahedra in red, P in orange, C in blue and H in grey.

Bond lengths /Å		Bond Angles /°	
Zn – S	2.22 (4)	S – Zn – S	91 (1)
	2.28 (3)		96 (1)
	2.42 (4)		113(1)
	2.43 (4)		115 (1)
			120 (1)
			124 (1)
W1 – S	2.03 (3)	S – W1 – S	102 (1)
	2.08 (4)		104 (1)
	2.17 (3)		106 (1)
	2.26 (3)		111 (1)
			113 (1)
			119 (1)
W2 – S	1.89 (3)	S – W2 – S	102 (1)
	2.13 (4)		106 (1)
	2.14(4)		109 (1)
	2.29 (3)		111 (1)
			111 (9)
			117 (1)

Table 5.8 Bond lengths and angles in the anion in monoclinic $(PPh_4)_2Zn(WS_4)_2$.

The range of bond lengths reported here and the large esd's associated with them, suggest that there are small inaccuracies in the refined model. For example W – S bond lengths below 2.13 Å are rarely observed in four coordinate tungsten polyhedra in crystal structures reported in the CSD.[10] This suggests that the bond length of 1.90 Å in particular is somewhat unreasonable. However a similar comparison of the Zn – S bond lengths shows they are all within the range of bond lengths found for 4 coordinate zinc atoms. In general the Zn – S bonds are longer than the W – S bonds and that the coordination geometry around the zinc atom is significantly more distorted than in the tungsten tetrahedra. This is similar to the behaviour seen in the tetragonal polymorph discussed in section 5.2.1. Despite the slightly unrealistic bond lengths, these data show definitively that a second, monoclinic polymorph of $(PPh_4)_2Zn(WS_4)_2$ exists and that its structure is closely related to that of the cobalt analogue already reported.

5.2.3 Variable temperature diffraction studies

The structure of the monoclinic polymorph of $(PPh_4)_2Zn(WS_4)_2$ was further probed using a variable temperature diffraction experiment. The sample was cooled from room temperature down to 16 K in order to see if there were any phase transitions in the sample.

Data were collected using a Bruker d8 Advance diffractometer fitted with the PheniX ccr cooling device and 1 ° divergence slits. A sample was prepared by sprinkling the powder onto an aluminium sample holder coated with Vaseline. The sample was cooled at a rate of 17 K/hr and during cooling data were collected over a 2θ range of 4.5 to 70 °, using a step size of 0.0144 °and a time per step of 0.35 s. This gives a scan time of ~30 minutes, a total of 33 scans were collected on cooling, with temperature steps of ~8 K. Cell parameters were determined using *multitopas* methodology (section 2.6), a Pawley fit was used to fit the two aluminium peaks and a full structural fit was used for the $(PPh_4)_2Zn(WS_4)_2$; atomic coordinates were not refined. The cell parameters for aluminium could not be accurately determined as only two peaks from the aluminium powder pattern were measured. The change of cell volume with temperature is shown in Figure 5.7.

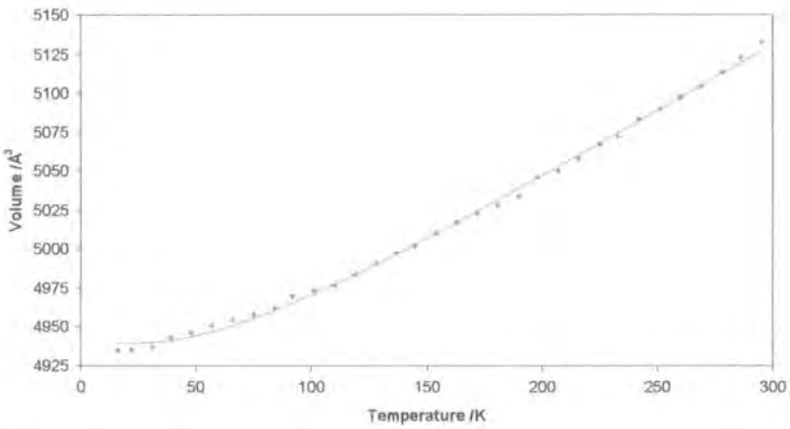

Figure 5.7 The variation in cell volume with temperature in monoclinic $(PPh_4)_2Zn(WS_4)_2$. Observed data are shown in green and values calculated using the Reeber equation are shown by the grey line.

The data show a smooth variation in the cell volume (within the bounds of experimental error) over the temperature range studied. This suggests that there are no phase transitions in the sample. The individual cell parameters show similar behaviour and their expansion was fitted using the Reeber equation (4.2) and a least squares fitting procedure in TOPAS. The values obtained for the parameters in the Reeber equation are given in Table 5.9.

	a	*b*	*c*
a_0 /Å	18.4096 (1)	15.077 (3)	18.871 (2)
θ_1 /K	174 (8)	258 (15)	77 (17)
c_1 /K^{-1}	56.5 (8) × 10^{-6}	98 (3) × 10^{-6}	22.6 (5) × 10^{-6}
$\alpha_{15K\text{-}300K}$ /K^{-1}	44 (1) × 10^{-6}	66 (3) × 10^{-6}	21.0 (9) × 10^{-6}

Table 5.9 Thermal expansion parameters for the monoclinic form of $(PPh_4)_2Zn(WS_4)_2$.

The data suggest that expansion is larger in the direction of the *b* axis and least significant in the direction of the *a* axis. As this is a molecular solid, these differences reflect differences in the way the molecules move apart as well as changes in bond lengths on expansion.

5.3 $(PPh_4)_2Ni(WS_4)_2$

Although the structure of many of the $(PPh_4)_2M(WS_4)_2$ materials have already been reported, the structure of the nickel containing compound has remained unknown, this is despite a number of investigations to provide indirect evidence of the speculated square planar nature of nickel. The crystallinity of a powdered sample of this complex was however of sufficient quality to attempt full structural solution from powder data. X-ray diffraction data were collected using a Bruker d8 Advance diffractometer. The sample was prepared by sprinkling powder onto a Vaseline coated silicon wafer; data were collected using v6 variable divergence slits, over a 2θ range of 5 to 70 ° using a step size of 0.0144 ° and time per step of 4.5 s. This was repeated 6 times and data from all scans were summed. The data were indexed using the SVD indexing function[11] in TOPAS (section 2.3); when selecting peaks from the pattern care was taken to ensure as far as possible that the peaks selected were single peaks and not overlapping combinations of two peaks. This was particularly important in this case due to the complexity of the pattern. This gave a triclinic cell with cell parameters of:

$a = 9.377$ Å $\quad b = 12.502$ Å $\quad c = 12.538$ Å

$\alpha = 65.85$ ° $\quad \beta = 83.71$ ° $\quad \gamma = 69.61$ ° $\quad FOM_{TOPAS} = 15.43$

Using these cell parameters an excellent Pawley fit to the data ($_wR_p$ 3.54 %) could be obtained, fitting all but two small peaks at ~ 7.5 and 9.5 ° 2θ . These peaks are believed to be an impurity phase, which could not be identified. For triclinic systems there are only two choices of space group; structure solution was initially attempted using the lower symmetry space group, P1.

Structure solution was performed using a simulated annealing protocol in TOPAS[12] (section 2.4). Comparison of the unit cell volume (~1249 Å^3) to that of the structure of the cobalt compound already reported (V = 5074 Å, four molecules per unit cell) suggests cell contents of one formula unit, *i.e.* two PPh_4^+ cations and one $[Ni(WS_4)_2]^{2-}$ anion. The structure was initially described using three rigid bodies, two for the PPh_4^+ cations and the other for the $[Ni(WS_4)_2]^{2-}$ anion. The PPh_4^+ cations were defined using C – C bond lengths of 1.39 Å, C – H bond lengths of 0.998 Å, P – C bond lengths of 1.792 Å (the mean bond length for P – C bonds in PPh_4 groups found in structures in the CSD) and idealised tetrahedral geometry around the phosphorus centre. As well as three translational and three rotational parameters to define the position of the rigid bodies,

four torsion angles defining the rotations of the phenyl rings around the P – C bonds were also refined for each unit. It has been previously suggested that the nickel ion in $[Ni(WS_4)_2]^{2-}$ is in a square planar coordination environment, indicated by the diamagnetism of its tetraphenylphosphonium salt.[13] For initial structure solution, this geometry was assumed to be correct and a rigid body was defined consisting of two WS_4 tetrahedra linked via a Ni atom with square planar geometry. W – S and Ni – S distances were fixed at values of 2.240 Å and 2.296 Å respectively; these values were calculated using bond valence considerations. The Ni atom was fixed at the cell origin (P1 has a floating origin in *x*, *y* and *z*) and the rotation of the rigid body around this point was annealed. On each cycle of annealing, the coordinates of the phosphorus atoms were moved by up to ± 5 Å in each direction, and the rotations of the rigid bodies were given random values between 0 and 180 °, torsion angles were given random values up to ± 30 ° from their values at the end of the previous cycle. A single overall temperature factor was refined; this was given a value of 0.01 $Å^2$ at the beginning of each cycle of annealing. Parameters describing the background, sample displacement and a simple axial model to model peak asymmetry were fixed at values determined from the Pawley fit, whilst cell parameters were allowed to refine during annealing. The structure solution process used data in the range 5 to 40 ° 2θ and was run for 200 000 cycles, the global minimum was found after ~2000 cycles and was found again approximately once every 3500 cycles, suggesting that this was the true global minimum for the solution process. The best solution found by this annealing process had a $_wR_p$ value of 6.81 %.

Inspection showed that the initial solution determined in space group P1 was very close to having a centre of inversion, so subsequent annealing and refinement was performed in space group $P\bar{1}$ as well as P1. The model determined from initial structure solution was annealed further in both space groups, subject to the following restraints. The positions of the atoms in the anions were refined, subject to bond length restraints; weighting was used to favour solutions with bond lengths of ~2.240 Å and ~2.296 Å for the W – S and Ni – S bond lengths respectively. The bond angles around the tungsten atoms were also restrained to be ~ 109.47 °. The bond angles around the nickel were not restrained, so that the geometry around the nickel atoms could change if the assumption of square planar geometry was wrong. The positions of the phosphorus atoms were fixed at the values determined from the initial solution and the orientation of the units and torsion angles were annealed.

The trial solutions obtained by this process were further refined to obtain the final structures. Coordinates of the W and S atoms were freely refined, without any bond length restraints, the PPh_4 units were modelled as rigid units throughout. The final R-factors obtained are given in Table 5.10.

	$P\bar{1}$	P1
$_wR_p$	4.44 %	4.09 %
R_{Bragg}	2.54%	1.93 %
χ^2	2.52	2.32
No. of refined parameters	60	85
No. of structural parameters	27	52

Table 5.10 R-factors for $[PPh_4]_2Ni(WS_4)_2$ structure solutions determined in space groups $P\bar{1}$ and P1.

The structures determined in each space group are shown schematically in Figure 5.8 for comparison and the Rietveld plots for the two solutions are shown in Figure 5.9.

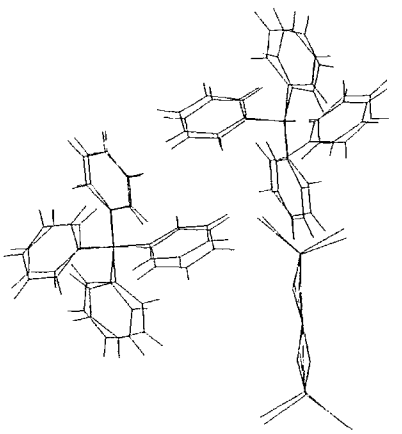

Figure 5.8 Skeletal representations of structure of $(PPh_4)_2Ni(WS_4)_2$ determined in space groups P1 (blue) and $P\bar{1}$ (red). In space group $P\bar{1}$ the two PPh_4^+ units and the two WS_4 tetrahedra are related by symmetry.

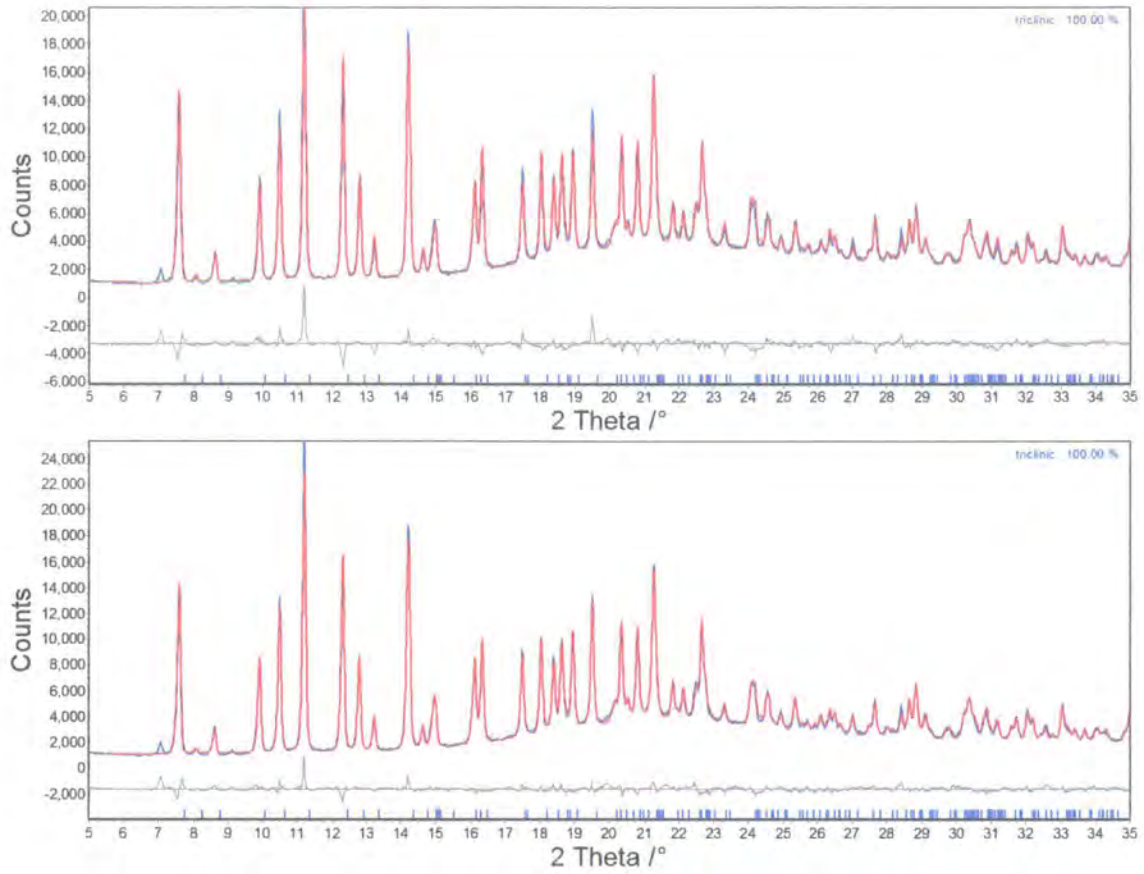

Figure 5.9 Rietveld plots for structure solution of $(PPh_4)_2Ni(WS_4)_2$ in space group $P\bar{1}$ (top) and P1 (bottom), zoomed over the region 5 to 35 ° 2θ. Observed data are shown in blue, calculated values in red and the difference in grey.

The $_wR_p$ for the solution in P1 is lower than that for solution in $P\bar{1}$, but the number of structural parameters refined is nearly double. A visual comparison of the structures shows that they are very nearly identical, the only significant differences being slight variation in the torsion angles describing the orientations of the phenyl rings and the movement of one sulfur atom in the P1 solution, which moves slightly out of the plane defined by the other sulfur atoms making up the nickel coordination environment. Close examination of the Rietveld fits does however reveal a problem. In the fits in both space groups, the maximum difference between calculated and observed data occurs for peaks at ~11.2 and 19.5 ° 2*θ*, these are the *111* and *211* peaks respectively. The higher intensity of the observed data compared to the calculated data suggests that preferred orientation could be a problem in this sample. In order to investigate this, the model was changed to include a correction for this effect, a 4th order preferred orientation spherical harmonic was used. This gives a visual improvement to the fits, the R-factors decrease and there are minor structural changes. The two structures after preferred orientation corrections had been applied are shown in Figure 5.10.

Figure 5.10 Skeletal representations of structures of $(PPh_4)_2Ni(WS_4)_2$ determined in space groups P1 (orange) and $P\bar{1}$ (green), after a preferred orientation correction had been applied to the data.

Although the structural changes on applying a preferred orientation correction are only slight, they are enough to make the P1/$P\bar{1}$ structures even more similar than those determined without the correction. The structural similarities between the two solutions suggest that from the powder data available, the true space group of this structure is $P\bar{1}$. The structure which will be reported is the one determined using a spherical harmonic correction; the reasons for this have already been discussed in section 3.3.2.

In final cycles of refinement a total of 74 parameters were refined. 18 coefficients of a Chebychev polynomial to describe the background, sample displacement, an axial coefficient to describe peak asymmetry, 6 pseudo-Voigt peak shape parameters, 14 coefficients of a spherical harmonic function to describe the preferred orientation, 6 cell parameters, 15 atomic coordinates for the anion, 10 parameters to describe the rigid PPh_4^+ unit and 2 temperature factors, one each for the anion and cation. The TOPAS input file is included in the e-appendix, the final Rietveld refinement and selected structural and refinement details are given in Figure 5.11 and Table 5.11.

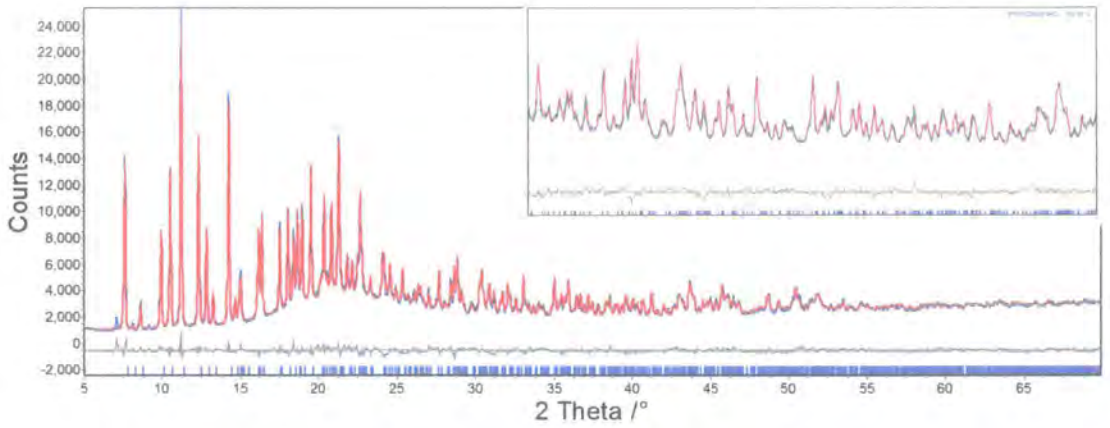

Figure 5.11 Rietveld plot for final structure of $(PPh_4)_2Ni(WS_4)_2$, determined with a spherical harmonic data correction. Observed data are shown in blue, calculated in red and difference in grey, the inset shows the region between 25 and 45 ° 2θ.

Space Group	$P\bar{1}$	2θ range	5 – 70 °
a	9.3730 (2) Å	2θ step	0.0144 °
b	12.4951 (3) Å	Time per step	27 s
c	12.5189 (3) Å	$_wR_p$	3.92 %
α	65.814 (1) °	R_{Bragg}	1.62 %
β	83.751 (1) °	χ^2	2.23
γ	69.571 (1) °	No. of refined parameters	74

Table 5.11 Selected crystallographic, data collection and refinement details for $(PPh_4)_2Ni(WS_4)_2$.

Selected atomic positions are given in Table 5.12, and the torsion angles and rotations about the axes for the rigid PPh_4^+ unit are given in Table 5.13. A full list of fractional atomic coordinates which includes the carbon and hydrogen atoms can be found in Appendix 5.4. Only two temperature factors were refined for the structure, one for atoms in the $Ni(WS_4)_2^{2-}$ unit, one for the atoms in the PPh_4^+ unit.

Atom	*x/a*	*y/b*	*z/c*	U_{iso} /Å^2
Ni	0.0	0.0	0.0	0.129 (1)
W	−0.0953 (4)	0.2609 (3)	−0.1236 (3)	0.129 (1)
S1	−0.227 (2)	0.142 (1)	−0.057 (1)	0.129 (1)
S2	0.135 (2)	0.130 (1)	−0.085 (1)	0.129 (1)
S3	−0.108 (1)	0.355 (1)	−0.021 (1)	0.129 (1)
S4	−0.137 (1)	0.375 (1)	−0.309 (1)	0.129 (1)
P	0.5782 (6)	0.2443 (5)	0.3395 (5)	0.153 (4)

Table 5.12 Fractional atomic coordinates and isotropic temperature factors for atoms in $(PPh_4)_2Ni(WS_4)_2$.

x_{rot} /°	16.0 (2)
y_{rot} /°	26.4 (2)
z_{rot} /°	203.0 (2)
torsion 1 /°	17.1 (8)
torsion 2 /°	−67.7 (7)
torsion 3 /°	18.9 (6)
torsion 4 /°	83.2 (7)

Table 5.13 Torsion angles and rotations about the axes for the rigid PPh_4^+ cation in $(PPh_4)_2Ni(WS_4)_2$.

The structure is made up of isolated $Ni(WS_4)_2$ units, which contain two WS_4 tetrahedra each linked by two sulfide ions to a nickel ion, giving the nickel ion square planar coordination geometry. These isolated units are interspersed by PPh_4^+ cations. Two views of the structure are shown Figure 5.12. The bond lengths and angles for the anionic units are given in Table 5.14.

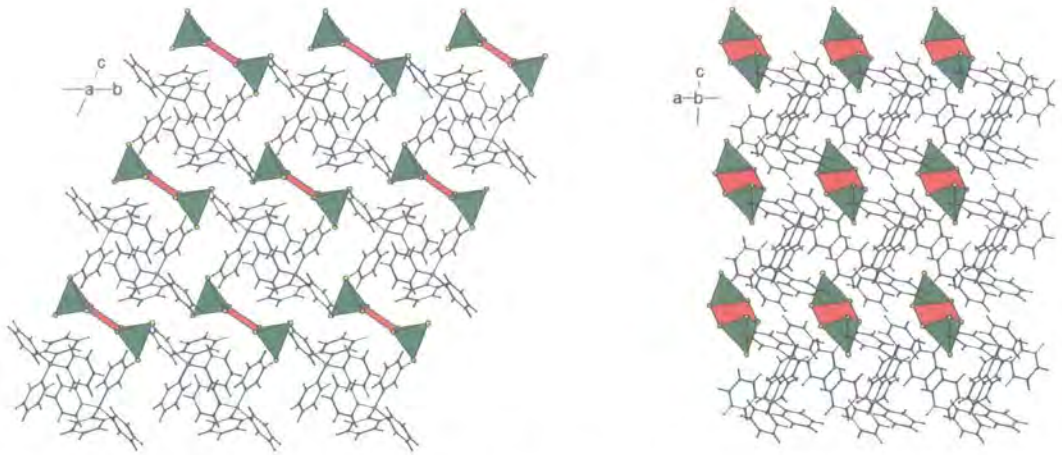

Figure 5.12 The structure of $(PPh_4)_2Ni(WS_4)_2$ viewed down the *a* axis (left) and down the *b* axis (right). W tetrahedra are shown in green, square planar Ni ions in red, S in yellow, P in orange, C in blue and H in grey.

Bond Lengths /Å		Bond Angles /°	
Ni – S	2.12 (1)	S– Ni – S	180
	2.25 (2)		83.4 (4)
			96.6 (4)
W – S	2.03 (2)	S– W – S	102.1 (4)
	2.11 (2)		102.3 (3)
	2.16 (1)		110.8 (4)
	2.17 (1)		111.7 (4)
			113.5 (6)
			115.2 (4)

Table 5.14 Bond lengths and angles in the anionic units in $(PPh_4)_2Ni(WS_4)_2$.

These bond angles show that the coordination geometry around the nickel atom is a slightly distorted square plane, and the geometry around the tungsten centre is a distorted tetrahedron. The Ni – S bond lengths are towards the lower and upper boundaries of the observed range of bond lengths, and the W – S bonds are at the short end of the range of bond lengths observed in similar coordination environments.

The structure of this material is somewhat different to the structures of similar compounds containing different transition metal ions (Mn, Co and Zn). The manganese compound has a tetragonal structure, with disordered anions; the cobalt compound is monoclinic; the zinc compound can adopt both of these structure types. The nickel compound crystallises in a lower symmetry space group than the others and the square planar preference of the Ni^{2+} causes the anion units to be packed in a slightly different way. It is interesting to compare the anion packing in the three different structure types shown by these materials. The different anion arrangements are shown in Figure 5.13.

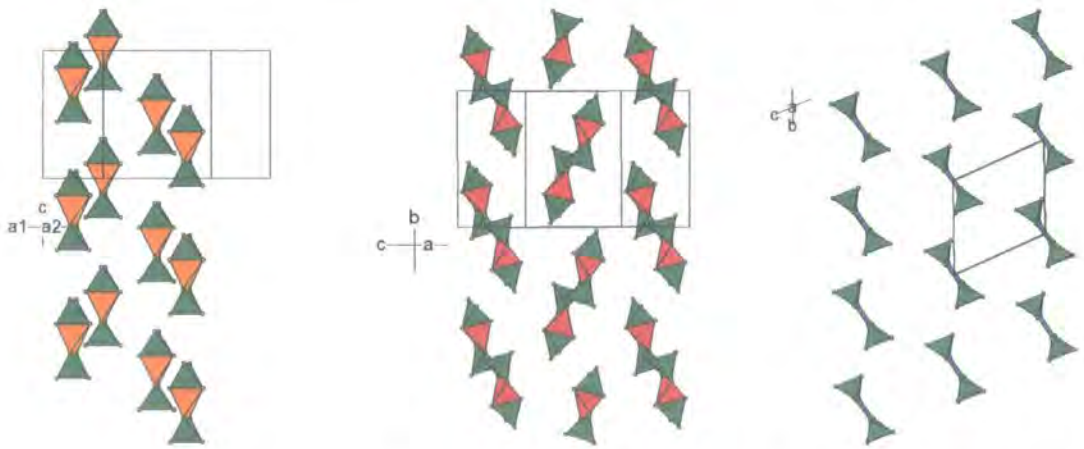

Figure 5.13 Packing of $M(WS_4)_2^{2-}$ units in tetragonal polymorph of $(PPh_4)_2Zn(WS_4)_2$ (left), $(PPh_4)_2Co(WS_4)_2$ (middle) and $(PPh_4)_2Ni(WS_4)_2$ (right). S is shown in yellow, W tetrahedra in green, Zn tetrahedra in orange, Co tetrahedra in red and Ni polyhedra in blue.

The primary differences between the three different structures exhibited by these materials is in the way that the $M(WS_4)_2^{2-}$ units stack up in the direction of the *b* (or *c*) axis, which are shown as vertical in Figure 5.13. For the zinc material (for which an ordered picture is shown, in reality there is anion disorder, as discussed in section 5.2.1), the units are aligned so that the W – M – W vector is along the *c* axis; units are stacked directly above each other in this direction. In the cobalt material the units are arranged in similar stacks, but the W – M – W vector is at an angle to the *b* axis. Units are tilted in one of two directions, in any individual stack they are all tilted the same way, adjacent stacks tilt in different directions. For the nickel material the units are arranged so that the central nickel atoms are stacked along the *b* axis and the W – M – W vectors are tilted with reference to the direction of the *b* axis, in contrast to the cobalt case, all of the units are tilted in the same way. All of the materials show an offset in the positions of the $M(WS_4)_2^{2-}$ units in adjacent stacks in the *a* and *c* (or *a* and *b*) axes. The unit cell volumes per formula unit for different $(PPh_4)_2M(WS_4)_2$ materials are given in Table 5.15.

Metal	Crystal symmetry	Cell volume per $(PPh_4)_2M(WS_4)_2$ unit /Å^3
Mn	Tetragonal	1210
Co	Monoclinic	1269
Ni	Triclinic	1361
Zn	Monoclinic	1368
Zn	Tetragonal	1186

Table 5.15 Summary of cell volumes per formula unit for $(PPh_4)_2M(WS_4)_2$ materials.

Comparison of these unit cell volumes shows that the cell volume per unit formula is slightly higher for the monoclinic form of the zinc containing compound and for the nickel containing material than for the other crystal structures. It is possible that these materials contain disordered solvent molecules in their crystal structures; both of them have been characterised from powder diffraction data, from which it would be very difficult to identify this kind of disorder. The presence of disordered solvent molecules in the powder samples would explain why the structural models obtained were not perfect.

The structural differences between the nickel compound and the cobalt, zinc and manganese cases can be rationalised in terms of the differing coordination geometries of the M centres, nickel being square planar, while the other metals have tetrahedral coordination geometry. The differences between the cobalt (monoclinic) and manganese (tetragonal) structures, either of which can be adopted by the zinc compound, is not so easy to explain. It may be a kinetic effect - the powdered monoclinic zinc polymorph forms very quickly from solution while the tetragonal crystals grow more slowly. It may

be due to solvent effects, as materials have been crystallised from different solvents. There may however be a totally different explanation; without further, systematic investigation this question cannot be answered.

5.3.1 VT data

In order to check if $(PPh_4)_2Ni(WS_4)_2$ shows any phase transitions on cooling, a variable temperature diffraction experiment was undertaken. Data were collected using a Bruker d8 Advance diffractometer fitted with the PheniX ccr cooling device.

The sample was prepared by sprinkling onto an aluminium sample holder coated with a layer of Vaseline. Data were collected over a 2θ range of 5 to 70 ° using a step size of 0.0144 ° and a time per step of 0.35 s; each data collection took a total of ~30 minutes. The sample was cooled at a rate of 17 K/hour from 300 to 16 K and data were collected continuously, a total of 34 sets of data, separated in temperature by ~8 K, were collected during cooling. The cell parameters were determined from these data using the multitopas methodology (section 2.6). A Pawley fit was used to model the aluminium (although the restricted data range meant that only two aluminium reflections were observed, so accurate cell parameter determination was not possible) and a structural fit in which none of the atomic coordinates were refined was used to model $(PPh_4)_2Ni(WS_4)_2$. Although preferred orientation was previously a problem in this material, no correction was made for this as only the cell parameters were determined from the data, these are not significantly affected by preferred orientation. The change in cell volume with temperature is shown in Figure 5.14.

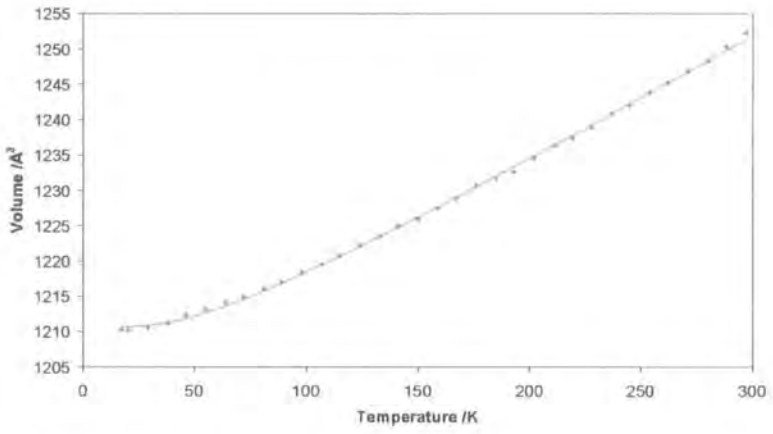

Figure 5.14 Change in cell volume of $(PPh_4)_2Ni(WS_4)_2$ on cooling. Data are shown in green, values calculated from the Reeber equation are shown in grey.

These data show that the overall cell volume increases smoothly over the temperature range studied. This smooth expansion was seen not only in the cell volume but also in the values of the *a*, *b* and *c* lattice parameters. This suggests that there are no phase transitions in this material in the temperature range studied. The expansion in the cell

parameters could be fitted using the Reeber equation (4.2); this was done using a least squares fitting procedure in TOPAS. The values obtained for the thermal expansion parameters are given in Table 5.16.

	a	*b*	*c*
a_0 /Å	9.2640 (6)	12.3422 (6)	12.3776 (6)
θ_1 /K	162 (7)	119 (4)	124 (6)
c_1 /K^{-1}	52.2 (7) × 10^{-6}	50.2 (4) × 10^{-6}	45.1 (4) × 10^{-6}
$\alpha_{15K\text{-}300K}$ /K^{-1}	41.6 (8) × 10^{-6}	43.3 (5) × 10^{-6}	38.5 (6) × 10^{-6}

Table 5.16 Thermal expansion parameters for $(PPh_4)_2Ni(WS_4)_2$.

The values of $\alpha_{15K\text{-}300K}$ for the different cell parameters show that the expansion of $(PPh_4)_2Ni(WS_4)_2$ is relatively isotropic.

5.4 Summary

In this chapter the structural characterisation of two members of the $(PPh_4)_2M(WS_4)_2$ family has been described. For the zinc containing material, a new monoclinic polymorph has been discovered, its structure is analogous to that of the cobalt containing complex already reported. The crystal structure of the tetragonal polymorph of the zinc containing material has been characterised using single crystal diffraction data. The crystals have a complex structure which displays disorder, this results in a superstructure; the superstructure has been modelled to determine more information about this disorder. The structure of $(PPh_4)_2Ni(WS_4)_2$ has been determined from powder data and represents a new structural form not seen for other related materials. Variable temperature diffraction data for $(PPh_4)_2Ni(WS_4)_2$ and the monoclinic form of $(PPh_4)_2Zn(WS_4)_2$ shows that neither of them undergoes phase transitions on cooling to 16 K.

5.5 References

1. A. Müller, E. Diemann and H. H. Heinsen, *Chem. Ber.*, 1971, **104**, 975-980.
2. K. P. Callahan and P. A. Piliero, *Inorg. Chem.*, 1980, **19**, 2619-2626.
3. A. Müller, N. Mohan and H. Bogge, *Z. Naturforsch., B: Anorg. Chem. Org. Chem.*, 1978, **33**, 978-982.
4. I. Paulat-Böschen, B. Krebs, A. Müller, et al., *Inorg. Chem.*, 1978, **17**, 1440-1443.
5. *SAINT+, Release 6.22. Bruker Analytical Systems, Madison, Wisconsin, USA*, 1997-2001.
6. G. M. Sheldrick, *SADABS, University of Göttingen, Germany*, 1998.
7. A. Altomare, G. Cascarano, C. Giacovazzo, et al., *J. Appl. Cryst.*, 1994, **27**, 435-436.
8. P. W. Betteridge, J. R. Carruthers, R. I. Cooper, et al., *J. Appl. Cryst.*, 2003, **36**, 1487.
9. J. R. Carruthers and D. J. Watkin, *Acta Cryst.*, 1979, **A35**, 698-699.
10. F. H. Allen and O. Kennard, *Chem. Des. Autom. News*, 1993, **8**, 31.
11. A. A. Coelho, *J. Appl. Cryst.*, 2003, **36**, 86-95.
12. A. A. Coelho, *J. Appl. Cryst.*, 2000, **33**, 899-908.
13. A. Müller and E. Diemann, *Chem. Commun.*, 1971, 65.

6 WS_2 intercalates

It has recently been reported[1] that a newly discovered mineral has a copper tungsten ratio near to 2:1 and an *I* centred cell of similar dimensions to those of *I* Cu_2WS_4. The mineral also contained a significant quantity of iron (the W:Fe ratio varied from 5.5 to 7.5). As a result of this report it was decided to investigate the possibility of the incorporation of iron and other transition metals as dopants on the copper site in Cu_2WS_4. One potential method by which this could be achieved is by synthesising Cu_2WS_4 in the presence of a source of transition metal. This chapter discusses attempts to synthesise and characterise the materials produced using this synthetic strategy.

6.1 Synthesis

Initial attempts to synthesise iron doped Cu_2WS_4 involved reacting $FeCl_2$ with $Cu(CH_3CN)_4BF_4$ and $(NH_4)_2WS_4$ under the same solvothermal conditions as those used to make Cu_2WS_4. Reactions were carried out in a solvothermal bomb using a solvent mixture of butyronitrile and DMF and heating at 200 °C for 48 hours; full details of all reaction conditions are given in section 2.10. This reaction led to the formation of a green powdered material, the X-ray diffraction pattern of this material is shown in Figure 6.1.

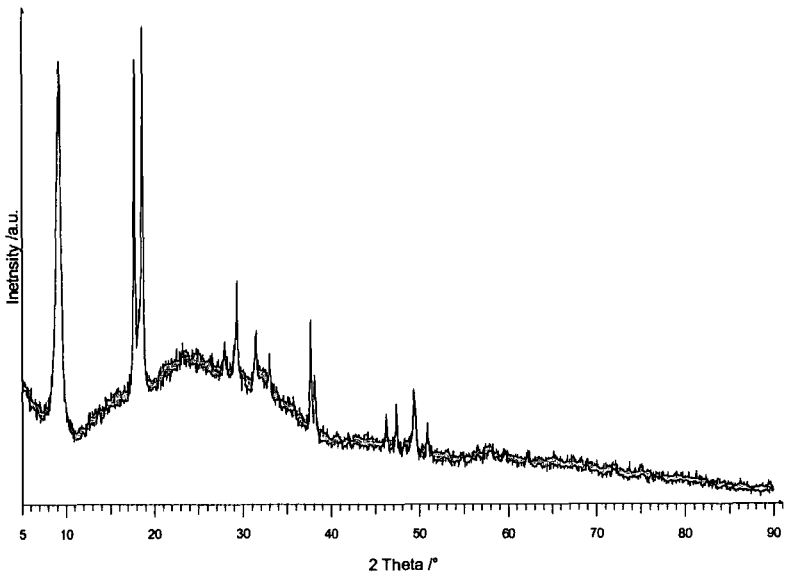

Figure 6.1 Powder pattern of material produced by reaction of $(NH_4)_2WS_4$, $Cu(CH_3CN)_4BF_4$ and $FeCl_2$ under solvothermal conditions.

The majority of the peaks in this powder pattern are those of *I* Cu_2WS_4 (compare with, for example, Figure 4.3); these peaks could be fitted by refinement of the structure of *I* Cu_2WS_4 (the structure is described in section 4.2.2). This refinement showed no evidence of changes in cell parameters or any other structural parameters which may

suggest that iron had been incorporated into the material. There are also additional peaks in the pattern which indicate the formation of a second phase, the most intense of these being at ~9 ° 2θ. This phase could not be identified from this powder pattern as it only has one peak which is easily visible, therefore attempts were made to synthesise a pure sample of the material. It is only formed in the presence of iron, so the most obvious reaction to try was that of $FeCl_2$ with $(NH_4)_2WS_4$ under the same solvothermal reaction conditions as those used to make the phase mixture. This reaction resulted in the formation of a black solid; the powder pattern of this material is shown in Figure 6.2.

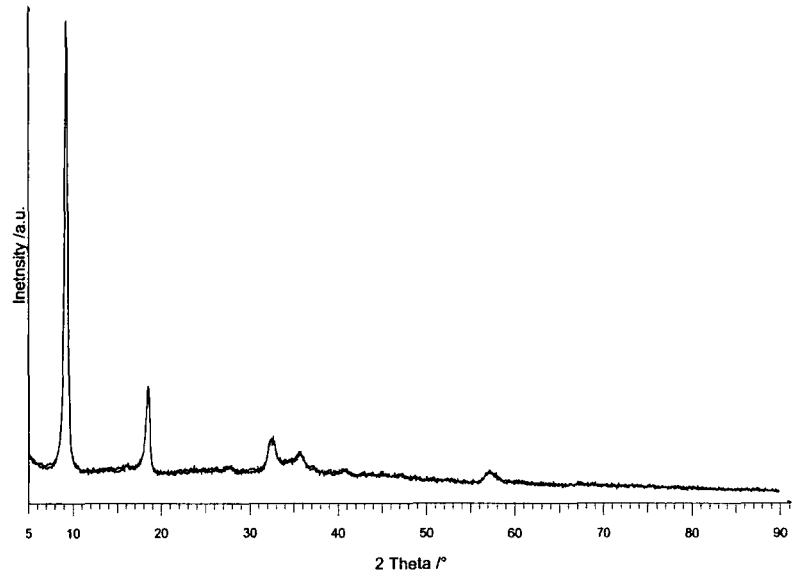

Figure 6.2 Powder pattern of the material produced by reaction of $(NH_4)_2WS_4$ and $FeCl_2$ under solvothermal conditions.

The powder pattern of this material has its strongest peak at the same 2θ value as the second phase present in the phase mixture for which the powder pattern is shown in Figure 6.1. This impurity phase could not be identified by comparison of the powder pattern to those in the PDF,[2] suggesting that it is a new material.

Further reactions were carried out to see if similar materials could be made by reactions of other transition metals with $(NH_4)_2WS_4$. $CoCl_2$, $NiCl_2$, $MnCl_2$ and $MnBr_2$ were all tested as transition metal sources and reacted with $(NH_4)_2WS_4$ under the same solvothermal conditions as those used to synthesise the iron containing material. In all cases a black solid was produced, the powder patterns of these are shown in Figure 6.3.

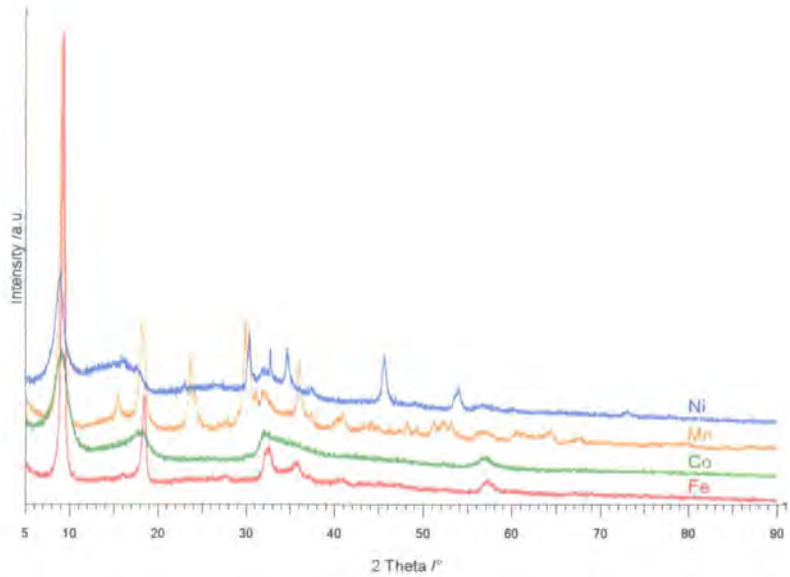

Figure 6.3 Powder patterns of materials made by reaction of transition metal salts with $(NH_4)_2WS_4$. The patterns are offset in the *y* direction for clarity.

The powder patterns in Figure 6.3 show that similar phases were produced for all the different transition metals tried but that they had different levels of crystallinity. For the manganese and nickel materials there are also significant additional phases present. Comparison of the powder patterns to the PDF shows these to be $MnWO_4$ and NiS respectively. Attempts to make materials free of these impurities by reaction under an inert atmosphere, use of anhydrous transition metal reagents or use of different transition metal salts were all unsuccessful.

The iron and cobalt materials, which appear to be the purest, were analysed by Rutherford Back Scattering (RBS) to determine the sulfur: tungsten: transition metal ratio in the powder. This analysis suggested bulk compositions of approximately $W_{1.5}FeS_3$ and $WCoS_3$. These measurements suggest that the materials do contain transition metals as well as sulfur and tungsten, though it is a bulk analysis technique so it does not rule out the possibility that there is more than one different phase present. Further attempts to identify and characterise the materials were carried out using magnetic measurements, EDAX analysis and SEM imaging.

6.2 Magnetic measurements

Both Fe^{2+} (d^6, high spin) and Co^{2+} (d^7) have unpaired electrons and would therefore be expected to exhibit paramagnetism. It is therefore possible to use magnetic property measurements to determine if these are present in a material. Magnetic property measurements were made using powdered samples of the cobalt and iron containing materials mounted in gelatin capsules using a squid magnetometer (as described in

section 2.8). For each material the change in magnetisation with magnetic field was measured, data for both materials are shown in Figure 6.4.

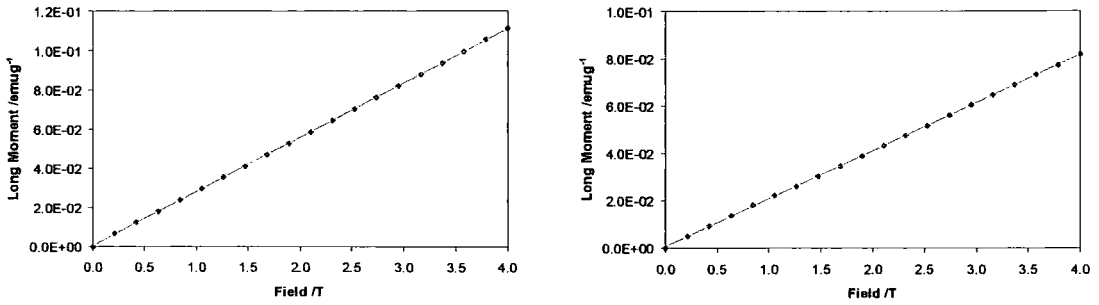

Figure 6.4 The variation of magnetisation with magnetic field for iron (left) and cobalt (right) containing materials. Grey lines are lines of best fit to the data, included as guides to the eye.

The variation of the magnetisation of the samples with the applied field shows that both samples are paramagnetic. For the iron containing sample variable temperature data collected for a sample cooled with and without application of a magnetic field showed the material followed simple Curie-Weiss type behaviour. The value of μ_{eff} calculated assuming the RBS molecular formula $Fe_{0.66}WS_2$ was 1.2 BM. This value is very low for an Fe^{2+} containing species, and suggests that the assumed molecular formula is not correct. The Curie-Weiss type behaviour of these materials is consistent with the RBS data which shows that both samples contain transition metals.

6.3 EDAX and SEM

Magnetic measurements and RBS analysis are bulk measurements. In order to investigate the microstructure of the materials formed and try to determine if they really are single phase materials they were analysed using EDAX. As well as checking the elemental composition of individual grains of the sample, SEM was used to allow visual analysis of the micro grains to see if they showed any evidence of being a mixed phase material. Measurements were carried out in a JEOL JSM IC-848 scanning electron microscope mounted with a Princeton Gamma-Tech x-ray detector (PRISM 2000) (with a thin window). Qualitative EDAX analysis used PGT Avalon software.

SEM images of the cobalt and iron samples showed that both appeared to be homogeneous in nature. Individual grains had plate like morphology in the iron sample, though in the cobalt sample the morphology was significantly different, grains had irregular shapes. Representative SEM images for both samples are shown in Figure 6.5.

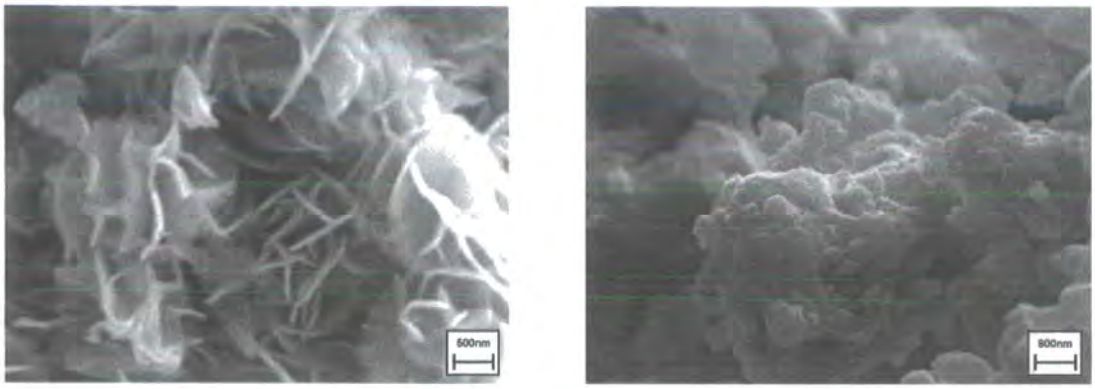

Figure 6.5 Representative secondary electron images of iron containing material (left) and cobalt containing material (right).

Areas of the sample were analysed using EDAX to determine what elements were present. All analyses of the sample containing iron showed a mixture of iron, sulfur and tungsten, while analyses of the cobalt containing sample consistently showed the presence of cobalt, tungsten and sulfur. No variation in composition could be detected when different areas of the sample were analysed. A representative EDAX spectrum for the iron containing sample is shown in Figure 6.6.

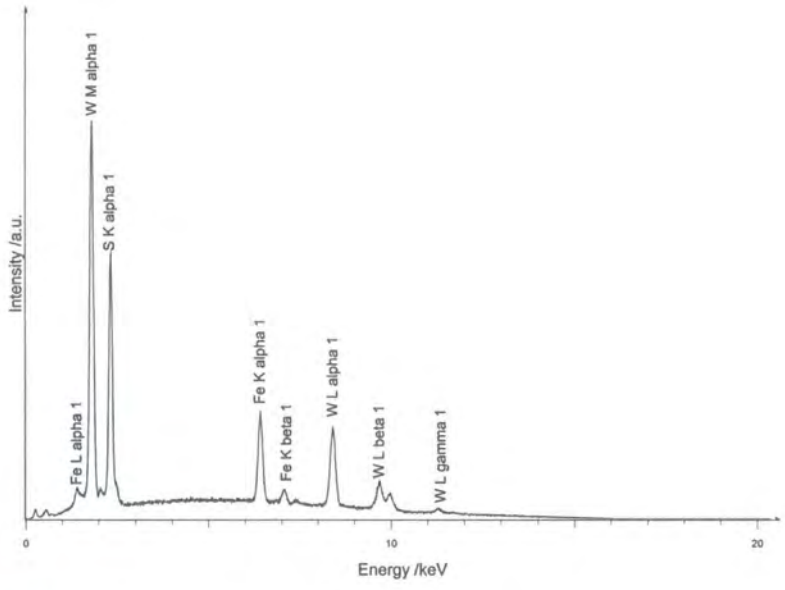

Figure 6.6 EDAX spectrum for iron containing sample.

The minimum size of an area analysed by EDAX had a diameter of ~500 nm. Peak shape analysis of the powder pattern suggests that the size of the crystallites was of the order of 10's of nm. Therefore EDAX analysis does not rule out the possibility of there being two different phases, although it does suggest that if two phases are present, they are very intimately mixed.

6.4 Diffraction data

The powder patterns of all of the materials can be fitted using a Pawley fit[3] in the trigonal space group, P3. The cell parameters obtained for the materials made with the different transition metals are given in Table 6.1.

Transition metal	*a* /Å	*c* /Å
Mn	3.230 (3)	9.84 (1)
Fe	3.192 (2)	9.699 (1)
Co	3.3 (1)	10.121 (3)
Ni	3.29 (7)	9.9 (3)

Table 6.1 Cell parameters for materials produced by solvothermal reaction of $(NH_4)_2WS_4$ with different transition metal salts.

The cell parameters obtained from these fits cannot be determined to a high degree of precision; this is partly because of the poor crystallinity of the samples and partly because of the weak nature of all peaks except for the *00l*'s. Comparison of these cell parameters to those for the trigonal[4] form of WS_2 (for which $a = 3.1532\ (4)$ Å and $c = 12.323\ (5)$ Å; interlayer spacing = 6.16 Å) suggests that these materials may be tungsten sulfide intercalation compounds. The diffraction data are consistent with the formation of a layered compound. Only *00l* type peaks are well defined and have large intensities, this suggests a lack of long range order in the *a* and *b* directions or significant preferred orientation. For a layered compound in which layers are stacked along the *c* axis but where there is random displacement of layers relative to each other in the *a* and *b* directions, this is exactly the type of intensity pattern that would be predicted.

There have been a large number of studies on the intercalation chemistry of WS_2 and MoS_2, many of which have utilised the fact that the materials can be lithiated by reaction with reagents such as n-butyllithium to form Li_xMoS_2 and Li_xWS_2. These materials can be exfoliated by reaction with deionised water to form a suspension of MX_2 monolayers;[5,6] these can then be restacked to form bulk materials. If this occurs in the presence of other molecules or ions it is possible to form MS_2 intercalation compounds.[7] Although it has not always been possible to determine the change in interlayer spacing on intercalation of guests, two studies[8,9] where this has been reported were on the intercalation of alkali metal cations into MoS_2/WS_2 and on the intercalation of naphthalene derivatives into MoS_2; both studies used the exfoliation restacking synthesis method. The increases in interlayer separation observed for incorporation of alkali metal cations and H_2O between the MX_2 layers ranged from 3.1 to 3.5 Å. For the naphthalene derivative intercalates, interlayer separation increases by values between 3.4 and 7.6 Å, depending on the orientation of the intercalated molecules within the

layers. The mean increase in interlayer spacing for the materials being studied here is ~3.7 Å, which is slightly larger than the value observed for the alkali metal/water intercalates and comparable to the increases observed when naphthalene derivatives are incorporated with the plane of the molecule parallel to the MoS_2 layers. This suggests that the observed change in interlayer separation may be a result of incorporation of a single layer of molecules or ions, possibly with additional solvent molecules. It is also interesting to note that the powder pattern of the materials presented here show a similar pattern of intensities and peak broadening to that observed in the powder patterns of the naphthalene/MoS_2 intercalates.

Although both bulk measurements and microanalysis have indicated that there are transition metals present in the samples, the possibility of the materials being phase mixtures, mixed on a scale too small to detect by SEM, cannot be ruled out. It is possible that the materials are intercalates containing organic solvent molecules or ammonium ions between the layers, with the transition metals being present in amorphous phases which are not detected by PXRD.

Fitting a structural model to data of this type is problematic because most of the information contained in the pattern is in the *00l* type peaks; in general this information is not sufficient to allow full structure determination. Additionally, for the cobalt containing material, the crystallinity of the material is very poor. Although the information obtained will not be definitive, structural models can be fitted to the data to see if they are consistent with the proposal that these materials are WS_2 intercalates.

Data for the iron and cobalt containing samples were collected using a Siemens D5000 diffractometer on samples prepared by sprinkling powder onto an amorphous glass slide coated with Vaseline. Data were collected over a 2θ range of 5 to 90 ° with a step size of 0.02 ° and a time per step of 10 s. In addition to structural parameters, 5 coefficients of a Chebychev polynomial and one parameter to describe a $1/2\theta$ type function were refined to describe the background. The patterns show severe anisotropic peak broadening which could be related to stacking faults in a layered sample; an attempt was made to model this using an 8^{th} order spherical harmonic for which 6 or 9 coefficients were refined depending on the space group of the model. For the iron containing sample the region between 35 and 36.5 ° 2θ was excluded from the refinement as it contained an additional broad peak believed to be from an impurity phase.

The different structural models used are a systematic group of structures which all contain layers of WS_2 polyhedra interspaced by layers of atoms which represent intercalated species. In different models the tungsten atoms have either octahedral or trigonal prismatic coordination geometry. The coordination geometry of the tungsten ion in WS_2 is a trigonal prism, while in the material made by exfoliation and restacking

it has octahedral coordination;[10] models which use both geometries were therefore used in this analysis. The relative positions of tungsten atoms in adjacent layers (in the *a* and *b* directions) changes in different models, for some models the metal atoms are offset; in others they are not. The number of layers in the repeat unit is either 2 or 3 for different models and the *c* cell parameters given in Table 6.1 were modified (multiplied by 2 or 3) in the structural fits to reflect this. Atoms are included at sites in the layers between the WS_2 layers to represent intercalated species, in some models these sites are surrounded by sulfur atoms which form a trigonal prism; in the others the sulfur atoms form an octahedron. Although metal atoms were used in the model, an overall occupancy parameter (constrained to be the same for all atoms in these intermediate sites) was refined to allow for the fact that the identity of the intercalated species was not known and also the possibility that sites are only partially occupied. The other structural parameters refined for each model were a parameter to describe the *z* coordinate of sulfur layers relative to the tungsten layers, a scale factor, temperature factors (one each for the tungsten, sulfur and intercalate atoms) and 2 cell parameters. Examples of two of the different structures which were used to fit the data are shown in Figure 6.7; input files which include all of the structural models are included in the e-appendix. A summary of structural information for the 5 different models that were used is given in Table 6.2.

Model	Space group	W coordination geometry	Coordination geometry of intercalate atom sites	No. of layers in repeat unit	*a*/*b* offset of W atoms between layers?
1	P3m1	Trigonal prism	Trigonal prism	2	Y
2	$R\bar{3}m$	Octahedron	Trigonal prism	3	Y
3	$P6_3/mmc$	Trigonal prism	Octahedron	2	N
4	$P6_3/mmc$	Octahedron	Trigonal prism	2	N
5	P3m1	Trigonal prism	Octahedron	3	Y

Table 6.2 Summary of structural information about the different WS_2 intercalate structural models.

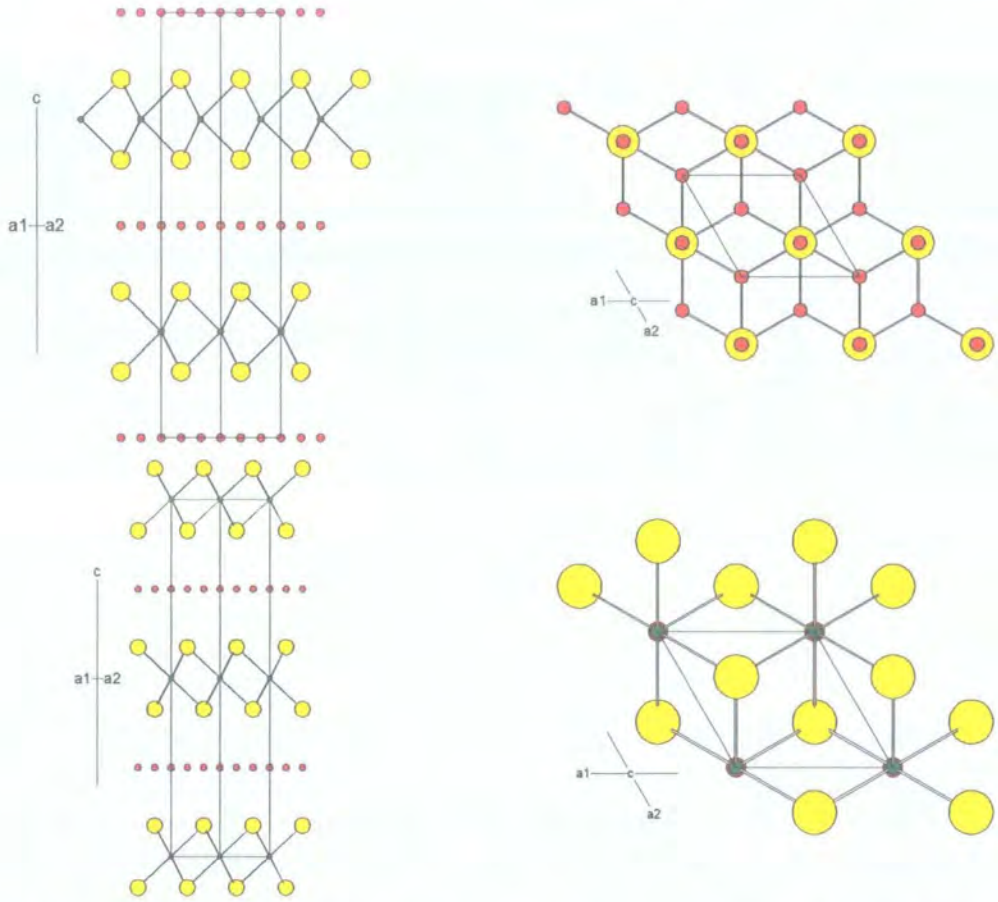

Figure 6.7 Views down the *c* axis (right) and perpendicular to the *c* axis (left) of two of the structural models used to describe WS_2 intercalates. W has trigonal prismatic coordination (top) and octahedral coordination (bottom). W atoms are shown in green, S in yellow and intercalated atom positions in red.

The powder patterns of the iron and cobalt containing materials were fitted using each of the structural models described in Table 6.2. Examples of Rietveld fits for each material are shown in Figure 6.8 and a summary of R-factors for different structural models is given in Table 6.3.

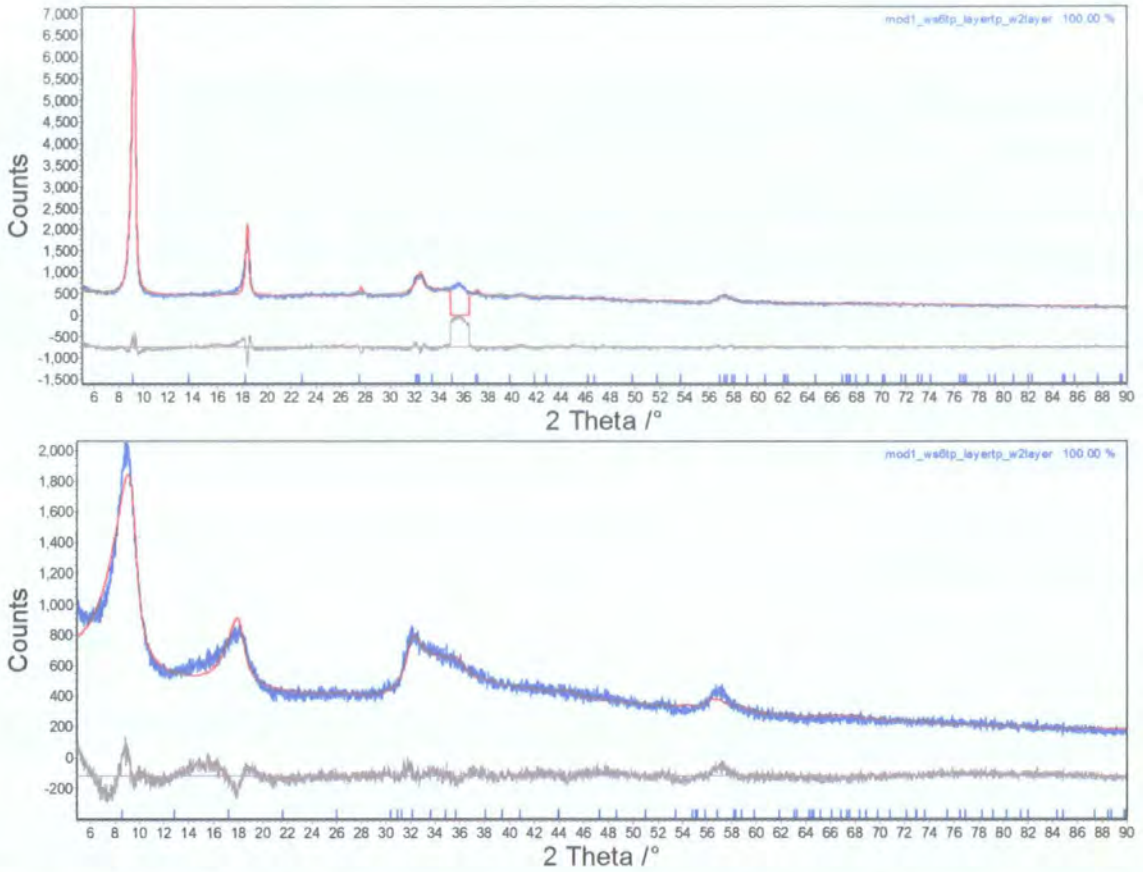

Figure 6.8 Rietveld fits for the iron containing material (top) and for the cobalt containing material (bottom) using structure number 1. Observed data are shown in blue, calculated in red and difference in grey.

	Fe		Co	
Structure	$_wR_p$ /%	R_{Bragg} /%	$_wR_p$ /%	R_{Bragg} /%
1	7.67	3.53	7.23	0.95
2	8.71	2.82	7.39	1.04
3	8.77	2.19	8.36	1.05
4	8.89	2.51	8.02	1.12
5	8.63	4.20	7.14	0.81

Table 6.3 R-factors for Rietveld refinements using different structural models for the WS_2 intercalates.

The R-factors obtained for the fits using different structural models show that reasonable agreement can be obtained between calculated and observed data using a structural model that contains layers of WS_2 with some atoms present in layers between them. The disparity in the quality of fit obtained for different models does not seem to show that any particular structural features (coordination geometries etc.) give a significantly better fit to the data. Therefore it can be concluded only that the data are not inconsistent with a structure of this type.

6.5 Summary

New materials have been made by the reaction of transition metal salts with $(NH_4)_2WS_4$ using low temperature solvothermal reaction conditions. Although analysis of these materials shows that they contain transition metals and a mixture of sulfur and tungsten it has not been possible to conclusively identify them. One possibility is that the materials are WS_2 intercalates, XRD data are not inconsistent with this possibility, although the nature of the intercalated species is unclear. The preliminary investigations presented in this chapter are not conclusive and a significant amount of additional work would have to be done in order to fully and conclusively characterise the materials that have been made.

6.6 References

1. E. Inan, Private Communication, June 2003.
2. *Powder Diffraction File, International Centre for Diffraction Data, Pennsylvania*, 1998.
3. G. S. Pawley, *J. Appl. Cryst.*, 1981, **14**, 357-361.
4. W. J. Schutte, J. L. de-Boer and F. Jellinek, *J Solid State Chem.*, 1987, **70**, 207-209.
5. P. Joensen, R. F. Frindt and S. R. Morrison, *Mater. Res. Bull.*, 1986, 457-461.
6. D. Yang and R. F. Frindt, *J. Phys. Chem. Solids*, 1996, **57**, 1113-1116.
7. W. M. R. Divigalpitiya, R. F. Frindt and S. R. Morrison, *Science*, 1989, **246**, 369-371.
8. J. Heising and M. G. Kanatzidis, *J. Am. Chem. Soc.*, 1999, **121**, 11720-11737.
9. A. V. Powell, K. L and A. McDowell, *J. Mater. Chem.*, 2001, **11**, 1086-1091.
10. V. Petkov, S. J. L. Billinge, J. Heising, et al., *J. Am. Chem. Soc.*, 2000, **122**, 11571-11576.

7 Structure solution of $(NH_4)_2WS_3O$

$(NH_4)_2WS_3O$ was prepared as part of an investigation into the synthesis of $(NH_4)_2MS_xO_{4-x}$ (M = W, Mo) type materials. Although some of the structures of other members of this family are known, including those of $(NH_4)_2WS_4$ and $(NH_4)_2WS_2O_2$, the structure of $(NH_4)_2WS_3O$ has never been reported. Attempts were made to determine the structure of this material from powder diffraction data, these are described in this chapter.

7.1 Synthesis

$(NH_4)_2WS_3O$ was prepared from a suspension of H_2WO_4 in ammonium hydroxide solution. $H_2S(g)$ was passed through the solution at room temperature, the reaction is a stepwise process in which oxide ions in WO_4^{2-} are successively replaced by sulfide ions. The reaction initially forms a green solid ($(NH_4)_2WS_2O_2$) and the solution changes from colourless to yellow, indicating the formation of $(NH_4)_2WS_3O$. Gas was only passed through the solution for ~20 minutes, longer reaction times favour the formation of $(NH_4)_2WS_4$. After removal of the $(NH_4)_2WS_2O_2$ by filtration, the solid product was precipitated by addition of isopropyl alcohol to the yellow filtrate. Full synthetic details are given in section 2.10. The yellow solid produced was characterised by powder diffraction and UV-vis spectroscopy.

The powder diffraction pattern of the material was recorded and compared to those of known compounds in the PDF; it did not correspond to the patterns of any other material reported, including $(NH_4)_2WS_4$ and $(NH_4)_2WS_2O_2$. The UV-vis absorbance spectrum of the material was also compared to those previously reported[1] for WS_4 and WS_3O. The strongest bands observed in the spectrum were at ~336 nm and ~380 nm, consistent with the values reported by Müller for the strongest bands in the spectrum of WS_3O (334 and 375 nm). Additionally the spectrum did not show a strong band at 392 nm, the position of the most intense feature in the spectrum of $(NH_4)_2WS_4$. Elemental analysis showed that the composition of the material was consistent with the molecular formula $(NH_4)_2WS_3O$ (C:H:N observed: C 0.07 %, H 2.43%, N 8.60 %; calculated: C 0 %, H 2.43 %, N 8.43 %).

7.2 Structure solution

Structure solution was attempted using diffraction data collected using a Bruker d8 Advance diffractometer operating in transmission mode on a sample contained in a 0.5 mm capillary. Data were collected over a 2θ range of 5 to 120 ° using a step size of 0.0144 ° and a time per step of 6.5 s. In total 3 individual datasets were collected and summed together to give a final diffraction pattern.

The diffraction pattern was indexed using the *multiviss* routine, a locally modified version of ITO,[2] as described in section 2.3. The best solution suggested by this process had the following unit cell parameters:

a = 9.328 Å b = 7.118 Å c = 11.566 Å $\alpha = \beta = \gamma = 90$ ° *FOM* = 50

The space group was determined by examining the systematic absences in the diffraction pattern. The reflections present were: (*00l*) $l = 2n$; (*0k0*) $k = 2n$; (*h00*) $h = 2n$; (*hk0*) $h = 2n$; (*h0l*) all; (*0kl*) $k + l = 2n$; (*hkl*) all. These conditions are consistent with the pair of space groups Pnma and $Pn2_1a$. A Pawley fit[3] to the data in Pnma gave good agreement between observed and calculated data ($_wR_p$ = 6.98 % over the range 6 to 60 ° 2θ), and initial structure solution was attempted in this space group. Attempts to solve the structure using direct methods in EXPO[4,5] located only the tungsten atom, which was on the mirror plane at $y = 0.25$. As tungsten contributes approximately half of the scattering power of $(NH_4)_2WS_3O$, positions of other atoms could not be determined using direct methods and were instead located by simulated annealing.

Simulated annealing was performed using TOPAS.[6] During this process the values of the cell parameters, a simple axial model parameter, a zero point error and peak shape parameters were fixed at values obtained from the Pawley fit. The structure was initially modelled as containing rigid WS_4 tetrahedra with W – S bond lengths of 2.177 Å (the bond length in an isolated WS_4^{2-} tetrahedron[1]) and individual N atoms. Comparison of the unit cell volume, 771 $Å^3$, with that of $(NH_4)_2WS_4$ (V = 823, Z = 4)[7] suggested cell contents of 4 WS_3O units and 8 nitrogen atoms per unit cell. There are 3 different types of site in space group Pnma: general positions (multiplicity 8), sites on a mirror plane (multiplicity 4) and sites on inversion centres (multiplicity 4). The only possible location for an ordered WS_4 tetrahedron is on the mirror plane; this is where W had been located when direct methods were used to try and solve the structure. The symmetry of a tetrahedron is such that if its central atom is on a mirror plane then two of the terminal atoms must also be in that plane. The WS_4 rigid body was therefore defined so that the tungsten atom and two of the sulfur atoms remained in the mirror plane while the tetrahedron rotated about an axis perpendicular to the plane. For each cycle of randomisation the rotation of the tetrahedron was varied by angles of up to ± 25 ° and the tungsten atom was randomly translated around the mirror plane in steps of up to ± 5 Å. Two nitrogen atoms were also placed in the unit cell and their positions annealed; positions were also varied by values up to ± 5 Å in any direction in sequential cycles of randomisation. The annealing process was repeated twice, once using two fully occupied nitrogen atoms and once using two half occupied atoms, in order to try to determine if the NH_4 tetrahedra should be located on the mirror place. The structure was annealed using data in the range 6 to 60 ° 2θ and hundreds of thousands of cycles of

randomisation were performed resulting in a structural model showing reasonable agreement with the experimental data.

The solution found by this process was examined to try to determine if the WS_3O tetrahedron was ordered in the structure. Initially individual temperature factors for the 3 different sulfur sites were refined. This showed that one site had a temperature factor an order of magnitude higher than the others (~0.2 $Å^2$ compared to ~0.01 $Å^2$) which suggested that this was probably the location of the oxygen atom. This solution also located the nitrogen atoms on the mirror plane, so their positions were constrained to remain on this plane in subsequent annealing and refinements. Further cycles of annealing were then performed in which the WS_4 tetrahedron was replaced by a WS_3O tetrahedron, for this a W – O bond length of 1.8 Å was used and the oxygen site was one of those constrained to remain in the mirror plane. Once a global minimum was found using this structural model, additional cycles of randomisation followed by refinement were performed to allow the structure to distort slightly from the rigid body model. For these cycles the atoms were all modelled individually, at the beginning of each cycle their positions were randomised but constrained to be at positions <0.6 Å from the position found by annealing with a rigid body model.

The final structure was determined by full refinement of the best model found by the annealing process. Additional fractional S/O occupancies on the 3 X sites were allowed to refine, subject to the constraint that the total occupancy of each site summed to 1. The positions of the tungsten and X sites were freely refined. The Rietveld fit obtained is shown in Figure 7.1.

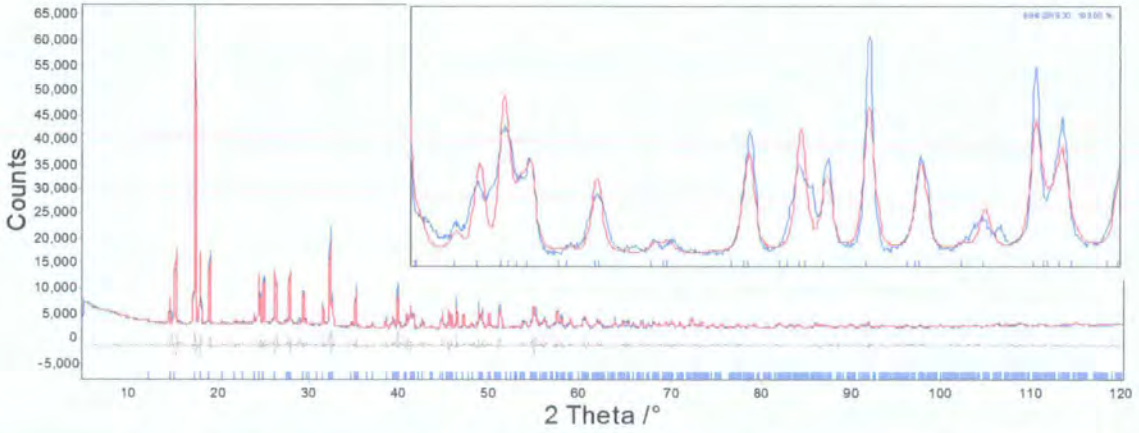

Figure 7.1 Rietveld fit for final model of $(NH_4)_2WS_3O$ using an isotropic PV peak shape. The inset shows a zoom of the region between 40 and 50 ° 2θ. Observed data are shown in blue, calculated in red and difference in grey.

It is apparent from Figure 7.1 that the structure determined by this process gives a good but not perfect fit to the observed data, this is partly due to the sample being slightly

impure (there are several small peaks that do not coincide with predicted peak positions). There are also other possible reasons, the most likely being either that observed anisotropic peak broadening is not being fitted sufficiently well by the isotropic peak shape model, or that material exhibits pseudo symmetry. Pseudo symmetry is a common phenomenon in materials which contain a heavy element and several lighter ones; in this case it is the tungsten atoms which dominate the X-ray scattering, if they are arranged in a way which is more symmetrical than other parts of the structure, the diffraction data may suggest the presence of symmetry elements that are not actually present. These possibilities were both examined.

In order to investigate the possibility of the structure displaying pseudo symmetry and really having a structure of lower symmetry than Pnma, the structure was annealed and refined in several related lower symmetry space groups to see if any improvement in fit could be obtained. Refinement was attempted in the following space groups: $Pn2_1a$, $P2_1/n11$, $P112_1/a$, $P12_1/m1$ and P1. None of the structure solutions obtained by this process gave a significant improvement in the fit to the data and all of the results had essentially Pnma symmetry. Another possible result of pseudo symmetry is that that the true unit cell of the material could be larger than the one obtained by indexing the strongest peaks in the diffraction pattern. However, the weak unexplained peaks could not be accounted for by simple unit cell doubling/tripling. This suggests that the problems in fitting these data are not a result of pseudo symmetry and that the true symmetry of the structure, at least as far as can be determined from laboratory powder diffraction data, is that of Pnma.

The problems of modelling the structures of materials which display anisotropic peak broadening along with ways in which it attempts can be made to model it using spherical harmonic functions have been discussed in chapter 3. There are several different ways of modelling an anisotropic peak shape for these data; in order to select the one most appropriate for use in this case, the effect of each model on a Pawley fit to the data was examined. Using a Pawley fit removes any possible bias due to an incorrect structural model. The R-factors for the different models, fitted over the 2θ range 6 to 60 ° are summarised in Table 7.1, more information about the peak shape models can be found in section 3.4.2.

Peak shape model	$_wR_p$ /%	No. refined parameters
PV only	6.989	668
G/L strain	7.576	664
PV convoluted G/L strain	6.990	670
PV add size SH 4	5.870	674
PV add size SH 6	5.797	678
PV add strain SH 4	5.692	674
PV add strain SH 6	5.686	678
PV convoluted size SH 4	5.789	675
PV convoluted size SH 6	5.702	679
PV convoluted strain SH 4	5.639	675
PV convoluted strain SH 6	5.617	679
PV convoluted size/strain SH 4	5.623	677
PV convoluted size/strain SH 6	5.609	681
G/L strain convoluted size SH4	6.038	671
G/L strain convoluted size SH6	5.974	675
G/L strain convoluted strain SH4	6.092	671
G/L strain convoluted strain SH6	6.058	675
G/L strain convoluted size/strain SH 4	5.952	673
G/L strain convoluted size/strain SH 6	5.909	677
4th order size/strain SH only	5.946	671
6th order size/strain SH only	5.909	675

Table 7.1 R-factors and number of parameters refined for different peak shape models applied to a Pawley fit to $(NH_4)_2WS_3O$ capillary data.

The R-factors for the different models show that the use of a pseudo-Voigt function convoluted with a strain dependent spherical harmonic gave significant improvement in the quality of the fit. Additional terms in the spherical harmonic gave marginal improvement, but this was judged to be insignificant. The anisotropic part of this peak shape model was allowed to contain both Gaussian and Lorentzian components, the relative contributions of each one were refined. There was almost no contribution from Lorentzian part of the spherical harmonic function, so a Gaussian spherical harmonic function is all that is required. This peak shape and a subset of the other anisotropic peak shapes (included for comparison) were used to perform a structural fit to the data; the peak shape parameters were fixed at the values obtained from the Pawley fits. The R-factors obtained for these fits, fitted over a 2θ range of 6 to 120 ° 2θ, are given in Table 7.2.

Peak shape model	${}_wR_p$ /%	R_{Bragg} /%
PV only	7.884	2.943
PV add size SH 4	7.068	2.773
PV add strain SH 4	6.205	2.189
PV convoluted size SH 4	6.990	2.987
PV convoluted strain SH 4	5.700	2.136
PV convoluted size/strain SH 4	6.014	2.105
G/L strain convoluted size SH4	6.911	3.013
G/L strain convoluted strain SH4	6.285	2.017
G/L strain convoluted size/strain SH 4	6.007	2.188
4th order size/strain SH only	5.975	2.184

Table 7.2 R-factors for structural fits of $(NH_4)_2WS_3O$ using different peak shape models.

The values of the R-factors for the structural fits confirm that the choice of a 4th order strain type spherical harmonic convoluted with a pseudo-Voigt peak shape is best for these data. The use of this kind of peak shape leads to a model with better agreement between observed and calculated data and a lower R_{Bragg} than that obtained if only an isotropic pseudo-Voigt peak shape is used. This peak shape was therefore used for the final structure refinements.

In final cycles of refinement a total of 38 parameters were refined. These included 13 coefficients of a Chebychev polynomial to describe the background, a zero point error, a simple axial model parameter to describe peak asymmetry, one scale factor, 3 lattice parameters, 13 atomic coordinates, 3 temperature factors (one for the W site, one for the X sites and one for the N sites) and 3 occupancy parameters to describe the relative occupancies of sulfur and oxygen on the X sites. 6 peak shape parameters and 5 coefficients of a spherical harmonic describing peak broadening were fixed at values determined from a Pawley fit to the data. If these were allowed to refine there was a slight improvement in R_{Bragg} (~0.3 %) but relatively small changes to the structural parameters.

Refinement details are summarised in Table 7.3, the Rietveld fit is shown in Figure 7.2 and atomic coordinates are given in Table 7.4; the input file and a cif file are included in the e-appendix.

Space Group	Pnma	2θ range	6 – 120 °
a	9.3478 (1) Å	2θ step	0.0144 °
b	7.1299 (1) Å	Time per step	19.5 s
c	11.5849 (3) Å	${}_wR_p$	5.70 %
$\alpha = \beta = \gamma$	90 °	R_{Bragg}	2.134 %
No. of refined parameters	38	χ^2	3.15

Table 7.3 Selected crystallographic, data collection and refinement details for $(NH_4)_2WS_3O$.

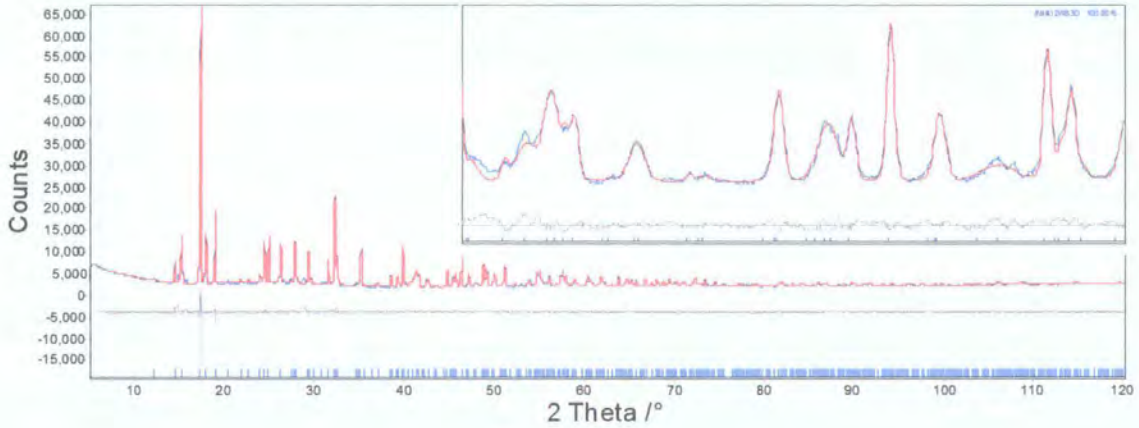

Figure 7.2 Rietveld fit for final model of $(NH_4)_2WS_3O$ using a spherical harmonic peak shape convoluted with a PV peak shape. The inset shows a zoom of the region between 40 and 50 ° 2θ. Observed data are shown in blue, calculated in red and difference in grey.

Atom	x/a	y/b	z/c	S occupancy	U_{iso} /Å^2
W1	0.7394 (2)	0.25	0.0448 (2)		−0.0032 (4)
X1	0.5041 (7)	0.25	0.0938 (7)	1.00 (3)	0.008 (2)
X2	0.745 (3)	0.25	0.874 (2)	0.00 (2)	0.008 (2)
X3	0.8487 (5)	0.4999 (6)	0.1198 (5)	0.97 (2)	0.008 (2)
N1	0.057 (2)	0.75	0.294 (2)		−0.019 (4)
N2	0.333 (2)	0.75	−0.372 (1)		−0.019 (4)

Table 7.4 Fractional atomic coordinates, temperature factors and occupancy of S on the X sites for $(NH_4)_2WS_3O$.

The refined occupancy parameters for the S/O sites show that $(NH_4)_2WS_3O$ contains WS_3O^{2-} units arranged in an ordered manner. The oxygen is located on the X2 site, while the sulfur is located on the X1 and X3 sites. The temperature factors for the tungsten and nitrogen sites are slightly negative; this is presumably due to absorption effects. The structure is shown in Figure 7.3 and selected bond lengths and angles are summarised in Table 7.5.

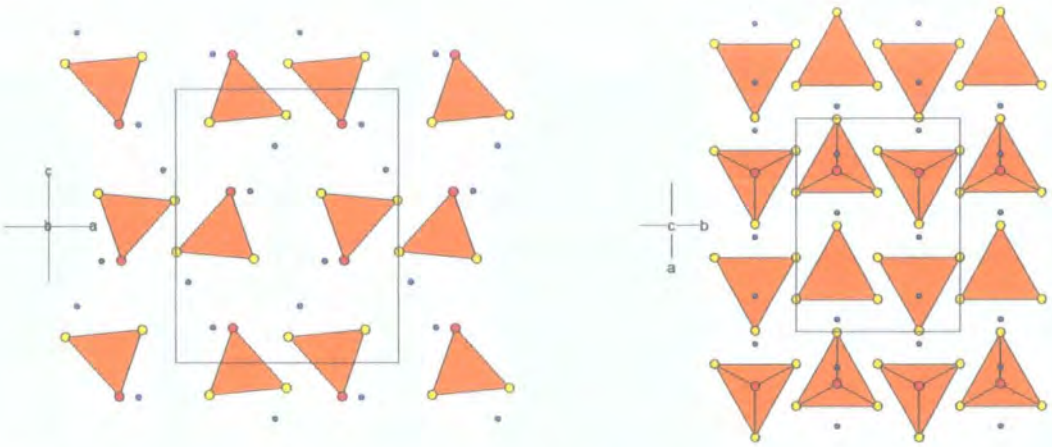

Figure 7.3 The structure of $(NH_4)_2WS_3O$ viewed down the *b* axis (left) and the *c* axis (right). O is shown in red, S in yellow, N in blue and WS_3O tetrahedra in orange.

Bond Lengths /Å		Bond Angles /°	
W – S1	2.271 (7)	S1 –W – O2	106.1 (7)
W – O2	1.98 (2)	S1 –W – S3 × 2	110.3 (2)
W – S3 × 2	2.230 (5)	O2 –W – S3 × 2	112.1 (4)
N1 –O2	2.68 (3)	S3 –W – S3	106.1 (3)
N2 –S1	3.173 (7)		

Table 7.5 Bond lengths and angles in the WS_3O tetrahedra in $(NH_4)_2WS_3O$.

The geometry of the WS_3O tetrahedron shows only slight distortion from idealised tetrahedral geometry. The W – S bond lengths determined are slightly longer than those reported for $(NH_4)_2WS_4$ (2.18 Å), $(NH_4)_2WS_2O_2$ (2.19 Å) and K_3WS_3OCl (2.20 Å).[1,8,9] The W – O bond length is also slightly longer than those in $(NH_4)_2WS_2O_2$ (1.78 Å) and in K_3WS_3OCl (1.76 Å). Accurate atomic coordinates for oxygen (and nitrogen) are however difficult to determine from X-ray powder data in the presence of a heavy element such as tungsten. The N – O and N – S distances are of about the right magnitude (less than the sum of the covalent radii of the atoms involved) to indicate that hydrogen bonds from the ammonium ions to the WS_3O units may be present. The structure is compared to that of $(NH_4)_2WS_4$ in Figure 7.4.

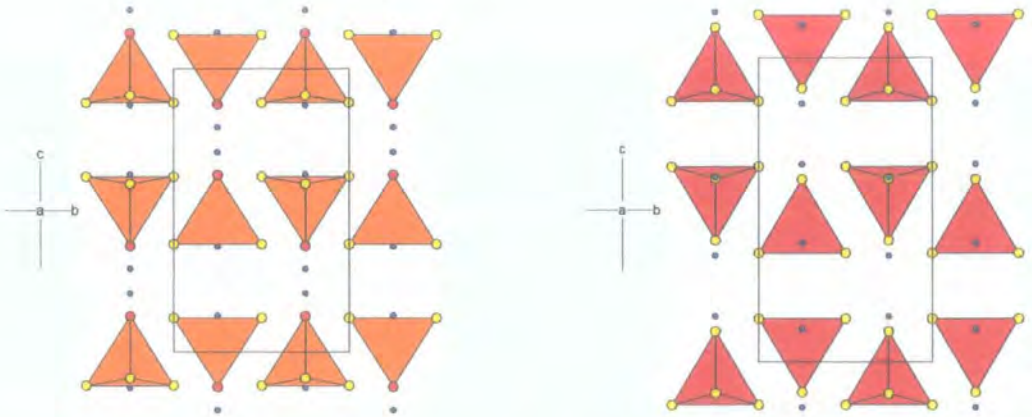

Figure 7.4 Views of the structures of $(NH_4)_2WS_3O$ (left) and $(NH_4)_2WS_4$ (right) viewed down the *a* axis. O is shown in red, S in yellow, N in blue, WS_3O tetrahedra in orange and WS_4 tetrahedra in red.

Figure 7.4 shows that the structures of $(NH_4)_2WS_3O$ and $(NH_4)_2WS_4$ are closely related. Comparison of the unit cell volume of $(NH_4)_2WS_3O$ ($V = 722$ Å^2) with those of $(NH_4)_2WS_4$ and $(NH_4)_2WS_2O_2$ ($V(WS_4) = 823$ Å^2, $V(WS_2O_2) = 699$ Å^2) shows that the decrease in cell volume is larger on going from WS_4 to WS_3O (− 12 %) than on going from WS_3O to WS_2O_2 (− 3 %). These differences in cell volumes can presumably be attributed to the smaller size of O^{2-} compared to S^{2-}. Additionally $(NH_4)_2WS_2O_2$ has a monoclinic cell, and is not isostructural with the WS_4 and WS_3O materials; offering a possible explanation for the smaller decrease in cell volume when changing from WS_3O to WS_2O_2 compared to changing from WS_4 to WS_3O.

Additional information about the physical nature of $(NH_4)WS_3O$ can be obtained by considering the shape of the spherical harmonic function used to fit these data; this is shown in Figure 7.5.

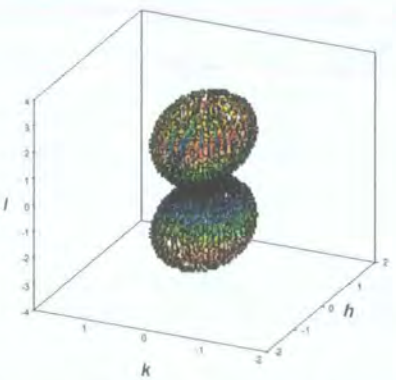

Figure 7.5 The shape of the 4th order strain type spherical harmonic function used to model peak broadening anisotropy in data from $(NH_4)_2WS_3O$.

The shape of this function shows that the largest increase in peak width (+ 209 %) occurs for *00l* and *h0l* type reflections, while the largest decrease in peak width

(− 74 %) occurs for *0k0* type reflections. This suggests that the strain is largest in the *h0l* plane, or that there are relatively more stacking faults along the *a* and *c* directions than along the *b* direction. It may also be an indication that the true symmetry of the material is lower than Pnma and that peaks which appear to be single in the diffraction pattern are in fact split. However no evidence was found from the current data to suggest that the structure really has symmetry lower than that of the space group Pnma.

7.3 Variable Temperature Diffraction

The structural properties of $(NH_4)_2WS_3O$ were further probed by undertaking a variable temperature diffraction experiment. The aim of this investigation was to see if any phase transitions occurred on heating or cooling the sample, one transition which would be likely for this kind of material is a transition from static to dynamic NH_4 groups.

Data were collected over a temperature range of 100 to 470 K on a sample prepared by sprinkling onto a Vaseline coated aluminium sample holder. A Bruker d8 Advance diffractometer with the TTK450 attachment and v6 divergence slits was used to measure the diffraction pattern over a 2θ range of 5 to 110 °, using a step size of 0.0144 ° and a time per step of 0.3 s; scans were collected on heating and separated in temperature by 10 K.

Cell parameters were obtained from the diffraction patterns using a two phase Rietveld refinement. Peaks due to the aluminium sample holder were fitted using a Pawley fit; the structural model used for the $(NH_4)_2WS_3O$ was the same as that discussed in section 7.2 and was not refined. Two sample height parameters (one for the sample and one for the sample holder), 13 coefficients of a Chebychev polynomial to describe the background, a simple axial model parameter and a scale factor for the $(NH_4)_2WS_3O$ phase were refined in addition to the cell parameters for both sample and holder. The variation in cell parameters and cell volume with temperature are shown in Figure 7.6.

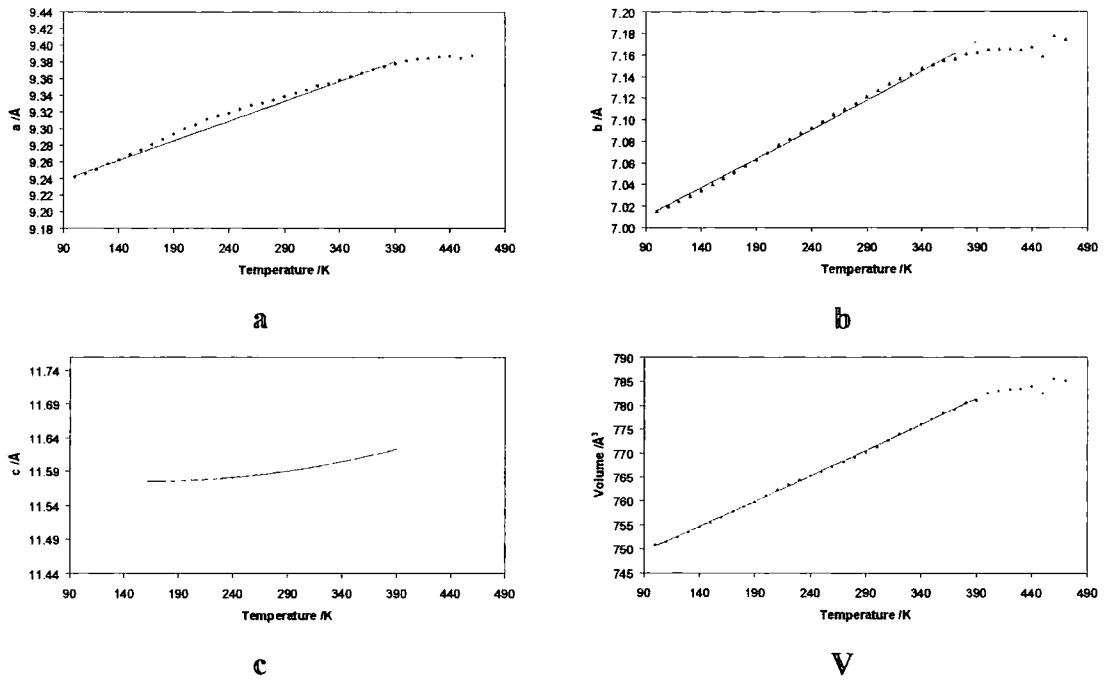

Figure 7.6 Variation in cell parameters and cell volume with temperature for $(NH_4)_2WS_3O$. *a* is shown in blue, *b* in red, *c* in yellow and volume in green. Values calculated using the Reeber equation are shown in grey.

The graphs in Figure 7.1 show that the expansion of cell parameters on heating $(NH_4)_2WS_3O$ is not smooth and is not fitted very well by using the Reeber equation (equation 4.2). The marked changes above ~390 K are caused by sample decomposition; the powder patterns at the highest temperatures show the material becomes amorphous in nature. Up until this point the unit cell shows a smooth increase in cell volume. However, the individual cell parameters all show slight changes in gradient around 300 K indicating that there may be a phase transition in this temperature region. The impure nature of this sample makes it difficult to be certain if this is really the case and further work would be needed to be sure if a phase transition occurs and to fully characterise the differences in the structure above and below the transition.

7.4 Summary

The structure of $(NH_4)_2WS_3O$ has been solved by simulated annealing in TOPAS. The material is a molecular solid which contains isolated WS_3O and NH_4 tetrahedra; it is structurally very similar to $(NH_4)_2WS_4$. A preliminary variable temperature investigation has identified a possible phase transition but further work would be needed to fully characterise the nature of the transition and be sure that it is a real phenomenon.

7.5 References

1. A. Müller, E. Diemann, R. Jostes, et al., *Angew. Chem. Int. Ed. Engl.*, 1981, **20**, 934-955.
2. J. S. O. Evans, *multivisser - A Fortran Routine for controlling Visser*, 2001.
3. G. S. Pawley, *J. Appl. Cryst.*, 1981, **14**, 357-361.
4. A. Altomare, M. C. Burla, G. Cascarano, et al., *J. Appl. Cryst.*, 1995, **28**, 842-846.
5. A. Altomare, G. Cascarano, C. Giacovazzo, et al., *J. Appl. Cryst.*, 1994, **27**, 435-436.
6. A. A. Coelho, *TOPAS v3.0 General Profile and Structure Analysis Software for Powder diffraction data, Bruker AXS, Karlsruhe*, 2001.
7. K. Sasvari, *Acta Cryst.*, 1963, **16**, 719-724.
8. W. Gonschorek, T. Hann and A. Mueller, *Z. Kristallogr.*, 1973, **138**, 380-389.
9. B. Krebs, B. Buss and A. Ferwahnah, *Z. Anorg. Allg. Chem.*, 1972, **387**, 142-153.

Appendix 2.1 Input file for simulated annealing of $(PPh_4)_2Ni(WS_4)_2$ structure

```
'------------------------------------------------
'Input file for structure solution of [Ph4P]2[Ni(WS4)2] structure
'Anneal rigid anion with centre fixed on origin and free rotation
'Anneal PPh4 units as rigid bodies with torsion angles, overall rotation and translation annealing
'Start annealing with PPh4 units on 0.5 0.5 0.5 and all the rotations of the anion at 0
'------------------------------------------------
continue_after_convergence
iters 10000000
'out_rwp(rfactors_anneal.txt)
'------------------------------------------------
'R factors
'------------------------------------------------
r_exp 1.699                          r_exp_dash 3.759          r_wp 6.426
r_wp_dash 14.214                     r_p 4.603                 r_p_dash 12.425
weighted_Durbin_Watson 0.194         gof 3.782
'------------------------------------------------
'General information about pattern/instrument
'------------------------------------------------
RAW(d8_02587_sum)
range 1
bkg  1942.41103 541.020012 -718.80711 -114.496376 451.224121 -78.6459046 -269.61824 80.7889508 178.085504
-51.0816 -59.0860661 60.166744 8.34904215
start_X  5
finish_X  40
Specimen_Displacement(, 0.25962)
Variable_Divergence_Intensity
LP_Factor( 27.26)
Rp 217.5
Rs 217.5
Simple_Axial_Model(, 6.95552)
lam
        ymin_on_ymax  0.001
        la  0.653817 lo  1.540596 lh  0.50184
'------------------------------------------------
'General structural information
'------------------------------------------------
str
'append_bond_lengths

scale  0.0037328123
PV_Peak_Type(, 0.06888,, 0.01637,, 0.01667,, 0.07691,, 3.21827,, 0.12659)
r_bragg  3.14927999
phase_name triclinic
space_group P1
MVW( 1361.716, 1253.1567, 100.000)
a @ 9.37510
al @ 65.81703
b @ 12.49702
be @ 83.74942
c @ 12.52234
ga @ 69.56599

'------------------------------------------------
'Atomic coordinates for anion
'------------------------------------------------
   macro A1(param,val) {x  val }
   macro A2(param,val) {y  val }
   macro A3(param,val) {z  val }
   macro bcont { val_on_continue = 1;}

site   Ni1   A1(xNi1 0     )    A2(yNi 0)          A3(zNi1 0)          occ   Ni   1  beq   b1   14.59   bcont
site   W1    A1(xW1 -0.09137)   A2(yW1 0.24803)    A3(zW1 -0.11715)    occ   W    1  beq   b1   14.59   bcont
site   W2    A1(xW2 0.09137)    A2(yW2 -0.24803)   A3(zW2 0.11715)     occ   W    1  beq   b1   14.59   bcont
```

```
site  S1  A1(xS1 0.15143)   A2(yS1 0.12193)   A3(zS1 -0.07537)   occ  S  1  beq  b1  14.59  bcont
site  S2  A1(xS2 -0.24605)  A2(yS2 0.13491)   A3(zS2 -0.04595)   occ  S  1  beq  b1  14.59  bcont
site  S3  A1(xS3 -0.13012)  A2(yS3 0.34909)   A3(zS3 -0.31171)   occ  S  1  beq  b1  14.59  bcont
site  S4  A1(xS4 -0.14074)  A2(yS4 0.38617)   A3(ZS4 -0.03559)   occ  S  1  beq  b1  14.59  bcont
site  S5  A1(xS5 0.24605)   A2(yS5 -0.13491)  A3(zS5 0.04595)    occ  S  1  beq  b1  14.59  bcont
site  S6  A1(xS6 -0.15143)  A2(yS6 -0.12193)  A3(zS6 0.07537)    occ  S  1  beq  b1  14.59  bcont
site  S7  A1(xS7 0.14074)   A2(yS7 -0.38617)  A3(zS7 0.03559)    occ  S  1  beq  b1  14.59  bcont
site  S8  A1(xS8 0.13012)   A2(yS8 -0.34909)  A3(zS8 0.31171)    occ  S  1  beq  b1  14.59  bcont

'-----------------------------------------------
'Atomic coordinates for cations
 '----------------------------------------------
'Cation 1
'-------
site  P1   A1(0.62598)   A2(0.22222)   A3(0.33374)   occ  P  1  beq  b1  14.59  bcont
site  C11  A1(0.82747)   A2(-0.00965)  A3(0.47065)   occ  C  1  beq  b1  14.59  bcont
site  C12  A1(0.95370)   A2(-0.11840)  A3(0.48887)   occ  C  1  beq  b1  14.59  bcont
site  C13  A1(0.87230)   A2(0.06821)   A3(0.26157)   occ  C  1  beq  b1  14.59  bcont
site  C14  A1(0.99857)   A2(-0.04054)  A3(0.27979)   occ  C  1  beq  b1  14.59  bcont
site  C15  A1(0.78679)   A2(0.08366)   A3(0.35700)   occ  C  1  beq  b1  14.59  bcont
site  C16  A1(1.03925)   A2(-0.13384)  A3(0.39344)   occ  C  1  beq  b1  14.59  bcont
site  C21  A1(0.60904)   A2(0.45395)   A3(0.16107)   occ  C  1  beq  b1  14.59  bcont
site  C22  A1(0.6557)    A2(0.55888)   A3(0.10661)   occ  C  1  beq  b1  14.59  bcont
site  C23  A1(0.80852)   A2(0.36275)   A3(0.31325)   occ  C  1  beq  b1  14.59  bcont
site  C24  A1(0.85518)   A2(0.46769)   A3(0.25879)   occ  C  1  beq  b1  14.59  bcont
site  C25  A1(0.68545)   A2(0.35589)   A3(0.26439)   occ  C  1  beq  b1  14.59  bcont
site  C26  A1(0.77877)   A2(0.56575)   A3(0.15547)   occ  C  1  beq  b1  14.59  bcont
site  C31  A1(0.3816)    A2(0.13258)   A3(0.15176)   occ  C  1  beq  b1  14.59  bcont
site  C32  A1(0.49251)   A2(0.12536)   A3(0.22395)   occ  C  1  beq  b1  14.59  bcont
site  C33  A1(0.25509)   A2(0.35180)   A3(0.11522)   occ  C  1  beq  b1  14.59  bcont
site  C35  A1(0.26289)   A2(0.24580)   A3(0.09739)   occ  C  1  beq  b1  14.59  bcont
site  C34  A1(0.36599)   A2(0.34459)   A3(0.18741)   occ  C  1  beq  b1  14.59  bcont
site  C36  A1(0.48470)   A2(0.23137)   A3(0.24178)   occ  C  1  beq  b1  14.59  bcont
site  C41  A1(0.49234)   A2(0.30052)   A3(0.62322)   occ  C  1  beq  b1  14.59  bcont
site  C42  A1(0.55435)   A2(0.30384)   A3(0.51485)   occ  C  1  beq  b1  14.59  bcont
site  C43  A1(0.41557)   A2(0.12543)   A3(0.64551)   occ  C  1  beq  b1  14.59  bcont
site  C44  A1(0.47758)   A2(0.12875)   A3(0.53714)   occ  C  1  beq  b1  14.59  bcont
site  C45  A1(0.42296)   A2(0.21132)   A3(0.68855)   occ  C  1  beq  b1  14.59  bcont
site  C46  A1(0.54697)   A2(0.21796)   A3(0.47181)   occ  C  1  beq  b1  14.59  bcont
site  H11  A1(0.76678)   A2(0.00130)   A3(0.53833)   occ  H  1  beq  b1  14.59  bcont
site  H12  A1(0.98255)   A2(-0.18459)  A3(0.56948)   occ  H  1  beq  b1  14.59  bcont
site  H13  A1(0.84349)   A2(0.13440)   A3(0.18096)   occ  H  1  beq  b1  14.59  bcont
site  H14  A1(1.05926)   A2(-0.05149)  A3(0.21210)   occ  H  1  beq  b1  14.59  bcont
site  H16  A1(1.12879)   A2(-0.21098)  A3(0.40637)   occ  H  1  beq  b1  14.59  bcont
site  H21  A1(0.52175)   A2(0.44908)   A3(0.12641)   occ  H  1  beq  b1  14.59  bcont
site  H22  A1(0.60150)   A2(0.62844)   A3(0.03332)   occ  H  1  beq  b1  14.59  bcont
site  H23  A1(0.86272)   A2(0.29319)   A3(0.38654)   occ  H  1  beq  b1  14.59  bcont
site  H24  A1(0.94247)   A2(0.47256)   A3(0.29345)   occ  H  1  beq  b1  14.59  bcont
site  H26  A1(0.81186)   A2(0.64018)   A3(0.11684)   occ  H  1  beq  b1  14.59  bcont
site  H31  A1(0.38714)   A2(0.05739)   A3(0.13911)   occ  H  1  beq  b1  14.59  bcont
site  H32  A1(0.57671)   A2(0.04506)   A3(0.26251)   occ  H  1  beq  b1  14.59  bcont
site  H33  A1(0.17088)   A2(0.43211)   A3(0.07666)   occ  H  1  beq  b1  14.59  bcont
site  H34  A1(0.36045)   A2(0.41978)   A3(0.20005)   occ  H  1  beq  b1  14.59  bcont
site  H35  A1(0.18423)   A2(0.25091)   A3(0.04619)   occ  H  1  beq  b1  14.59  bcont
site  H41  A1(0.49758)   A2(0.36144)   A3(0.65374)   occ  H  1  beq  b1  14.59  bcont
site  H42  A1(0.60357)   A2(0.36711)   A3(0.46851)   occ  H  1  beq  b1  14.59  bcont
site  H43  A1(0.36636)   A2(0.06216)   A3(0.69185)   occ  H  1  beq  b1  14.01  bcont
site  H44  A1(0.47235)   A2(0.06783)   A3(0.50662)   occ  H  1  beq  b1  14.59  bcont
site  H45  A1(0.37897)   A2(0.20896)   A3(0.76542)   occ  H  1  beq  b1  14.59  bcont

site  D11  A1(0.71904)   A2(0.04266)   A3(0.34498)   occ  P  0  beq  1
site  D12  A1(0.78679)   A2(0.08366)   A3(0.35700)   occ  P  0  beq  1
site  D21  A1(0.61350)   A2(0.39728)   A3(0.31208)   occ  P  0  beq  1
site  D22  A1(0.68545)   A2(0.35589)   A3(0.26439)   occ  P  0  beq  1
site  D31  A1(0.48470)   A2(0.23137)   A3(0.24178)   occ  P  0  beq  1
site  D32  A1(0.42091)   A2(0.20777)   A3(0.31117)   occ  P  0  beq  1
site  D41  A1(0.54697)   A2(0.21796)   A3(0.47181)   occ  P  0  beq  1
site  D42  A1(0.44675)   A2(0.27719)   A3(0.43111)   occ  P  0  beq  1
```

```
'Cation 2
'-------

site    P2      A1(-0.5)        A2(0.73014)     A3(0.65415)     occ     P   1   beq     b1      14.59
site    C51     A1(-0.77278)    A2(0.87487)     A3(0.70511)     occ     C   1   beq     b1      14.59   bcont
site    C52     A1(-0.90234)    A2(0.98278)     A3(0.67845)     occ     C   1   beq     b1      14.59   bcont
site    C53     A1(-0.68163)    A2(0.96387)     A3(0.50964)     occ     C   1   beq     b1      14.59   bcont
site    C54     A1(-0.81119)    A2(1.07178)     A3(0.48298)     occ     C   1   beq     b1      14.59   bcont
site    C55     A1(-0.66242)    A2(0.86542)     A3(0.62071)     occ     C   1   beq     b1      14.59   bcont
site    C56     A1(-0.92154)    A2(1.08123)     A3(0.56738)     occ     C   1   beq     b1      14.59   bcont
site    C61     A1(-0.45110)    A2(0.51751)     A3(0.85627)     occ     C   1   beq     b1      14.59   bcont
site    C62     A1(-0.48782)    A2(0.41416)     A3(0.93744)     occ     C   1   beq     b1      14.59   bcont
site    C63     A1(-0.67769)    A2(0.58027)     A3(0.73671)     occ     C   1   beq     b1      14.59   bcont
site    C64     A1(-0.71441)    A2(0.47692)     A3(0.81788)     occ     C   1   beq     b1      14.59   bcont
site    C65     A1(-0.54603)    A2(0.60057)     A3(0.75591)     occ     C   1   beq     b1      14.59   bcont
site    C66     A1(-0.61947)    A2(0.39386)     A3(0.91825)     occ     C   1   beq     b1      14.59   bcont
site    C71     A1(-0.25820)    A2(0.71334)     A3(0.36842)     occ     C   1   beq     b1      14.59   bcont
site    C72     A1(-0.30759)    A2(0.73253)     A3(0.47140)     occ     C   1   beq     b1      14.59   bcont
site    C73     A1(-0.46983)    A2(0.64125)     A3(0.37271)     occ     C   1   beq     b1      14.59   bcont
site    C75     A1(-0.33933)    A2(0.66770)     A3(0.31907)     occ     C   1   beq     b1      14.59   bcont
site    C74     A1(-0.51921)    A2(0.66044)     A3(0.47569)     occ     C   1   beq     b1      14.59   bcont
site    C76     A1(-0.43809)    A2(0.70608)     A3(0.52504)     occ     C   1   beq     b1      14.59   bcont
site    C81     A1(-0.27300)    A2(0.84337)     A3(0.82244)     occ     C   1   beq     b1      14.59   bcont
site    C82     A1(-0.38989)    A2(0.82873)     A3(0.77395)     occ     C   1   beq     b1      14.59   bcont
site    C83     A1(-0.08321)    A2(0.69751)     A3(0.75286)     occ     C   1   beq     b1      14.59   bcont
site    C84     A1(-0.20011)    A2(0.68288)     A3(0.70438)     occ     C   1   beq     b1      14.59   bcont
site    C85     A1(-0.11966)    A2(0.77776)     A3(0.81189)     occ     C   1   beq     b1      14.59   bcont
site    C86     A1(-0.35345)    A2(0.74849)     A3(0.71493)     occ     C   1   beq     b1      14.59   bcont
site    H51     A1(-0.75916)    A2(0.80504)     A3(0.78390)     occ     H   1   beq     b1      14.59   bcont
site    H52     A1(-0.98062)    A2(0.98948)     A3(0.73832)     occ     H   1   beq     b1      14.59   bcont
site    H53     A1(-0.60335)    A2(0.95717)     A3(0.44977)     occ     H   1   beq     b1      14.59   bcont
site    H54     A1(-0.82481)    A2(1.14161)     A3(0.40419)     occ     H   1   beq     b1      14.59   bcont
site    H56     A1(-1.01344)    A2(1.15777)     A3(0.54846)     occ     H   1   beq     b1      14.59   bcont
site    H61     A1(-0.35771)    A2(0.53191)     A3(0.86989)     occ     H   1   beq     b1      14.59   bcont
site    H62     A1(-0.42048)    A2(0.35524)     A3(1.00863)     occ     H   1   beq     b1      14.59   bcont
site    H63     A1(-0.74503)    A2(0.63919)     A3(0.66552)     occ     H   1   beq     b1      14.59   bcont
site    H64     A1(-0.80779)    A2(0.46253)     A3(0.80426)     occ     H   1   beq     b1      14.59   bcont
site    H66     A1(-0.64552)    A2(0.32055)     A3(0.97582)     occ     H   1   beq     b1      14.59   bcont
site    H71     A1(-0.16564)    A2(0.73210)     A3(0.33037)     occ     H   1   beq     b1      14.59   bcont
site    H72     A1(-0.25005)    A2(0.76490)     A3(0.50640)     occ     H   1   beq     b1      14.59   bcont
site    H73     A1(-0.52737)    A2(0.60888)     A3(0.33770)     occ     H   1   beq     b1      14.59   bcont
site    H74     A1(-0.61178)    A2(0.64168)     A3(0.51373)     occ     H   1   beq     b1      14.59   bcont
site    H75     A1(-0.3043)     A2(0.65409)     A3(0.24602)     occ     H   1   beq     b1      14.59   bcont
site    H81     A1(-0.29885)    A2(0.90028)     A3(0.86431)     occ     H   1   beq     b1      14.59   bcont
site    H82     A1(-0.49866)    A2(0.87527)     A3(0.78144)     occ     H   1   beq     b1      14.59   bcont
site    H83     A1(0.02555)     A2(0.65098)     A3(0.74538)     occ     H   1   beq     b1      14.59   bcont
site    H84     A1(-0.17426)    A2(0.62596)     A3(0.66251)     occ     H   1   beq     b1      14.59   bcont
site    H85     A1(-0.03674)    A2(0.78814)     A3(0.84628)     occ     H   1   beq     b1      14.59   bcont

site    D51     A1(-0.60675)    A2(0.90363)     A3(0.65037)     occ     P   0   beq     1
site    D52     A1(-0.66242)    A2(0.86542)     A3(0.62071)     occ     P   0   beq     1
site    D61     A1(-0.60646)    A2(0.65172)     A3(0.79992)     occ     P   0   beq     1
site    D62     A1(-0.54603)    A2(0.60057)     A3(0.75591)     occ     P   0   beq     1
site    D71     A1(-0.43809)    A2(0.70608)     A3(0.52504)     occ     P   0   beq     1
site    D72     A1(-0.37325)    A2(0.61882)     A3(0.57312)     occ     P   0   beq     1
site    D81     A1(-0.35345)    A2(0.74849)     A3(0.71493)     occ     P   0   beq     1
site    D82     A1(-0.35668)    A2(0.67788)     A3(0.79023)     occ     P   0   beq     1


'-----------------------------------------------
'Definitions of rigid bodies
'-----------------------------------------------

macro VRgu  { val_on_continue = Val + T Rand( -180,  180); }
macro VRtor { val_on_continue = 0 +  T Rand( -30,  30); }
macro Gux { val_on_continue = Val + T Rand(5, 5)/Lpa;  min -0.5 max 1.5}
macro Guy { val_on_continue = Val + T Rand(5, 5)/Lpb;  min -0.5 max 1.5}
macro Guz { val_on_continue = Val + T Rand(5, 5)/Lpc;  min -0.5 max 1.5}
```

```
'--------------------------------------------
'Definition the anion rigid body - use S-W-S angles as 109.47, a W-S distance of 2.240 and a Ni-S distance of 2.296,
geometry around Ni atom is distorted
'--------------------------------------------
rigid
'Ni(WS4)2 rigid unit
anion(Ni1,W1,S1,S2,S3,S4,W2,S5,S6,S7,S8)

'whole molecule position/rotation:
Rotate_about_axies(xrotNi1 156.08645 VRgu, yrotNi1  -0.00662 VRgu, zrotNi1 -92.13320 VRgu)
Translate(!xNi1  0.0 , !yNi1 0.0 , !zNi1  0.0 )

'--------------------------------------------
'Definition the 1st PPh4 rigid body
'--------------------------------------------
'rigid
'Central P atom
single_atom(P1)

'C6H5 ring2 in plane 1
 ring_1(C11,C12,C13,C14,C15,C16,H11,H12,H13,H14,H16,D11,D12,1.407)
Rotate_about_points(54.75 ,D11,D12, "C11 C12 C13 C14 C16 C15 H11 H12 H13 H14 H16")
Translate(-1.4636,-2.4419,0,"C11 C12 C13 C14 C15 C16 H11 H12 H13 H14 H16 D11 D12")
in_cartesian
Rotate_about_points(tor1 122.85833 min=-180; max=180; VRtor ,P1,C15,"C11 C12 C13 C14 C16 C15 H11 H12
H13 H14 H16 D11 D12")

'C6H5 ring2 in plane 1
 ring_1(C21,C22,C23,C24,C25,C26,H21,H22,H23,H24,H26,D21,D22,1.407)
Rotate_about_points(-54.75 ,D21,D22, "C21 C22 C23 C24 C26 C25 H21 H22 H23 H24 H26")
Translate(1.4636,-2.4419,0,"C21 C22 C23 C24 C25 C26 H21 H22 H23 H24 H26 D21 D22")
in_cartesian
Rotate_about_points(tor2 -52.57722 min=-180; max=180; VRtor ,P1,C25,"C21 C22 C23 C24 C26 C25 H21 H22
H23 H24 H26 D21 D22")

'C6H5 ring3 perpendicular to plane 1
 ring_2(C31,C32,C33,C34,C35,C36,H31,H32,H33,H34,H35,D31,D32,1.407)
 Rotate_about_points(-54.75 ,D31,D32, "C31 C32 C33 C34 C35 C36 H31 H32 H33 H34 H35")
Translate(0,2.4419,-1.46365,"C31 C32 C33 C34 C35 C36 H31 H32 H33 H34 H35 D31 D32")
in_cartesian
Rotate_about_points(tor3 -104.26126 min=-180; max=180; VRtor ,P1,C36,"C31 C32 C33 C34 C35 C36 H31 H32
H33 H34 H35 D31 D32")

'C6H5 ring4 perpendicular to plane 1
ring_2(C41,C42,C43,C44,C45,C46,H41,H42,H43,H44,H45,D41,D42,1.407)
Rotate_about_points(54.75 ,D41,D42, "C41 C42 C43 C44 C45 C46 H41 H42 H43 H44 H45")
Translate(0,2.4419,1.4636,"C41 C42 C43 C44 C45 C46 H41 H42 H43 H44 H45 D41 D42")
in_cartesian
Rotate_about_points(tor4 53.31435 min=-180; max=180; VRtor ,P1,C46,"C41 C42 C43 C44 C45 C46 H41 H42 H43
H44 H45 D41 D42")

'whole molecule position/rotation:
Rotate_about_axies(xrotP1 215.38165 VRgu, yrotP1  -188.94451 VRgu, zrotP1 -50.94896 VRgu)
Translate(xP1  0.62598 Gux, yP1 0.22222 Guy, zP1  0.33374 Guz)


'--------------------------------------------
'Definition of second PPh4 rigid body (Cation 2)
'--------------------------------------------
rigid
'Central P atom
single_atom(P2)

'C6H5 ring1 in plane 1
 ring_1(C51,C52,C53,C54,C55,C56,H51,H52,H53,H54,H56,D51,D52,1.407)
Rotate_about_points(54.75 ,D51,D52, "C51 C52 C53 C54 C56 C55 H51 H52 H53 H54 H56")
Translate(-1.4405,-2.425,0,"C51 C52 C53 C54 C55 C56 H51 H52 H53 H54 H56 D51 D52")
in_cartesian
```

```
Rotate_about_points(tor5 30.12681 min=-180; max=180; VRtor,P2,C55,"C51 C52 C53 C54 C56 C55 H51 H52 H53
H54 H56 D51 D52")

'C6H5 ring2 in plane 1
ring_1(C61,C62,C63,C64,C65,C66,H61,H62,H63,H64,H66,D61,D62,1.407)
Rotate_about_points(-54.75 ,D61,D62, "C61 C62 C63 C64 C66 C65 H61 H62 H63 H64 H66")
Translate(1.4405,-2.425,0,"C61 C62 C63 C64 C65 C66 H61 H62 H63 H64 H66 D61 D62")
in_cartesian
Rotate_about_points(tor6 48.38298 min=-180; max=180; VRtor,P2,C65,"C61 C62 C63 C64 C66 C65 H61 H62 H63
H64 H66 D61 D62")

'C6H5 ring3 perpendicular to plane 1
 ring_2(C71,C72,C73,C74,C75,C76,H71,H72,H73,H74,H75,D71,D72,1.407)
 Rotate_about_points(-54.75 ,D71,D72, "C71 C72 C73 C74 C75 C76 H71 H72 H73 H74 H75")
Translate(0,2.425,-1.4405,"C71 C72 C73 C74 C75 C76 H71 H72 H73 H74 H75 D71 D72")
in_cartesian
Rotate_about_points(tor7 -14.86342 min=-180; max=180; VRtor ,P2,C76,"C71 C72 C73 C74 C75 C76 H71 H72
H73 H74 H75 D71 D72")

'C6H5 ring4 perpendicular to plane 1
ring_2(C81,C82,C83,C84,C85,C86,H81,H82,H83,H84,H85,D81,D82,1.407)
Rotate_about_points(54.75 ,D81,D82, "C81 C82 C83 C84 C85 C86 H81 H82 H83 H84 H85")
Translate(0,2.425,1.4405,"C81 C82 C83 C84 C85 C86 H81 H82 H83 H84 H85 D81 D82")
in_cartesian
Rotate_about_points(tor8 -33.59419 min=-180; max=180; VRtor,P2,C86,"C81 C82 C83 C84 C85 C86 H81 H82 H83
H84 H85 D81 D82")

'whole molecule position/rotation:
Rotate_about_axies(xrotP2 -41.98086 VRgu, yrotP2  -3.34846 VRgu,zrotP2 -87.36576 VRgu)
Translate( xP2  -0.50000 Gux , yP2   0.73014 Guy, zP2   0.65415 Guz)

'-----------------------------------------------
'macro to define (WS4)Ni(WS4) unit
'-----------------------------------------------
'S3      S2      S5      S8
'   W1      Ni1     W2
'S4      S1      S6      S7

macro anion(s0, s1, s2, s3, s4, s5, s6, s7, s8, s9, s10)
{
  point_for_site s0  ux=  0.00000  ; uy=  0.00000  ; uz=  0.00000  ;
  point_for_site s1  ux= -2.68073  ; uy=  0.00000  ; uz=  0.00000  ;
  point_for_site s2  ux= -1.38802  ; uy= -1.82893  ; uz=  0.00000  ;
  point_for_site s3  ux= -1.38802  ; uy=  1.82893  ; uz=  0.00000  ;
  point_for_site s4  ux= -3.97344  ; uy=  0.00000  ; uz=  1.82893  ;
  point_for_site s5  ux= -3.97344  ; uy=  0.00000  ; uz= -1.82893  ;
  point_for_site s6  ux=  2.68073  ; uy=  0.00000  ; uz=  0.00000  ;
  point_for_site s7  ux=  1.38802  ; uy= -1.82893  ; uz=  0.00000  ;
  point_for_site s8  ux=  1.38802  ; uy=  1.82893  ; uz=  0.00000  ;
  point_for_site s9  ux=  3.97344  ; uy=  0.00000  ; uz=  1.82893  ;
  point_for_site s10 ux=  3.97344  ; uy=  0.00000  ; uz= -1.82893  ;
}


'-----------------------------------------------
'Macro to define a C6H6 ring sitting in the xy plane, with centre of hexagon at 0,0
'-----------------------------------------------
'          s5
's3                  s1
's4                  s2
'          s6

macro ring_1(s1,s2,s3,s4,s5,s6,s7,s8,s9,s10,s12,s13,s14,a)
{
  point_for_site s1  ux =  a Sqrt(3)/2; uy =  a/2;uz = 0;
  point_for_site s2  ux =  a Sqrt(3)/2; uy = -a/2;uz = 0;
  point_for_site s3  ux = -a Sqrt(3)/2; uy =  a/2;uz = 0;
  point_for_site s4  ux = -a Sqrt(3)/2; uy = -a/2;uz = 0;
  point_for_site s5  ux = 0; uy =  a; uz = 0;
```

```
  point_for_site s6  ux = 0; uy = -a; uz = 0;
  point_for_site s7  ux =  (a+0.998) Sqrt(3)/2; uy =  (a+0.998)/2; uz = 0;
  point_for_site s8  ux =  (a+0.998) Sqrt(3)/2; uy = -(a+0.998)/2; uz = 0;
  point_for_site s9  ux = -(a+0.998) Sqrt(3)/2; uy =  (a+0.998)/2; uz = 0;
  point_for_site s10 ux = -(a+0.998) Sqrt(3)/2; uy = -(a+0.998)/2; uz = 0;
  point_for_site s12 uy = -(a+0.998);
  point_for_site s13 ux = 0; uy = a; uz = 1;
  point_for_site s14 ux = 0; uy = a; uz = 0;
}
'-----------------------------------------------
'Macro to define a C6H6 ring sitting in the zy plane, with centre of hexagon at 0,0
'-----------------------------------------------
'          s5
's3                  s1
's4                  s2
'          s6

macro ring_2(s1,s2,s3,s4,s5,s6,s7,s8,s9,s10,s11,s13,s14,a)
{
  point_for_site s1  ux =  0; uy =  a/2;uz = a Sqrt(3)/2;
  point_for_site s2  ux =  0; uy = -a/2;uz = a Sqrt(3)/2;
  point_for_site s3  ux =  0; uy =  a/2;uz = -a Sqrt(3)/2;
  point_for_site s4  ux =  0; uy = -a/2;uz = -a Sqrt(3)/2;
  point_for_site s5  ux =  0; uy =  a;  uz = 0;
  point_for_site s6  ux =  0; uy =  -a; uz = 0;
  point_for_site s7  ux =  0; uy =  (a+0.998)/2; uz = (a+0.998) Sqrt(3)/2;
  point_for_site s8  ux =  0; uy = -(a+0.998)/2; uz = (a+0.998) Sqrt(3)/2;
  point_for_site s9  ux =  0; uy =  (a+0.998)/2; uz = -(a+0.998) Sqrt(3)/2;
  point_for_site s10 ux =  0; uy = -(a+0.998)/2; uz = -(a+0.998) Sqrt(3)/2;
  point_for_site s11 ux =  0; uy =  (a+0.998); uz = 0;
  point_for_site s13 ux =  0; uy = -a; uz = 0;
  point_for_site s14 ux =  1; uy = -a; uz = 0;
}
'-----------------------------------------------
'Macro to define a single atom at the centre of the rigid body
'-----------------------------------------------
macro single_atom(s1)
{
  point_for_site s1  ux = 0; uy = 0; uz = 0;
```

Appendix 2.2 Reagent Sources and Purities

Reagent	Source	Purity / Grade
Acetonitrile	Aldrich	99.5 %
butyronitrile	Lancaster	98 %
$(C_6H5)_4PCl$	Avocado	98 %
$(C_6H5)_4PBr$	Aldrich	97 %
$CoCl_2$	Aldrich	98 %
$Co(NO_3)_2.6H_2O$	Aldrich	98 %
Cu_2O	Avocado	98 %
Et_2O	Fischer Scientific	A.R.
N,N-Dimethylformamide	Aldrich	99.8 %
$FeCl_2$	Aldrich	98 %
HBF_4	Aldrich	48% by wt. solution in H_2O
H_2S	BOC	99 %
H_2WO_4	Aldrich	99 %
K	Aldrich	99.5 %
$MnCl_2$	Acros	97 %
$Mo(CO)_6$	Aldrich	98 %
$NH_3(g)$	BOC	99.98 %
NH_4OH	Aldrich	A.C.S
Na_2MoO_4	BDH	98 %
$NiCl_2$	Acros	97 %
Se	Alfa	99.999 % (200 mesh)
Tetrahydrofuran	Fischer Scientific	L.R.
$W(CO)_6$	Aldrich	97 %
$ZnCl_2$	Aldrich	98 %

Table A2.2.1 Reagent manufacturers and purities.

Appendix 3.1 Peak shape models for anisotropic peak shapes

The peak shape models used to describe anisotropic peak broadening in powder data were combinations of two isotropic models (pseudo Voigt and a combination of additional Gaussian and Lorentzian strain terms) and an anisotropic spherical harmonic function. These were combined either by simple addition or by convolution of the different functions. This appendix summarises the TOPAS commands for each of the individual peak shape functions and summarises which functions were used for each peak shape model.

Expressions 3.1.1 to 3.1.9 are the different commands which were used, multiplication by a factor of $\tan(\theta)$ shows the function is a strain type function, multiplication by a factor of $1/\cos(\theta)$ shows that the function is a size type function; the spherical harmonic function is represented as *sh* throughout.

Fwhm of the isotropic pseudo Voigt peak shape; *pka1*, *pka2* and *pka3* are refined parameters:

$$pv\_fwhm = pka1 + pka2 \times \tan(\theta) + pka3 / \cos(\theta) \qquad [3.1.1]$$

Isotropic Gaussian and Lorentzian strain peak shape; *pka4* and *pk5* are refined parameters:

$$gauss\_fwhm = pka4 \times \tan(\theta) \qquad [3.1.2]$$

$$lor\_fwhm = pka5 \times \tan(\theta) \qquad [3.1.3]$$

Isotropic PV with added spherical harmonic; *p1* and *p2* are refined scaling parameter:

$$pv\_fwhm = pka1 + pka2 \times \tan(\theta) + pka3 / \cos(\theta) + p1 \times sh / \cos(\theta) \qquad [3.1.4]$$

$$pv\_fwhm = pka1 + pka2 \times \tan(\theta) + pka3 / \cos(\theta) + p2 \times sh \times \tan(\theta) \qquad [3.1.5]$$

Gaussian and Lorentzian type spherical harmonic functions used if the spherical harmonic was convoluted with the isotropic peak shape; *p3*, *p4*, *p5* and *p6* are refined scaling factors:

$$gauss\_fwhm = p3 \times sh \times \tan(\theta) \qquad [3.1.6]$$

$$gauss\_fwhm = p4 \times sh / \cos(\theta) \qquad [3.1.7]$$

$$lor\_fwhm = p5 \times sh \times \tan(\theta) \qquad [3.1.8]$$

$$lor\_fwhm = p6 \times sh / \cos(\theta) \qquad [3.1.9]$$

Peak shape	Functions used
PV only	3.1.1
G/L strain	3.1.2, 3.1.3
PV convoluted G/L strain	3.1.1, 3.1.2, 3.1.3
PV add size SH	3.1.4
PV add strain SH	3.1.5
PV convoluted size SH	3.1.1, 3.1.7, 3.1.9
PV convoluted strain SH	3.1.1, 3.1.6, 3.1.8
G/L strain convoluted size SH	3.1.2, 3.1.3, 3.1.7, 3.1.9
G/L strain convoluted strain SH	3.1.2, 3.1.3, 3.1.6, 3.1.8
PV convoluted size/strain SH	3.1.1, 3.1.6, 3.1.7, 3.1.8, 3.1.9
G/L strain convoluted size/strain SH	3.1.2, 3.1.3, 3.1.6, 3.1.7, 3.1.8, 3.1.9
size/strain SH only	3.1.6, 3.1.7, 3.1.8, 3.1.9

Table A3.1.1 Functions included in TOPAS input file for different peak shape models.

Appendix 4.1 Fractional atomic coordinates for PPh_4CuWS_4

Atom	*x/a*	*y/b*	*z/c*	U_{iso} /Å^2
M1	0.124 (1)	0.4956 (9)	0.2485 (5)	0.118 (5)
M1	0.3734 (9)	0.4998 (8)	0.2480 (4)	0.092 (5)
Se1	0.0	0.329 (2)	0.25	0.098 (1)
Se2	0.0	0.652 (2)	0.25	0.098 (1)
Se3	0.235 (1)	0.500 (1)	0.153 (1)	0.098 (1)
Se4	0.255 (2)	0.512 (1)	0.344 (1)	0.098 (1)
Se5	0.5	0.672 (2)	0.25	0.098 (1)
Se6	0.5	0.329 (2)	0.25	0.098 (1)
P1	0.235 (1)	0.1028 (4)	0.5071 (6)	0.051 (3)
C11	0.428	0.208	0.450	0.051 (3)
C12	0.527	0.281	0.451	0.051 (3)
C13	0.399	0.257	0.567	0.051 (3)
C14	0.498	0.329	0.568	0.051 (3)
C15	0.364	0.196	0.508	0.051 (3)
C16	0.562	0.341	0.510	0.051 (3)
C21	0.143	0.058	0.377	0.051 (3)
C22	0.134	0.996	0.316	0.051 (3)
C23	0.299	0.927	0.417	0.051 (3)
C24	0.290	0.866	0.356	0.051 (3)
C25	0.225	0.023	0.428	0.051 (3)
C26	0.207	0.900	0.305	0.051 (3)
C31	0.171	0.837	0.640	0.051 (3)
C32	0.161	0.916	0.586	0.051 (3)
C33	0.355	0.928	0.677	0.051 (3)
C35	0.268	0.843	0.686	0.051 (3)
C34	0.344	0.007	0.623	0.051 (3)
C36	0.248	0.000	0.577	0.051 (3)
C41	0.995	0.369	0.488	0.051 (3)
C42	0.095	0.300	0.482	0.051 (3)
C43	0.915	0.222	0.561	0.051 (3)
C44	0.015	0.153	0.555	0.051 (3)
C45	0.905	0.330	0.528	0.051 (3)
C46	0.105	0.192	0.515	0.051 (3)
H11	0.403	0.165	0.407	0.051 (3)
H12	0.573	0.289	0.409	0.051 (3)
H13	0.354	0.248	0.608	0.051 (3)
H14	0.524	0.372	0.610	0.051 (3)
H16	0.633	0.393	0.511	0.051 (3)
H21	0.090	0.126	0.385	0.051 (3)
H22	0.075	0.021	0.280	0.051 (3)
H23	0.358	0.902	0.454	0.051 (3)
H24	0.343	0.797	0.349	0.051 (3)
H26	0.201	0.857	0.261	0.051 (3)
H31	0.109	0.776	0.646	0.051 (3)
H32	0.091	0.911	0.553	0.051 (3)
H33	0.424	0.932	0.710	0.051 (3)
H34	0.407	0.067	0.617	0.051 (3)
H35	0.275	0.787	0.725	0.051 (3)
H41	0.988	0.447	0.464	0.051 (3)
H42	0.160	0.328	0.454	0.051 (3)
H43	0.850	0.194	0.590	0.051 (3)
H44	0.022	0.075	0.579	0.051 (3)
H45	0.833	0.380	0.532	0.051 (3)

Table A4.1.1 Fractional atomic coordinates for atoms in PPh_4CuWS_4.

Appendix 5.1 Fractional atomic coordinates, anisotropic temperature factors and bond lengths and angles for the substructure of the tetragonal form of $(PPh_4)_2Zn(WS_4)_2$

Atom	*x/a*	*y/b*	*z/c*	Occupancy	U_{eq} /Å^2
Zn1	0	0	0	0.5	0.0166
W1	0	0	-0.43141(3)	0.5	0.0115
S1	0.12914(9)	0.03952(10)	0.2335(2)	0.5	0.017
S2	-0.03870(11)	0.12713(11)	-0.3831(2)	0.5	0.0194
P1	0	0.5	-0.25	1	0.0177
C1	0.0990(2)	0.4532(2)	-0.4054(4)	1	0.0195
C2	0.1280(2)	0.3512(2)	-0.4051(5)	1	0.0242
C3	0.2045(3)	0.3195(2)	-0.5300(5)	1	0.0312
C4	0.1452(2)	0.5208(2)	-0.5349(5)	1	0.0277
C5	0.2529(4)	0.3873(3)	-0.6514(6)	1	0.0407
C6	0.2232(3)	0.4889(3)	-0.6558(5)	1	0.0368
H21	0.093	0.3018	-0.3153	1	0.0291
H31	0.2248	0.2461	-0.5327	1	0.0358
H41	0.1213	0.5930	-0.5404	1	0.032
H51	0.3109	0.3641	-0.7370	1	0.0485
H61	0.2586	0.5389	-0.7452	1	0.0431

Table A5.1.1 Fractional atomic coordinates for the substructure of the tetragonal form of $(PPh_4)_2Zn(WS_4)_2$.

Atom	u_{11}	u_{22}	u_{33}	u_{23}	u_{13}	u_{12}
Zn1	0.0191(3)	0.0191(3)	0.0115(4)	0	0	0
W1	0.01286(15)	0.01047(14)	0.01105(8)	0	0	0.00078(12)
S1	0.0136(5)	0.0210(5)	0.0165(5)	0.0008(5)	0.0015(4)	-0.0020(4)
S2	0.0207(6)	0.0186(6)	0.0190(6)	-0.0037(5)	0.0020(5)	-0.0005(4)
P1	0.0164(3)	0.0164(3)	0.0202(6)	0	0	0
C1	0.0217(11)	0.0183(10)	0.0186(13)	0.0012(10)	0.0011(10)	0.0025(8)
C2	0.0320(14)	0.0161(11)	0.0246(15)	-0.0016(11)	-0.0019(12)	0.0011(9)
C3	0.0463(17)	0.0245(12)	0.023(3)	-0.0011(10)	0.0068(12)	0.0137(12)
C4	0.0329(14)	0.0235(12)	0.027(2)	0.0063(10)	0.0062(11)	0.0099(10)
C5	0.056(3)	0.0371(19)	0.0292(18)	0.0038(14)	0.0171(16)	0.0222(18)
C6	0.046(2)	0.0342(18)	0.0300(17)	0.0105(13)	0.0193(15)	0.0143(16)

Table A5.1.2 Anisotropic temperature factors for the substructure of the tetragonal form of $(PPh_4)_2Zn(WS_4)_2$.

Bond Lengths /Å		Bond Angles /°	
Zn1 – W1	2.9237(3)	W(1) – W(1) – S(1)	126.90(4)
Zn1 – W1	2.9237(3)	S(1) – W(1) – S(1)	106.20(7)
Zn1 – S1	2.3866(13)	Zn(1) – W(1) – S(2)	79.45(5)
Zn1 – S1	2.3866(13)	W(1) – W(1) – S(2)	100.55(5)
Zn1 – S1	2.3866(13)	S(1) – W(1) – S(2)	132.56(6)
Zn1 – S1	2.3866(13)	S(1) – W(1) – S(2)	26.35(6)
W1 – W1	0.9296(5)	Zn(1) – W(1) – S(2)	125.56(4)
W1 – S1	2.2342(13)	W(1) – W(1) – S(2)	54.44(4)
W1 – S1	2.2342(13)	S(1) – W(1) – S(2)	110.38(5)
W1 – S2	1.7883(15)	S(1) – W(1) – S(2)	110.50(5)
W1 – S2	2.1611(14)	S(2) – W(1) – S(2)	96.11(3)
W1 – S2	1.7883(15)	Zn(1) – W(1) – S(2)	79.45(5)
W1 – S2	2.1611(14)	W(1) – W(1) – S(2)	100.55(5)
S1 – S2	1.015(2)	S(1) – W(1) – S(2)	26.35(6)
P1 – C1	1.791(3)	S(1) – W(1) – S(2)	132.56(6)
P1 – C1	1.791(3)	S(2) – W(1) – S(2)	158.91(9)
P1 – C1	1.791(3)	Zn(1) – W(1) – S(2)	125.56(4)
P1 – C1	1.791(3)	W(1) – W(1) – S(2)	54.44(4)
C1 – C2	1.403(4)	S(1) – W(1) – S(2)	110.50(5)
C1 – C4	1.395(4)	S(1) – W(1) – S(2)	110.38(5)
C2 – C3	1.385(4)	S(2) – W(1) – S(2)	96.11(3)
C3 – C5	1.375(5)	S(2) – W(1) – S(2)	96.11(3)
C4 – C6	1.382(4)	S(2) – W(1) – S(2)	108.88(8)
C5 – C6	1.402(5)	S(2) – W(1) – S(2)	96.11(3)
		Zn(1) – S(1) – W(1)	78.43(4)
Bond Angles /°		Zn(1) - S(1) - S(2)	129.91(14)
W(1) – Zn(1) – W(1)	180	W(1) – S(1) – S(2)	51.48(11)
W(1) – Zn(1) – S(1)	131.53(3)	W(1) – S(2) – W(1)	25.02(2)
W(1) – Zn(1) – S(1)	48.47(3)	W(1) – S(2) – S(1)	102.16(14)
W(1) – Zn(1) – S(1)	48.47(3)	W(1) – S(2) – S(1)	127.18(14)
W(1) – Zn(1) – S(1)	131.53(3)	C(1) – P(1) – C(1)	110.21(9)
S(1) – Zn(1) – S(1)	116.07(3)	C(1) – P(1) – C(1)	107.99(18)
W(1) – Zn(1) – S(1)	131.53(3)	C(1) – P(1) – C(1)	110.21(9)
W(1) – Zn(1) – S(1)	48.47(3)	C(1) – P(1) – C(1)	110.21(9)
S(1) – Zn(1) – S(1)	96.95(6)	C(1) – P(1) – C(1)	107.99(18)
S(1) – Zn(1) – S(1)	116.07(3)	C(1) – P(1) – C(1)	110.21(9)
W(1) – Zn(1) – S(1)	48.47(3)	P(1) – C(1) – C(2)	122.1(2)
W(1) – Zn(1) – S(1)	131.53(3)	P(1) – C(1) – C(4)	118.0(2)
S(1) – Zn(1) – S(1)	116.07(3)	C(2) – C(1) – C(4)	119.9(3)
S(1) – Zn(1) – S(1)	96.95(6)	C(1) – C(2) – C(3)	119.3(3)
S(1) – Zn(1) – S(1)	116.07(3)	C(2) – C(3) – C(5)	120.6(3)
Zn(1) – W(1) – W(1)	179.99	C(1) – C(4) – C(6)	120.3(3)
Zn(1) – W(1) – S(1)	53.10(4)	C(3) – C(5) – C(6)	120.5(3)
W(1) – W(1) – S(1)	126.90(4)	C(4) – C(6) – C(5)	119.3(3)
Zn(1) – W(1) – S(1)	53.10(4)		

Table A5.1.3 Bond lengths and angles in the substructure of the tetragonal form of $(PPh_4)_2Zn(WS_4)_2$.

Appendix 5.2 Fractional atomic coordinates and bond lengths and angles for the superstructure of the tetragonal form of $(PPh_4)_2Zn(WS_4)_2$

Atom	*x/a*	*y/b*	*z/c*	Occupancy	U_{iso} /Å^2
Zn(1)	0	0	0	0.64212(3)	0.01264(7)
Zn(2)	-0.5	0	0.25	0.77202(3)	0.01457(7)
Zn(3)	0	0	-0.5	0.35788(3)	0.01307(7)
Zn(4)	-0.5	0	0.75	0.22798(3)	0.09228(7)
W(1)	-0.5	0	0.46544(5)	0.77202(3)	0.01218(6)
W(2)	0	0	-0.21553(7)	0.64212(3)	0.00539(6)
W(3)	-0.5	0	0.53221(9)	0.22798(3)	0.09076(7)
W(4)	0	0	-0.28467(7)	0.35788(3)	0.00978(6)
S(1)	-0.08535(8)	0.04132(9)	0.11725(9)	0.64212(3)	0.01185(3)
S(2)	-0.54741(8)	-0.08354(8)	0.13360(9)	0.77202(3)	0.01185(3)
S(3)	-0.08666(8)	0.04323(9)	-0.30639(9)	0.64212(3)	0.01185(3)
S(4)	-0.54483(8)	-0.08040(8)	0.56026(9)	0.77202(3)	0.01185(3)
S(5)	-0.04521(9)	-0.08939(9)	-0.19561(9)	0.35788(3)	0.01838(3)
S(6)	-0.44409(9)	0.08304(9)	0.63566(9)	0.22798(3)	0.01838(3)
S(7)	-0.57241(9)	0.04575(9)	0.43553(9)	0.22798(3)	0.01838(3)
S(8)	-0.08599(9)	0.03909(9)	-0.38189(9)	0.35788(3)	0.01838(3)
P(1)	-0.24958(8)	0.25306(7)	0.12067(9)		0.01256(7)
C(11)	-0.22821(9)	0.17588(9)	0.04485(9)		0.03105(7)
C(12)	-0.17392(7)	0.18958(7)	-0.02216(7)		0.02905(7)
C(13)	-0.14999(7)	0.13579(6)	-0.08470(7)		0.01126(7)
C(14)	-0.18136(7)	0.06870(7)	-0.08112(7)		0.03134(7)
C(15)	-0.23784(7)	0.05573(7)	-0.01742(7)		0.03199(7)
C(16)	-0.26126(7)	0.10928(7)	0.04570(7)		0.02628(7)
C(21)	-0.31947(9)	0.22613(9)	0.20336(9)		0.00105(7)
C(22)	-0.31061(7)	0.16833(7)	0.26681(7)		0.01679(7)
C(23)	-0.36745(7)	0.14698(7)	0.32534(7)		0.02966(7)
C(24)	-0.43011(7)	0.18731(7)	0.32772(7)		0.01529(7)
C(25)	-0.43881(6)	0.24562(7)	0.26512(7)		0.00924(7)
C(26)	-0.38315(6)	0.26504(7)	0.20264(7)		0.00943(7)
C(31)	-0.27396(9)	0.32912(9)	0.04362(9)		0.02515(7)
C(32)	-0.32872(7)	0.31333(7)	-0.02179(7)		0.04463(7)
C(33)	-0.35306(7)	0.36577(7)	-0.08582(7)		0.01495(7)
C(34)	-0.32631(7)	0.43467(7)	-0.07970(7)		0.03020(7)
C(35)	-0.27014(7)	0.44976(7)	-0.01597(7)		0.02015(7)
C(36)	-0.24272(7)	0.39632(7)	0.04401(7)		0.01686(7)
C(41)	-0.17915(9)	0.27983(9)	0.20211(9)		0.00252(7)
C(42)	-0.11613(6)	0.24058(7)	0.20251(7)		0.01192(7)
C(43)	-0.05972(7)	0.26185(7)	0.26288(7)		0.02237(7)
C(44)	-0.06575(7)	0.32419(7)	0.31873(7)		0.03015(7)
C(45)	-0.12822(7)	0.36433(7)	0.31619(7)		0.01441(7)
C(46)	-0.18605(6)	0.34012(6)	0.26115(7)		0.01161(7)
H(121)	-0.15379(7)	0.23887(7)	-0.02809(7)		0.0441
H(131)	-0.10802(7)	0.14492(6)	-0.12850(7)		0.0493
H(141)	-0.15995(7)	0.02851(7)	-0.11965(7)		0.0525
H(151)	-0.25942(7)	0.00695(7)	-0.01355(7)		0.0559
H(161)	-0.30386(7)	0.10059(7)	0.08853(7)		0.0548
H(221)	-0.26460(7)	0.14127(7)	0.26403(7)		0.0406
H(231)	-0.36022(7)	0.10439(7)	0.36870(7)		0.0394
H(241)	-0.46929(7)	0.17130(7)	0.37270(7)		0.0437
H(251)	-0.48537(6)	0.27178(7)	0.26597(7)		0.0451
H(261)	-0.38938(6)	0.30905(7)	0.16175(7)		0.0457
H(321)	-0.35052(7)	0.26463(7)	-0.02523(7)		0.0525
H(331)	-0.39768(7)	0.35789(7)	-0.12487(7)		0.0478
H(341)	-0.34808(7)	0.47513(7)	-0.11730(7)		0.0486

Atom	*x/a*	*y/b*	*z/c*	Occupancy	U_{iso} /Å^2
H(351)	-0.24737(7)	0.49806(7)	-0.01420(7)		0.0514
H(361)	-0.19903(7)	0.40445(7)	0.08491(7)		0.0522
H(421)	-0.10989(6)	0.19753(7)	0.15973(7)		0.0445
H(431)	-0.01414(7)	0.23406(7)	0.26526(7)		0.0458
H(441)	-0.02699(7)	0.33860(7)	0.36541(7)		0.0466
H(451)	-0.13335(7)	0.40902(7)	0.35594(7)		0.0428
H(461)	-0.23194(6)	0.36741(6)	0.25943(7)		0.0436

Table A5.2.1 Fractional atomic coordinates for the superstructure of the tetragonal form of $(PPh_4)_2Zn(WS_4)_2$.

Bond Lengths /Å

Zn(1) - W(2)	2.9233(13)	W(1) - S(4)	2.1504(15)	P(1) - C(31)	1.824(2)
Zn(1) - W(2)	2.9233(13)	W(1) - S(7)	1.6542(17)	P(1) - C(41)	1.792(2)
Zn(1) - S(1)	2.3835(15)	W(1) - S(7)	1.6542(17)	C(11) - C(12)	1.3876(19)
Zn(1) - S(1)	2.3835(15)	W(2) - W(4)	0.9378(13)	C(11) - C(16)	1.392(2)
Zn(1) - S(1)	2.3835(15)	W(2) - S(1)	2.2201(16)	C(12) - C(13)	1.3909(16)
Zn(1) - S(1)	2.3835(15)	W(2) - S(1)	2.2201(16)	C(13) - C(14)	1.3874(17)
Zn(2) - W(1)	2.9220(12)	W(2) - S(3)	2.1923(16)	C(14) - C(15)	1.3870(16)
Zn(2) - W(1)	2.9220(12)	W(2) - S(3)	2.1923(16)	C(15) - C(16)	1.3894(16)
Zn(2) - S(2)	2.3931(14)	W(2) - S(5)	1.8948(17)	C(21) - C(22)	1.3926(19)
Zn(2) - S(2)	2.3931(14)	W(2) - S(5)	1.8948(17)	C(21) - C(26)	1.397(2)
Zn(2) - S(2)	2.3931(14)	W(3) - S(4)	1.7649(16)	C(22) - C(23)	1.3866(16)
Zn(2) - S(2)	2.3931(14)	W(3) - S(4)	1.7649(16)	C(23) - C(24)	1.3955(17)
Zn(3) - W(4)	2.9206(13)	W(3) - S(6)	2.3413(18)	C(24) - C(25)	1.3926(16)
Zn(3) - W(4)	2.9206(13)	W(3) - S(6)	2.3413(18)	C(25) - C(26)	1.3916(16)
Zn(3) - S(8)	2.3862(16)	W(3) - S(7)	2.0715(18)	C(31) - C(32)	1.3876(19)
Zn(3) - S(8)	2.3862(16)	W(3) - S(7)	2.0715(18)	C(31) - C(36)	1.388(2)
Zn(3) - S(8)	2.3862(16)	W(4) - S(3)	1.8370(16)	C(32) - C(33)	1.3879(16)
Zn(3) - S(8)	2.3862(16)	W(4) - S(3)	1.8370(16)	C(33) - C(34)	1.3863(17)
Zn(4) - W(3)	2.9539(16)	W(4) - S(5)	2.2308(17)	C(34) - C(35)	1.3902(16)
Zn(4) - W(3)	2.9539(16)	W(4) - S(5)	2.2308(17)	C(35) - C(36)	1.3879(16)
Zn(4) - S(6)	2.4327(16)	W(4) - S(8)	2.2059(17)	C(41) - C(42)	1.390(2)
Zn(4) - S(6)	2.4327(16)	W(4) - S(8)	2.2059(17)	C(41) - C(46)	1.3898(19)
Zn(4) - S(6)	2.4327(16)	S(1) - S(5)	1.0680(18)	C(42) - C(43)	1.3943(16)
Zn(4) - S(6)	2.4327(16)	S(2) - S(7)	0.9610(18)	C(43) - C(44)	1.3961(16)
W(1) - W(3)	0.9057(15)	S(3) - S(8)	1.0270(18)	C(44) - C(45)	1.3906(17)
W(1) - S(2)	2.2447(15)	S(4) - S(6)	1.0447(18)	C(45) - C(46)	1.3912(16)
W(1) - S(2)	2.2447(15)	P(1) - C(11)	1.818(2)		
W(1) - S(4)	2.1504(15)	P(1) - C(21)	1.796(2)		

Bond Angles /°

W(2) - Zn(1) - W(2)	180	Zn(4) - W(3) - S(4)	77.55(6)
W(2) - Zn(1) - S(1)	131.85(3)	W(1) - W(3) - S(4)	102.45(6)
W(2) - Zn(1) - S(1)	48.15(3)	Zn(4) - W(3) - S(4)	77.55(6)
W(2) - Zn(1) - S(1)	48.15(3)	W(1) - W(3) - S(4)	102.45(6)
W(2) - Zn(1) - S(1)	131.85(3)	S(4) - W(3) - S(4)	155.10(11)
S(1) - Zn(1) - S(1)	116.44(4)	Zn(4) - W(3) - S(6)	53.18(4)
W(2) - Zn(1) - S(1)	131.85(3)	W(1) - W(3) - S(6)	126.82(4)
W(2) - Zn(1) - S(1)	48.15(3)	S(4) - W(3) - S(6)	130.53(8)
S(1) - Zn(1) - S(1)	96.29(7)	S(4) - W(3) - S(6)	24.75(6)
S(1) - Zn(1) - S(1)	116.44(4)	Zn(4) - W(3) - S(6)	53.18(4)
W(2) - Zn(1) - S(1)	48.15(3)	W(1) - W(3) - S(6)	126.82(4)
W(2) - Zn(1) - S(1)	131.85(3)	S(4) - W(3) - S(6)	24.75(6)
S(1) - Zn(1) - S(1)	116.44(4)	S(4) - W(3) - S(6)	130.53(8)
S(1) - Zn(1) - S(1)	96.29(7)	S(6) - W(3) - S(6)	106.36(9)
S(1) - Zn(1) - S(1)	116.44(4)	Zn(4) - W(3) - S(7)	129.27(5)
W(1) - Zn(2) - W(1)	180	W(1) - W(3) - S(7)	50.73(5)
W(1) - Zn(2) - S(2)	131.28(3)	S(4) - W(3) - S(7)	100.25(7)

Bond Angles /°

W(1) - Zn(2) - S(2)	48.72(3)	S(4) - W(3) - S(7)	95.45(7)
W(1) - Zn(2) - S(2)	48.72(3)	S(6) - W(3) - S(7)	113.42(6)
W(1) - Zn(2) - S(2)	131.28(3)	Zn(4) - W(3) - S(7)	129.27(5)
S(2) - Zn(2) - S(2)	115.80(4)	W(1) - W(3) - S(7)	50.73(5)
W(1) - Zn(2) - S(2)	131.28(3)	S(4) - W(3) - S(7)	95.45(7)
W(1) - Zn(2) - S(2)	48.72(3)	S(4) - W(3) - S(7)	100.25(7)
S(2) - Zn(2) - S(2)	97.44(7)	S(6) - W(3) - S(7)	111.18(6)
S(2) - Zn(2) - S(2)	115.80(4)	S(6) - W(3) - S(7)	111.18(6)
W(1) - Zn(2) - S(2)	48.72(3)	S(6) - W(3) - S(7)	113.42(6)
W(1) - Zn(2) - S(2)	131.28(3)	S(7) - W(3) - S(7)	101.45(10)
S(2) - Zn(2) - S(2)	115.80(4)	Zn(3) - W(4) - W(2)	179.99
S(2) - Zn(2) - S(2)	97.44(7)	Zn(3) - W(4) - S(3)	80.77(5)
S(2) - Zn(2) - S(2)	115.80(4)	W(2) - W(4) - S(3)	99.23(5)
W(4) - Zn(3) - W(4)	180	Zn(3) - W(4) - S(3)	80.77(5)
W(4) - Zn(3) - S(8)	47.83(4)	W(2) - W(4) - S(3)	99.23(5)
W(4) - Zn(3) - S(8)	132.17(4)	S(3) - W(4) - S(3)	161.55(10)
W(4) - Zn(3) - S(8)	132.17(4)	Zn(3) - W(4) - S(5)	122.78(4)
W(4) - Zn(3) - S(8)	47.83(4)	W(2) - W(4) - S(5)	57.22(4)
S(8) - Zn(3) - S(8)	116.79(4)	S(3) - W(4) - S(5)	94.72(7)
W(4) - Zn(3) - S(8)	47.83(4)	S(3) - W(4) - S(5)	95.24(6)
W(4) - Zn(3) - S(8)	132.17(4)	Zn(3) - W(4) - S(5)	122.78(4)
S(8) - Zn(3) - S(8)	95.66(7)	W(2) - W(4) - S(5)	57.22(4)
S(8) - Zn(3) - S(8)	116.79(4)	S(3) - W(4) - S(5)	95.24(6)
W(4) - Zn(3) - S(8)	132.17(4)	S(3) - W(4) - S(5)	94.72(7)
W(4) - Zn(3) - S(8)	47.83(4)	S(5) - W(4) - S(5)	114.43(9)
S(8) - Zn(3) - S(8)	116.79(4)	Zn(3) - W(4) - S(8)	53.29(4)
S(8) - Zn(3) - S(8)	95.66(7)	W(2) - W(4) - S(8)	126.71(4)
S(8) - Zn(3) - S(8)	116.79(4)	S(3) - W(4) - S(8)	27.54(5)
W(3) - Zn(4) - W(3)	180	S(3) - W(4) - S(8)	134.03(7)
W(3) - Zn(4) - S(6)	50.39(4)	S(5) - W(4) - S(8)	107.20(6)
W(3) - Zn(4) - S(6)	129.61(4)	Zn(3) - W(4) - S(8)	53.29(4)
W(3) - Zn(4) - S(6)	129.61(4)	W(2) - W(4) - S(8)	126.71(4)
W(3) - Zn(4) - S(6)	50.39(4)	S(3) - W(4) - S(8)	134.03(7)
S(6) - Zn(4) - S(6)	113.98(4)	S(3) - W(4) - S(8)	27.55(5)
W(3) - Zn(4) - S(6)	50.39(4)	S(5) - W(4) - S(8)	110.59(6)
W(3) - Zn(4) - S(6)	129.61(4)	S(5) - W(4) - S(8)	110.59(6)
S(6) - Zn(4) - S(6)	100.79(7)	S(5) - W(4) - S(8)	107.20(6)
S(6) - Zn(4) - S(6)	113.98(4)	S(8) - W(4) - S(8)	106.59(9)
W(3) - Zn(4) - S(6)	129.61(4)	Zn(1) - S(1) - W(2)	78.75(6)
W(3) - Zn(4) - S(6)	50.39(4)	Zn(1) - S(1) - S(5)	137.19(15)
S(6) - Zn(4) - S(6)	113.98(4)	W(2) - S(1) - S(5)	58.48(12)
S(6) - Zn(4) - S(6)	100.79(7)	Zn(2) - S(2) - W(1)	78.03(5)
S(6) - Zn(4) - S(6)	113.98(4)	Zn(2) - S(2) - S(7)	119.33(15)
Zn(2) - W(1) - W(3)	179.99	W(1) - S(2) - S(7)	41.60(12)
Zn(2) - W(1) - S(2)	53.24(4)	W(2) - S(3) - W(4)	24.98(4)
W(3) - W(1) - S(2)	126.76(4)	W(2) - S(3) - S(8)	121.57(15)
Zn(2) - W(1) - S(2)	53.24(4)	W(4) - S(3) - S(8)	96.65(14)
W(3) - W(1) - S(2)	126.76(4)	W(1) - S(4) - W(3)	24.28(5)
S(2) - W(1) - S(2)	106.49(8)	W(1) - S(4) - S(6)	134.12(15)
Zn(2) - W(1) - S(4)	126.73(4)	W(3) - S(4) - S(6)	110.23(15)
W(3) - W(1) - S(4)	53.27(4)	W(2) - S(5) - W(4)	24.59(4)
S(2) - W(1) - S(4)	111.27(6)	W(2) - S(5) - S(1)	92.80(14)
S(2) - W(1) - S(4)	110.67(6)	W(4) - S(5) - S(1)	117.38(15)
Zn(2) - W(1) - S(4)	126.73(4)	Zn(4) - S(6) - W(3)	76.42(6)
W(3) - W(1) - S(4)	53.27(4)	Zn(4) - S(6) - S(4)	120.55(15)
S(2) - W(1) - S(4)	110.67(6)	W(3) - S(6) - S(4)	45.02(11)
S(2) - W(1) - S(4)	111.27(6)	W(1) - S(7) - W(3)	25.08(4)
S(4) - W(1) - S(4)	106.54(8)	W(1) - S(7) - S(2)	115.71(16)
Zn(2) - W(1) - S(7)	75.80(5)	W(3) - S(7) - S(2)	140.62(17)
W(3) - W(1) - S(7)	104.20(5)	Zn(3) - S(8) - W(4)	78.88(6)

Bond Angles /°			
S(2) - W(1) - S(7)	22.69(6)	Zn(3) - S(8) - S(3)	134.49(15)
S(2) - W(1) - S(7)	128.98(7)	W(4) - S(8) - S(3)	55.81(12)
S(4) - W(1) - S(7)	100.91(7)	C(11) - P(1) - C(21)	106.88(10)
Zn(2) - W(1) - S(7)	75.80(5)	C(11) - P(1) - C(31)	110.58(9)
W(3) - W(1) - S(7)	104.20(5)	C(21) - P(1) - C(31)	113.24(11)
S(2) - W(1) - S(7)	128.98(7)	C(11) - P(1) - C(41)	114.14(11)
S(2) - W(1) - S(7)	22.69(6)	C(21) - P(1) - C(41)	103.29(9)
S(4) - W(1) - S(7)	95.97(7)	C(31) - P(1) - C(41)	108.60(10)
S(4) - W(1) - S(7)	95.97(7)	P(1) - C(11) - C(12)	112.62(12)
S(4) - W(1) - S(7)	100.91(7)	P(1) - C(11) - C(16)	127.55(12)
S(7) - W(1) - S(7)	151.61(10)	C(12) - C(11) - C(16)	119.78(13)
Zn(1) - W(2) - W(4)	179.99	C(11) - C(12) - C(13)	120.10(12)
Zn(1) - W(2) - S(1)	53.10(4)	C(12) - C(13) - C(14)	119.87(10)
W(4) - W(2) - S(1)	126.90(4)	C(13) - C(14) - C(15)	120.20(10)
Zn(1) - W(2) - S(1)	53.10(4)	C(14) - C(15) - C(16)	119.86(11)
W(4) - W(2) - S(1)	126.90(4)	C(11) - C(16) - C(15)	120.07(11)
S(1) - W(2) - S(1)	106.20(8)	P(1) - C(21) - C(22)	121.16(13)
Zn(1) - W(2) - S(3)	124.20(4)	P(1) - C(21) - C(26)	118.10(11)
W(4) - W(2) - S(3)	55.80(4)	C(22) - C(21) - C(26)	120.75(13)
S(1) - W(2) - S(3)	109.24(6)	C(21) - C(22) - C(23)	119.10(12)
S(1) - W(2) - S(3)	110.21(6)	C(22) - C(23) - C(24)	120.16(11)
Zn(1) - W(2) - S(3)	124.20(4)	C(23) - C(24) - C(25)	120.56(10)
W(4) - W(2) - S(3)	55.80(4)	C(24) - C(25) - C(26)	119.25(11)
S(1) - W(2) - S(3)	110.21(6)	C(21) - C(26) - C(25)	119.90(11)
S(1) - W(2) - S(3)	109.24(6)	P(1) - C(31) - C(32)	112.63(12)
S(3) - W(2) - S(3)	111.60(8)	P(1) - C(31) - C(36)	126.87(12)
Zn(1) - W(2) - S(5)	81.80(5)	C(32) - C(31) - C(36)	120.48(13)
W(4) - W(2) - S(5)	98.20(5)	C(31) - C(32) - C(33)	119.46(12)
S(1) - W(2) - S(5)	134.90(7)	C(32) - C(33) - C(34)	120.15(10)
S(1) - W(2) - S(5)	28.72(5)	C(33) - C(34) - C(35)	119.97(10)
S(3) - W(2) - S(5)	94.34(7)	C(34) - C(35) - C(36)	119.86(11)
Zn(1) - W(2) - S(5)	81.80(5)	C(31) - C(36) - C(35)	119.70(11)
W(4) - W(2) - S(5)	98.20(5)	P(1) - C(41) - C(42)	118.64(12)
S(1) - W(2) - S(5)	28.72(5)	P(1) - C(41) - C(46)	120.92(13)
S(1) - W(2) - S(5)	134.90(7)	C(42) - C(41) - C(46)	120.40(13)
S(3) - W(2) - S(5)	94.85(6)	C(41) - C(42) - C(43)	119.62(11)
S(3) - W(2) - S(5)	94.85(6)	C(42) - C(43) - C(44)	119.75(11)
S(3) - W(2) - S(5)	94.34(7)	C(43) - C(44) - C(45)	120.41(10)
S(5) - W(2) - S(5)	163.61(10)	C(44) - C(45) - C(46)	119.47(11)
Zn(4) - W(3) - W(1)	179.99	C(41) - C(46) - C(45)	120.09(12)

Table A5.2.2 Bond lengths and angles in the superstructure of tetragonal form of $(PPh_4)_2Zn(WS_4)_2$.

Appendix 5.3 Fractional atomic coordinates for monoclinic $(PPh_4)_2Zn(WS_4)_2$

Atom	*x/a*	*y/b*	*z/c*	U_{iso} /Å^2
W1	0.1830 (3)	0.0195 (4)	-0.0784 (4)	0.125 (3)
W2	0.2612 (3)	0.3761 (5)	0.0079 (4)	0.125 (3)
Zn1	0.2214 (7)	0.194 (1)	-0.0312 (8)	0.084 (6)
S1	0.286 (1)	0.078 (2)	-0.047 (1)	0.168 (5)
S2	0.168 (1)	-0.030 (2)	-0.190 (2)	0.168 (5)
S3	0.179 (1)	-0.087 (2)	-0.013 (2)	0.168 (5)
S4	0.106 (1)	0.127 (2)	-0.065 (1)	0.168 (5)
S5	0.253 (2)	0.277 (2)	0.083 (2)	0.168 (5)
S6	0.239 (2)	0.320 (2)	-0.100 (2)	0.168 (5)
S7	0.191 (1)	0.459 (2)	0.018 (2)	0.168 (5)
S8	0.382 (1)	0.430 (2)	0.054 (2)	0.168 (5)
P1	0.8851 (5)	0.327 (1)	0.2266 (6)	0.112 (5)
P2	0.5391 (5)	0.092 (1)	0.2111 (6)	0.112 (5)
C11	0.760	0.244	0.127	0.112 (5)
C12	0.686	0.241	0.077	0.112 (5)
C13	0.745	0.397	0.147	0.112 (5)
C14	0.671	0.393	0.097	0.112 (5)
C15	0.789	0.322	0.162	0.112 (5)
C16	0.642	0.316	0.062	0.112 (5)
C21	1.025	0.350	0.207	0.112 (5)
C22	1.075	0.346	0.168	0.112 (5)
C23	0.926	0.290	0.102	0.112 (5)
C24	0.977	0.286	0.062	0.112
C25	0.950	0.322	0.174	0.112
C26	1.052	0.314	0.095	0.112
C31	0.905	0.507	0.390	0.112
C32	0.894	0.429	0.350	0.112
C33	0.925	0.581	0.287	0.112
C35	0.920	0.583	0.358	0.112
C34	0.914	0.504	0.247	0.112
C36	0.899	0.428	0.279	0.112
C41	0.986	0.128	0.364	0.112
C42	0.972	0.197	0.314	0.112
C43	0.858	0.140	0.367	0.112
C44	0.845	0.209	0.318	0.112
C45	0.929	0.099	0.391	0.112
C46	0.902	0.238	0.291	0.112
H11	0.792	0.191	0.138	0.112
H12	0.665	0.185	0.052	0.112
H13	0.766	0.453	0.172	0.112
H14	0.639	0.447	0.087	0.112
H16	0.589	0.313	0.027	0.112
H21	1.042	0.373	0.260	0.112
H22	1.129	0.366	0.191	0.112
H23	0.873	0.270	0.078	0.112
H24	0.960	0.263	0.010	0.112
H26	1.088	0.311	0.067	0.112
H31	0.901	0.508	0.441	0.112
H32	0.883	0.374	0.373	0.112
H33	0.936	0.636	0.264	0.112
H34	0.918	0.503	0.196	0.112
H35	0.928	0.638	0.387	0.112
H41	1.037	0.099	0.381	0.112
H42	1.013	0.218	0.295	0.112
H43	0.817	0.119	0.386	0.112

Atom	*x/a*	*y/b*	*z/c*	U_{iso} /Å^2
H44	0.794	0.238	0.301	0.112
H45	0.939	0.049	0.427	0.112
C51	0.477	0.199	0.088	0.112
C52	0.462	0.223	0.014	0.112
C53	0.549	0.076	0.069	0.112
C54	0.534	0.101	-0.005	0.112
C55	0.520	0.125	0.116	0.112
C56	0.491	0.174	-0.032	0.112
C61	0.643	0.150	0.344	0.112
C62	0.690	0.211	0.390	0.112
C63	0.604	0.256	0.245	0.112
C64	0.651	0.318	0.292	0.112
C65	0.600	0.172	0.271	0.112
C66	0.694	0.295	0.364	0.112
C71	0.384	0.078	0.319	0.112
C72	0.452	0.085	0.305	0.112
C73	0.315	0.069	0.188	0.112
C75	0.315	0.070	0.261	0.112
C74	0.383	0.075	0.173	0.112
C76	0.451	0.083	0.231	0.112
C81	0.697	-0.100	0.241	0.112
C82	0.661	-0.019	0.229	0.112
C83	0.583	-0.167	0.248	0.112
C84	0.546	-0.087	0.236	0.112
C85	0.658	-0.173	0.251	0.112
C86	0.585	-0.013	0.227	0.112
H51	0.456	0.234	0.121	0.112
H52	0.431	0.276	-0.006	0.112
H53	0.580	0.023	0.089	0.112
H54	0.555	0.065	-0.038	0.112
H56	0.481	0.192	-0.085	0.112
H61	0.640	0.090	0.362	0.112
H62	0.721	0.195	0.442	0.112
H63	0.573	0.272	0.193	0.112
H64	0.653	0.378	0.273	0.112
H66	0.727	0.339	0.398	0.112
H71	0.384	0.079	0.372	0.112
H72	0.501	0.090	0.346	0.112
H73	0.266	0.063	0.146	0.112
H74	0.383	0.074	0.120	0.112
H75	0.267	0.065	0.272	0.112
H81	0.751	-0.104	0.243	0.112
H82	0.689	0.034	0.223	0.112
H83	0.555	-0.220	0.254	0.112
H84	0.492	-0.082	0.234	0.112
H85	0.684	-0.231	0.259	0.112

Table A5.3.1 Fractional atomic coordinates for the monoclinic form of $(PPh_4)_2Zn(WS_4)_2$.

Appendix 5.4 Fractional atomic coordinates for $(PPh_4)_2Ni(WS_4)_2$

Atom	*x/a*	*y/b*	*z/c*	U_{iso} /Å^2
Ni	0.0	0.0	0.0	0.129 (1)
W	-0.0953 (4)	0.2609 (3)	-0.1236 (3)	0.129 (1)
S1	-0.227 (2)	0.142 (1)	-0.057 (1)	0.129 (1)
S2	0.135 (2)	0.130 (1)	-0.085 (1)	0.129 (1)
S3	-0.108 (1)	0.355 (1)	-0.021 (1)	0.129 (1)
S4	-0.137 (1)	0.375 (1)	-0.309 (1)	0.129 (1)
P	0.5782 (6)	0.2443 (5)	0.3395 (5)	0.153 (4)
C11	0.5259	0.47566	0.15502	0.153 (4)
C12	0.56151	0.58196	0.0855	0.153 (4)
C13	0.75572	0.39576	0.27283	0.153 (4)
C14	0.79133	0.50207	0.20332	0.153 (4)
C15	0.623	0.38256	0.24868	0.153 (4)
C16	0.69423	0.59516	0.10965	0.153 (4)
C21	0.47413	0.1369	0.22396	0.153 (4)
C22	0.36536	0.12709	0.16466	0.153 (4)
C23	0.2892	0.31848	0.24216	0.153 (4)
C24	0.18043	0.30867	0.18286	0.153 (4)
C25	0.43605	0.23259	0.26271	0.153 (4)
C26	0.21851	0.21298	0.14411	0.153 (4)
C31	0.90719	-0.09084	0.5044	0.153 (4)
C32	0.77652	0.01322	0.48152	0.153 (4)
C33	0.97915	-0.00364	0.3049	0.153 (4)
C35	1.0085	-0.09927	0.4161	0.153 (4)
C34	0.84848	0.10041	0.28201	0.153 (4)
C36	0.74717	0.10884	0.37032	0.153 (4)
C41	0.33395	0.21243	0.63327	0.153 (4)
C42	0.39009	0.20609	0.5278	0.153 (4)
C43	0.51041	0.31273	0.63571	0.153 (4)
C44	0.56654	0.30639	0.53024	0.153 (4)
C45	0.39411	0.26575	0.68723	0.153 (4)
C46	0.50638	0.25307	0.47628	0.153 (4)
H11	0.43061	0.46618	0.13768	0.153 (4)
H12	0.49179	0.6488	0.01825	0.153 (4)
H13	0.82544	0.32892	0.34008	0.153 (4)
H14	0.88662	0.51155	0.22066	0.153 (4)
H16	0.7198	0.67149	0.05974	0.153 (4)
H21	0.57956	0.07523	0.23871	0.153 (4)
H22	0.3927	0.05839	0.13684	0.153 (4)
H23	0.26186	0.38719	0.26998	0.153 (4)
H24	0.07499	0.37034	0.1681	0.153 (4)
H26	0.14041	0.20594	0.10153	0.153 (4)
H31	0.92826	-0.1595	0.58424	0.153 (4)
H32	0.70378	0.01927	0.54492	0.153 (4)
H33	1.05189	-0.0097	0.2415	0.153 (4)
H34	0.82741	0.16907	0.20218	0.153 (4)
H35	1.10232	-0.17398	0.43253	0.153 (4)
H41	0.25046	0.1787	0.67026	0.153 (4)
H42	0.34689	0.16781	0.48906	0.153 (4)
H43	0.5536	0.35101	0.67445	0.153 (4)
H44	0.65004	0.34012	0.49325	0.153 (4)
H45	0.35381	0.27031	0.76296	0.153 (4)

Table A5.4.1 Fractional atomic coordinates for $(PPh_4)_2Ni(WS_4)$.